UNIVERSIDAD COMPLUTENSE DE MADRID

FACULTAD DE CIENCIAS FÍSICAS

TESIS DOCTORAL

Magnetic tunnel junctions based on complex oxides

Uniones túnel magnéticas basadas en óxidos complejos

MEMORIA PARA OPTAR AL GRADO DE DOCTOR

PRESENTADA POR

Fabián Andrés Cuéllar Jiménez

Directores

Zouhair Sefrioui
Carlos León Yebra

Madrid, 2013

MAGNETIC TUNNEL JUNCTIONS BASED ON COMPLEX OXIDES

Dissertation by:

Fabián Andres Cuéllar Jiménez

for the Physics Doctor degree

Thesis Supervisors:

Zouhair Sefrioui

Carlos León Yebra

Facultad de Ciencias Físicas

Universidad Complutense de Madrid

March 21st, 2012

UNIONES TÚNEL MAGNÉTICAS BASADAS EN ÓXIDOS COMPLEJOS

Disertacion presentada por:

Fabián Andres Cuéllar Jiménez

para optar al título de Doctor en Física

Directores de Tesis:

Zouhair Sefrioui

Carlos León Yebra

Facultad de Ciencias Físicas

Universidad Complutense de Madrid

Marzo 21 de 2012

RESUMEN

La espintrónica es un campo en desarrollo con miras a ampliar las capacidades de la tecnología actual principalmente por la posibilidad de manipular otro grado de libertad (espín) del electrón, lo que representa la posibilidad de actualizar o crear nuevos dispositivos, como por ejemplo la (actualmente comercial) MRAM basada en válvulas de espín. Cuando una capa aislante ultradelgada se crece en medio de dos electrodos metálicos ferromagnéticos se tiene una unión túnel magnética (MTJ), y la magnitud de la corriente que puede atravesar este dispositivo depende de las alineaciones relativas de las magnetizaciones de los electrodos. Al medir la resistencia del dispositivo en la dirección perpendicular a las capas mientras se aplica un campo magnético externo variable, se registra un cambio en la resistencia en los valores de campo magnético correspondientes a los campos coercitivos de cada una de las capas ferromagnéticas. Dicho cambio es llamado magneto-resistencia túnel (TMR), y permite el desarrollo de dispositivos para almacenamiento de memoria.

Los óxidos complejos de metales de transición son sistemas electrónicos altamente correlacionados que ofrecen diagramas de fases de una riqueza no exhibida por otros sistemas. De hecho un material puede cambiarse, por ejemplo, de ferromagnético a antiferromagnético o de metal a aislante, únicamente modificando la concentración electrónica con pequeñas perturbaciones tales como un campo eléctrico o simplemente una tensión epitaxial, ofreciendo versatilidad mayor que los semiconductores convencionales. Estas son las razones por las cuales se decidió estudiar sistemas espintrónicos basados en heteroestructuras de óxidos complejos. Entre los óxidos utilizados se encuentran las manganitas, los titanatos y los cupratos. La manganita de lantano $LaMnO_3$ (LMO) es un aislante de Mott, y

al doparle con metales de transición se incluyen huecos en su estructura electrónica que disminuyen la repulsión electrónica y llevan al material a la transición metal-aislante (MIT). Las manganitas ofrecen una riqueza de fases difícilmente observable en otros compuestos. La manganita de La y Ca $La_{0.7}Ca_{0.3}MnO_3$ (LCMO) y la manganita de La y Sr $La_{0.7}Sr_{0.3}MnO_3$ (LSMO) son ferromagnéticas con temperaturas de Curie (T_C) de 250 K y 340 K respectivamente; la manganita de La y Ca $La_{0.3}Ca_{0.7}MnO_3$ (LC7MO) con distinta concentración de huecos (x = 0.7) es antiferromagnética con temperatura de Neél (T_N) de 140 K.

A continuación se resume el trabajo realizado durante el período de tesis doctoral y el contenido de la memoria, haciendo especial énfasis en los objetivos, resultados y conclusiones de la investigación realizada. La primera etapa en la realización del trabajo de investigación consistió en la implementación y actualización del sistema de caracterización de magneto-transporte, donde se realizaron tareas de renovación del cableado de instrumentación en el criostato de medidas, y se realizó el diseño y fabricación de portamuestras para microcircuitos en el sistema de caracterización eléctrica. Igualmente se llevó a cabo la optimización de las etapas eléctricas en el conjunto criostato-controladores-medidores y la actualización del conjunto de programas para el sistema de medida: migración al entorno de programación LabVIEW 7, desde los controladores de cada uno de las unidades hasta los instrumentos virtuales particulares para cada tipo de medida. Finalmente es relevante mencionar el diseño e implementación de medidas a cuatro puntas en microcircuitos, tanto a nivel procedimental como al nivel informático.

Fruto del trabajo de investigación realizado se han adquirido y desarrollado distintas técnicas y habilidades experimentales que se relacionan a

continuación: control de las técnicas de crecimiento de películas delgadas por pulverización catódica y evaporación; técnicas de micro-fabricación por litografía óptica como los ataques por plasma y procesamiento de las resinas ópticas; técnicas de caracterización estructural por difracción y reflexión de rayos X; técnicas de caracterización eléctrica por magneto-transporte; técnicas de nano-fabricación por litografía de haz de electrones. Asimismo el trabajo ha permitido la familiarización con otras técnicas de caracterización estructural: STEM. EELS, XNR, AFM, así como con técnicas de caracterización magnética: VSM, SQUID, PNR, XMCD, MFM.

Los objetivos del trabajo de investigación de tesis son:

- Diseñar un proceso de micro-fabricación que permita obtener uniones túnel magnéticas a partir de heteroestructuras de películas delgadas
- Aplicar el proceso diseñado a los óxidos complejos ya utilizados en el grupo de investigación, como lo son las manganitas LCMO, LSMO, LMO el titanato STO y el cuprato PBCO
- Establecer los criterios procedimentales necesarios para asegurar la correcta caracterización del transporte dependiente de espín en los dispositivos fabricados, y actualizar el sistema de medidas eléctricas para cumplir con dichos criterios.
- Identificar estados interfaciales en heteroestructuras de óxidos complejos (de predicción teórica o de reporte experimental) que puedan ser provechosos para el desempeño de dispositivos espintrónicos e imbuirlos en uniones túnel magnéticas para su caracterización experimental.
- Estudiar la posibilidad de usar el estado predicho en la interfase de manganitas ferromagnética-antiferromagnética [1-3], para su aplicación en dispositivos de espintrónica.

- Estudiar las características de transporte electrónico de la interfase titanato de estroncio dopado con Nb (NSTO)- manganita de La y Ca (LCMO). con objeto de utilizar tal interfase en futuros dispositivos basados en manganitas que requieran de un sustrato conductor.
- Utilizar el estado magnético reportado por Barriocanal et al. En la interfase de manganita-titanato (LMO-STO) [4], dentro de uniones túnel magnéticas y estudiar su desempeño.
- Estudiar el efecto del momento magnético inducido en la interfase manganita-cuprato reportado por varios autores [5, 6], en las características de magneto-transporte de uniones túnel magnéticas.

El primer capítulo de la memoria de tesis es una introducción que contiene los elementos de mención continua a lo largo de toda la memoria. Inicialmente se resume la teoría necesaria para la compresión y tratamiento de la fenomenología principal de este trabajo de investigación, literalmente: transporte electrónico dependiente de espín por efecto túnel en uniones túnel magnéticas. Inicialmente se presenta el efecto túnel, a continuación se describe el tratamiento del transporte electrónico por efecto túnel a través del modelo de Jullière; se amplía luego al transporte electrónico dependiente de espín por efecto túnel para llegar finalmente al dispositivo principal de esta tesis: las uniones túnel magnéticas. Ya entrada la descripción fundamental de dichos fenómenos, se procede a la explicación de los fenómenos que constituyen la espintrónica actual: efecto túnel de electrones polarizados a través de manganitas medio metálicas, filtrado de espines y fenómenos de transporte dependiente de espín en interfases; todos estos elementos especialmente enfocados a su aplicación en dispositivos de óxidos complejos. Dado que el principal elemento material de este conjunto de experimentos es la manganita de Lantano y Calcio (principalmente con

dopado del 30% de huecos) la última sección del capítulo introductorio está dedicada a la descripción de este compuesto óxido ($La_{1-x}Ca_xMnO_3$).

El segundo capítulo del escrito contiene la descripción de las técnicas de caracterización utilizadas a lo largo del trabajo de investigación. Para la caracterización de propiedades estructurales se describen las técnicas de difracción y reflexión de rayos x en las diferentes configuraciones que tienen relevancia en la caracterización de películas delgadas. Así mismo la microscopía de transmisión electrónica y su utilización para la espectroscopia de pérdidas de energía electrónica. La caracterización eléctrica se realizó por medio de la geometría de corriente perpendicular al plano, que se describe antes de las técnicas de caracterización magnética: magnetometría de muestra vibrante, magnetometría SQUID (dispositivo de interferencia cuántica en superconductor) y reflexión de neutrones polarizados. Finalmente se describe la técnica utilizada para la caracterización de propiedades magnéticas en interfases llamada dicroísmo circular magnético.

La segunda etapa en la realización del trabajo consistió en el diseño e implementación del procedimiento de fabricación de los microcircuitos contenedores de las uniones túnel magnéticas a partir de heteroestructuras compuestas por películas delgadas. Dicha etapa del trabajo de investigación está descrita en el Capítulo 3 de la memoria, dedicado a las técnicas de fabricación utilizadas, comenzando con el sistema de pulverización catódica para crecimiento de películas delgadas, seguida por una descripción de los conceptos de litografía óptica, los equipos utilizados para la micro-fabricación de uniones, tales como técnicas de remoción húmeda, técnicas de remoción seca en plasma y asistida químicamente. El tercer capítulo se cierra con la presentación del diseño creado en cuatro etapas de litografía, y las etapas de deposición, litografía y remoción que deben seguirse para obtener los micro-circuitos contenedores de uniones túnel magnéticas.

Finalmente se listan los detalles concernientes a cada una de las muestras procesadas con el procedimiento presentado. La siguiente etapa del trabajo de investigación consiste en la fabricación de diferentes dispositivos de óxidos complejos enfocados hacia el estudio de sus características de transporte. Usando el método de fabricación de uniones túnel magnéticas en microcircuito se estudiaron los sistemas que constituyen cada uno de los capítulos siguientes.

El capítulo cuarto presenta el estudio de la interfase manganita-titanato usando el micro-circuito diseñado, se crecieron películas delgadas de manganita sobre titanato de estroncio dopado con niobio (NSTO\\ LCMO). La caracterización del transporte reveló comportamiento del tipo barrera Schottky, además del comportamiento inusual de la permitividad eléctrica del titanato al variar la temperatura de trabajo. Con la finalidad de describir correctamente las características de corriente vs. voltaje se propone en esta tesis un modelo fenomenológico que tiene en cuenta el comportamiento observado de la permitividad eléctrica del titanato.

El quinto capítulo de esta memoria contiene un estudio que toma como punto de partida el estudio realizado por Barriocanal et al. [4] acerca del estado fundamental magnético modificado en la interfase de los materiales titanato de estroncio y manganita de lantano (STO\ LMO). Se utiliza entonces dicho estado dentro de la barrera túnel de uniones túnel magnéticas fabricadas con manganita de lantano y estroncio dopada 30 % de huecos (STO\\ LSMO\ STO\ LMO\ STO\ LSMO). Se encontraron dos diferentes dependencias con la temperatura en la magnetoresistencia túnel del dispositivo, en el rango de alto voltaje aplicado (200 mV < V < 400 mV) la magnetoresistencia túnel presenta escasos cambios en su magnitud hasta los 60 K, mientras que decrece fuertemente al aumentar la temperatura en el rango de bajo voltaje (V < 200 mV). Se observa entonces que el dispositivo

presenta un estado muy estable por debajo de una temperatura límite, bajo la condición de que se aplique un voltaje de trabajo alto, dicha estabilidad se explica en términos del estado fundamental magnético diseñado en la interfase de la tricapa utilizada como barrera.

El sexto capítulo de esta memoria describe el estudio de dispositivos creados con dos fases distintas de la manganita de lantano y calcio, al utilizar la fase metálica ferromagnética (LCMO) y la fase aislante antiferromagnética (LC7MO) como componentes de uniones túnel magnéticas se obtuvo en la interfase un estado intermedio de acuerdo a la propuesta teórica de Salafranca et al. [7]. Utilizando titanato de estroncio dopado con niobio (NSTO) como sustrato conductor, se estudiaron bicapas metal-aislante-metal (NSTO\\ LC7MO\ LCMO). Las características magnéticas revelaron orden magnético en la manganita aislante, las medidas de magneto-transporte revelaron transporte electrónico dependiente de espín por efecto túnel, que al originarse en el orden ferromagnético del aislante se corresponde con el fenómeno de filtrado de espines. Además se presenta un estudio realizado en este mismo grupo de investigación, en el cual se reemplaza el sustrato conductor por otra capa de manganita ferromagnética (LCMO\ LC7MO\ LCMO). En dichas tricapas se observaron los fenómenos de filtrado de espines (hasta la temperatura de Néel de la capa de LC7MO) y el transporte electrónico dependiente de espín por efecto túnel (hasta la temperatura de Curie de la capa de LCMO más voluminosa). Se presenta además el análisis de las características de transporte de la forma propuesta por Müller et al. [8], que muestra el comienzo del régimen de transporte del tipo Fowler-Nordheim dependiente de la temperatura y el voltaje.

El capítulo séptimo contiene el estudio del transporte electrónico dependiente de espín por efecto túnel en el sistema compuesto por manganita de lantano y calcio (LCMO) como electrodos ferromagnéticos y el

cuprato de praseodimio y bario $PrBa_2Cu_3O_7$ (PBCO) como barrera. Las uniones túnel magnéticas (LCMO\ PBCO\ LCMO) presentaron supresión de la magnetoresistencia túnel para bajas temperaturas. Las medidas de caracterización magnética por reflexión de neutrones polarizados revelaron diferentes anisotropías magneto-cristalinas para ambos electrodos, que domina el comportamiento de los dispositivos en baja temperatura. El estudio de estado magnético en interfase XMCD reveló momento magnético inducido en los átomos de cobre posicionados en la interfase, alineados antiferromagnéticamente con sus primeros átomos vecinos de manganeso. Dos tipos anómalos de magneto-resistencia por efecto túnel se observaron, y en esta tesis se proponen sendos escenarios para explicar cada uno de los comportamientos no convencionales observados. Uno de ellos es de especial importancia tecnológica ya que permite acceder a la conmutación de estados resistivos por medio del voltaje aplicado en campo magnético aplicado igual a cero, y es compatible con cálculos realizados por Salafranca y Okamoto en sistemas manganita-cuprato-manganita [9].

A continuación se resumen los principales resultados y conclusiones del trabajo de investigación realizado. Las uniones Schottky NSTO\\ LCMO fueron analizadas por medio de los modelos de Schottky, emisión termoiónica y emisión de campo, y se encontraron valores del factor de idealidad que son físicamente no significativos al salir del rango de interpretación del modelo. Por otro lado las alturas de barrera Schottky encontradas están en acuerdo con los valores reportados para sistemas similares. También se estudiaron utilizando la aproximación propuesta por H. Hwang et al. [10] corrigiendo la energía térmica en las ecuaciones de tunelamiento por una función de origen empírico, los resultados obtenidos mejoran pero aún no explican el origen físico de las características del transporte del dispositivo. Se propone en esta tesis una corrección basada en

el comportamiento de la permitividad eléctrica del STO [11], incluyendo dicho modelo fenomenológico las características de transporte de las uniones Schottky se explicaron con un modelo corregido que reproduce con fiabilidad los resultados experimentales y explica las características de transporte del sistema asumiendo cambios en las cantidades físicas adecuadas.

Las características de transporte de los dispositivos con los materiales NSTO\\ LC7MO\ LCMO exhibieron la presencia de magneto-resistencia túnel (TMR), con una magnitud máxima de 20 % a 60 K y 10 mV, magnitud que disminuye al aumentar la temperatura hasta 140 K, a partir de dicha temperatura no se observa TMR. La característica de resistencia contra temperatura muestra las dos transiciones MIT de ambas manganitas a 250 K (LCMO) y 140 K (LC7MO), el límite superior de funcionamiento de los dispositivos es 140 K, que es una temperatura límite particularmente alta ya que los filtros de espín más estudiados (basados en compuestos de europio) sólo trabajan hasta 4 K. Las características de transporte observadas son consistentes únicamente con el fenómeno "filtrado de espín" debido a ferromagnetismo inducido en la LC7MO o en la interfase entre las dos manganitas, de forma que el transporte es análogo a una capa aislante ultradelgada de LC7MO ferromagnética. Esta es la primera vez que se evidencia ferromagnetismo inducido en el sistema LC7MO\ LCMO por medio del filtrado de espines [12], también es este el primer filtro de espín fabricado con óxidos complejos que trabaja hasta 140 K (se observa comúnmente por debajo de 10 K).

Las uniones túnel magnéticas basadas en el estado magnético inducido en la interfase STO\ LMO\ STO realizado por Barriocanal [4, 13], se observó la presencia de momento magnético inducido en la tricapa STO\ LMO\ STO. Por medio de caracterización magnética de susceptibilidad AC se obsevaron las

transiciones magnéticas de las capas inferior y superior de LSMO utilizadas como electrodos ferromagnéticos, además se observó en 60 K la temperatura de transición magnética de la tricapa [STO\ LMO\ STO]. Las características de magneto-transporte exhibieron TMR casi independiente de la temperatura para los voltajes 200 mV < *V* < 400 mV en temperaturas inferiores a 60 K; en voltajes pequeños se observó una TMR máxima de 100 % en 15 K, seguida por una caída rápida al aumentar la temperatura hasta 135 K donde TMR = 0 %. Estas características llevan a la conclusión de que el estado magnético inducido en la tricapa [STO\ LMO\ STO] es responsable por la elevada estabilidad de la TMR en voltajes altos (hasta 60 K). De esta forma se demuestra cómo la utilización de interfases diseñadas artificialmente puede mejorar las características de magneto-transporte de los dispositivos de espintrónica. Particularmente este capítulo deja abierta una puerta para futuras investigaciones usando estados artificiales como parte activa de los dispositivos de óxidos complejos, con muchas posibilidades aún sin explorar.

En un trabajo previo Sefrioui et al. [14] estudiaron la TMR en MTJs de LCMO\ PBCO\ LCMO dentro del rango 80 K < *T* < 110 K. En esta tesis se realizó un estudio midiendo en un rango de temperatura más amplio. Además se encontró la necesidad de conocer el límite inferior de espesor para que la LCMO constituya un electrodo inferior metálico-ferromagnético, y para ello se fabricaron conjuntos de muestras con diferentes espesores de electrodo inferior. La caracterización por Reflectometría de Neutrones Polarizados (PNR) puso en evidencia las anisotropías magnetocristalinas de las capas, de forma que el electrodo inferior tiene el eje fácil a lo largo de [100] mientras el electrodo superior lo tiene a lo largo de [110]. En las características de transporte se observó también una contribución no convencional a la TMR, debida a la formación de dominios alineados con el eje fácil del electrodo superior. Estos resultados muestran cómo la LCMO puede tener su eje fácil

en cualquiera de las dos direcciones de su anisotropía biaxial, según el espesor de capa y el del material subyacente, además de su efecto en la polarización de espín y la resistencia del dispositivo, resultando en diferentes estados de resistencia de acuerdo a la configuración magnética relativa de las capas.

La caracterización magnética de interfase por dicroísmo circular magnético de rayos X (XMCD) mostró momento magnético inducido en los primeros átomos de Cu de manera análoga a la observada en otros cupratos isoestructurales junto a la LCMO [5]. Tal momento inducido se observó desde baja temperatura hasta la temperatura de Curie de la capa más voluminosa de manganita. La supresión de magnetoresistencia túnel observada se explica por medio de las diferentes anisotropías magneto-cristalinas de los electrodos, que evitan la obtención de un estado magnético de alineación antiparalela, de forma tal que no se observa la conmutación resistiva característica del transporte electrónico dependiente de espín por efecto túnel. La diferencia en anisotropías magnetocristalinas solamente es equiparable energéticamente por la inducción magnética del campo externo en altas temperaturas, régimen en el cuál la magnetoresistencia túnel se hace finalmente observable. Además se estudió un mecanismo de conmutación resistiva por medio de voltaje aplicado en campo magnético igual a cero. Este resultado es de remarcable importancia tecnológica, ya que por medio del mecanismo aquí presentado se podría plantear un método para conmutar los estados resistivos de las válvulas de espín aplicando únicamente un campo eléctrico. Un posible escenario para explicar el comportamiento observado se basa en la aparición de un momento magnético inducido en los átomos de cobre localizados en la interfase y a su interacción con su capa ferromagnética no-inmediatamente adyacente,

mostrando la importancia de la hibridación orbital en las interfases y su posible aplicación en dispositivos basados en óxidos complejos.

Referencias

[1] S. Yunoki, A. Moreo, E. Dagotto, S. Okamoto, S. S. Kancharla, and A. Fujimori, Physical Review B 76 (2007) 064532.

[2] D. Niebieskikwiat, L. E. Hueso, J. A. Borchers, N. D. Mathur, and M. B. Salamon, Physical Review Letters 99 (2007) 247207.

[3] J. Salafranca, M. J. Calderón, and L. Brey, Physical Review B 77 (2008) 014441.

[4] J. Garcia-Barriocanal, F. Y. Bruno, A. Rivera-Calzada, Z. Sefrioui, N. M. Nemes, M. Garcia-Hernández, J. Rubio-Zuazo, G. R. Castro, M. Varela, S. J. Pennycook, C. León, and J. Santamaría, Advanced Materials 22 (2010) 627.

[5] J. Chakalian, J. W. Freeland, H. U. Habermeier, G. Cristiani, G. Khaliullin, M. v. Veenendaal, and B. Keimer, Science 318 (2007) 1114.

[6] C. Visani, in Applied Physics, Vol. PhD in Physics, Universidad Complutense de Madrid, Madrid, 2010.

[7] M. J. Calderón, J. Salafranca, and L. Brey, Physical Review B 78 (2008) 024415.

[8] K. I. Lee, S. J. Joo, J. H. Lee, K. Rhie, T.-S. Kim, W. Y. Lee, K. H. Shin, B. C. Lee, P. LeClair, J. S. Lee, and J. H. Park, Physical Review Letters 98 (2007) 107202.

[9] J. Salafranca and S. Okamoto, Physical Review Letters 105 (2010) 256804.

[10] T. Susaki, N. Nakagawa, and H. Y. Hwang, Physical Review B 75 (2007) 104409.

[11] K. A. Müller and H. Burkard, Physical Review B 19 (1979) 3593.

[12] Z. Sefrioui, C. Visani, M. J. Calderón, K. March, C. Carrétéro, M. Walls, A. Rivera-Calzada, C. León, R. L. Anton, T. R. Charlton, F. A. Cuéllar, E. Iborra, F. Ott, D. Imhoff, L. Brey, M. Bibes, J. Santamaria, and A. Barthelemy, Advanced Materials 22 (2010) 5029.

[13] J. Garcia-Barriocanal, J. C. Cezar, F. Y. Bruno, P. Thakur, N. B. Brookes, C. Utfeld, A. Rivera-Calzada, S. R. Giblin, J. W. Taylor, J. A. Duffy, S. B. Dugdale, T. Nakamura, K. Kodama, C. Leon, S. Okamoto, and J. Santamaria, Nature Communications (2010)

[14] Z. Sefrioui, V. Cros, A. Barthelemy, V. Peña, C. León, J. Santamaría, M. Varela, and S. J. Pennycook, Applied Physics Letters 88 (2006) 022512.

CONTENTS

1 INTRODUCTION

1.1 Motivation

Spin-based electronics, commonly known as spintronics, is an emerging field which fully exploits the quantum nature of electrons [1, 2]. It relies on the magnetic degree of freedom (spin) of the electrons to control their conduction. Manifestations of electron spin are mostly found in ferromagnetic metals, where an imbalance of spin populations at the Fermi surface results in a non-null charge carrier spin polarization. In that case magnetic fields can be used to manipulate spin polarized electrical currents, providing an additional channel of information as well as an additional degree of freedom for designing novel devices. In this context, and in good approximation, the current of spin-up and spin-down electrons behave independently from each other with separate conduction channels, having an asymmetric behavior due to a different carrier density and / or mobility [3]. Typical spintronic devices have already made the way towards applications, namely the Giant Magnetoresistance (GMR) read head [4, 5], which detects the magnetically stored data by a change of resistance in the read head originated by the magnetic field of the bit. Another application is data storage itself using Magnetic Tunnel Junctions (MTJs), which consist of a non-magnetic ultrathin insulating layer separated by two metallic ferromagnetic electrodes. The device resistance can be again controlled by an applied magnetic field.

The experimental development of spintronics is first of all a challenge for physicists and materials scientists. As a first challenge there is the need to develop a highly spin polarized current source. The band exchange splitting in ferromagnets leads to different carrier densities of the two spin channels,

and thus the ideal materials to be used as a spin-polarized current source are the half-metals, which show a metallic behavior for one spin direction and semiconducting behavior for the other one [6, 7]. Some examples rely on complex manganese oxides which have been used as electrodes in MTJs [8-14]. The high conduction band spin polarization of manganites —confirmed for $La_{0.7}$ $Sr_{0.3}MnO_3$ (LSMO) by photoemission spectroscopy [15, 16]— was expected to yield large tunnel magneto-resistance (TMR). Indeed, transport experiments unveiling large spin polarization degrees confirm this expectation (P = 95 % at 4 K [3], and 86 % at 77 K [11, 17]).

In contrast to conventional spin polarized tunneling devices which use a ferromagnetic metal as spin polarized electron source, the novel spin filter approach uses a ferromagnetic tunnel barrier to generate a spin polarized current (spin filter effect). In this type of MTJ the tunneling current is modulated through the barrier height dependence on the magnetization configuration, relative to each tunneling electron spin direction, and thus Zeeman exchange splitting is used to obtain different current densities for each spin sub-band [18]. The advantage of this highly spin-polarized current source is that even though the electron source is not spin polarized the resulting tunneling current *is* spin polarized, since one spin carrier state tunnels through the barrier preferentially. The spin-filter effect has been well observed in Europium chalcogenide tunnel barriers made of EuS [19, 20], EuSe [21] and EuO [22]. However, the rapid temperature TMR decrease due to the very low Eu chalcogenides Curie temperature, together with their low chemical compatibility with metallic electrodes limit their potential for spin filtering applications. In this regard large efforts have been made in using ferromagnetic insulators (FMI) complex oxides with higher Curie temperature to be integrated in magnetic tunnel junctions as barriers, but the scarce examples of FMI complex oxides based tunnel junctions show also a rapid decrease of TMR with increasing temperature, vanishing at

temperatures well below the Curie temperature of the bulk FMI barriers [23-25]. Thus native FMI complex oxides spacers as a choice has remained very limited and their operation restricted to very low temperatures.

Recent research interest is also focused on oxide heterostructures made of strongly correlated electron systems, like transition metal oxides (TMO), that exhibit a large set of different behaviors, and where the symmetry breakdown provided by interfaces may result in unexpected novel effects. At interfaces, due to the discontinuity between two different materials causing electronic or atomic reconstructions, several interesting new ground states as the conducting interfacial state between two insulators [26, 27] which may be magnetic [28] or even superconducting [29], or the interfacial ferromagnetism induced between two paramagnets [30], or even the magnetism suppression at manganite-cuprate interfaces [31]. They all are examples showing novel electronic properties arising at interfaces in oxide heterostructures. In this context, the phase diagram wealth exhibited by mixed-valence manganites make them target of study, especially concerning new states arising at interfaces, due to their strong tendency to change their electronic properties under the action of small perturbations.

This thesis comprehends the study of new artificial magnetic states engineered at interfaces between non-magnetic and magnetic materials based on complex oxides, mainly probed by spin-dependent transport characterization, and complemented with structural and magnetic characterization techniques. MTJs are the device used here as primary tools to test the artificial behaviors and functionalities that can be tailored at the interfaces in complex oxide heterostructures. Section 1.10 at the end of this chapter lists in detail the different systems studied in this work as well as the characterization techniques used to reach these goals.

1.2 Electron Tunneling

Quantum physics predicts unexpected behavior that defies ordinary intuition, and tunnel effect, one of the primary derivations of quantum mechanics in solids, is an example. When two conductors, under the effect of a bias potential between them, are separated by an ultrathin insulating barrier, a finite current can be detected across the barrier. This is a current that the classical particle framework does not explain, and then the wave-particle electronic nature must be taken into account. The quantum framework explains the current flow across the barrier by non-null transmission probability across the insulating layer if the electronic wave function decay length is larger than the insulating layer thickness, since then the electron tunneling probability is non-null. Sommerfeld and Bethe [32] in 1930 and Frenkel [33] in 1933 were the first ones to put forward the mechanism behind tunneling in metal-insulator-metal junctions, and experimental evidence of tunneling was clearly visible also in superconducting tunneling junctions [34]. Some overviews of tunneling in solids are found in [35, 36]. The usual setup for tunneling junctions in solids is achieved by separating two metallic sheets M_1, M_2 by a thin insulator I (1 nm to 2 nm), which is called a metal-insulator-metal junction (MIM). In the following a model for this structure is presented which considers the MIM junction in one dimension normal to the metal-insulator interfaces. Figure 1-1 shows metals M_1 and M_2 with Fermi levels E_{F1} and E_{F2} respectively separated by a general barrier I, where the work functions W_1 and W_2 represent the required energy to emit an electron from the metal to the vacuum without thermal assistance. The barrier potential is given by $\varphi(x)$, and the probability $D(Ex)$ of an electron tunneling through the potential barrier in the WKB approximation [37] is:

$$D(Ex) = \exp\left(-\frac{4\pi}{h} \int_0^d \sqrt{2m(\varphi(x) - Ex)}\, dx \right) \qquad (1.1)$$

with *x = 0* being the starting point of the barrier, *x = d* being the end point, and $Ex = mv_x^2/2$ the x-direction tunneling electron energy component.

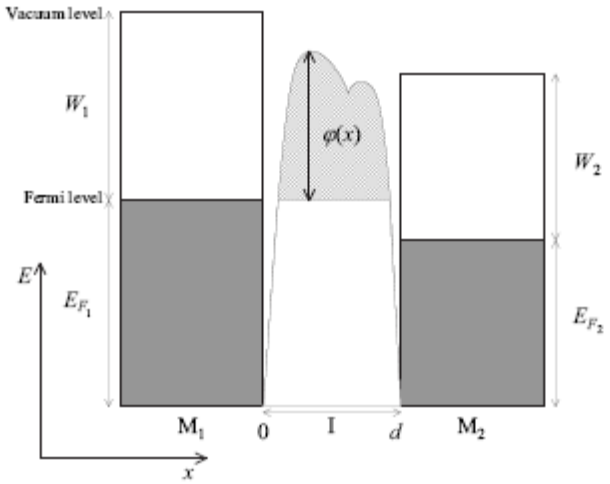

Figure 1-1. Potential schematic of MIM contact with general barrier

If *Ex > φ(x)* over the whole barrier *D(Ex)* has a periodic solution and the electron is transported through the conduction band of the insulator. In the case where *Ex < φ (x)* an exponentially decreasing solution is found for *D(Ex)*. The tunneling current consists of the difference between tunneling currents from M_1 to M_2 and from M_2 to M_1; let us first consider the current from M_1 to M_2 solely. If a bias voltage *U* is applied across the barrier the electrode Fermi levels are shifted against each other, an electron tunnels from an occupied state in M_1 to an unoccupied state in M_2, and the tunneling current is proportional to the Fermi distribution function *f* [38]:

$$j_{1\to 2} \propto \int_{-\infty}^{\infty} \rho_1(E)\,\rho_2(E - eU)\,D(E)\,f(E)\,dE \qquad (1.2)$$

where ρ_1 and ρ_2 are the densities of states (DOS).

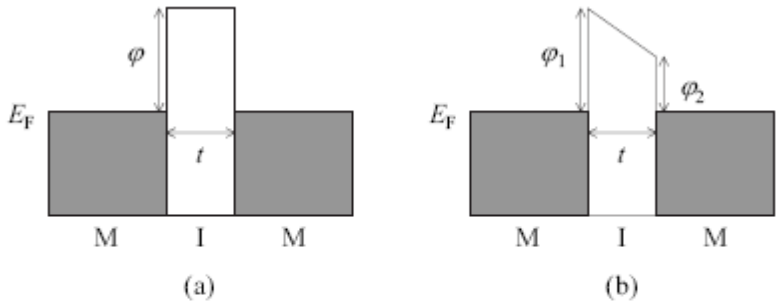

Figure 1-2. Potential schematic of tunnel barrier models (a) Simmons model and (b) Brinkman model

The net tunneling current thus results to:

$$j = j_{1\to 2} - j_{2\to 1}$$
$$j = \frac{4\pi}{\hbar}\int_{-\infty}^{\infty} \rho_1(E)\,\rho_2(E-eU)\,D(E)\big(f(E)-f(E-eU)\big)\,dE \tag{1.3}$$

In the simplest model (Figure 1-2 (a)) the barrier is described by a rectangular potential of height φ and width t which was reported in [39], which reflects the case when both metals have the same Fermi level E_F and identical interfaces to the insulator (the image potential was not included, which rounds the barrier potential and effectively decreases the height and width). The tunneling probability then becomes:

$$D(E) = \exp\left(-\frac{2d}{\hbar}\sqrt{2m(\varphi - E)}\right) \tag{1.4}$$

Simmons [39] continued to develop the resulting current equation for the different voltage regimes. In the intermediate voltage regime ($eU < \varphi$) the tunneling current is given by:

$$j = \frac{e}{2\pi h t^2}\left[\left(\varphi - \frac{eU}{2}\right)\exp\left(-\alpha t\sqrt{\varphi - \frac{eU}{2}}\right) - \left(\varphi + \frac{eU}{2}\right)\exp\left(-\alpha t\sqrt{\varphi + \frac{eU}{2}}\right)\right]$$
$$where, \alpha = \frac{2\sqrt{2m}}{\hbar} = 1.025\left[\frac{1}{\text{Å}\sqrt{eV}}\right] \tag{1.5}$$

Simmons also developed the expression for a junction with different electrodes at [40], and in the low voltage regime ($eU << \varphi$) the current expression becomes:

$$\begin{aligned} j &= \theta\left(U + \gamma U^3\right) where \\ \theta &= \left(\frac{e}{h}\right)^2 \frac{\sqrt{2m\varphi}}{t} \exp\left(-\alpha t\sqrt{\varphi}\right), \\ \gamma &= \frac{\left(\alpha te\right)^2}{96\varphi} - \frac{ate^2}{32}\varphi^{-3/2} \end{aligned} \tag{1.6}$$

Replacing the natural constants with their numerical values the Simmons equation is obtained:

$$j = 3.16\times10^{10}\frac{\sqrt{\varphi}}{t}\exp\left(-1.025t\sqrt{\varphi}\right)\left[U + \left(0.0109\frac{t^2}{\varphi} - 0.032\frac{t}{\varphi^{3/2}}\right)U^3\right] \tag{1.7}$$

Here, the current density j is given in A/cm^2, the barrier thickness t in Å and the barrier height φ in eV.

In practice even junctions with equal electrode materials present different interface properties leading to unequal energy profiles on each side of the insulator. An asymmetric barrier model was reported by Brinkman [41] using a trapezoidal potential barrier model (cf. Figure 1-2 (b)). Such a model describes the barrier by the width t and the potentials φ_1, φ_2 at the metal-insulator interfaces, where the potential spatial function is:

$$\varphi\left(x\right) = \varphi_1 + \frac{x}{t}\left(\varphi_2 - eU - \varphi_1\right) \tag{1.8}$$

Brinkman arrives to an approximate conductivity expression with 10 % accuracy when barriers are thicker than 10 Å and for $\Delta\varphi/\varphi < 1$:

$$\frac{G(U)}{G(0)} = 1 - \frac{A_0 \Delta\varphi}{16\bar{\varphi}^{3/2}} eU + \frac{9A_0^2}{128\bar{\varphi}}(eU)^2, where$$

$$\Delta\varphi = \varphi_2 - \varphi_1, \bar{\varphi} = \frac{\varphi_1 + \varphi_2}{2},$$

$$A_0 = \frac{4\sqrt{2m}t}{3\hbar}, \qquad (1.9)$$

$$G(0) = 3.16 \times 10^{10} \frac{\sqrt{\bar{\varphi}}}{t} \exp\left(-1.025 t\sqrt{\bar{\varphi}}\right)$$

Integration of Eq. (1.9) leads to the Brinkman tunneling current equation:

$$j = G(0)\left(U - 0.0213\frac{t\Delta\varphi}{\bar{\varphi}^{3/2}}U^2 + 0.0109\frac{t^2}{\bar{\varphi}}U^3\right) \qquad (1.10)$$

where current density j is in A/cm^2, the barrier thickness t in Å, and the barrier asymmetry $\Delta\varphi$ and the effective barrier height $\bar{\varphi}$ in eV.

1.3 The Jullière Model

In 1975 Jullière explained his original tunneling magneto-resistance (TMR) results on Fe/Ge/Co junctions [42]. The rationale behind his experiments is that, since electron tunneling is spin dependent, the tunneling current should be dependent on the spin polarization of metallic electrodes when they are ferromagnetic. Tunneling current by First-Order Perturbation Theory is calculated as the summation over all the available "tunneling channels":

$$I_T = \frac{2\pi e}{\hbar}\sum_{\mu,\nu}\Big(f\left[E_\mu\right] - f\left[E_\nu\right]\Big)\left|M_{\mu\nu}\right|^2 \delta\left[E_\nu + U_T - E\mu\right]$$

Where $f\left[E\right]$ is the Fermi-Dirac distribution function, U_T the applied voltage, $M_{\mu\nu}$ the tunneling matrix element between states Ψ_μ and Ψ_ν, and E_μ, E_ν their respective energies. In the limit $T \to 0$ (Fermi-Dirac distributions take the form of step functions), constant *M* and infinitesimal barrier asymmetry, this expression reduces to:

$$\frac{I}{U} \propto \left|M_{\mu\nu}\left(E,V\right)\right|^2 \rho_\mu\left(E_F\right)\rho_\nu\left(E_F\right) \qquad (1.11)$$

Therefore, in this extensive simplification the linearized tunnel conductance is directly related to the electrodes DOS $\left(\rho_\mu, \rho_\nu\right)$ at the Fermi level. Considering spin-dependent tunneling transport, Jullière delivered the following definition of a ferromagnet spin polarization:

$$P = \frac{\rho^{\uparrow}\left(E_F\right) - \rho^{\downarrow}\left(E_F\right)}{\rho^{\uparrow}\left(E_F\right) + \rho^{\downarrow}\left(E_F\right)} \qquad (1.12)$$

In a picture of two electronic spin-independent conduction channels, given the electrodes spin polarization and the requirement of electron spin

conservation during the (elastic) tunneling process, the currents in the parallel and antiparallel electrode magnetization alignments will differ. For instance, majority –corresponding to the spin sub-band with higher population– electrons will tunnel towards majority (minority) empty states in the parallel (antiparallel) configuration. These considerations are summarized in the schematic of Figure 1-3. In fact, magnetically engineered tunnel junctions have worked their way as non-volatile storage cells in high-performance solid-state magnetic random access memories (MRAM) [43, 44]. The TMR ratio may be expressed as:

$$TMR = \frac{I_P - I_{AP}}{I_{AP}} = \frac{R_{AP} - R_P}{R_P} = \frac{2P_{Inj}P_{Col}}{1 - P_{Inj}P_{Col}} \tag{1.13}$$

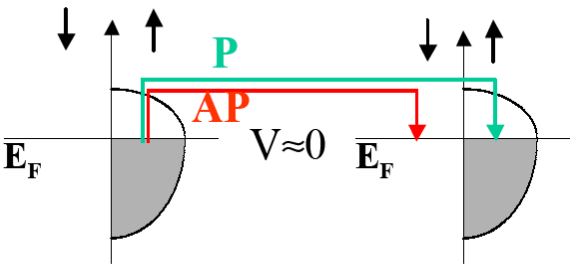

Figure 1-3. Schematic of the spin-dependent tunneling process through an insulating barrier in the special case of half-metallic electrodes when their magnetizations are aligned parallel (P) and antiparallel (AP) to one another. The process is assumed to be purely elastic, so that no spin states mixing occurs

1.4 Spin Dependent Tunneling

The tunneling current spin polarization from a ferromagnet may be defined:

$$PT = \frac{\rho^{\uparrow}(E_F)\left|M^{\uparrow}\right|^2 - \rho^{\downarrow}(E_F)\left|M^{\downarrow}\right|^2}{\rho^{\uparrow}(E_F)\left|M^{\uparrow}\right|^2 + \rho^{\downarrow}(E_F)\left|M^{\downarrow}\right|^2} \tag{1.14}$$

If the tunneling matrix *M* is considered constant, this expression reduces to the much used Eq. (1.12). However, as argued by Mazin [45], the nature of the physical process underlying this spin polarization may result in specific dependencies of *M* on the Fermi velocity (v_F). This is notably the case regarding the Andreev reflection technique, for which $\left|M^{\uparrow}\right|^2 \propto v_F$. Such a technique, originally discussed by Blonder, Tinkham and Klapwijk in 1982 [46], was extended to ferromagnets [47] and used to probe the spin polarization *P* of a variety of ferromagnetic materials [48, 49].

In the tunneling process, $\left|M^{\uparrow}\right|^2 \propto v_F^2$, therefore in the context of spin-dependent tunneling it is more salient to consider the spin polarization as measured through a technique which exploits this transport phenomenon. In 1970 Meservey and Tedrow developed the first technique to measure the magnitude and sign of the spin-polarized tunneling probability from the ferromagnet (FM) by performing tunneling experiments on FM/Al_2O_3/Al junctions and thus the experimental field of spin dependent tunneling (SDT) was founded [50-52]. They used ferromagnet / insulator / superconductor (FM/I/S) tunnel junctions to measure the tunneling current spin polarization originating from various ferromagnetic metals across an alumina insulating barrier. In such experiments electrons tunnel through the barrier to a superconducting Al film which acts as a spin detector. The superconducting DOS has a gap of 2Δ in the quasiparticle spectrum and characteristic singularities at $E = \pm \Delta$. If the thin superconducting film (a few nm or less) is

placed in a magnetic field *H* applied parallel (subscript P) to the film plane, the quasiparticle states in the superconductor split due to the Zeeman interaction of the magnetic field with the electron spin magnetic moment. In this case, the superconductor DOS is the superposition of the up- and down-spin contributions separated by energy of $2\mu_B H$, as shown in Figure 1-4(a).

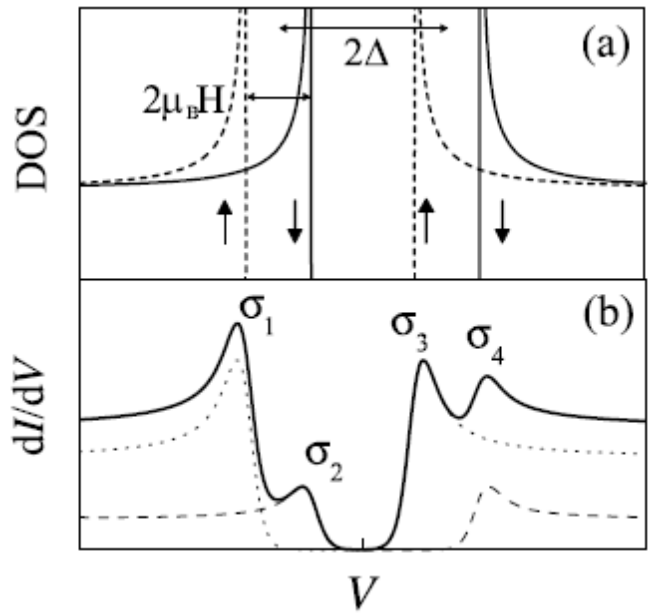

Figure 1-4. Tunneling in a ferromagnet/ insulator/ superconductor junction. (a) The superconductor DOS is split by $2\mu_B H$ into the up- and down-spin contributions. (b) Conductance as a function of voltage for each spin orientation (dotted and dashed curves) and the total conductance (solid curve) (after [52])

The magnetic moment orientation and therefore the spin directions are defined by the applied field, and the sharply peaked superconductor DOS makes it possible to separate the contributions from the up- and down-spin electrons in the tunneling current. As a result tunneling from a ferromagnetic metal into a superconductor gives rise to an asymmetric conductance curve, which is schematically shown in Figure 1-4(b), the asymmetry is the consequence of the electronic states in the ferromagnetic metal being exchange split, which leads to an unequal DOS in the ferromagnet at the Fermi energy, $\rho^{\uparrow} \neq \rho^{\downarrow}$. Since $\rho^{\uparrow}$ and $\rho^{\downarrow}$ determine the number of electrons

which can tunnel within each spin channel, the spin conductance is weighted by the respective spin DOS. Since spin does not change in the tunneling process, i.e. the total conductance is the sum over the up- and down-spin channels, $G = G^{\uparrow} + G^{\downarrow}$, the tunneling spin polarization can be obtained by measuring the relative heights of the conductance peaks.

$$P = \frac{G^{\uparrow} - G^{\downarrow}}{G^{\uparrow} + G^{\downarrow}} = \frac{(\sigma_4 - \sigma_2) - (\sigma_1 - \sigma_3)}{(\sigma_4 - \sigma_2) + (\sigma_1 - \sigma_3)} \tag{1.15}$$

A more accurate tunneling spin polarization determination in FM/ I/ S junctions must account for spin–orbit scattering in the superconductor [52-57].

There have been several other methods employed for the *P* measurement such as spin-resolved photoemission, Andreev reflection and spin polarized scanning tunneling measurements. However the measured quantity *P* in dissimilar measurement techniques does not necessarily have the same physical origins (nevertheless all values are intimately related to DOS) because each technique probes slightly different physical entities with different energy scales [39, 40, 58]; that is, the measured *P* does not necessarily represent the DOS of spin sub-bands at E_F only. Andreev reflection technique probes the spin currents ratio in the superconducting and the normal states. Photoemission measurement probes the exited electrons from few eV below E_F in the band at the FM/vacuum interface. In the FM/ I/ S tunnel junctions, direct tunneling conductance is measured under typically a few mV of bias, and spin polarization is obtained via the height variations in the conductance peaks.

1.5 Magnetic Tunnel Junctions

Magnetic tunnel junctions (MTJs) involve two ferromagnetic metal layers separated by a thin insulating barrier layer. The insulating layer must be thin enough (a few nanometers or less) so that electrons can tunnel through the barrier if a bias voltage is applied between the two metal electrodes. The most important property of a MTJ, as proposed by Jullière, is that the tunneling current depends on the relative ferromagnetic layers magnetization orientations, which can be changed by an applied magnetic field (See Figure 1-5).

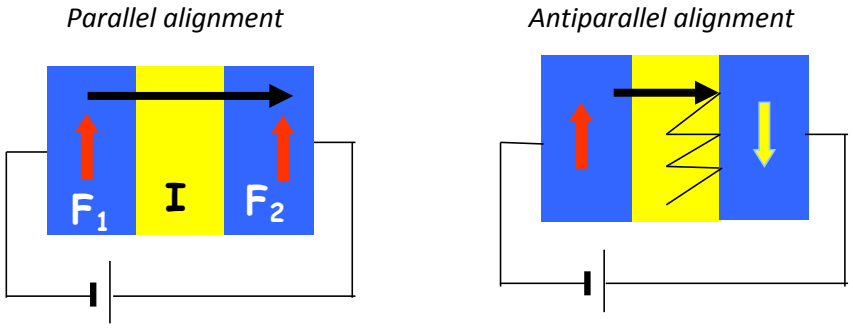

Figure 1-5. Schematic of the spin transport between two ferromagnets

The resistance change resulting from such a phenomenon is called TMR (sometimes referred to as junction magnetoresistance). In this context the resistance exhibits a maximum (minimum) when both magnetizations are antiparallel (parallel). Although TMR has been known from the experiments of Jullière [42] for over 30 years, only a relatively modest number of studies were performed in this field up to the mid-1990s. Partly this was caused by the technologically demanding fabrication process, which makes it difficult to fabricate robust and reliable tunnel junctions. The small TMR reported values (at most a few percent at low temperatures) led to no great interest triggered for possible applications. Almost two decades ago Miyazaki and Tezuka [59] demonstrated the possibility of TMR large values in MTJs with

Al_2O_3 insulating layers, and Moodera et al. [60] developed a fabrication process which appeared to fulfill the requirements for smooth and pinhole-free Al_2O_3 deposition. Since the first observation of reproducible large TMR at room temperature (shown in Figure 1-6) there has been enormous increase in the research amount in this field; at the end of the 1990 decade, MTJs that are based on 3d-metal ferromagnets and Al_2O_3 barriers could be routinely fabricated with reproducible characteristics and with TMR values up to 50% at room temperature, making them suitable for industrial applications (see e.g.,[61]).

In contrast to the direct measurement techniques mentioned above, the F_1/ I/ F_2 tunnel junction measurements allow *P* calculation from the obtained TMR, that is from the relation between TMR and *P* that was first put forward by Jullière [42]:

$$TMR = \frac{\left(G_P - G_{AP}\right)}{G_P} = \frac{\left(R_{AP} - R_P\right)}{R_P} = \frac{2P_1P_2}{\left(1 - P_1P_2\right)}, \qquad (1.16)$$

where G_P and R_P are the conductance and the resistance with parallel ($G_p \propto n_{1\uparrow} n_{2\uparrow} + n_{1\downarrow} n_{2\downarrow}$) and antiparallel ($G_{ap} \propto n_{1\uparrow} n_{2\downarrow} + n_{1\downarrow} n_{2\uparrow}$) magnetization between F_1 and F_2, and P_i is the inferred *P* of F_i. Note that Jullière's relation involves strong simplifications such as no spin mixing between the two spin current channels. However, it is still readily accepted mainly because the relation between TMR and *P* is straightforward, and the inferred *P* agrees well with the value obtained from direct measurements.

Although Jullière's model served as a useful basis for interpreting a number of experiments on TMR, this model is too simple to describe all the available experimental data. In particular Jullière's model assumes that the tunneling current spin polarization (SP) is determined solely by the total spin polarizations at the Fermi energy of the ferromagnetic layers. Later Stearns improved this understanding by only considering the itinerant electrons DOS [62], the TMR interpretation in terms of the ferromagnet intrinsic properties

constituting the MTJ remained unchanged. Experimental results show however, that the tunneling SP strongly depends on the structural quality of MTJs [63], and improvements in the quality of the alumina barrier and the metal/alumina interfaces resulted in the enhancement of the measured values of the SP. The permalloy 32 % spin polarization was first obtained in tunneling towards superconductors experiments [52], but later Moodera et al. using improved deposition techniques reported a value for SP of 48 % (see [53]). Experiments also show that the SP depends on the choice of the tunneling barrier, de Teresa et al. found that tunneling from Co across a $SrTiO_3$ barrier exhibits a negative SP [8, 9], which is opposite to the tunneling spin polarization across an Al_2O_3 barrier, for which all *3d* ferromagnets show positive SP [52, 54-56]; also recent experiments by LeClair et al. [40–42] demonstrated the interfacial electronic structure decisive role in spin dependent tunneling (SDT).

It is then evident that the tunneling SP is not an intrinsic property of the ferromagnet alone but depends on the structural and electronic properties of the entire junction including the insulator and the ferromagnet/insulator interfaces. This fact makes the quantitative description of MTJs transport characteristics much more complicated. However it broadens dramatically the possibilities for altering the MTJs properties. In particular, by modifying the electronic properties of the tunneling barrier and the ferromagnet/insulator interfaces, it is possible to engineer MTJs towards desirable properties for device applications.

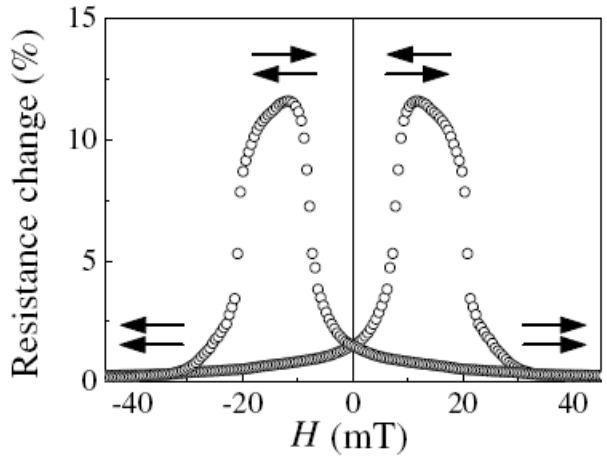

Figure 1-6. The first observation of reproducible, large, room temperature magnetoresistance in a CoFe/Al_2O_3/Co MTJ. The arrows indicate the relative magnetization orientation in the CoFe and Co layers (after [60])

It is evident from the relation between TMR and polarization in Eq. (1.16) that the highest possible TMR can be achieved by employing ferromagnetic metals of the highest spin polarization. There have been extensive world-wide research efforts to explore such high polarization materials, where the conduction electrons are fully spin polarized, namely half-metals [64]. So far several complex compounds are predicted to be half-metals such as the spinels $CuCr_2S_4$ and Fe_3O_4; Heusler alloys NiMnSb and Co_2MnSi, and rutile CrO_2. There are even more complicated oxides such as perovskite manganites $La_{0.7}Ca_{0.3}MnO_3$ (LCMO) and $La_{0.7}Sr_{0.3}MnO_3$ (LSMO); double perovskites Sr_2FeMoO_6 and Sr_2ReMoO_6; and pyrochlore $Tl_2Mn_2O_7$.

Among such materials, mixed valence manganites have received considerable attention, mainly because of their intrinsic large magnetoresistance (up to 10^6 % in a few T), called colossal magnetoresistance (CMR) since its discovery in 1994 [65, 66]. In fact the major motivation investigating the mixed valence manganites is rather different and arises due to fundamental physics [67-69] of strong electron correlations such as CMR, charge/orbital ordering and the explicit half-

metallicity. Spin polarized tunneling based on these materials is separately discussed later in this Chapter.

1.5.1 TMR bias and temperature dependence

Several experimental viewpoints are presented in this section, most notably those from recent years are discussed. First the common magnetic tunnel junctions' features are presented and then in addition manganite based junctions are discussed separately. In addition to the case of elastic tunneling between occupied and unoccupied electron states on each side of the barrier, effective transmission may also occur through other mechanisms: inelastic tunneling through interfacial spin wave and phonon excitations, and impurity-assisted tunneling. In particular, spin wave excitations mix the two spin-independent channels. As reported previously, the bias dependence of junction conductance is expected to follow a parabolic law. However for applied bias values below ~ 150 mV, a dip in conductance called zero-bias anomaly (ZBA) occurs for junctions integrating transition metal electrodes. Theoretical and experimental investigations have attributed this ZBA to spin wave excitations at the carrier-collecting interface [70, 71]. Indeed at a given applied bias V, electrons from the Fermi level of the injecting electrode enter unoccupied states above the Fermi level of the collecting electrode after elastic tunneling. In order to thermalize with their environment, these "hot" electrons may dissipate energy by emitting a magnon of energy $\hbar\omega \leq eV$, and given their bosonic distribution the only constraint on magnon generation is the maximum energy of such spin waves sustainable by the ferromagnetic medium. This energy corresponds, within a mean field approximation, to $3k_BT_C / (S + 1)$ for a transition metal with spin S and Curie temperature T_C. As illustrated in Figure 1.6a, in the case of a Co/Al_2O_3 interface, the cutoff appears at ~ 140 mV, in relative agreement with this

estimate if one considers a lower interface T_C for Co. Zhang et al. propose a somewhat modified explanation for the ZBA saturation bias, arguing in terms of a shorter wavelength cutoff in the magnon generation spectrum representing either anisotropy at the interfaces between the magnetic electrodes and the insulator, or a finite coherence length due to (for example) grain boundaries [70]; leading to a mixing of the two tunneling spin channels. Finally, it should be noted that spin wave excitations may interact in the inelastic tunneling process at both the collecting and injecting interfaces through the emission and absorption of magnons [61, 71-76] respectively.

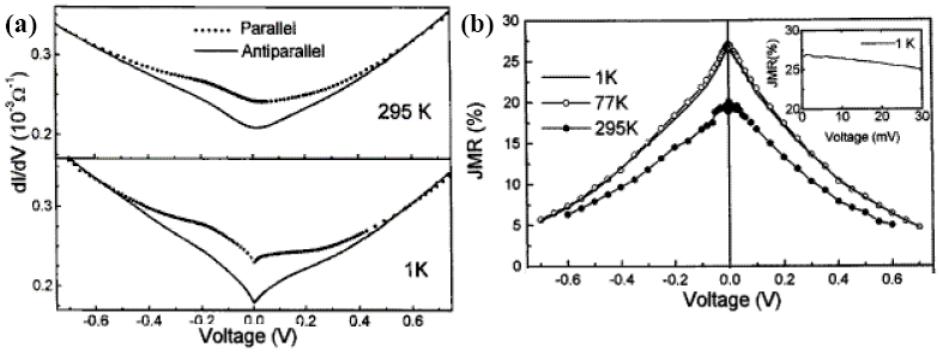

Figure 1-7. $Co/Al_2O_3/Ni_{80}Fe_{20}$: temperature evolution of (a) Conductance in the parallel and antiparallel configurations, and (b) JMR bias dependence. *JMR = $\Delta R/R_{AP}$* . From Moodera et al. [71]

Concerning TMR temperature dependence, it decreases with increasing temperature. Although most theoretical models of spin polarized tunneling are based on the zero temperature and zero bias limits, the temperature dependence of spin polarized tunneling has potentially both a spin independent and spin dependent component. Normal tunneling conductance itself is temperature-dependent due to thermally activated conduction of inelastic processes as magnon generation [70], and elastic processes as thermionic emission, or thermally assisted tunneling [77, 78]. If the interfacial spin polarization and magnetization decreases result from the

magnon activation mechanism, then as argued by Shang et al. [79] and corroborated by MacDonald [80], both should follow a $T^{3/2}$ law, e.g. $P(T) = P(0)\,(1-\alpha T^{3/2})$.

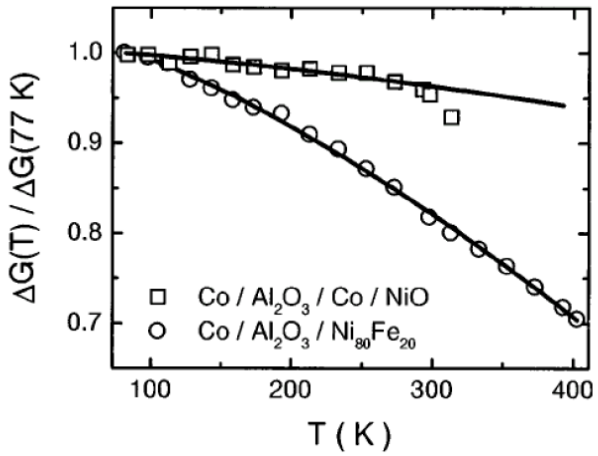

Figure 1-8. Temperature dependence of the normalized conductance of two ferromagnetic junctions. The solid lines are fits to the thermal spin-wave excitations-based theory. From Shang et al. [79]

1.5.2 Bonding at the ferromagnet/insulator interface

One of the important properties of MTJs which strongly affects the SDT is the chemical bonding at the ferromagnet/ insulator interface. The bonding mechanism determines the effectiveness of transmission across the interface which can be different for electrons of different characters. Tsymbal and Pettifor [81] showed that for tunneling from transition metal ferromagnets across a thin barrier layer, the conductance spin polarization depends strongly on the interfacial ferromagnet-insulator bonding. They found that under *ssσ* bonding the conductance spin polarization is positive, which is in agreement with tunneling through an alumina spacer experimental data [9]. Increasing the *sdσ* bonding at the interface results in a large *d*-electron contribution to the tunneling current; in this case due to the interfacial *sdσ* bonding, the ferromagnet *d*-states can evolve into insulator *s*-states and be

transmitted across the MTJ. The negative *d*-DOS spin polarization at the Fermi energy (see Figure 1-9) can then be reflected in the tunneling current.

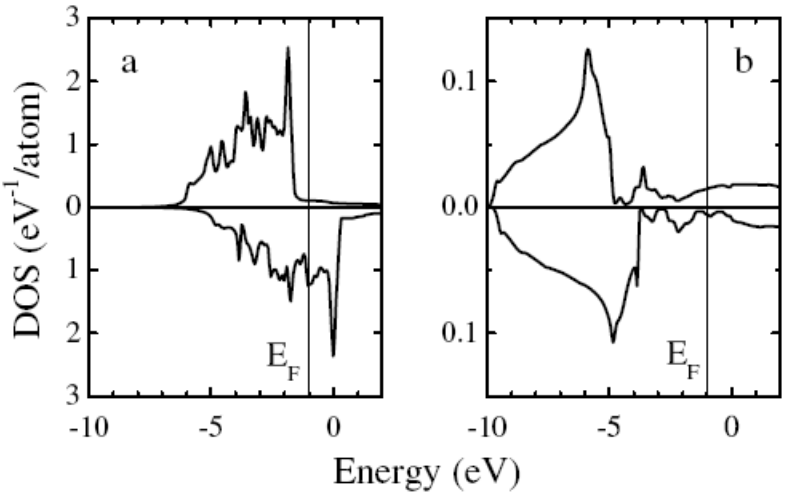

Figure 1-9. DOS for bulk fcc Co projected to *d*-orbitals (a) and *s*-orbitals (b) for majority-spin electrons (positive values in vertical axis) and minority-spin electrons (negative values in vertical axis). *d*-DOS spin polarization at the Fermi energy is opposite to that for the *s*-DOS. Note the different scales in (a) and (b). After Tsymbal et al. [57]

The bonding effect at the ferromagnet/ insulator interface was proposed to explain the experimentally observed spin polarization inversion for tunneling electrons from Co across a $SrTiO_3$ barrier [8, 9]. The bonding mechanism was also put forward to explain TMR positive and negative values depending on the applied voltage in MTJs with Ta_2O_5 and Ta_2O_5/ Al_2O_3 barriers [82]. Among other barriers, successful MTJs magneto-transport experiments based on MgO barriers have been performed by Parkin et al. [74] who reported 220 % TMR at room temperature, which increased to 500 % at low temperatures.

1.6 Spin Polarized Tunneling Based On Half-Metallic Manganites

Magnetic tunnel junctions based on half metallic manganese oxides have gathered considerable interest due to their potential for producing large magnetoresistance spintronics devices. Most noticeable is the very large tunneling magnetoresistance (TMR) observed at low temperatures in magnetic tunnel junctions (MTJ's) based on $La_{0.7}Sr_{0.3}MnO_3$ [10, 11]. However, all reported manganite based tunnel junctions show a rapid decrease of TMR with increasing temperature, vanishing at temperatures well below the bulk electrodes Curie temperature [11, 12, 17], indicating that spin polarization (SP) and/or TMR is not only determined by the intrinsic properties of the bulk ferromagnetic electrodes, but also depends on the tunneling barrier structural and electronic properties including the ferromagnet/ insulator interfaces [57, 83, 84]. In fact the TMR value and sign strongly depend on the barrier and electrodes choice. As an example, different values of TMR have been reported in LSMO [2, 10, 12, 13] and LCMO [11, 17, 85, 86] based tunnel junctions with different insulating barriers. In this regard inverse TMR has been observed in Co/ $SrTiO_3$/ LSMO MTJs [9], while both positive and negative TMR values have been reported in Co/ Al_2O_3/ LSMO MTJs [8]. Theoretical reports (see section 1.5.2) have highlighted the role played by chemical bonding at the ferromagnetic/ insulator interface and the barrier electronic structure in determining the preferential transmission of electrons at *s*, *p* or *d* bands via metal induced gap states [51, 57]. Also, spin polarized photoemission (SPPE) experiments have shown a free LSMO surface spin polarization decreasing much more rapidly with temperature than the bulk material magnetization. It has been often postulated that the spin polarization rapid decrease with temperature should be a common surfaces and interfaces intrinsic property, for half-metallic oxides like LSMO [15, 16].

This would limit the half-metallic character exploitation in spintronics devices, which in most cases probe the spin polarization at an interface with another material. Garcia et al. [12] reported on the spin polarization temperature dependence of several LSMO/ insulator interfaces derived from the tunnel magnetoresistance temperature dependence in MTJs with two LSMO electrodes and different insulating barrier (STO, TiO_2, and $LaAlO_3$).; They find similar spin polarization thermal decay of three LSMO/ I interfaces, very different from that of a free surface spin polarization, and similar to that of the bulk magnetization, but with a critical temperature some 60 K lower. These results indicate that the magnetism at LSMO interfaces can be as robust as that of transition metals and that in manganites surfaces and interfaces are two very different discontinuities.

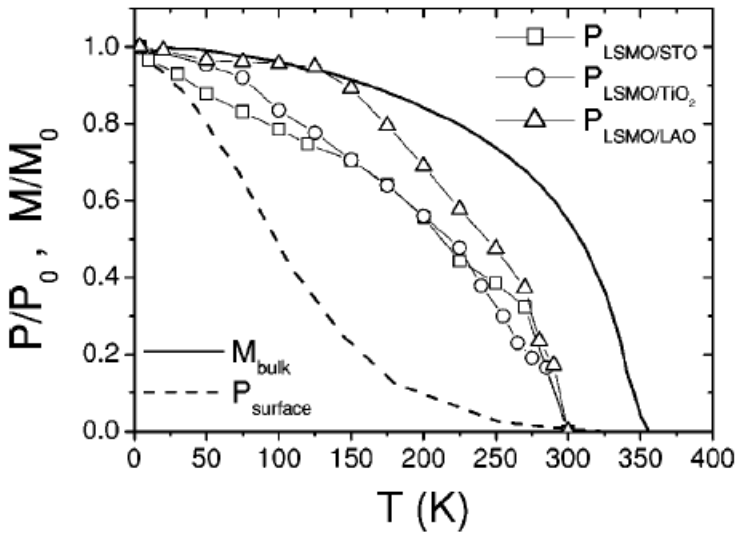

Figure 1-10. Normalized spin polarization temperature dependence at the interface between LSMO and three different insulators, STO, TiO_2, and LAO for bulk magnetization and free LSMO surface spin polarization. After Garcia et al. [12]

This decay is much smoother than the free surface spin polarization decay, and resembles the magnetization decay but with an apparent interface Curie temperature lower than the bulk one by about 60 K. This striking difference between the spin polarization variation at the interface and a free surface SP

underlines the fundamental importance of continuity in the oxygen ions sublattice, –existing at interfaces but not at surfaces– in the local magnetic properties determination (see Figure 1-10).

Another interesting problem is the electrode-barrier interface magnetic state. While some reports have shown increased magnetoresistance in magnetic impurity-doped barrier [87], Lee et al. [88] have shown a strong TMR and/or spin polarization degradation attributed to tunneling electrons Kondo scattering at the magnetic impurities, occurring at the interface as a barrier and electrode species bonding result. Kondo impurities act as strongly temperature dependent scattering centers blocking the electron flow between ferromagnetic electrodes. However, while these reports illustrate the effect of changing the barrier magnetic state, the possibility of a modified ground state at the interface, changing the junction response through modified bonding, strain, or charge transfer, has been less explored.

1.7 Spin Filtering

Compared to the classical spin-dependent tunneling through a non-magnetic insulating barrier, the spin filtering through a ferromagnetic or ferrimagnetic insulating barrier has been little studied; the spin filtering concept was introduced in the late 1960's [89] and extensively studied by Moodera et al. [18-20] using low-T_C ferromagnetic Eu chalcogenides as barriers. Due to the exchange splitting, the barrier material conduction band bottom lies at different energies for majority and mionority electrons, which yields different tunnel barrier heights. In an intuitive vision based on the free electron model, due to the tunnel transmission exponential dependence on the barrier height, carriers from a non-polarized electrode are differently transmitted depending on their spin, if the conduction band bottom is at a lower energy for spin-up than for spin-down (see Figure 1-11), then a large positive spin polarized current is expected to tunnel; the current spin polarization (spin filtering efficiency of the barrier) is expressed as:

$$P_F^{spin} = \frac{J_\uparrow - J_\downarrow}{J_\uparrow + J_\downarrow}$$

where $J_\uparrow$ ($J_\downarrow$) is the spin-up (spin-down) current expressed by the Simmons model at small bias as [40]:

$$J_\uparrow = \sqrt{\phi_0 - \frac{\Delta\phi}{2}} \exp\left(-A\sqrt{\phi_0 - \frac{\Delta\phi}{2}}\, d \right),$$

$$J_\downarrow = \sqrt{\phi_0 + \frac{\Delta\phi}{2}} \exp\left(-A\sqrt{\phi_0 + \frac{\Delta\phi}{2}}\, d \right)$$

In these expressions, ϕ is the average barrier height, $\Delta\phi$ the conduction band bottom spin-splitting, and d the barrier thickness, it follows that the spin filtering efficiency P_F^{spin} increases whit $\Delta\phi$ and d .

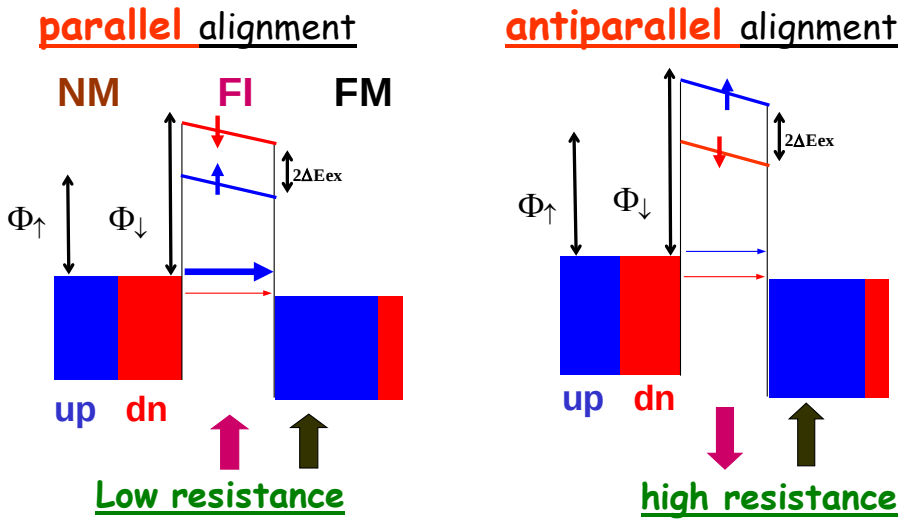

Figure 1-11. Sketch for the tunneling process through a spin-filtering tunnel barrier. Thick vertical arrows indicate the magnetization directions. Red and blue vertical arrows indicate the spin direction and the horizontal one the tunneling current

The exponential dependence makes this filtering mechanism very efficient and large current spin polarization is expected. In order to measure the spin-filtering efficiency a reference layer acting as a spin detector is added, and when a ferromagnetic counter-electrode is used this defines a spin-filter tunnel junction (SFJ). The current is large or small depending on the barrier and counter-electrode magnetization orientations. Figure 1-11 sketches – from left to right– the non-spin polarized metallic conduction band, the barrier height represents the distance from the metallic Fermi level to the barrier material conduction band bottom, with lower (higher) energy difference for the majority (minority) carriers, and a metallic ferromagnetic counter-electrode (non-equal spin carrier populations). In that cartoon when the magnetizations are parallel, non-magnetic electrode spin-up electrons are highly transmitted through the barrier and have a large DOS to be injected into, resulting in a large tunneling current. When the magnetizations are antiparallel, the highly transmitted spin-up carriers find small DOS to be

injected into, resulting in a low tunneling current. In terms of the Jullière model the SFJ TMR can be expressed as:

$$TMR = \frac{2P_1^{spin}P_F^{spin}}{1-P_1^{spin}P_F^{spin}}$$

The spin-filter effect has been well observed in europium chalcogenide tunnel barriers EuS [19, 20] and EuSe [21] and more recently with EuO [22]: EuS barriers have shown P_F as high as 85% even at zero applied magnetic field. In the case of EuSe which is an antiferromagnet becoming ferromagnetic under small applied magnetic fields, field-dependent conduction band exchange splitting is observed, then the resulting P_F is field dependent; $P_F\ (H = 0) = 0$ and increases with applied field reaching nearly 100% at 1 T. EuS and EuSe have magnetic ordering temperatures of 16.6 K (ferromagnetic) and 4.6 K (antiferromagnetic) respectively, and thus filter spins only at the liquid helium temperature range. With a higher T_C = 69.3 K and greater exchange splitting, EuO holds promise to reach greater spin-filter efficiency at higher temperatures. Furthermore, the T_C of EuO can be raised well above liquid nitrogen temperatures (even at 170 K) by rare-earth metals doping (discussed later), although the doping side effect is the lowering of exchange splitting ($2\Delta E_{ex}$). The EuS T_C can also be raised by extrinsic doping or by making Eu-rich EuS [40], but still remains well below the EuO T_C. However, demonstrating the spin-filter effect in EuO is a more challenging task than for EuS and EuSe, provided the difficulty in obtaining high quality, stoichiometric, and ultrathin EuO films. Good quality ultrathin films of EuS and EuSe are easily evaporated directly from a EuS or EuSe powder sources, but EuO is metastable while (non-magnetic) Eu_2O_3 is the most stable Eu oxide, thus the latter has readily available powder sources while the former is not available, and therefore it is much more difficult to grow the ultrathin film needed as tunnel barrier.

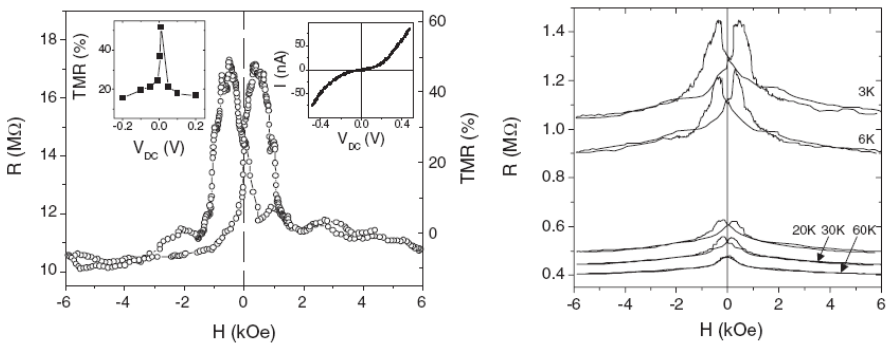

Figure 1-12. (left) LSMO/ BMO/ Au spin-filter junction at 3 K, 10 mV TMR, TMR bias dependence (left inset) and junction *I(V)* curve (right inset), (right) TMR at different temperatures for a second junction. From Gajek et al. [23]

Europium chalcogenides are not the only candidates for spin-filter materials, the choice of ferromagnetic insulator (FMI) spacers has remained very limited and the operation restricted to very low temperatures; there has been some recent progress with other promising candidates, namely ferrites and perovskites; ferrites have magnetic ordering temperatures well above room temperature and thus could potentially filter spins at a convenient temperature range, as their structure is complex the materials aspects are complicated. Among perovskites spin filtering has been observed using FMI $BiMnO_3$ with T_C = 105 K [23].

Another interesting aspect of spin filter devices is their bias dependence, while conventional MTJs TMR consistently decreases with increasing applied voltage (see Figure 1-12 right panel), the SFJ TMR bias dependence shows a different behavior: electrons tunneling through the thin FMI in which the conduction band is exchange spin-split, experience different barrier heights depending on their spin orientation ($\Phi_\uparrow$ for spin-up and $\Phi_\downarrow$ for spin-down). As the tunnel probability is a barrier height exponential function the result is a highly spin-polarized current.

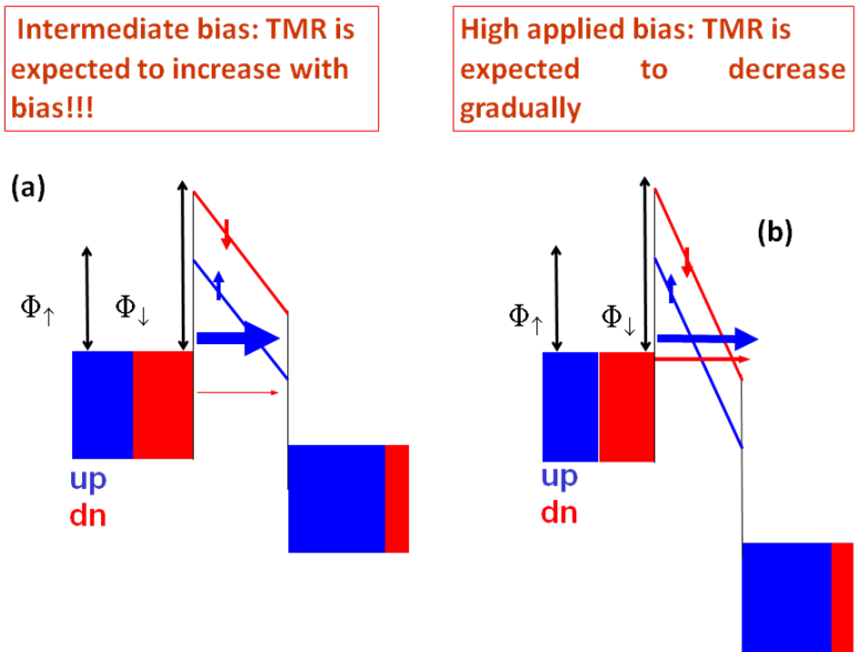

Figure 1-13. Tunneling process cartoon for a spin-filtering tunnel barrier at (a) intermediate and (b) high applied bias. The red and blue vertical arrows indicate spin directions and the horizontal ones indicate tunneling current

The SFJ TMR first increases smoothly with applied bias [90],and then more abruptly when the tunneling electrons energy exceeds the barrier height $\Phi_{\uparrow}$ for majority spins; when the bias exceeds $\Phi_{\uparrow}$ but it is lower than $\Phi_{\downarrow}$ transport still occurs by direct tunneling (DT) for minority spin carriers while majority spin carriers travel by the so called Fowler-Nordheim tunneling (FNT) carrying a larger current; the Fowler–Nordheim regime results from the available states in the barrier when the applied bias is larger than the barrier height (see Figure 1-13), TMR attains a maximum upon further raising the bias voltage, when tunneling electrons energy exceeds the barrier height for minority spins ($\Phi_{\downarrow}$) and finally decreases gradually [90].

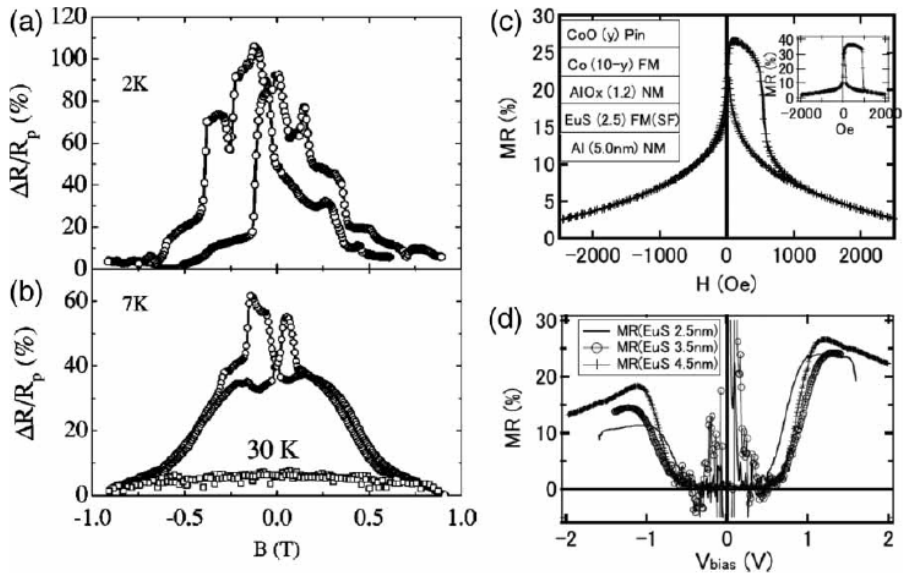

Figure 1-14. (a, b) TMR at different temperatures for Gd/ EuS/ Al SFJs from P. LeClair et al. [91]. (c) TMR curves and (d) TMR bias dependence for Co/ AlOx/ EuS/ Al SFJs at 4.2 K from Nagahama et al. [90]

It is only recently that magnetic tunnel junctions with ferromagnetic barriers (also called 'quasi-magnetic tunnel junctions' or SFJs) have been defined and measured. The earliest report was [91] by LeClair et al. who measured 100 % TMR at 2 K in Gd/ EuS/ Al junctions. These results are shown in Figure 1-14 (a) and (b). A few years later Nagahama et al. [90] reported a detailed study of Al/ EuS/ AlOx/ Co junctions showing above 25 % TMR (Figure 1-14c). A 1.2 nm AlO_x layer was inserted between the EuS magnetic barrier and the Co magnetic electrode to decouple both layers, improving the magnetic switching compared to the case of LeClair et al. A detailed analysis of the TMR bias dependence (Figure 1-14(d)) showed TMR increase in the high bias range after the low bias decrease, as expected for SFJs from a simple tunneling model (see e.g. [92] or the model included in [90]).

1.8 Interfaces

The wealth of physical phenomena exhibited by transition metal oxides, as strongly correlated electron systems, constitutes an exciting playground for new fundamental physics and a world of opportunities for novel devices [68, 92]. Their range of functionalities spans from superconductivity to ferromagnetism in bulk and can be further broadened by considering their interfaces in heterostructures [93]. The symmetry breakdown at the discontinuity between two different materials ensuing electronic or atomic reconstruction may result in unexpected effects that can inspire novel device concepts. The conducting interfacial state between two insulators [26, 27] which may be magnetic [28] or even superconducting [29], the interface ferromagnetism induced between two paramagnets [30], or the suppressed magnetism near manganite-cuprate interfaces [31] represent typical interfaces with novel properties.

Substantial theoretical work [93-96] has highlighted the role played by a number of interface phenomena (modified screening, band bending, polarity mismatch) in the determination of important electronic parameters (bandwidth, on-site Coulomb interaction) potentially responsible for profound changes in the local charge, spin and orbital structure. In this regard the possibility of artificially manipulating spin states at interfaces is particularly attractive for the design and operation of novel spintronics devices. As interfaces are key to the operation of spintronic devices (such as MTJs), engineered interfaces with a modified ground state may enhance the response of present devices and inspire novel spin-based architectures with additional functionalities. Mixed-valence manganites are ideal systems for the investigation of this issue due to their strong intrinsic tendency to change their electronic properties under the action of small perturbations such as strain and / or charge transfer [68, 97]. For example, recent several studies

suggested that the ultrathin manganite layers antiferromagnetic state can be interfacially modified with a half-metallic ferromagnetic layer of e.g. LSMO [94, 98, 99]. The present work contains extensive use of manganites, particularly LCMO, as ferromagnetic electrode in MTJs, but also tried these materials as potential barriers with new functionalities. Thus, in the next section a brief summary of several important aspects concerning manganites is presented.

1.9 $La_{1-x}Ca_xMnO_3$

Manganites also belong to the family of strongly correlated transition metal oxides showing strong coupling between, charge, spin and lattice degrees of freedom, which produce a variety of phases in a chemically homogeneous material. *d*-electrons experience competing forces in transition metal ions: Coulomb repulsion tends to localize individual electrons at atomic lattice sites, while oxygen *p*-electron states hybridization promote delocalization [100]. Their properties are strongly dependent on doping and disorder, and each compound's phase diagram often displays a great number of phase boundaries. Manganites can be represented by the general formula $A_{1-x}B_xMnO_3$ where A is a large rare-earth trivalent cation and B is a divalent alkaline cation, and the mixed valence oxides can be regarded as solid solutions between end members. The compound LCMO used in this work follows the formula $La_{0.7}Ca_{0.3}MnO_3$ with the formal end member valence states $La^{3+}Mn^{3+}O_3^{2-}$ and $Ca^{2+}Mn^{4+}O_3^{2-}$. The first intense study of the structural, electric and magnetic properties of manganite of the type $La_{0.7}B_{0.3}MnO_3$ was made by Jonker and van Santen in 1950 on polycrystalline samples [101, 102]. In their work they captured some of the most important results about the intermixing of Mn^{3+} and Mn^{4+} and the effect on the magnetic/conducting sample state although interpreted on a short range interactions basis, they also underlined the importance of the oxygen content and doping on the Mn valence by measuring the Curie temperature (which coincide with the metal-insulator transition temperature) and saturation magnetization of several compounds, and finding a correlation between the conducting and ferromagnetic states. In 1954 Volger first reported on the $La_{0.8}Sr_{0.2}MnO_3$ negative magnetoresistance [103] which showed a peak close to the Curie temperature, later recognized as a typical behavior in manganites.

1.9.1 Colossal magnetoresistance

The magnetoresistance (MR) is defined as the change in the resistance due to the application of a magnetic field:

$$MR = \frac{R_H - R_0}{R_0}$$

The change Volger observed was quite small (10%), probably due to the sample polycrystalline nature and the fabrication method. Only at the 90's it was possible to improve the MR effect due to the development of growth techniques for high quality thin films. In 1994 Jin et al. [65] obtained low temperature MR of 100000 % from a $La_{0.67}Ca_{0.33}MnO_3$ thin film grown on $LaAlO_3$, it was called *colossal magnetoresistance* (CMR). This fact together with the renewed general interest on complex oxides, the possibility of growing layered heterostructures and the advent of interfaces concurred to renovate the interest in these materials.

1.9.2 LCMO phase diagram

A fundamental contribution in understanding the manganites' phase diagram was given by Wollan and Koehler in 1955 [104]. They presented and extended neutron diffraction analysis of the La, Ca manganite and showed unexpected complex phases existence (including charge and orbital order) and several different magnetic structures (for example the CE type) depending on the doping content. Figure 1-15 shows the temperature vs. Ca content phase diagram for $La_{1-x}Ca_xMnO_3$ [67]. The presence of so many phases is a consequence of the strong correlation between the crystal structure and the fraction of Mn^{4+} and Mn^{3+}. The compound $La_{0.7}Ca_{0.3}MnO_3$ (LCMO) becomes ferromagnetic at a relative high temperature (270 K).

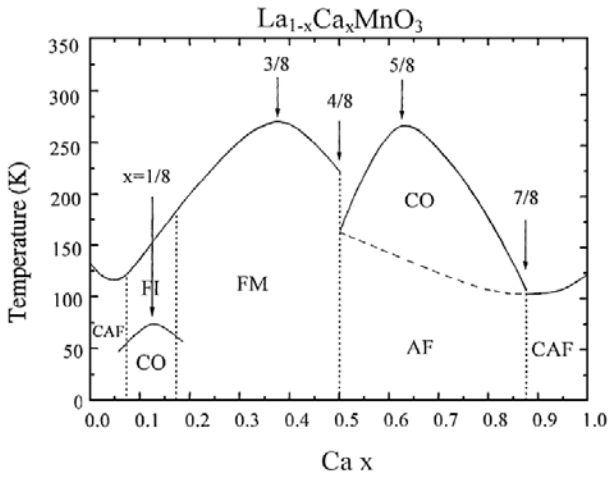

Figure 1-15. $La_{1-x}Ca_xMnO_3$ phase diagram [67]

1.9.3 LCMO crystal structure

The LCMO crystal structure is a cubic perovskite as shown in Figure 1-16. In the undistorted structure Mn atoms occupy the cube's four corners while the central position is occupied either by La or Ca randomly distributed in the whole crystal according to the stoichiometry. Each Mn ion is centrically placed at an oxygen octahedron forming a MnO_6 structure.

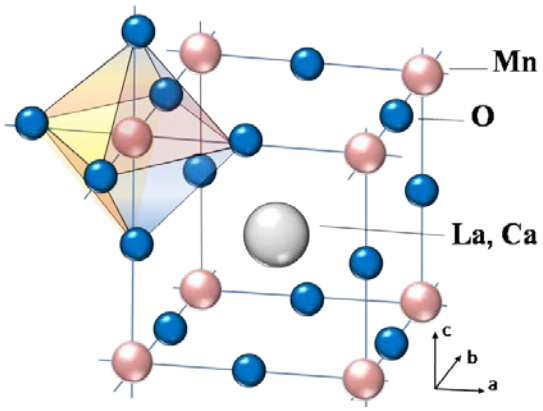

Figure 1-16. Undistorted LCMO crystal structure

A wide range of divalent cations can occupy the body-center position like Ca, Sr, Ba, or Pb. The ideal cubic structure is distorted by cation size mismatch, affecting the oxygen octahedron through deformation, or by the relative orientation between adjacent octahedra under cooperative tilting; this effect is called the Jahn-Teller (JT) distortion and yields to energy levels splitting in order to lower the system energy. Such an effect arises in manganites from an electronic instability inherent to the Mn^{3+} ions in asymmetric MnO_6 octahedra. In the cubic lattice environment the five-fold degenerate 3*d*-orbitals of an isolated atom or ion are split into a manifold of three lower energy levels usually referred to as t_{2g}, once mixing with the surrounding oxygen is included, and two higher energy states called e_g. Figure 1-17 shows the orbital resulting from the final energy split.

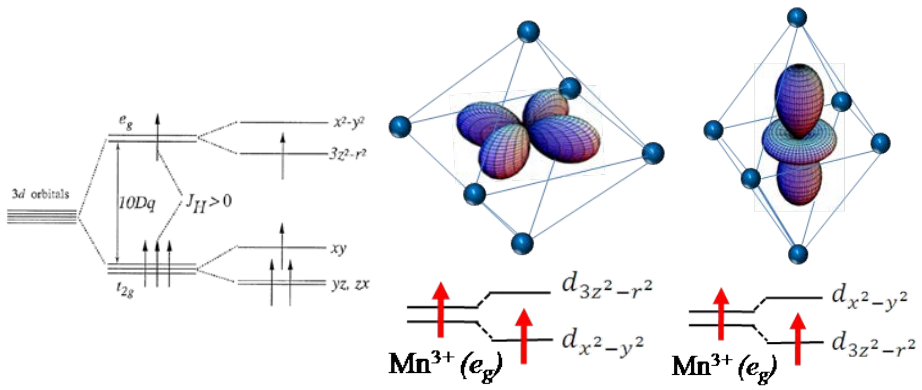

Figure 1-17. Five-fold degenerate atomic 3*d* levels field splitting into lower t_{2g} and higher e_g levels [105]

The distortion lifts e_g orbital degeneracy and favors either $d_{x^2-y^2}$ or $d_{3z^2-r^2}$ occupation. The JT distortion can be cooperative since neighboring octahedra share one oxygen ion. The cooperative rotation of MnO_6 octahedra leads to a lattice symmetry change which is usually accompanied by shortening and stretching of the six Mn-O bonds. Consequently, the resulting various JT distortion modes lead to different electronic structures for the Mn^{3+} ionic e_g states (see Figure 1-18). The end-member compounds

such as $LaMnO_3$ have a distorted perovskite structure where the Fermi level falls in a gap between the two Jahn-Teller split e_g bands.

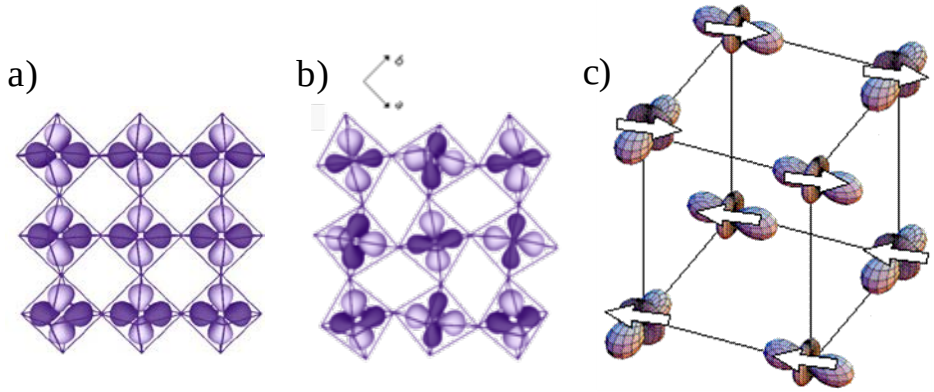

Figure 1-18. a) Undistorted perovskite structure, b) cooperative octahedra tilting c) prototypical $LaMnO_3$ e_g orbital ordering

A local linear combination of those orbitals produces the stable states $d_{3y^2-y^2}$, $d_{3x^2-y^2}$ alternating on Mn sites, which leads to *xy* plane orbital ordering and *z* direction antiferromagnetic ordering. A mixture of Mn^{4+} and Mn^{3+} is introduced in the sample by adding holes, (doping with Ca for example), and the number of *d*-band electrons, interatomic distances and bond angles are altered as well. This causes a strong reduction of JT distortion which has dramatic consequences on the compound magnetic and metallic states. Moving towards x = 0.5 Ca content the crystal structure approximates a stable cubic perovskite [101] and the material shows ferromagnetic-metallic behavior. In view of the strong intra-atomic Hund coupling the metallic behavior found an explanation thanks to double exchange Zener's model [106]. He considered the problem of exchange between Mn^3+ and Mn^{4+} ions via an oxygen ion and introduced the concept of simultaneous electron transfer from the Mn^{3+} to the oxygen and from oxygen to the neighboring Mn^{4+}. The Hund coupling requires all the involved electrons spin to be parallel in simultaneous hopping, what explains the ferromagnetic interaction (see Figure 1-19). The hopping intensity (or

transfer integral) t is modulated by a factor depending on the spins relative angle: $t = t_0 \cos\left(\frac{\theta}{2}\right)$, describing favored hopping for parallel spins.

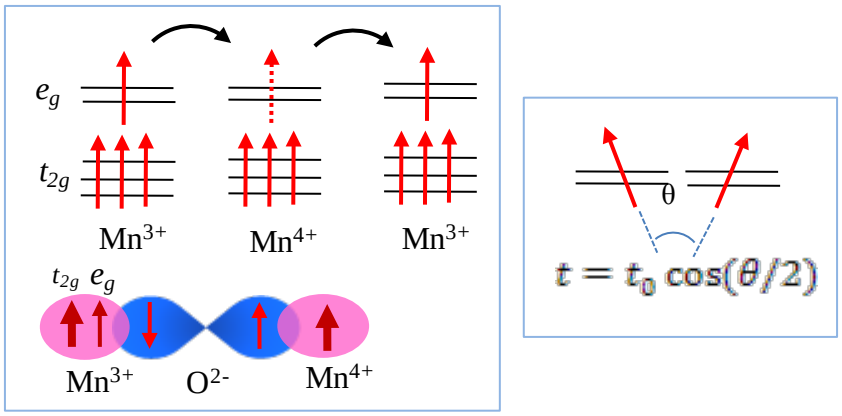

Figure 1-19. (Left) schematic illustrating the double exchange mechanism (Right) the hopping integral *t* depends on the relative angle between spins

If the localized spins in the one-orbital model for manganites are polarized e.g. up, then up spin conduction electrons can move freely while down spin conduction electrons cannot readily hop due to the large Hund coupling preventing their movement. In other words, Fermi level conduction electrons are 100 % polarized at low temperature. Among manganites, $La_{1-x}Ca_xMnO_3$ and $La_{1-x}Sr_xMnO_3$ may present half-metallic character. Although how close to 100 % is the polarization is still under debate, $La_{1-x}Sr_xMnO_3$ has been largely used to probe the half metallicity of CMR manganites [107-109] due to its room temperature ferromagnetic behavior.

Hopping angle is then determined not only by sample Mn^{4+} and Mn^{3+} fraction but also by temperature, spins are dynamically disordered above the Curie temperature T_C and the paramagnetic insulator state emerges, nevertheless below T_C but close to it spins can be easily aligned by applying a magnetic field, this can be regarded as one of the concomitant agents for CMR occurrence. Another quantity affected by JT distortion is the tight-binding bandwidth $W= 2zt$, where t is the transfer integral and z is the manganese nearest neighbor number. The e_g bandwidth W is in fact sensitive to Mn-O

distances and Mn-O-Mn bond angles [110]. $La_{1-x}Ca_xMnO_3$ can be labeled as *intermediate-bandwidth* manganite to distinguish it from the truly low-bandwidth compound $Pr_{1-x}Ca_xMnO_3$ where a metallic ferromagnetic phase can only be stabilized by the application of magnetic fields, and from the large bandwidth $La_{1-x}Sr_xMnO_3$ which shows robust ferromagnetism at room temperature but with reduced CMR effect.

1.9.4 Phase separation

A wide variety of experimental results and theoretical investigations have convincingly demonstrated that magnetic phases in mixed-valence manganites are not spatially homogeneous. These inhomogeneities are intrinsic features of single crystals not related to grain boundary effects in polycrystals; theoretical investigations [67, 111, 112] show that in a broad region of parameter space, the ground state is actually a nanoscale phases mixture, particularly under quenched disorder presence. The two key competing states in manganites, metallic ferromagnetic (FM) and insulating antiferromagnetic (AFI), mix up in a temperature range between the Curie and the Néel temperature. In this regime perturbations such as small magnetic fields can have dramatic consequences, because forced alignment of the preformed nanosize FM clusters randomly oriented magnetic moments is the only requirement to render the system globally ferromagnetic (see [113] and references there in). This nanoscale phase separation is commonly regarded as the origin of the CMR effect and has been corroborated by several experimental results.
Some of the relevant experiments are listed below, for the case of La, Ca manganites:

- neutron diffraction experiments showed anomalies below T_C [114] which might be explained by the two phase state
- transport measurements realized by Jaime et al. [72] –including not only free electrons but also polarons– reveal the possibility of charge inhomogeneities being present at the FM phase ($T < T_C$)

- muon spin- relaxation and resistivity measurements by Heffner et al. showed the polarons effect on the spin and charge dynamics interpreted as spatially inhomogeneous Mn-ion correlation times [115]
- magnetic resonance experiments for similar parameters by Allodi et al. [116] showed the coexistence of FM and AFM microdomains without spin canting
- Lynn et al. [117] and de Teresa et al. [118] observed a short FM correlation length at $T > T_C$ (magnetic polarons) through SANS measurements for $x = 1/3$ Ca concentration
- Hennion et al. [119] observed disordered distribution of FM 'droplets' by low temperature and low angle neutron scattering experiment (SANS), for $x = 0.05$ and $x = 0.08$ concentrations
- FM metallic phase localized states were found through Raman spectroscopy at low temperature by Yoon et al. [120]
- X-ray absorption by Booth et al. [121] showed evidence for localized and delocalized vacants at $T < T_C$. [122].

1.9.5 LCMO anisotropy

LCMO magnetic anisotropy has been controversially discussed in literature since, as many other lanthanum manganites properties it is strongly related to film thickness, doping and strain. Stoner and Wohlfarth modeled a magnetic hysteresis mechanism for heterogeneous alloys based on the single spheroidal particle simplified problem [123]. As shown in Figure 1-20 remanence and coercive field are smaller for a 45 degrees loop in comparison to the 0 degrees loop, and this is taken as a measure to identify the in-plane easy axis in thin films.

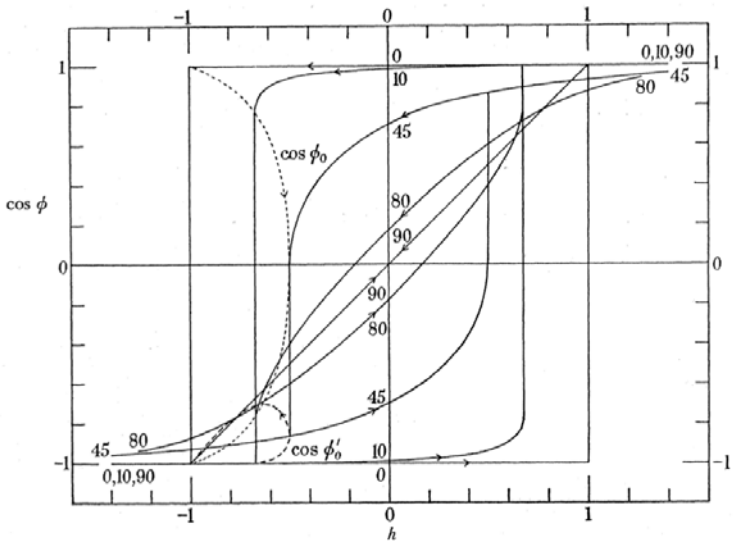

Figure 1-20. Magnetization curves for a prolate spheriod for the Stoner-Wohlfarth model [123], hysteresis loops are shown for angles: 0, 10, 45, 80 and 90 degrees between the spheriodal polar axis and the field direction

It has been shown that bulk LSMO magnetic anisotropy leads to a <111> directed easy axis and only under reduced thickness the easy axis is projected along <110>. Thin films magnetic anisotropy can be strongly influenced by substrate lattice mismatch. It is well known that ferromagnetic La manganites grown on $LaAlO_3$ display perpendicular anisotropy due to in-plane compressive strain induced by the LAO substrate smaller lattice parameters. Contradictory results have been found by different groups [124-128] for LCMO thin films grown on STO, yielding different easy axis directions this fact can be justified by the different growth techniques used introducing different structural defects types, and by the lattice parameters extreme sensitivity to oxygen and calcium content. Although the much better studied LSMO showed [110] easy axis the majority of research studies involving magnetometry and field dependent transport properties of heterostructures and thin film containing LCMO has been carried out applying the magnetic field along the [100] substrate direction. LCMO effectively shows small changes in magnetization hysteresis loops which don't seem to affect, for example, the CMR effect.

Thin films anisotropy may be controlled by artificial structures in the substrate. Magnetic domains may be oriented (for example) along steps on

the substrate/film interface induced by substrate production miscut [129]. Room temperature uniaxial magnetization along the step edges can be induced in $La_{0.67}Sr_{0.33}MnO_3$ films grown on STO, but biaxial anisotropy with easy (hard) axis along [110] ([100]) direction appears at low temperature [130]. A study on $La_{0.7}Sr_{0.3}MnO_3$ on [110] STO shows that the in-plane easy axis lies in [001] and the anisotropy strength can be tuned by varying film thickness [131], where relaxation with a resulting anisotropic stress determines the magnitude of the in-plane magnetic anisotropy.

1.10 Thesis Outline

- Chapter 2: Description of the characterization techniques used throughout this thesis comprehending: X-ray diffraction, transmission electron microscopy and electron energy loss spectroscopy for structural characterization; current perpendicular to plane geometry for electrical characterization techniques, besides some notes on micron-sized-feature junctions electrical measuring; vibrating sample magnetometry and SQUID magnetometry for magnetic characterization; polarized neutron reflectivity x-ray absorption spectroscopy and x-ray magnetic circular dichroism for studying the details on bulk and interfacial magnetic profiles.

- Chapter 3: Description of fabrication techniques used and developed throughout this thesis, starting with sputtering system for thin film growth, followed by a description of the optical lithography concepts and equipment used for micron-size feature junction fabrication: optical lithography, and removal techniques. After having presented the required concepts and equipment, the micron-size junction device design is presented,. Such a design is used for all the studies concerning this thesis and some details on the processed samples are listed.

- Chapter 4: Manganite-titanate interface is studied by using the perpendicular transport devices previously designed (Chapter 3); a manganite thin film grown on a niobium-doped strontium titanate substrate is processed and studied. Transport characterization reveals Schottky-like behavior, plus an unusual electrical permittivity behavior with temperature. A phenomenological model is here used to successfully describe the current voltage characteristics according to this permittivity behavior.

- Chapter 5: Based on the artificially modified magnetic ground state on [$SrTiO_3$\ $LaMnO_3$] superlattices that was found in this research group by J. García Barriocanal [132, 133], here now an [$SrTiO_3$\ $LaMnO_3$\ $SrTiO_3$] ultrathin trilayer is studied by using it as tunnel barrier sandwiched between two $La_{0.7}Sr_{0.3}MnO_3$ electrodes. Two different temperature dependences were found for TMR: high applied bias (200 to 400 mV) TMR barely shows changes below 60 K, and a strongly decreasing TMR (increasing temperature) for low applied biases. The system then yields a TMR stable state below certain temperature. Such an interesting behavior is explained in terms of an engineered magnetic state at the trilayer interface.

- Chapter 6: Nb:STO\ $La_{0.3}Ca_{0.7}MnO_3$\ $La_{0.7}Ca_{0.3}MnO_3$ all manganite tunnel junctions spin dependent transport study: an induced magnetic moment is found at the interface between both manganites and such an engineered interfacial state is used in order to obtain spin filtering behavior.

- Chapter 7: Spin dependent transport through the manganite/cuprate interface is characterized in [$La_{0.7}Ca_{0.3}MnO_3$\ $PrBa_2Cu_3O_7$\ $La_{0.7}Ca_{0.3}MnO_3$] magnetic tunnel junctions. TMR temperature dependence shows an anomalous behavior at low temperatures: TMR initially increases decreasing temperature and is suppressed below T ~ 70 K. Polarized neutron reflectivity (PNR) and XMCD measurements were carried on searching for an induced manganite-cuprate interfacial magnetic moment. PNR measurements revealed different anisotropies and different magnetic dynamics for top and bottom electrodes. XMCD revealed the induced Cu moment at both PBCO interfaces, resulting from an antiferromagnetic superexchange with the interfacial Mn atoms. As the induced magnetic

moment and the spin dependent transport characteristics were found mutually exclusive in temperature, then interfacial spin depolarization caused by the enormous effective exchange field is proposed as explanation for TMR suppression. Other possible mechanism playing an important role is the different easy axis observed for the magnetization of top and bottom electrodes. In fact, anisotropy fields may compete with a ferromagnetic coupling between both electrodes through the induced Cu moments, and this is proposed to explain the possibility of controlling magnetization switching (and thus resistance of the MTJs) by only using an electric field.

1.11 References

[1] A. Baruth, D. J. Keavney, J. D. Burton, K. Janicka, E. Y. Tsymbal, L. Yuan, S. H. Liou, and S. Adenwalla, Physical Review B 74 (2006) 054419.

[2] C. Chappert, A. Fert, and F. N. V. Dau, Nature Materials 6 (2007) 813.

[3] J. F. Gregg, I. Petej, E. Jouguelet, and C. Dennis, Journal of Physics D: Applied Physics 35 (2002) R121.

[4] M. N. Baibich, J. M. Broto, A. Fert, F. N. V. Dau, F. Petroff, P. Eitenne, G. Creuzet, A. Friederich, and J. Chazelas, Physical Review Letters 61 (1988) 2472.

[5] G. Binasch, P. Grünberg, F. Sauernbach, and W. Zinn, Physical Review B 38 (1989) 4828.

[6] R. A. d. Groot, F. M. Mueller, P. G. v. Engen, and K. H. J. Buschow, Physical Review Letters 50 (1983) 2024.

[7] R. A. d. Groot and K. H. J. Buschow, Journal of Magnetism and Magnetic Materials 54-57 (1986) 1377.

[8] J. M. d. Teresa, A. Barthélèmy, A. Fert, J. P. Contour, F. Montaigne, and P. Seneor, Science 286 (1999) 507.

[9] J. M. d. Teresa, A. Barthélèmy, A. Fert, J. P. Contour, R. Lyonnet, F. Montaigne, P. Seneor, and A. Vaurès, Physical Review Letters 82 (1999) 4288.

[10] M. Bowen, M. Bibes, A. Berthélémy, J.-P. Contour, A. Anane, Y. Lemaître, and A. Fert, Applied Physics Letters 82 (2003) 233.

[11] M. O. Bowen, Vol. Doctor in Sciences, Universite de Paris-Sud U.F.R. Scientifique D'Orsay, Paris, 2003.

[12] V. Garcia, M. Bibes, A. Barthelemy, M. Bowen, E. Jacquet, J. P. Contour, and A. Fert, Physical Review B 69 (2004) 052403.

[13] M. Viret, M. Drouet, J. Nassar, J. P. Contour, C. Fermon, and A. Fert, Europhysics Letters 39 (1997) 545.

[14] Y. Lu, X. W. Li, G. Q. Gong, G. Xiao, A. Gupta, P. Lecoeur, J. Z. Sun, Y. Y. Wang, and V. P. Dravid, Physical Review B 54 (1996) R8357.

[15] J. H. Park, E. Vescovo, H. J. Kim, C. Kwon, R. Ramesh, and T. Venkatesan, Nature 392 (1998) 794.

[16] J. H. Park, E. Vescovo, H. J. Kim, C. Kwon, R. Ramesh, and T. Venkatesan, Physical Review Letters 81 (1998) 1953.

[17] M.-H. Jo, N. D. Mathur, N. K. Todd, and M. G. Blamire, Physical Review B 61 (2000) R14905
[18] J. S. Moodera, T. S. Santos, and T. Nagahama, Journal of Physics : Condensed Matter 19 (2007) 165202.
[19] J. S. Moodera, X. Hao, G. A. Gibson, and R. Meservey, Physical Review Letters 61 (1988) 637
[20] X. Hao, J. S. Moodera, and R. Meservey, Physical Review B 42 (1990) 8235.
[21] J. S. Moodera, R. Meservey, and X. Hao, Physical Review Letters 70 (1993) 853
[22] T. S. Santos and J. S. Moodera, Physical Review B 69 (2004) 241203(R).
[23] M. Gajek, M. Bibes, A. Barthélémy, K.Bouzehouane, S. Fusil, M. Varela, J. Foncuberta, and A. Fert, Physical Review B 72 (2005) 020406(R).
[24] U. Lüders, A. Barthélèmy, M. Bibes, K. Bouzehouane, S. Fusil, E. Jacquet, J. P. Contour, J. F. Bobo, J. Foncuberta, and A. Fert, Advanced Materials 18 (2006) 1733.
[25] U. Lüders, M. Bibes, K. Bouzehouane, E. Jacquet, J. P. Contour, S. Fusil, J. F. Bobo, J. Foncuberta, A. Barthélèmy, and A. Fert, Applied Physics Letters 88 (2006) 082505.
[26] A. Ohtomo and H. Y. Hwang, Nature 427 (2004) 423.
[27] M. Basletic, M. J. L., C. Carretero, G. Herranz, O. Copie, M. Bibes, E. Jacquet, K. Bouzehouane, S. Fusil, and A. Barthelemy, Nature Materials 7 (2008) 621.
[28] A. Brinkman, M. Huijben, M. V. Zalk, J. Huijben, U. Zeitler, J. C. Maan, W. G. V. d. Wiel, G. Rijnders, D. H. A. Blank, and H. Hilgenkamp, Nature Materials 6 (2007) 493.
[29] N. Reyren, S. Thiel, A. D. Caviglia, L. F. Kourkoutis, G. Hammerl, C. Richter, C. W. Schenider, T. Koop, A. S. Ruetschi, D. Jaccard, M. Gabay, D. A. Muller, J. M. Triscone, and J. Mannhart, Science 317 (2007) 1196.
[30] K. S. Takahashi, M. Kawasaki, and Y. Tokura, Applied Physics Letters 79 (2001) 1324.
[31] A. Hoffmann, S. G. E. t. Velthuis, Z. Sefrioui, J. Santamaría, M. R. Fitzsimmons, S. Park, and M. Varela, Physical Review B 72 (2005) 140407.
[32] H. Geiger, K. Scheel, H. B. P. C. o. t. H. o. Q. Mechanics, and t. T. o. Relativity, Handbuch der Physik, Verlag von Julius Springer, 1933.

[33] J. Frenkel, Physical Review 36 (1930) 1604.
[34] I. Giaever and K. Megerle, Physical Review 122 (1961) 1101.
[35] C. B. Duke, Tunneling in Solids, Academic Press, 1969.
[36] E. L. Wolf, Principles of Electron Tunneling Spectroscopy, Oxford Universtity Press, New York, 1985.
[37] F. Schwabl, Quantum Mechanics, Springer, 2007.
[38] M. H. Cohen, L. M. Falicov, and J. C. Phillips, Physical Review Letters 8 (1962) 316.
[39] J. G. Simmons, Journal of Applied Physics 34 (1963) 1793.
[40] J. G. Simmons, Journal of Applied Physics 34 (1963) 2581.
[41] W. F. Brinkman, R. C. Dynes, and J. M. Rowell, Journal of Applied Physics 41 (1970) 1915.
[42] M. Jullière, Physics Letters A 54 (1975) 225
[43] S. S. P. Parkin, K. P. Roche, M. G. Samant, P. M. Rice, R. B. Beyers, R. E. Scheuerlein, E. J. O'Sullivan, S. L. Brown, J. Bucchigano, D. W. Abraham, Y. Lu, M. Rooks, P. L. Trouilloud, R. A. Wanner, and W. J. Gallagher, Journal of Applied Physics 85 (1999) 5828.
[44] W. J. Fallagher and S. S. P. Parkin, IBM Journal of Research and Development - Spintronics 50 (2006)
[45] I. I. Mazin, Physical Review Letters 83 (1999) 1427.
[46] G. E. Blonder, M. Tinkham, and T. M. Klapwijk, Physical Review B 25 (1982) 4515.
[47] S. K. Upadhyay, A. Palanisami, R. N. Louie, and R. A. Buhrman, Physical Review Letters 81 (1998) 3247.
[48] R. J. S. Jr., J. M. Byers, M. S. Osofsky, B. Nadgorny, T. Ambrose, S. F. Cheng, P. R. Broussard, C. T. Tanaka, J. Nowak, J. S. Moodera, A. Barry, and J. M. D. Coey, Science 282 (1998) 85.
[49] P. Raychaudhun, A. P. Mackenzie, J. W. Reiner, and M. R. Beasley, Physical Review B 67 (2003) 020411(R).
[50] R. Meservey, P. M. Tedrow, and P. Fulde, Physical Review Letters 25 (1970) 1270.
[51] P. M. Tedrow and R. Meservey, Physical Review B 7 (1973) 318.
[52] R. Meservey and P. M. Tedrow, Physics Reports 238 (1994) 173.
[53] J. S. Moodera and J. Nassar, Annual Review of Materials Science 29 (1999) 381.
[54] P. LeClair, H. J. M. Swagten, J. T. Kohlhepp, R. J. M. v. d. Veerdonk, and W. J. M. d. Jonge, Physical Review Letters 84 (2000) 2933.

[55] P. LeClair, J. T. Kohlhepp, H. J. M. Swagten, and W. J. M. d. Jonge, Physical Review Letters 86 (2001) 1066.
[56] P. LeClair, B. Hoex, H. Wieldraaijer, J. T. Kohlhepp, H. J. M. Swagten, and W. J. M. d. Jonge, Physical Review B 64 (2001) 100406(R).
[57] E. Y. Tsymbal, O. N. Mryasov, and P. R. LeClair, Journal of Physics : Condensed Matter 15 (2003) R109.
[58] J. Bardeen, Physical Review Letters 6 (1961) 57.
[59] T. Miyazaki and N. Tezuka, Journal of Magnetism and Magnetic Materials 139 (1995) L231.
[60] J. S. Moodera, L. R. Kinder, T. M. Wong, and R. Meservey, Physical Review Letters 74 (1995) 3273
[61] R. Y. Gu, L. Sheng, and C. S. Ting, Physical Review B 63 (2001) 220406(R).
[62] M. B. Stearns, Journal of Magnetism and Magnetic Materials 5 (1977) 167.
[63] L. Samet, D. Imhoff, J.-L. Maurice, J.-P. Contour, A. Gloter, T. Manoubi, A. Fert, and C. Colliex, European Physical Journal B 34 (2003) 179.
[64] W. E. Pickett and J. S. Moodera, Physics Today 54 (2001)
[65] S. Jin, T. H. Fiefel, M. McCormack, R. A. Fastnacht, R. Ramesh, and L. H. Chen, Science 264 (1994) 413.
[66] M. McCormack, S. Jin, T. H. Tiefel, R. M. Fleming, J. M. Phillips, and R. Ramesh, Applied Physics Letters 64 (1994) 3045.
[67] E. Dagotto, T. Hotta, and A. Moreo, Physics Reports 344 (2001) 1
[68] M. Imada, A. Fujimori, and Y. Tokura, Reviews of Modern Physics 70 (1998) 1039
[69] J. M. D. Coey and M. Viret, Advances in Physics 48 (1999) 167.
[70] S. Zhang, P. M. Levy, A. C. Marley, and S. S. P. Parkin, Physical Review Letters 79 (1997) 3744.
[71] J. S. Moodera, J. Nowak, and R. J. M. v. d. Veerdonk, Physical Review Letters 80 (1998) 2941
[72] M. Jaime, M. B. Salamon, M. Rubinstein, R. E. Treece, J. S. Horwitz, and D. B. Chrisey, Physical Review B 54 (1996) 11914.
[73] Y. Xu, D. Ephron, and M. R. Beasley, Physical Review B 52 (1995) 2843.
[74] J. Zhang and R. M. White, Journal of Applied Physics 83 (1998) 6512.

[75] A. Vedyayaev, D. Bagrets, A. Bagrets, and B. Dieny, Physical Review B 63 (2001) 064429.
[76] A. M. Bratkovsky, Applied Physics Letters 72 (1998) 2334.
[77] T. Susaki, N. Nakagawa, and H. Y. Hwang, Physical Review B 75 (2007) 104409.
[78] F. A. Padovani and R. Stratton, Solid-State Electronics 9 (1966) 695.
[79] C. H. Shang, J. Nowak, R. Jansen, and J. S. Moodera, Physical Review B 58 (1998) R2917.
[80] A. H. MacDonald, T. Jungwirth, and M. Kasner, Physical Review Letters 81 (1998) 705.
[81] E. Y. Tsymbal and D. G. Pettifor, Journal of Physics : Condensed Matter 9 (1997) L411.
[82] M. Sharma, S. X. Wang, and J. H. Nickel, Physical Review Letters 82 (1999) 616.
[83] M. Bibes and A. Barthelemy, IEEE Transactions on Electron Devices 54 (2007) 1003.
[84] M. Bibes, J. E. Villegas, and A. Barthélémy, Advances in Physics 60 (2011) 5.
[85] L. M. B. Alldredge and Y. Suzuki, Applied Physics Letters 85 (2004) 437.
[86] M.-H. Jo, M. G. Blamire, D. Ozkaya, and A. K. Petford-Long, Journal of Physics : Condensed Matter 15 (2003) 5243.
[87] R. Jansen and J. S. Moodera, Applied Physics Letters 75 (1999) 400.
[88] K. I. Lee, S. J. Joo, J. H. Lee, K. Rhie, T.-S. Kim, W. Y. Lee, K. H. Shin, B. C. Lee, P. LeClair, J. S. Lee, and J. H. Park, Physical Review Letters 98 (2007) 107202.
[89] L. Esaki, P. J. Stiles, and S. v. Molnar, Physical Review Letters 19 (1967) 852
[90] T. Nagahama, T. S. Santos, and J. S. Moodera, Physical Review Letters 99 (2007) 016602.
[91] P. LeClair, J. K. Ha, H. J. M. Swagten, J. T. Kohlhepp, C. H. v. d. Vin, and W. J. M. d. Jonge, Applied Physics Letters 80 (2002) 625.
[92] A. Saffarzadeh, Journal of Magnetism and Magnetic Materials 269 (2004) 327.
[93] S. Okamoto and A. J. Millis, Nature 428 (2004) 630.
[94] S. Yunoki, A. Moreo, E. Dagotto, S. Okamoto, S. S. Kancharla, and A. Fujimori, Physical Review B 76 (2007) 064532.

[95] B. R. K. Nanda, S. Satpathy, and M. S. Springborg, Physical Review Letters 98 (2007) 216804.
[96] M. J. Calderón, J. Salafranca, and L. Brey, Physical Review B 78 (2008) 024415.
[97] K. H. Ahn, T. Lookman, and A. R. Bishop, Nature 428 (2004) 401
[98] D. Niebieskikwiat, L. E. Hueso, J. A. Borchers, N. D. Mathur, and M. B. Salamon, Physical Review Letters 99 (2007) 247207.
[99] J. Salafranca, M. J. Calderón, and L. Brey, Physical Review B 77 (2007) 014441.
[100] Y. Tokura, Physics Today 56 (2003) 50
[101] G. H. Jonker and J. H. V. Santen, Physica 16 (1950) 337.
[102] J. H. V. Santen and G. H. Jonker, Physica 16 (1950) 599.
[103] J. Volger, Physica 20 (1954) 49.
[104] E. O. Wollan and W. C. Koehler, Physical Review 100 (1955) 545.
[105] Y. Tokura, Colossal magnetoresistive oxides, Gordon and Breach Science Publishers, 2000.
[106] C. Zener, Physical Review 82 (1951) 403.
[107] J. H. Park, C. T. Chen, S.-W. Cheong, W. Bao, G. Meigs, V. Chakarian, and Y. U. Idzerda, Physical Review Letters 76 (1996) 4215.
[108] B. Nadgorny, I. I. Mazin, M. Osofsky, J. R. J. Soulen, P. Broussard, R. M. Stroud, D. J. Singh, V. G. Harris, A. Arsenov, and Y. Mukovskii, Physical Review B 63 (2001) 184433.
[109] G. M. Müller, J. Walowski, M. Djordjevic, G.-X. Miao, A. Gupta, A. V. Ramos, K. Gehrke, V. Moshnyaga, K. Samwer, J. Schmalhorst, A. Thomas, A. Hütten, G. Reiss, J. S. Moodera, and M. Münzenberg, Nature Materials 8 (209) 56.
[110] J. L. García-Muñoz, J. Foncuberta, M. Suaaidi, and X. Obradors, Journal of Physics : Condensed Matter 8 (1996) L787.
[111] S. Yunoki, J. Hu, A. L. Malvezzi, A. Moreo, N. Furukawa, and E. Dagotto, Physical Review Letters 80 (1998) 845.
[112] J. Burgy, A. Moreo, and E. Dagotto, Physical Review Letters 92 (2004) 097202.
[113] E. Dagotto, Nanoscale phase separation and colossal magnetoresistance: the physics of manganites and related compounds, Springer, 2003.
[114] I. O. Troyanchuk, Journal of Experimental and Theoretical Physics 75 (1992) 132.

[115] R. H. Heffner, L. P. Le, M. F. Hundley, J. J. Neumeier, G. M. Luke, K. Kojima, B. Nachumi, Y. Uemura, D. E. MacLaughlin, and S.-W. Cheong, Physical Review Letters 77 (1996) 1869.
[116] G. Allodi, R. D. Renzi, G. Guidi, F. Licci, and M. W. Pieper, Physical Review B 56 (1997) 6036.
[117] J. W. Lynn, R. W. Erwin, J. A. Borchers, Q. Huang, A. Santoro, J.-L. Peng, and Z. Y. Li, Physical Review Letters 76 (1996) 4046.
[118] J. M. d. Teresa, M. R. Ibarra, P. A. Algarabel, C. Ritter, C. Marquina, J. Blasco, J. García, A. d. Moral, and Z. Arnold, Nature 386 (1997) 256.
[119] M. Hennion, F. Moussa, G. Biotteau, J. Rodríguez-Carvajal, L. Pinsard, and A. Revcolevschi, Physical Review Letters 81 (1998) 1957.
[120] S. Yoon, H. L. Liu, G. Schollerer, S. L. Cooper, P. D. Han, D. A. Payne, S.-W.Cheong, and Z. Fisk, Physical Review B 58 (1998) 2795.
[121] N. Mannella, C. H. Booth, A. Rosenhahn, B. C. Sell, A. Nambu, S. Marchesini, B. S. Mun, S.-H. Yang, M. Watanabe, K. Ibrahim, E. Arenholz, A. Young, J. Guo, Y. Tomioka, and C. S. Fadley, Physical Review B 77 (2008) 125134.
[122] C. H. Booth, F. Bridges, G. H. Kwei, J. M. Lawrence, A. L. Cornelius, and J. J. Neumeier, Physical Review Letters 80 (1998) 853.
[123] E. C. Stoner and E. P. Wohlfarth, IEEE Transactions on Magnetics 27 (1991) 3475.
[124] Y. Suzuki, H. Y. Wang, S.-W. Cheong, and R. B. v. Dover, Applied Physics Letters 71 (1997) 140.
[125] J. O'Donnell, M. S. Rzchowski, J. N. Eckstein, and I. Bozovic, Applied Physics Letters 72 (1998) 1775.
[126] K. Steenbeck and R. Hiergeist, Applied Physics Letters 75 (1999) 1778.
[127] T. K. Nath, R. A. Rao, D. Lavric, C. B. Eom, L. Wu, and F. Tsui, Applied Physics Letters 74 (1999) 1615.
[128] M. Ziese, Physical Review B 62 (2000) 1044.
[129] Z.-H. Wang, G. Cristiani, and H.-U. Habermeier, Applied Physics Letters 82 (2003) 3731.
[130] M. Mathews, F. M. Postma, J. C. Lodder, R. Jansen, G. Rijnders, and D. H. A. Blank, Applied Physics Letters 87 (2005) 242507.
[131] I. C. Infante, J. O. Ossó, F. Sánchez, and J. Foncuberta, Applied Physics Letters 92 (2008) 012508.

[132] J. Garcia-Barriocanal, J. C. Cezar, F. Y. Bruno, P. Thakur, N. B. Brookes, C. Utfeld, A. Rivera-Calzada, S. R. Giblin, J. W. Taylor, J. A. Duffy, S. B. Dugdale, T. Nakamura, K. Kodama, C. Leon, S. Okamoto, and J. Santamaria, Nature Communications (2010)
[133] J. G. Barriocanal, in Física Aplicada III, Vol. Doctor en Ciencias Físicas, Universidad Complutense de Madrid, Madrid, 2007.

2 CHARACTERIZATION TECHNIQUES

2.1 X-Ray Diffraction

The material physical properties (electronic, optic, magnetic, etc.) depend on its structural qualities. For thin films and heterostructures the structural tolerance levels are necessarily reduced and thus it is necessary to precisely know the composition, individual films and total layer thicknesses, epitaxial grade, defects, etc. and the X Ray Diffraction analysis helps to obtain this information. In particular it is of interest to check the individual film growth orientation, its thickness, modulation length in superlattices, and structural coherence length. It is not sufficient by itself, and shall be completed by other structural characterization techniques, but the greatest advantage of this technique is its non-destructive and non-invasive character.

2.1.1 Diffraction patterns obtention

The Diffraction Patterns have been measured in a Philips X'Pert D500-I diffractometer, which uses as a radiation source an x-ray tube with copper anticathode working at 45 KV and 40 mA. The used radiation contains the copper lines $K\alpha 1$ = 0.15406 nm and $K\alpha 2$ = 0.15444 nm. This diffractometer is a high resolution device, consisting of a four circles goniometer with a quarter circle Eulerian cradle and sample holder stage. The used measurement geometry is the Bragg geometry, also called ω-2ϑ. In such geometry the x-ray beam incidence angle on the sample (ω) is changed, and in synchronized movement, the detector

angle is changed in the double quantity (2ϑ); in that way the detected radiation corresponds to the perfect reflection direction. The alignment is done such that the x-ray dispersion vector is always perpendicular to the substrate, observing the diffraction peaks related with the distances in the out-of-plane direction.

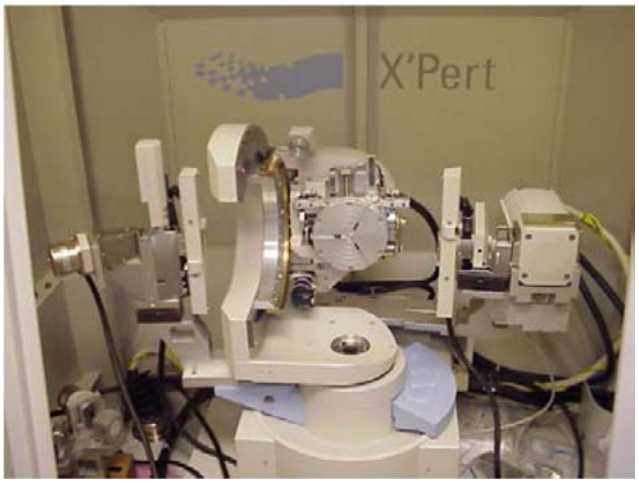

Figure 2-1. PANalytical diffractometer at the Universidad Complutense de Madrid microscopy facilities

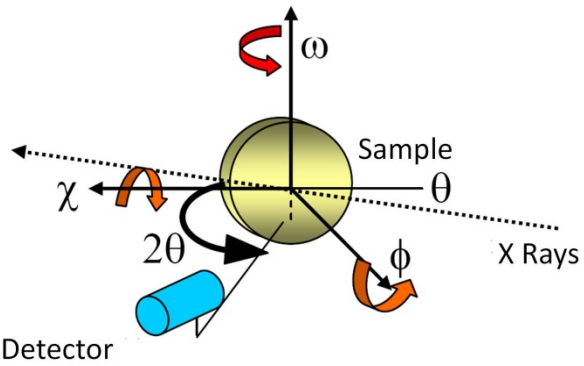

Figure 2-2. Angles associated to the diffractometer movement [1]

2.1.2 High angle diffraction

A solid's lattice formed by parallel planes separated a distance "*d*", specularly reflects the incident waves, each plane reflects a little radiation fraction. The path difference between two adjacent planes is $2d\sin(\theta)$, where θ is measured from the plane. Interference is constructive when the path difference of successive planes reflected radiation is an integral number of wave lengths "λ". The condition leading to reflected radiation constructive interference, known as the Bragg Law states:

$$2d_{hkl}\sin(\theta) = n\lambda \qquad (2.1)$$

where d_{hkl} is the $\{hkl\}$ family interplanar distance, θ is the incidence angle, λ_x is the x-ray wavelength and n is the reflection order. In specular geometry the high angle diffraction spectrum shows only the parallel to the surface plane families, obtaining the peaks corresponding to the (001) reflection, and therefore the perpendicular to "*c*" axis $\{hkl\}$ family planes. Structural Coherence Length is obtained from the peak width in the Scherrer formulae[2]:

$$\xi = \frac{0.9\lambda}{b\cos(\theta)} \qquad (2.2)$$

where "*b*" is the Half Width Full Maximum and 2θ its angle.

2.1.3 Low angle diffraction

A measurement of X-ray reflectivity is obtained in the angular range $2\theta \leq 10°$. At the Bragg Geometry, the dispersion vector length corresponds to longer than interplanar crystallographic distances of the studied materials:

$$q = \frac{2\sin(\theta)}{\lambda} \qquad (2.3)$$

where $\lambda = 1.54\text{Å}$, therefore the incident wavevector is 4.07 Å^{-1} thus the dispersion vector is shorter than 0.71 Å^{-1} (because 2θ < 10 in XRR), and the distances "*d*" giving rise to the diffraction phenomena are $d \sim \left(\frac{1}{q}\right) > 8.83\text{Å}$, which is longer than most interplanar distances. X-rays are sensitive to the material chemical composition through the refraction index, which is proportional to the average electronic density [3].

$$n = 1 - \frac{\rho_N r_e \lambda_x^2}{2\pi}\left(f_0 + \Delta f' - \imath \Delta f''\right) \qquad (2.4)$$

where ρ_N is the electronic density, r_e is the electronic radius, λ_x the x-ray wavelength, f_0 the atomic dispersion factor and $\Delta f'$ besides $\Delta f''$ are the anomalous dispersion correction factors. The refraction index is the complex number:

$$n = 1 - \delta - \imath\beta,$$

$$\delta = \frac{\rho_N r_e \lambda_x^2}{2\pi}\left(f_0 + \Delta f'\right)$$

$$\beta = \frac{\rho_N r_e \lambda_x^2}{2\pi}\Delta f''$$

The diffraction index real component is $(1-\delta)$, where $\delta \sim 3\times 10^{-5}$. Part of the incident radiation is reflected at the surface and other part penetrates the film, the latter is reflected at the film substrate interface and traverses the film surface again. When both beam interfere a maxima and minima diffraction patterns is

obtained, the ripples are called “finite thickness oscillations”. Starting from these oscillations the film thickness can be measured, by using Bragg’s Law for the maxima and minima angular positions:

$$\sin^2(\theta) = \left[\frac{(n+k)\lambda_x}{2d}\right]^2 + 2\delta \qquad (2.5)$$

where “*d*” is the film thickness, $(1-\delta)$ is the refraction index real component, and $k = 0$ corresponds to a minimum intensity, while $k = \frac{1}{2}$ corresponds to a maximum, if the substrate has a lower than film’s electronic density [4].

Besides, the beam footprint is large due to grazing incidence, and then it is averaged over a large area of the sample. The appearing of finite thickness oscillations indicates a surface roughness lower than a unit cell over long lateral distances.

2.1.4 X ray diffraction from superlattices

If a coherent stacking of two materials (A and B) is studied instead a single film, and such a bilayer is repeated forming a superlattice, the x-ray pattern contains additional intensity maxima related with the “artificial” periodicity. Modulation Length is the repeating bilayer thickness and it is defined as:

$$\Lambda = N_A \cdot c_A + N_B \cdot c_B \qquad (2.6)$$

where c_A and c_B are the lattice parameters in the growth direction; N_A and N_B are the quantity of unit cells of each material (A and B) in the basis bilayer. In low angle diffraction, the patterns is resulting from chemical modulation scattering,

since the incident angle is low, it is averaged over sample extensions longer than in high angle diffraction; from Bragg's Law:

$$\sin^2\left(\frac{n\lambda_x}{2\Lambda}\right)+2\delta_s,$$

where θ is the angle corresponding to the reflection direction, "*n*" corresponds to its order, λ_x is the x-ray wavelength, and $\left(1-\delta_s\right)$ is the real component of the superlattice average refraction index. The typical numerical value is $\delta_s \sim 3\times10^{-5}$. In principle the Low Angle Patterns represents the composition profile Fourier Transform of the composition profile, although the disorder, multiple reflections, refraction effects or surface reflection limit the information that can be extracted from the Fourier Transform. The most common approximation to quantitatively analyze the patterns is realized through recursive application of optical formalisms, assuming the layers are continuous media and calculating the reflection at each interface [5]. The disorder effect affects the low angle diffraction patterns through the possible fluctuations of each layer thickness; such fluctuations diminish the peak intensity and increase the peak width, resulting in a bigger distortion for higher order peaks. The pattern background between peaks increases, and the oscillations' intensity decreases when thickness fluctuation (roughness) increases.

In high angle diffraction there is a different situation, and it gives rise to the opportunity of studying the materials at the microscopic level. The Structural Coherence Length (ξ) in the growth direction strongly influences the high angle diffraction patterns. If $\xi > \Lambda$ superlattice peak modulation is observed; satellite peaks are indexed around the average superlattice parameter $\overline{d}$:

$$2\frac{\sin(\theta)}{\lambda_x}=\frac{1}{\overline{d}}\pm\frac{n}{\Lambda} \qquad (2.7)$$

where "*n*" is an integer, which indexes the satellite order around the Bragg peak and

$$\overline{d} = \frac{\Lambda}{\left(N_A + N_B\right)}$$

$\overline{d}$ and Λ are the only quantities that can be directly determined from the peak position, while ξ can be obtained from the peak's Full Width Half Maximum. According to kinematic theory, the x ray diffracted intensity of a crystal for a reflection of indexes $\left(hkl\right)$ is proportional to the structural factor squared $F\left(hkl\right)$. This can be written as:

$$F\left(hkl\right) = \int_a^{cell} f_a \cdot \exp\left(\imath q r_a\right) dr \qquad (2.8)$$

where f_a is the atomic dispersion factor of each atom, $\exp\left(iqr_a\right)$ is the phase factor introduced by the atom in the dispersed radiation as a function of the relative position inside the cell $\vec{r_a}$, and the integration is extended to all the unit cell atoms. For an ideal superlattice, along the stacking direction, the expression can be generalized, writing the structural factor as:

$$F_{SL}\left(q\right) = F_A + F_B \exp\left(\imath q t_A\right) \qquad (2.9)$$

where F_A and F_B are the structural factors of each constituent layer and t_A is the "A" layer thickness, which introduces the needed phase term to correctly include the relative displacement between layers. In this way main diffraction maxima appear, associated to the average lattice parameter, and secondary diffraction maxima related to an interplanar distance equal to the modulation length Λ.

2.2 Transmission Electron Microscopy

In order to probe the local structure of materials and low dimensional systems high spatial resolution real space probes are needed. Here, transmission electron microscopy (TEM) techniques were used to study heterostructures and interfaces.

In the electron microscope a sample is probed with a focused beam of electrons accelerated tens to hundreds of kilovolts. These relativistic electrons exhibit wavelengths in the picometer range, which sets the theoretical spatial resolution achievable. Factors such as magnetic lens imperfections limit the spatial resolution (e.g. spherical or chromatic aberrations) to the 0.1 nm regime. Specimen thickness (less than 200 nm) also imposes constrains on the experiments. Images with magnifications ranging from fifty to a million times can be recorded, usually with a CCD, film plate or video camera. Figure 2-3 shows a diagram of a TEM [6].

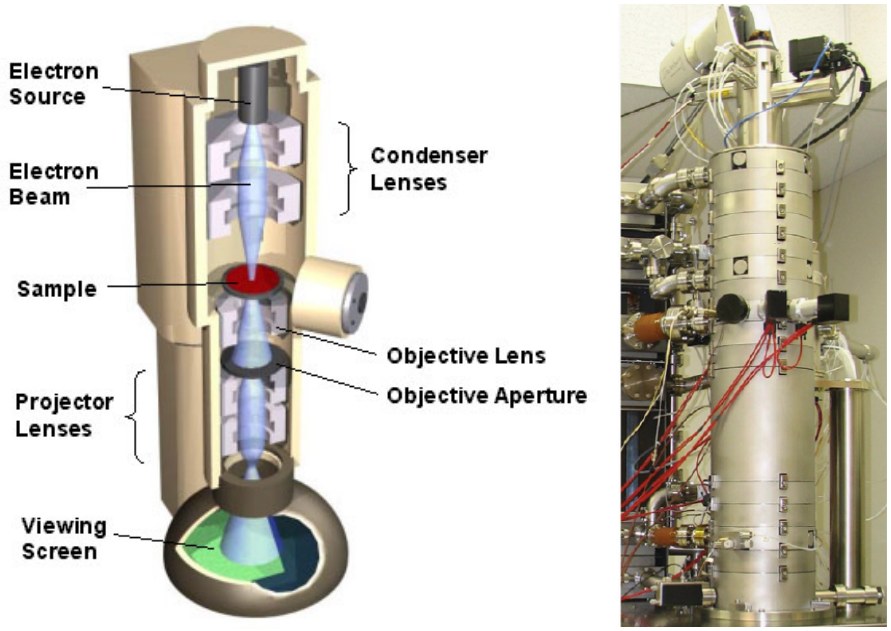

Figure 2-3. Schematics of a TEM instrument (left) and photograph (right) of a NION ULTRASTEM column [7]

The main TEM disadvantage is that image interpretation is not straightforward, especially since a two-dimensional image of the three-dimensional sample is projected onto the detector. Analytical techniques, such as electron energy loss spectroscopy (EELS) or energy disperse x-ray spectroscopy (EDS), can be used in some cases to extract additional chemical information, measure thickness and optical properties using plasmon loss or even obtain details of the density of states through the EELS fine structure.

Electrons interact with the potential field of an atomic nucleus, but also with the electron cloud surrounding the nucleus. The scattering of an electron by an atomic nucleus occurs by Rutherford Scattering. This elastic scattering can be used to produce images with direct compositional contrast such as *Z*-contrast images in the scanning transmission electron microscope (STEM). The magnitude of elastic electron-nucleus interaction scales with the square of the atomic number, giving rise to a contrast where regions of high-*Z* appear brighter than regions of low-*Z*. The scattering of an electron by the electron cloud of an atom is most often an inelastic interaction.

2.3 Electron Energy Loss Spectroscopy

Electron energy loss spectroscopy (EELS) is a powerful analytical tool that relies on the measurement of the energy lost by the electron beam while travelling through a thin specimen [6]. The beam can transfer energy to the atoms through excitations of core electrons, valence electrons and other processes. While the edge fine structures are closely related to the unoccupied density of states of the material, signal under the absorption edges is proportional to the local elemental concentration. EELS, therefore, is an ideal technique to simultaneously measure composition and electronic properties: electronic structure, chemical bonding, and average nearest neighbor distances can be obtained by the analyst. In practice, the inner shell excitations studied have binding energies less than 3 KeV. Quantitative concentration determinations can be obtained for the elements $3 \leq Z \leq 35$ using data analysis procedures. The energy resolution of the technique is limited by the inherent energy spread of the electron source used in the microscope and for a cold field emission gun is of the order of 0.3 - 0.4 eV.

EELS is a direct result of the Coulombic interaction of a fast monochromatic electron beam with the atoms in the sample. Inelastic scattering, either with tightly bound core electrons or loosely bound valence electrons, causes electronic excitations towards high energy states, or even Auger electrons. Energy distribution of the incident electrons after interaction is changed to reflect this energy transfer. Because EELS is the primary interaction event, all the other analytical signals derived from electron excitation are the result of secondary decay processes. Therefore, EELS yields the highest amount of information per inelastic scattering event, among all the electron column-based spectroscopies.

The low loss regime is defined from about 1 eV to 50 eV, and is composed of a series of broad spectral features related to inelastic scattering with the valence

electron structure of the sample. Extending for thousands of eV above that range there is a continuously decreasing background superimposed upon a series of edges resulting from electrons that have lost energy corresponding to the creation of vacancies in the deeper core levels of the atom (*K, L_3, L_2, L_1, M_5*, and so forth). As the energy needed to eject electrons from the material is characteristic of each element, by measuring the threshold energy of each edge it is possible to determine the identity of the atom giving rise to the signal. Besides, the integrated intensity can be analyzed to obtain the number of atoms producing the signal. It is important to realize that the atomic transitions probed by EELS as edges are subject to the dipole selection rule: $\Delta l = \pm 1$.

2.4 Electrical Characterization

2.4.1 Current in plane

In order to measure the resistance of a thin film it is necessary to avoid the measurement of the contact resistance, which is a series resistance in a single loop measurement circuit; at 1958 Van der Pauw [8] reported the widely known Four Probe Measurement method which was developed to measure the resistance associated to an arbitrary shape surface. Although all of the experiments developed in this thesis comprehend thin film materials, Current in Plane (CIP) measurements were not used since interface effects shall be measured in the Current Perpendicular to Plane (CPP) configuration.

2.4.2 Current perpendicular to plane

As in the CIP case, the contact in-series resistance needs to be avoided when measuring the device resistance, then a two probe measurement is not the optimal measurement configuration. In order to avoid the measurement of undesired in-series resistance four probe measurements shall be used; Figure 2-4 shows the circuit schematics of this kind of measurement (see also Figure 3-8). The voltage source gives rise to a current flow in the left loop of the circuit, and this current is measured at the ammeter. Since the voltmeter has “infinite” input impedance no current flows at the right loop of the circuit and the voltage drop measured corresponds to that at the ends of the resistance R_T of the tunneling junction. Then the measured resistance R_m is calculated with these two simple measurements, eliminating bottom electrode resistance and the contact resistance

$R_L = R_{L1} + R_{L2}$ that has been divided in two fractions whose magnitudes will depend on the particular position of each junction above the bottom electrode.

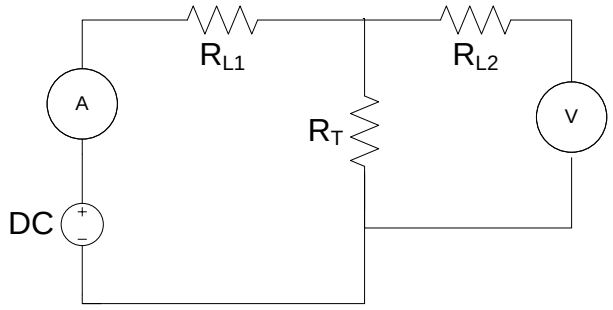

Figure 2-4. Measurement circuit in the four probe measurement configuration

The contact geometry used in this work is the same that was analyzed by Lenczowski et al. [9, 10], and that was recalled in those reports as "Geometry I". Such a geometry consists in a bottom electrode with a pillar above it, then the whole structure is covered with an insulator (in the case of this work mostly SiO_2 and in two cases Si_3N_4) that is patterned by means of optical lithography to obtain etched holes by Reactive Ion Etching, which will serve as a pathway for the next metallic layer covering the insulator. Figure 2-5 shows the geometry used (taken from [9]), the length scales indicated in Figure 2-5 (a) have not been followed in this work; other length scales have been used instead since the materials here studied can be grown in different thicknesses more appropriate for the materials characteristics needed.

In the Lenczowski et al. reports and the works they cited, the devices under study were comprised by metallic ferromagnetic multilayers, then the resistance order of magnitude was much lower than the one here expected; the recalled "Geometry II" that contains trenched metallic contacts was not considered for implementation in this work because the target here is characterization by perpendicular tunneling

current, then the device resistance is indeed higher than the resistance corresponding to the metallic multilayers previously cited.

After having completed the task of checking the electrode resistance vs. the junction resistance orders of magnitude, the two-probe or four-probe technique can be used; if the tunneling resistance is orders of magnitude larger than the electrode resistance then both techniques can be used, if the electrode resistance is comparable to the tunneling resistance then the use of four-probe measurements technique is mandatory. Connections *I+* and *V+* go to the bottom electrode while the top electrode has connection with *I-* and *V-* probes; the signs have been inverted (compared to Figure 2-5) in order to have the lower potential contacted to the junction, thus diminishing the possibility of leading the tunnel junction to electric rupture by high applied bias.

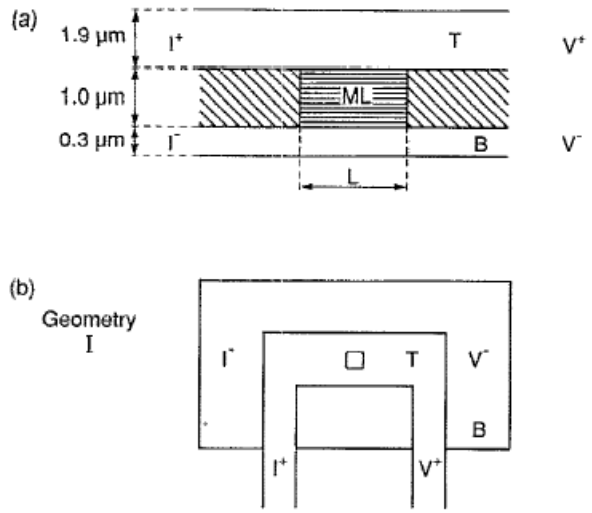

Figure 2-5. Contact geometry as taken from Ref [9], the figure legend therein reads: (a) Side view of the central part of the structure for the perpendicular resistance experiment. The actual multilayer is indicated by ML, whereas T and B mark the top and bottom electrodes, respectively. The hatched part of the structure is insulating material. (b) Schematic top view of our geometry I. The constriction is indicated by the square-like structure in the center. For clarity, the insulating layer has been omitted

All the electrical measurements were done inside a closed-cycle cryostat composed by an *Advanced Research Systems* expander model DE-202 coupled with an *APD Cryogenics* helium compressor model HC–2D, such a system works with the expansion of highly-pure He gas compressed in a Gifford McMahon cycle with expansion through the capillaries at two steps in 50 K and 8.5 K. The system is evacuated by a rotary pump capable of a pressure down to 4×10^{-3} mbar measured with a Pirani vacuum sensor. The sample is mounted onto a cooled copper piece in contact with the second cooling step; a silicon diode thermometer is in contact with the sample holder calibrated for measuring between 10 K and 325 K with a *LakeShore* 331 temperature controller; a rolled nichrome wire works as heater also controlled by the *LakeShore* 331 equipment, that configuration allows temperature control between 10 K and 325 K with a 10 mK accuracy. Micro-coaxial wires are used to measure with low noise contribution, connected in a configuration with shielding open loops [11] , the magnetic field (available range is ± 4200 Oe) is provided by a water cooled *Oxford* electromagnet controlled by a *Kepko* Bipolar Operation Power source, the magnetic induction is measured by a *Magnet-Physik* teslameter with a transverse Hall sensor.

2.5 Vibrating Sample Magnetometer and SQUID

All of the VSM measurements shown in this thesis were done on a Quantum Design PPMS equipped with the VSM option. Faraday's law is the physical basis of Vibrating Sample Magnetometer (VSM), the basic measurement is accomplished by oscillating the sample near a detection (pickup) coil and synchronously detecting the voltage induced. By using a compact gradiometer pickup coil configuration, relatively large oscillation amplitude (1-3 mm peak) and a frequency of 40 Hz, the system is able to resolve magnetization changes of less than 10^{-6} emu at a data rate of 1 Hz. The VSM option in this particular system consists primarily of a VSM linear motor transport (head) for vibrating the sample, a coilset puck for detection, electronics for driving the linear motor transport and detecting the response from the pickup coils, and the corresponding automation and control software. The basic principle of operation for a VSM is that a changing magnetic flux induces a voltage in a pickup coil. The time-dependent induced voltage is given by the following equation:

$$V_{coil} = \frac{d\Phi}{dt} = \left(\frac{d\Phi}{dz}\right)\left(\frac{dz}{dt}\right) \qquad (2.9)$$

In equation (2.9), "Φ" is the magnetic flux enclosed by the pickup coil, "z" is the vertical position of the sample with respect to the coil, and "t" is time. For a sinusoidally oscillating sample position, the voltage is based on the following equation:

$$V_{coil} = 2\pi f C m A \sin\left(2\pi f t\right) \qquad (2.9)$$

In equation (2.9), "C" is a coupling constant, "m" is the DC magnetic moment of the sample, "A" is the amplitude of oscillation, and "f" is the frequency of the

oscillation. The acquisition of magnetic moment measurements involves measuring the coefficient of the sinusoidal voltage response from the detection coil. Figure 2-6 illustrates how this is done with the PPMS VSM option.

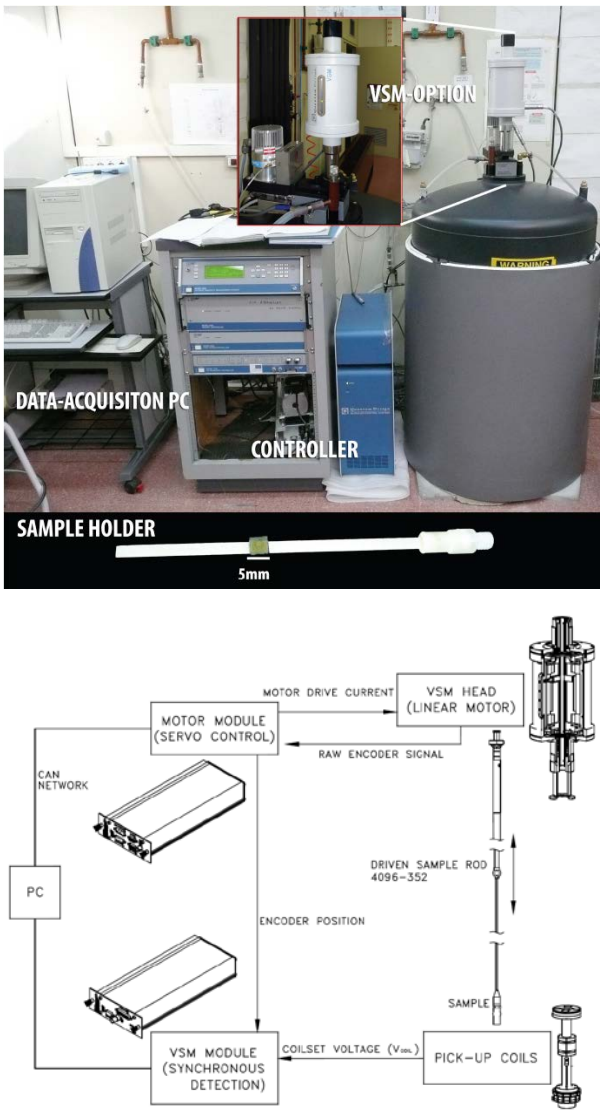

Figure 2-6. Photograph (up) of the *Quantum Design PPMS* containing the VSM instrument, and (down) VSM operation schematic

The SQUID detection hardware contains the superconducting detection coils that are configured as a second-order gradiometer, with counter-wound outer loops

which make the set of coils non-responsive to uniform magnetic fields and linear magnetic field gradients. The detection coils only generate a current in response to local magnetic field disturbances. Assuming the sample dimensions are much smaller than the dimensions of the detection coils, the current in the detection coils is a function of the sample position. It is relevant to note that SQUID feedback nulls the current in the detection coils so no current actually flows in them, and the feedback current yields the actual SQUID voltage for analysis.

The SQUID measurement technique vibrates the sample at frequency "*ω*" about the very center of the detection coils, where the signal peaks as a function of sample position, "*z*". This generates a SQUID signal, V, as a function of time, "*t*"

$$V(t) = AB^2 \sin^2(\omega t) \qquad (2.10)$$

Because $V(z) = Az^2$ for small vibration amplitudes, and $z(t) = B\sin(\omega t)$. Here, "*A*" is a scaling factor relating to the magnetic moment of the sample. "*B*" is the amplitude of sample vibration. Since $\sin 2(\omega t) = \frac{1}{2}(1 - \cos(2\omega t))$ the techniques of a lock-in amplifier may be applied to isolate and quantify the signal occurring at frequency *2ω*, which should be caused exclusively by the sample if the vibration frequency is correctly selected. This is achieved by multiplying the measured signal with a phase-corrected reference signal at *2ω* and then extracting the DC component of the result. This DC component is proportional to the 2ω component of the measured signal. This technique quickly and precisely isolates the sample signal from other noise sources, including the drifting SQUID signal and mechanical noise sources synchronized to the sample vibration.

2.6 Polarized Neutron Reflectivity

In diffraction by non-magnetic crystals, certain aspects of the theory of x-ray scattering can be transferred to scattering by cold and thermal neutrons bearing in mind that neutrons sense atoms by two interactions, namely the nuclear strong force, and the effect of the magnetic field created by the atom. Scattering techniques (diffraction, inelastic scattering) were developed after the discovery of the neutron but Polarized Neutron Reflectivity (PNR) is a relatively new technique [12-14]. The adequate treatment of interference requires the description in terms of scattering amplitudes, or scattering cross sections. For reflection geometries, the scattering problems are treated in the optics framework. From Snell's Law it is easy to show that total external reflection occurs when the incidence angle is $\theta < \sqrt{2\delta}$; above this critical angle the reflectivity decreases and the shape of this decrease contains all the information pertinent to gradients in the concentration normal to the surface of the specimen. The reflected radiation is related to the refraction index depth dependence averaged over the surface or interface lateral dimensions; an extremely high depth resolution characterizes PNR such that in a several hundred nanometers film the resolution is a fraction of nanometer. For instance, any parallel or antiparallel magnetic alignment can be uniquely distinguished in a ferromagnetic/ non-ferromagnetic multilayer stack. The neutron is a very well suited magnetic probe for thin films due to its large sample penetration with no structural damages.

As the neutron's momentum changes with λ and ϑ, these two parameters define two instrumentation schemes, steady state neutron sources or spallation sources. For reactor sources (steady-state method), a narrow band of wavelengths λ is selected with a monochromator crystal and the scattering angle (2ϑ) is varied to scan d spacings. Pulsed sources (time-of-flight method) use almost the entire

available neutron spectrum, fix the scattering angle (2ϑ), and simultaneously detect a neutron while determining its time of flight (since the neutron time of flight is proportional to its wavelength, the incident neutron wavelength is obtained by measuring its time of flight). Then, knowing the incident distribution of wavelengths and measuring the reflected wavelengths distribution at an angle ϑ with respect to the surface furnishes directly the sample reflectivity.

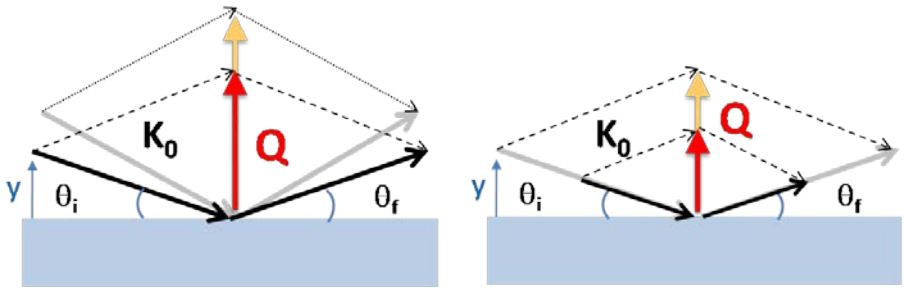

Figure 2-7. The wave vector transfer can be modulated by (left) changing the incidence angle of the beam or changing the neutron wavelength (right)

In cases where the changes in the magnetic moments are probed, four similar experiments are performed in which the incident neutrons are polarized parallel and perpendicular to the surface of the specimen and the reflected neutrons polarization is similarly analyzed. Combining reflectivity measurements under these two polarization conditions in a similar way to the unpolarized case allows the determination of the gradient in the magnetic moments of components parallel to the sample surface.

To take into account the magnetic behavior of the layers, interaction potential between incident neutron and the internal magnetic field in the magnetic layer is studied [15-17].

The main magnetic interaction is the dipolar interaction of the neutron spin with the magnetic field created by the unpaired electrons of the magnetic atoms. This field contains two terms, the spin part and the orbital part[18]:

$$\mathbf{B} = \frac{\mu_0}{4\pi}\left(\nabla \times \left\{ \frac{\mu_e \times \mathbf{R}}{|\mathbf{R}|^3} \right\} - \frac{e\mathbf{v}_e \times \mathbf{R}}{|\mathbf{R}|^3} \right) \qquad (2.11)$$

where $\mu_e = -2\mu_B\sigma$ is the magnetic moment of the electron, μ_B is the Bohr magneton and $\mathbf{v_e}$ is the electron speed. Now, the magnetic interaction is expressed as:

$$V_M(r) = -\mu \cdot \mathbf{B} = -g_n\mu_n\sigma \cdot \mathbf{B} \qquad (2.12)$$

then, combining eqs (2.11) and (2.12) , only the spin dependent part of the interaction is written as:

$$\frac{1}{2\pi^2}\int \frac{1}{q^2}\left(\mathbf{q}\times\left(\mu_e \times \mathbf{q}\right)\right)\exp(\imath\mathbf{q}\cdot\mathbf{r})d\mathbf{q} \qquad (2.13)$$

Expression (2.13) is integrated assuming a constant atomic density, obtaining the expression:

$$\frac{2\pi\hbar^2}{m} p\sigma \cdot \mathbf{M}_{||}\rho\left[\theta\left(r_{0z} + L/2\right) - \theta\left(r_{0z} - L/2\right)\right] \qquad (2.14)$$

with p = 2.696 fm, ρ is the atomic density, r_0 is the distance between the neutron and the center of the layer; $\mathbf{M}_{||}$ is given in μ_B per atom and represents the in-plane component of the magnetization, and $\vartheta(r)$ is the Heaviside function. Equation (2.14) shows two important points: it is only possible to measure the in-plane magnetization and the magnetic interaction is zero out of the layer. These two properties are essential, the first is the main limitation to the use of neutrons for the study of magnetic thin films, and the second is the justification for solving the Schrödinger equation in each layer, independent of the others. One should note that polarized reflectivity is sensitive to the induction in the thin films: no difference is made between the spin and orbital magnetic moments.

In a PNR experiment the guiding field, the incident beam polarization axis and the detector field are usually collinear so the guiding magnetic field outside the sample

provides a quantization axis for the neutron spin. If the sample magnetic induction (***B***) lies in a finite angle with respect to the applied field (***H***), the induction perpendicular to the applied field component leads to spin-flip scattering (the reflected neutron spin state flips 2π depending on the time the neutron spent in that region and the induction strength) as a consequence of the neutron spin precession around the induction vector. As a convention, R^{++} and R^{--} indicate the non-spin flip (NSF) reflectivities (where the uppercase + indicates spin parallel and the uppercase - indicates antiparallel to the applied field respectively), while *R+-* and *R-+* indicate spin-flip (SF) reflectivities. In practice, it is possible to measure the four different signals, the NSF reflectivities corresponding to the number of incoming "up" ("down") neutrons reflected with an "up" ("down") polarization, and the two SF reflectivities corresponding to the number of neutrons incoming "up" ("down") neutrons reflected with a "down" ("up") polarization during the reflection on the sample.

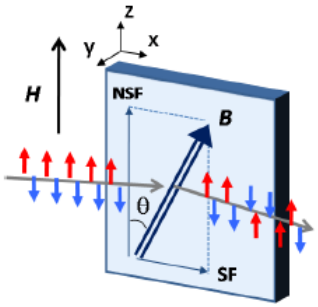

Figure 2-8. Schematic representation of the magnetization components which induce spin flip (SF) and non-spin flip (NSF) scattering, relative to the neutron polarization

Since $\nabla \cdot B = 0$, perpendicular components of the induction are constant across a reflecting interface and there is not specularly reflected intensity coming from them [19].

In a first approximation, the NSF reflectivities probe the components of the magnetization which are parallel to the applied field; the SF cross reflectivities are

sensitive to the component of the magnetization perpendicular to the applied field in the sample plane. Combining this information it is possible to reconstruct the magnetization direction and magnitude along the depth of the film.

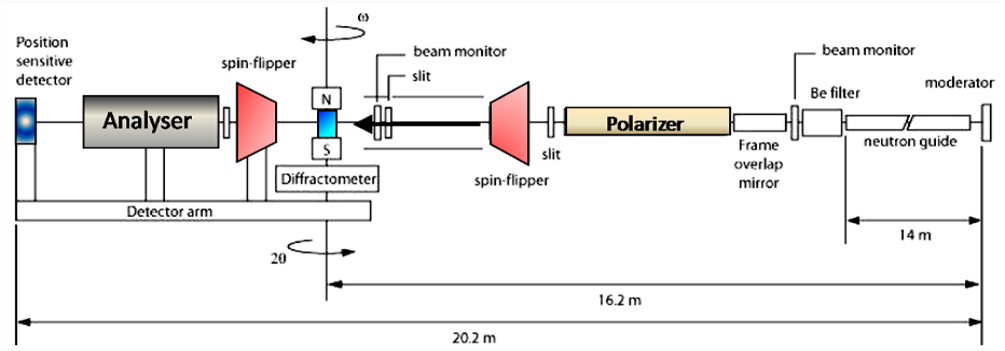

Figure 2-9. Schematic diagram of the polarized neutron reflectometer/diffractometer at a pulsed neutron source (LANSCE) [20]

Figure 2-9 shows a schematic of the reflectometer/diffractometer ASTERIX at Los Alamos Neutron Science Center (LANSCE), the sample is illuminated at a fixed incident angle, while a magnetic field is applied parallel to the sample surface; several devices placed along the neutron beam accomplish different tasks, some of them have the capability to change the neutron spin precession around ***B***, as the polarizer which consists in a system of wedge-shaped supermirrors inside a cavity through which neutrons are transmitted, that allows only spin-down neutrons with wavelengths greater than a minimum value; the final part of the polarization cavity is properly magnetized by a special arrangement of magnetic fields which make an angle with the axis of the beam and vary in time. The beam polarization can be switched using a radio-frequency gradient field spin-flipper, which consists of two orthogonal magnetic fields; the static field is produced by a wedge shaped yoke, and the rotating field is produced by a radio-frequency solenoid, the frequency of this field is chosen to favor resonance in the middle of the spin flipper every time the device is activated, resulting in an adiabatic beam polarization inversion.

2.6.1 Analysis of PNR data

M. R. Fitzsimmons and C. F. Maykrzak [15] developed the computer algorithm (CO_REFINE) used to analyze the data taken at the instrument called ASTERIX installed at Los Alamos Neutron Science Center (LANSCE). Structural, chemical and magnetic parameters are optimized in order to reproduce R^{++} and R^{--} reflectivity curves. The performance function is the minimization of the error measurement between the observed and calculated reflectivities (χ^2). Parrat reported at 1954 [21] the development of a procedure useful to analyze the shape of the reflected x-ray vs. glancing angle in the region of total reflection, such an iterative procedure is used first to optimize the structural model with the unpolarized beam reflectivity. If x-ray reflectivities are available, the initial ideal model comprehends each layer thickness, x-ray scattering length density real and imaginary parts, plus surface and interface roughness; those are the parameters to optimize in the structural refinement runs. After having optimized the structural model, the magnetic Scattering Length Density (SLD) magnetic profile is generated by the SPIN_FLIP routine which optimizes the NSF and SF reflectivities in a similar way to that used by CO_REFINE to optimize the x-ray reflectivity; besides the generation of the magnetic SLD profile, the angle between magnetization and guiding field of each layer is provided. As it is not unusual to see a gradient in the magnetization where the structural profile shows a sharp interface, another optimization parameter is the error function $erf\left(\frac{y-\Delta}{\sigma\sqrt{2}}\right)$ that describes the SLD variation across the interface: "y" is the depth into the sample, "Δ" is the layer thickness and "σ" is the interface width.

2.7 X-Ray Absorption Spectroscopy

In X Ray Absorption Spectroscopy (XAS) experiments samples are irradiated by photons and the absorption coefficient is measured. Photons are absorbed by an atom giving rise to an electronic transition from a core state to an empty state above the Fermi level; the absorption cross-section of the process depends on the incident x-rays energy and on the measured element [22], the photon energy needed to excite an electron in a given core level is equal or higher than such element characteristic core level, and a sudden increase in the absorption intensity is observed when that energy level is crossed, as shown in Figure 2-10.

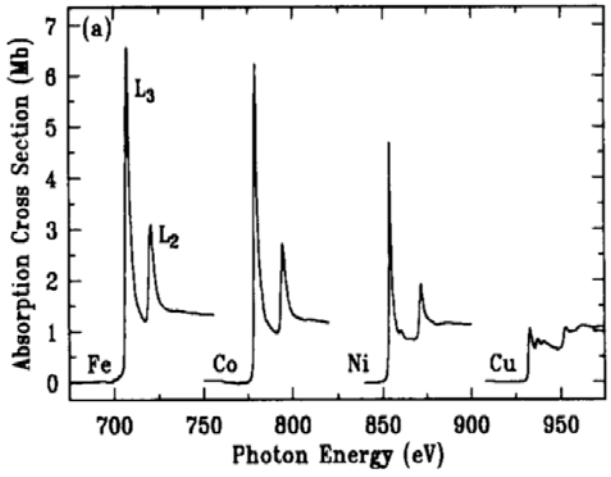

Figure 2-10. X- ray absorption spectra recorded by TEY detection near the *L*, and *L1* edges for Fe, Co , Ni and Cu metal, showing the existence of white lines for Fe, Co and Ni and its near absence for Cu, due to its nearly filled d shell [23]

Core holes are created by the excitation of photoelectrons, which decay by either radiative or non-radiative transitions; those vacancies represent an unstable condition for the atom and the stable condition is recovered transferring outer-shells electrons to the inner-shell empty states. The energy difference between the two corresponding shell binding energies composes the characteristic emitted x-

rays which can be detected in the Fluorescence Yield (FY) mode. Secondary x-ray excitations can promote additional electronic transitions; in fact when a vacancy is created in the *L*-shell, an electron from the *M* or *N* shell "jumps in" to occupy the vacancy; as a result from this process *M* or *N* vacancies are produced together with an emitted photon. If an x-ray has enough energy to excite a core level the resultant photoelectron will leap into unoccupied states above the Fermi level; the inner atom excitation energy can be transferred to one of the outer electrons and this (Auger) electron is ejected from the atom. The emitted electrons energy spectrum consists of well-defined lines due to photoelectrons and Auger electrons on top of a background due to secondary electrons, the inelastic collisions low-energy secondary electrons of initially exited photoelectrons or Auger electrons give rise to a major portion of the electron emission, and the sample can be regarded as an effective electron multiplier.

Monitoring the total electron yield (TEY) offers the simplest mode for detecting the photo-absorption process; it is often easier to measure not the emitted electrons directly but their complement given by the sample drain current flowing into the sample; the transitions are usually labeled according to the energy position of the excited electron. Transitions from the $p_{1/2}$ level would lead to the L_{II} line, while transition from $p_{3/2}$ would lead to the L_{III} line. Low energy secondary electrons have short escape depth which limits the available information, all the electrons that escape must originate at the surface. In spite of the short inelastic mean free path of secondary electrons, it has been shown that by monitoring the x-ray induced TEY vs. grazing incident angle at a fixed incoming energy, microstructural information can be obtained not only from the near-surface region but also about the buried interfaces [24, 25]. This is due to the fact that electron emission from stratified medium is determined by the radiant energy losses in the near-surface region, which is the primary source of TEY, and this process is governed by the

electromagnetic distribution in the entire stratified medium. Spectra taken from a single metal mainly show two broad peaks (see figure 10), reflecting the width of the empty *d*-bands; in general the oxide spectra are more complicated exhibiting multiplet structure due to the electrostatic interactions between *2p* core-hole and *3d* valence electrons and *2p* core-hole spin-orbit interactions, as well as by the local crystal fields and the hybridization with the O *2p* ligands [26-28].

2.8 X-Ray Magnetic Circular Dichroism

X-Ray Magnetic Circular Dichroism (XMCD) spectroscopy probes the magnetic properties of matter with x-rays. It was suggested by Erskine and Stern [29] and pioneered by Schütz et al.[30]. As compared with traditional magnetic probes XMCD provides with an element-specific quantitative determination of spin and orbital magnetic moments and their anisotropies [23], chemical sensitivity [31], lateral resolution of at least 1 μm^2 [32], and sub-monolayer sensitivity [33]. Its origin is a local anisotropy of the absorbing atom as a result of a local magnetic field. The magnetic field breaks the local symmetry of the absorber and lifts the degeneracy of the Zeeman levels. The photoelectron transitions depend on the helicity of the photon polarization.

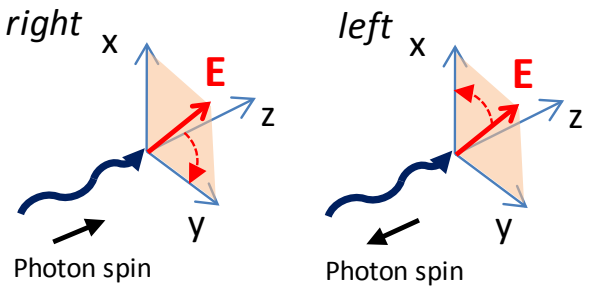

Figure 2-11. Representation of the incident photon polarization and spin direction

The XMCD signal is the difference between the absorption spectra obtained with left versus right circular polarization [34]. The absorption experiment has an extra selection rule that takes into account the photon helicity: $\Delta m = \pm 1$, where "m" is the magnetic orbital quantum number. $\Delta m = +1$ applies for left-handed polarization and $\Delta m = -1$ applies for right-handed polarization. In a magnetic compound the levels with $|m|$ and $-|m|$ quantum numbers are unequally populated; and XMCD originates from this difference. Different effects can be

detected as a consequence of the absorption and reflection of x-rays on the surface, as production of fluorescence, secondary electrons, and altered reflected intensity; each of these effects yield information about the sample magnetic state and can be simultaneously collected using different detectors, the detection modes are Fluorescence Yield (FY), Total Electron Yield (TEY) and Reflectivity [22].

Because it is often experimentally easier to reverse the magnetic field than the polarization, most XMCD experiments are performed at constant helicity with a magnetic field parallel or antiparallel to the x-ray beam. During an XMCD experiment, a first spectrum is recorded with the magnetic field parallel to the propagation vector of the photons. A second spectrum is then recorded with the magnetic field anti-parallel to the propagation vector of the photons. The XMCD signal is the difference between the two spectra. There are two main approaches to analyze the dichroic signal, one is to simulate the spectra by calculations, and the other is the use of sum rules; although the applicability of the sum rules has been confirmed to bulk-like Co and Fe films [35], the applicability for low-symmetry systems (like strongly correlated electron systems) and their practical application is complicated by the spectral density weight spreading over a broad energy interval [23].

In x-ray absorption spectroscopy two nonmagnetic sum rules were suggested at first; one relates the integrated absorption to the ground state expectation value of the number of holes in the final level of the transition; the second, that can be applied to the core hole split edges, states that the branching ratio is proportional to the average value of the angular part of the spin-orbit coupling operator. After the development of XMCD several magnetic sum rules were derived, among these sum rules, two are widely used by XMCD experimentalists: the orbital and spin-sum rules.

The orbital sum rule states that the integrated dichroic signal is proportional to the ground state expectation value of the operator $\boldsymbol{L_z}$ (*z* component of the orbital operator) acting on the shell that receives the photoelectron in the final state. The spin-sum rule relates a linear combination of dichroic signals at core hole split edges to the average value of two operators (*Sz*, *z* component of the spin operator; *Tz*, *z* component of the magnetic dipole operator) acting on the shell that receives the photoelectron in the final state. The strength of the sum rules resides in the fact that the experimenter can obtain valuable information such as $\langle Lz \rangle$ or $\langle Sz \rangle$ by the simple numerical integration of experimental signals. The validity of the information extracted from the sum rules resides in a correct understanding of the various theoretical and experimental approximations present in their derivation.

Constraints on the transition are represented by the selection rules. Because of the $\Delta J = 0, \pm 1$ dipole selection rule the $1/2 \rightarrow 5/2$ (or inverse) transition is forbidden (spin flips are forbidden in electric dipole transition), spin-up (spin-down) photoelectrons from the p core shell can only be excited into spin-up (spin-down) *d*-hole states; then the spin-split valence shell acts as a detector for the spin of the excited photoelectron and the transition intensity is simply proportional to the number of empty *d*-states of a given spin, the quantization axis of the valence shell "detector" is given by the magnetization direction. When the photon beam is circularly polarized the electromagnetic field vector turns around the direction of the propagation vector, and the difference between the transition probability for left and right circularly polarized light gives the circular magnetic dichroism; since the dipole selection rule is different for right (RCP) and left (LCP) circularly polarized light, the respective components may be absorbed differently depending on the nature of the two magnetic band states. The emitted radiation will reflect this imbalance in its elliptical polarization with the major polarization axis rotated

relative to that of the incident light. If a spin-orbit splitting is assumed both in the *p* and *d* state, the L_{III}/L_{II} line and dichroism can be drastically affected.

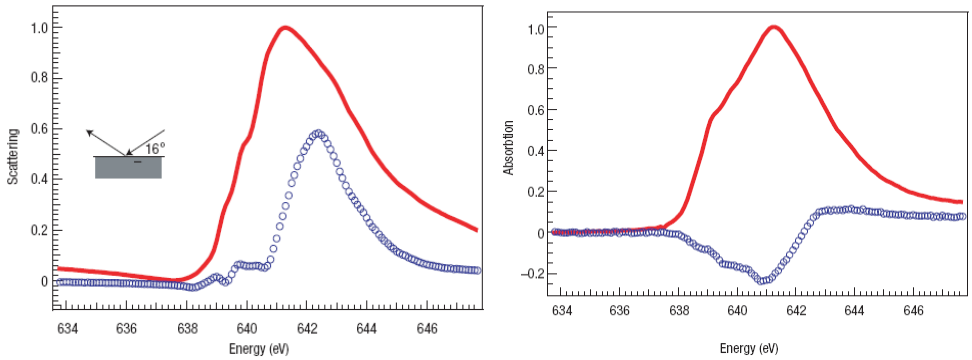

Figure 2-12. "Polarization-dependent scattering and absorption data at the Mn L_3 edge. The sum (red lines) and difference (blue circles) of signals at 35 K obtained with circularly polarized x-rays parallel (I^+) or antiparallel (I^-) to the magnetic moment are shown. The XRMS is extremely sensitive to the magnetization profile (left panel), whereas the magnetic properties averaged over the near-surface region are probed by XMCD (right panel). Electronic properties are measured by $I^+ + I^-$." Figure and caption Taken from [36]

X-ray resonant magnetic reflectivity (XRMR) provides an alternative method for measuring the magnetic dichroism from the subsurface region; XRMR present some advantages if compared to other techniques, it is an element selective technique [35] due to the presence of a core excitation permitted because XRMR is a coherent elastic scattering process with no complex final state effect. It also presents some strictly experimental advantages, it is not affected by the presence of magnetic fields acting on the sample because it is a photon-in/photon-out process, the probing depth can be tuned by changing angle for reflected intensity collection [36-38]. XRMR and XMCD signals cannot be directly compared (see Figure 2-12) since the reflected intensity measured is a dynamically scattered beam that depends upon both the absorptive and dispersive parameters of the material, the most common way of measuring XMCD in the soft X-Ray region is TEY, because of the easy experimental setup and high signal/noise ratio compared to FY.

After having determined the energy position of the maximum magnetic signal the magnetic field can be swept to construct a magnetic hysteresis loop, the determination of the intensity, shape, coercivity of a XMCD hysteresis loop can be used to distinguish between the magnetic behavior of the single layers in the multilayers of alternating soft and hard ferromagnets [39] and as further information about induced ferromagnetic moment at interfaces [40]. As a result of the complex current behavior as a function of the applied magnetic field, TEY was marginally used in the past for magnetization curves due to the corresponding normalization problems [41].

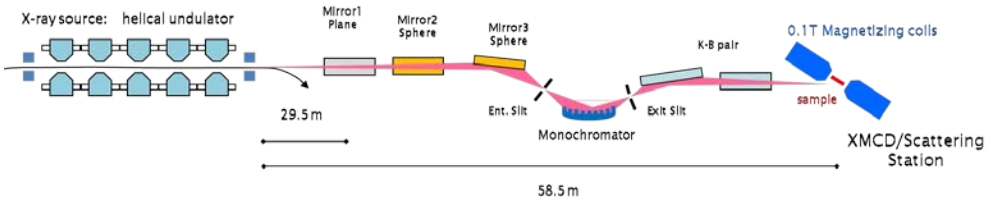

Figure 2-13. Schematics of the 4-ID-C beamline at the Advanced Photon Source (Argonne National Laboratory)

2.9 References

[1] P. F. Fewster, X-Ray Scattering from Semiconductors, World Scientific Publishing Co. Pe. Ltd., London, 2003.

[2] A. Guinier, X-Ray Diffraction: In Crystals, Imperfect Crystals, and Amorphous Bodies, Dover Publications, 1994.

[3] E. E. Fullerton, I. K. Schuller, H. Vanderstraeten, and Y. Bruynseraede, Physical Review B 45 (1992) 9292

[4] O. Nakamura, E. E. Fullerton, J. Guimpel, and I. K. Schuller, Applied Physics Letters 60 (1992) 120.

[5] C. Calle, F. Cuéllar, O. Guzmán, and A. Mendoza, Revista Colombiana de Física 38 (2006) 541.

[6] C. R. Brundle, C. A. E. Jr., and S. Wilson, Encyclopedia of Materials Characterization, Manning Publications Co., Greenwich, 1992.

[7] O. L. Krivanek, G. J. Corbin, N. Dellby, B. F. Elston, R. J. Keyse, M. F. Murfitt, C. S. Own, Z. S. Szilagyi, and J. W. Woodruff, Ultramicroscopy 108 (2008) 179.

[8] L. J. v. d. Pauw, Philips Research Reports 13 (1958) 1.

[9] S. K. J. Lenczowski, R. J. M. v. d. Veerdonk, M. A. M. Gijs, J. B. Giesbers, and H. H. J. M. Janssen, Journal of Applied Physics 75 (1994) 5154.

[10] R. J. M. v. d. Veerdonk, J. Nowak, R. Meservey, J. S. Moodera, and W. J. M. d. Jonge, Applied Physics Letters 71 (1997) 2839.

[11] R. C. Richardson and E. N. Smith, eds., Experimental Techniques in Condensed Matter Physics at Low Temperatures, Addison-Wesley, Ithaca, New York, 1988.

[12] J. Sears, Neutron News 3 (1992) 29.

[13] C. F. Majkrzak, J. W. Cable, R. Kwo, M. Hong, D. B. McWhan, Y. Yafet, J. V. Waszczak, and C. Vettier, Physical Review Letters 56 (1986) 2700.

[14] G. P. Felcher, R. O. Hilleke, R. K. Crawford, J. Haumann, R. Kleb, and G. Ostrowski, Review of Scientific Instruments 58 (1987) 609.

[15] Y. Zhu, Modern Techniques for Characterizing Magnetic Materials, Springer, 2005.

[16] J. Daillant and A. Gibaud, X-Ray and Neutron Reflectivity, Springer, 2009.

[17] H. Ekstein, Physical Review 76 (1949) 1328.

[18] J. Daillant and A. Gibaud, X Ray and Neutron Reflectivity: Principles and Applications, Heidelberg, 2009.

[19] J. F. Ankner and G. P. Felcher, Journal of Magnetism and Magnetic Materials 200 (1999) 741.

[20] M. R. Fitzsimmons and C. F. Majkrzak, Modern Techniques for Characterizing Materials, Springer, Berlin, 2005.

[21] L. G. Parrat, Physical Review 95 (1954) 359.

[22] F. Hippert, E. Geissier, J. L. Hodeau, and E. Lelièvre-Berna, Neutron and X-Ray Spectroscopy, Springer, 2005.

[23] J. Stöhr, Journal of Electron Spectroscopy and Related Phenomena 75 (1995) 253.

[24] A. Krol, C. J. Sher, and Y. H. Kao, Physical Review B 42 (1990) 3829.

[25] V. Chakarian, Y. U. Idzerda, and C. T. Chen, Physical Review B 57 (1998) 5312.

[26] G. v. d. Laan and B. T. Thole, Physical Review B 43 (1991) 13401.

[27] M. Kobayashi, Y. Ishida, J. I. Wang, T. Mizokawa, A. Fujimori, K. Mamiya, J. Okamoto, Y. Takeda, T. Okane, Y. Saitoh, Y. Muramatsu, A. Tanaka, H. Saeki, H. Tabata, and T. Kawai, Physical Review B 72 (2005) 20120(R).
[28] T. Burnus, Z. Hu, H. H. Hsieh, V. L. J. Joly, P. A. Joy, M. W. Haverkort, H. Wu, A. Tanaka, H. J. Lin, C. T. Chen, and L. H. Tjeng, Physical Review B 77 (2008) 125124.
[29] J. L. Erskine and E. A. Stern, Physical Review B 12 (1975) 5016.
[30] G. Schütz, W. Wagner, W. Wilhelm, P. Kienle, R. Zeller, R. Frahm, and G. Materlik, Physical Review Letters 58 (1987) 737.
[31] F. Sette, C. T. Chen, Y. Ma, S. Modesti, and N. V. Smith, X-Ray Absorption Fine Structure, Ellis Horwood, 1991.
[32] J. Stöhr, Y. Wu, B. D. Hermsmeier, M. G. Samant, G. R. Harp, S. Koranda, D. Dunham, and B. P. Tonner, Science 259 (1993) 658.
[33] L. H. Tjeng, Y. U. Idzerda, P. Rudolf, F. Sette, and C. T. Chen, Journal of Magnetism and Magnetic Materials 109 (1992) 288.
[34] J. S. Miller and M. Drillon, Models and Experiments, Wiley-VCH, 2002.
[35] C. Kao, J. B. Hastings, E. D. Johnson, D. P. Siddons, G. C. Smith, and G. A. Prinz, Physical Review Letters 65 (1990) 373.
[36] J. W. Freeland, K. E. Gray, L. Ozyuzer, P. Berghuis, E. Badica, J. Kavich, H. Zheng, and J. F. Mitchell, Nature Materials 4 (2005) 62.
[37] M. Sacchi, J. Vogel, and S. Iacobucci, Journal of Magnetism and Magnetic Materials 147 (1995) L11.
[38] S. Valencia, A. Gaupp, W. Gudat, L. Abad, L. Balcells, and B. Martinez, Journal of Applied Physics 104 (2008) 023903.
[39] M.-h. Yu, J. Hattrick-Simpers, I. Takeuchi, J. Li, Z. L. Wang, J. P. Liu, S. E. Lofland, S. Tyagi, J. W. Freeland, D. Giubertoni, M. Bersani, and M. Anderle, Journal of Applied Physics 98 (2005) 063908.
[40] A. Baruth, D. J. Keavney, J. D. Burton, K. Janicka, E. Y. Tsymbal, L. Yuan, S. H. Liou, and S. Adenwalla, Physical Review B 74 (2006) 054419.
[41] E. Goering, A. Fuss, W. Weber, J. Will, and G. Schütz, Journal of Applied Physics 88 (2000) 5920.

3 FABRICATION TECHNIQUES

3.1 Motivation

The measurement of spin dependent transport (SDT) in the current perpendicular to plane (CPP) configuration is the main characterization toolset of this work, and the elements needed in order to obtain the required physical structure of characterization devices are the focus of this chapter. First, the thin film growth system is presented, followed by some microfabrication concepts. Then some physical considerations about junction measurements are discussed before the design of the devices is presented. All the lithography mask layers were designed by using the free software "*Layout Editor*" (by Jürgen Thies) that can be found for download at internet.

The CPP geometry can be used to clearly identify the separate contributions from spin-dependent bulk and interface scattering in SDT, but the fulfillment of a CPP-SDT experiment is not straightforward, essentially because of the low perpendicular thin film resistance involved and the further distortion that it may involve at measuring [1-5]. A possible solution is to increase the perpendicular multilayer resistance up to a measurable range by fabricating micron-size structures by means of optical lithography and removal techniques [6, 7]. Thus it is necessary to develop a fabrication process that allows the transformation of the trilayer or bilayer structures into CPP-geometry devices suitable for SDT characterization; since this is the first time that such kind of structures are fabricated in this research group, the design and implementation of a fabrication process of CPP-geometry devices is a fundamental part of this experimental work and is presented in some detail within this document. The here explained design follows the conventional MTJ fabrication scheme as Worledge and Abraham [8]

wrote in the introduction to their paper. The usual process [9] involves defining and etching the bottom wire, defining and etching the MTJs, backfilling with dielectric to protect the MTJs, removing the dielectric from the top of the MTJs, depositing metal, and defining and etching the top wire.

Other fabrication approaches for measuring magnetoresistance or spin polarization have been reported, as the use of Conducting Tip Atomic Force Microscopy [10] by Worledge [8], AFM nano-indentation by Bouzehouane et al. [11], superconducting point contacts by Soulen et al. [12], or Current In Plane Tunneling (CIPT) by Worledge and Trouilloud [13]; the implementation of a procedure following those works is out of the scope of this thesis work.

3.2 Sputtering System

Samples used in this work were grown in a High Oxygen Pressure Sputtering System installed at the Clean Room in the Applied Physics Department of the Physics Faculty at the "Universidad Complutense de Madrid". Details of this Sputtering System can be found in [14]. Sputtering takes place inside a controlled atmosphere chamber, which initially is in high vacuum, and then led towards 3.4 mbar of oxygen pressure; this pressure range is considered high pressure since the typical growth pressure in a sputtering system is 10^{-2} mbar. When DC sputtering is used, the target is the cathode and the substrate is the anode; when RF sputtering is used the RF signal is connected to the target, where the plasma is formed. Although electrically conducting materials such as $La_{0.7}Ca_{0.3}MnO_3$ (LCMO) can be grown by using DC sputtering, all the samples used in this work were grown in the RF sputtering configuration. When an AC signal with frequency below 50 kHz is applied to the electrodes, ions are sufficiently mobile to establish a complete discharge at each electrode on each half-cycle; direct current sputtering conditions essentially prevail at both electrodes, which behave as cathodes and anodes alternately. Above 50 kHz two important effects occur; electrons oscillating in the glow region acquire enough energy to cause ionizing collisions reducing the need for secondary electrons to sustain the discharge; secondly, RF voltages can be coupled through any kind of impedance so that the electrodes need not to be conductors. Typical RF frequencies employed range from 5 to 30 MHz. However, 13.56 MHz has been reserved for plasma processing by the Federal Communications Commission and is widely used.

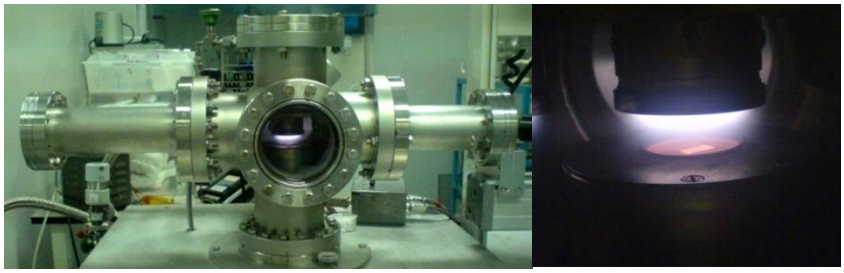

Figure 3-1. (left) Sputtering chamber, the targets in there are mounted on a remotely controlled arm that switches between the different materials, (right) enlarged view of the sputtering target above the substrate

The chamber shown in Figure 3-1 is connected to a turbo-molecular pump backed up by a membrane pump, a constant oxygen flow is injected and controlled by a valve system including a needle valve as precision element. Sputtering occurs when the ion impact establishes a train of collision events in the target leading to the ejection of a matrix atom. Since the sputter yield depends on the incoming O_2 ion energy and the source atom species, the material removed from the target deposits on the substrate in a matter which strongly depends on several controllable parameters as the substrate temperature, target-to-substrate distance, applied bias, and chamber pressure. These are all key parameters, whose individual values are not very critical but they strongly depend on each other, and thus they shall be optimized in order to obtain epitaxial high quality films.

Semiconductors and insulators such as $PrBa_2Cu_3O_7$ (PBCO) or $SrTiO_3$ (STO) require the use of RF sputtering, mainly because charge accumulation at the target surface in DC configuration avoids plasma formation. The sputtered atoms come from targets made of the stoichiometric compound to be grown as thin film on the substrate, while the oxygen plays the role of the sputtering element. The oxygen flow is controlled by a system composed of a needle valve as a flow source and a tight section conduct towards the turbo molecular pump as the flow sink. The oxygen ions are attracted towards the target by the electric field generating atomic

disgregation by kinetic impact and; the extracted atoms move towards the substrate where they are finally deposited. The high pressure used prevents re-sputtering and prevents substrate ion bombardment; a very low growth rate (less than 1 nm per minute) is also allowed by the high pressure, which gives highly controllable film thickness. Substrate is placed in a high temperature sample holder (reaches up to 1000˚ C) and the samples are typically grown at 900 ˚C; that high temperature assists incoming ions surface diffusion, this condition highly favors ordered growth and results in high quality and fully epitaxial films. In order to reach the desired temperatures, the sample holder is made of Inconel superalloy and is cold-water refrigerated.

All samples used in this work were grown under the conditions necessary to obtain the fully-oxygenated phases of the materials, i.e. $PrBa_2Cu_3O_{7-\delta}$, and $La_{1-X}Ca_XMnO_{3-\delta}$, with $\delta = 0$. The growth procedure includes an annealing lasting 30 minutes at 550˚C and 1 bar oxygen pressure, which is indispensable to obtain the fully oxygenated phase of the grown complex oxides.

3.3 Optical Lithography

Thin films must be geometrically defined laterally or patterned in the film plane in order to obtain circuits or devices; the complexity of the patterning process depends on the nature of the film, the feature dimensions and its spatial tolerance. The desired pattern could be possibly machined into a thin sheet stencil or mechanical mask, direct contact with this mask template and substrate allows pattern transference; this method is obviously too crude to permit the patterning of features in the micron size, such demanding applications require lithographic techniques.

Photolithography is a technique used to produce high precision two-dimensional patterns in the microscopic scale on a photoresist material [15], it is the equivalent to the negative used in photography. These patterns are optically projected from a master pattern in a highly-resistant photomask, which are generally made of a thin chromium or ferrite layer on a glass or quartz plate. Masks for integrated circuit use are generated employing computer-driven electron beams to precisely define regions that are either opaque or transparent to light. Printing of this negative mask requires physical transference of the pattern to the film surface in question through the use of a photoresist. Two types of photoresist are available and their behaviors are distinguished in the effect of the light; the positive photoresist faithfully reproduces the opaque mask pattern, in this case light exposure causes scission of polymerized chains rendering the resist soluble in the developer; alternatively, negative resists reproduce the transparent portion of the mask pattern because photon-induced polymerization leaves a chemically inert resist layer behind [16]. For yet greater feature resolution x-ray and electron-beam lithography techniques must be practiced. At the end of the lithography process,

the molded photoresist is used to create a useful structure on the device under construction.

Figure 3-2. Photograph of a Karl Suss alignment equipment

The core of the microlithography process is the exposure system, Figure 3-2 shows the alignment and exposure system installed at the Universidad Complutense de Madrid; this complex piece of machinery projects the image of the desired pattern from a photomask, on the surface of a solid state device built on a substrate and even another layers; the image is captured in a thin resist layer and transformed into a permanent part of the device, by means of a series of etching and deposition processes. Few-micron sized motifs can be reproduced with lateral tolerances of tenths of a micron; the pattern must be aligned with underlying layers in less than a fourth part of the minimum line width. All tolerances must be found using an

exposure field of several squared centimeters. An exposure system for optical microlithography consists of three parts: a lithographic lens, an illumination system, and a wafer positioning system.

3.4 Selective Removal Techniques

The task of removing a layer above a substrate, usually by means of a molded protective resist, is called etching. Etching can be achieved by chemical methods, where a compound easily removable is formed with the material; or using physical methods, where the material is removed by sputtering or by abrasion, or a combination of both. The central function of the shape resist image is to allow the pattern transfer to the underlying layer, while acting as a protective layer for the covered areas.

In *Chemical Etching* a solution that dissolves the material but not the resist or the substrate is used. The products of the reaction must be dissolved at the carrier fluid or be retired. When very small cavities or channels are etched, the solution can get saturated quickly and shall be removed by using agitation (i.e. ultrasonic) assuring in that way that the material to be removed is always in contact with fresh solvent. If one of the reaction sub-products is gaseous, bubbles will be formed at the interaction surface, ultrasonic removal of bubbles helps maintaining the fresh solution in contact with the etched material. Some etching chemicals attack particular crystalline facets much faster than others, and this generates the anisotropic etching [17]. An important disadvantage of the chemical etching is the phenomenon called undercutting, which consists in the attack of the areas near the shaped resist edge, resulting in a resolution loss of the molded pattern. In practice, for isotropic etching the layer thickness must be around a third or less of the desired resolution. If special patterns with resolution lower than the film thickness are required, it is necessary to use anisotropic etching or other special etching methods.

The pattern transfer to such materials shall be achieved with the almost perfect reproduction of the original pattern attributes: vertical walls, smooth line edges

and no residues left; in order to achieve such requirements the material shall be etched faster than the resist layer used as a mask, and the etching must be highly directional with minimal or null lateral etching. The most usual way to achieve these goals is the use of low pressure plasmas. High ionic density plasmas have been developed in order to reach the performance goals consistent with the processing of a wafer, realizing up to 1 micron per minute (or higher) removal rates.

To obtain a good aspect ratio, directed surface bombardment is used; it is called Sputter Etching or Ion Beam Etching, the ion sources for Ion Beam Etching are generally based in the Kaufman ion propeller developed by the NASA [18], where a magnetically confined gas discharge is obtained between a thermionic cathode and a concentric cylindrical anode. In order to extract an ion beam from the discharge region, a bias is applied between a pair of aligned nets. The ions are injected in the work space as a collimated energetic beam. The beam is neutralized extracting the low energy electrons from an auxiliary thermionic cathode, in order to use the beam to Sputter Etch insulators as well as conductors.

Figure 3-3. Photograph of an Oxford Reactive Ion Etcher

Large differences can be obtained in the etch rate for different materials by using Reactive Plasma Etching unlike to Ion Beam Etching. In this technique the layer is

exposed to plasma of a reactive gas, but there is no acceleration of ions by a high voltage towards the film to be etched, this is why Sputter Etching is not a very important surface removal mechanism. The components of the reactive plasma are adsorbed at the surface, where they are dissociated by the plasma particle bombardment. The products of the reaction are desorbed and extracted from the reactor. Anisotropic etch can be present due to the low working pressures, the etch rate at horizontal surfaces is much higher than in the walls; in this regime the mean free path of the molecules is typically much longer than the desired etching depth. Due to the chemical nature, the adequate material choice allows obtaining a high control degree on the relative etch rates of the film, resist and substrate.

3.5 CPP Device Design

The cross-point architecture is a well-known way to connect a device-matrix with the advantages of leakage current reduction and end point connections minimization, which are clearly desirable characteristics in the aims of low scale integration (LSI); thus the implementation of a common electrode to connect several devices is a desirable architecture characteristic for the devices here designed; but non-desirable additional resistance due to the contact leads would be present if the designed devices have cross-point architecture; then four-probe resistance measurement is necessary to obtain a signal coming from the interface under study with minimal contribution from the bottom electrode.

Figure 3-4. shows the first layer of the device design for insulating substrate (upper panel) and conducting substrate (lower panel); in this first stage all the alignment marks to be used in the overlaying stages are set. Three junction rows by fourteen junction columns constitute the matrix device designed with square and rectangular junctions present, the upper junctions row (labeled 1) contains only rectangular devices, while the other two rows (labeled 2 and 3) contain square devices only; their sizes change from column to column (letters A-N) according to the arrangement listed in Table 3-1. The difference between both layer designs is the bottom electrode: in the case of a conducting substrate it is the substrate which plays the role of bottom electrode, while in the case of an insulating substrate three horizontal bars are placed below the junctions in the second layer to act as bottom electrodes. The need to ensure the possibility of top layer magnetization change [19] to obtain a coherent switching between the magnetic layers composing the devices, is subjected to the easy magnetization axis of the material; as the majority of magnetic materials that have been studied by this research group have cubic symmetry and were grown in thin film configuration

[20-25], and following the Neumann's principle: "*the symmetry elements of any physical property of a crystal must include all the symmetry elements of the point group of the crystal"*[26] or stated in other words "*if a crystal is invariant with respect to certain symmetry elements, any of its physical properties must also be invariant with respect to the same symmetry elements"*; the higher magnetization symmetry expected is three-axial, thus squares and rectangles are the geometries considered to shape the junctions, in order to favor the application of magnetic field along the different crystallographic symmetry axis, and thus the design here presented has only square and rectangular junction shapes.

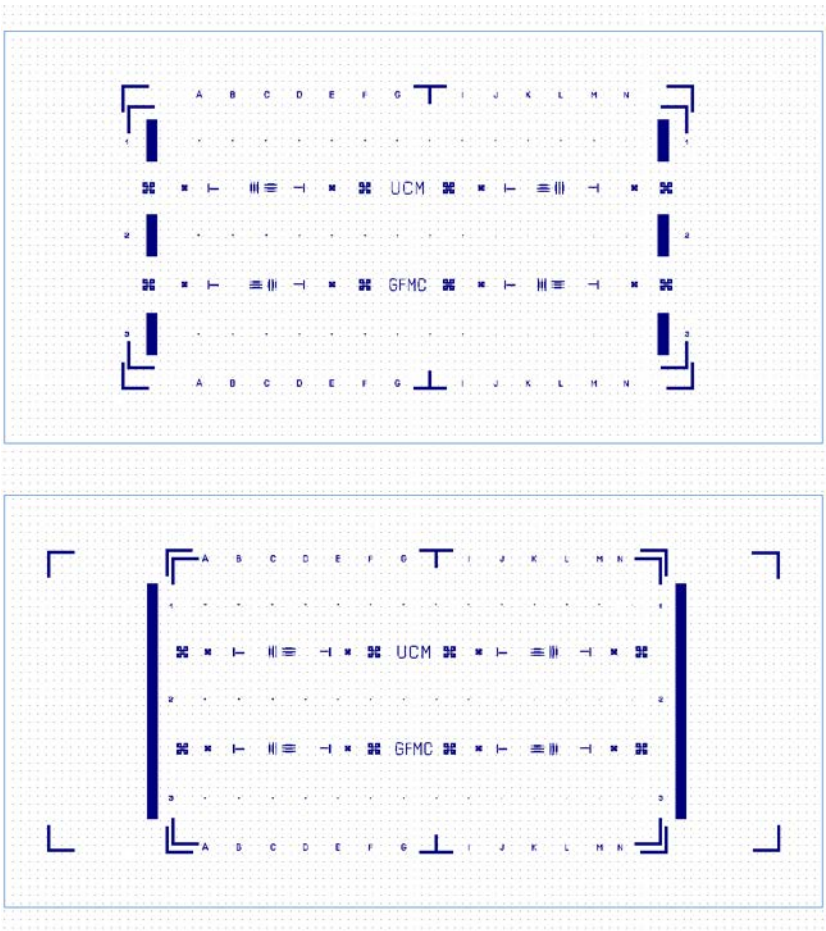

Figure 3-4. Layer 1 layout for insulating (upper panel) and conducting (lower panel) substrates

Rectangular Junctions	Area (μm^2)	Square Junctions	Area (μm^2)
1A, 1B	9x18	2A, 2B, 2C, 3A, 3B, 3C	12x12
1C,1D	7x14	2D, 2E, 2F, 3D, 3E, 3F	10x10
1E,1F,1G	6x12	2G, 2H, 2I	8x8
1H,1I,1J	5x10	2J, 2K, 2L	6x6
1K,1L,1M	4x8	2M, 2N	4x4
1N	4x6		

Table 3-1. Junction sizes

Before this first lithography stage is patterned a thick metal layer must be deposited on top of the heterostructure, it will be used in the next fabrication stages as capping layer for the Ar plasma etching, as light reflective element for further layers alignment and as metal contact for the junctions top electrode. The outer light-blue rectangle has the typical substrate size of 10 x 5 mm^2. The top-most and lower-most rows have the letters from A to N used to label the different junctions, the labeling letters and numbers can be used as alignment marks since they appear at different layers in bright field (transparent surroundings and filled polygons) or dark field (filled surroundings and transparent polygons); also there are two alignment marks rows above and below the electrode 2 (see Figure 3-5).

When these shapes are formed in the photoresist, removal techniques must be used in order to remove the capping metal, the top electrode and the barrier layer, leaving the lower material layer ready to be shaped into the lower electrode, with a large rectangle (125 x 500 μm^2) at each electrode end and the junction columns all over the sample surface in the case of an insulating substrate; and in the case of a conducting substrate, the remaining underlayer is the substrate ready to be metal contacted at the metal pad rectangles.

The alignment mark size is defined by the smaller feature size to be aligned, as was previously stated at the “Optical Lithography” section; according to such idea the

layer 2 alignment marks are the biggest ones, only the rectangular shapes at the corners and the “T” shapes are available as alignment marks since the feature contained in this layer is in the largest order of magnitude, as shown in Figure 3-5. The insulating substrate layout (upper panel) has such marks in bright field (BF), while the conducting substrate layout (lower panel) contains these marks in dark field.

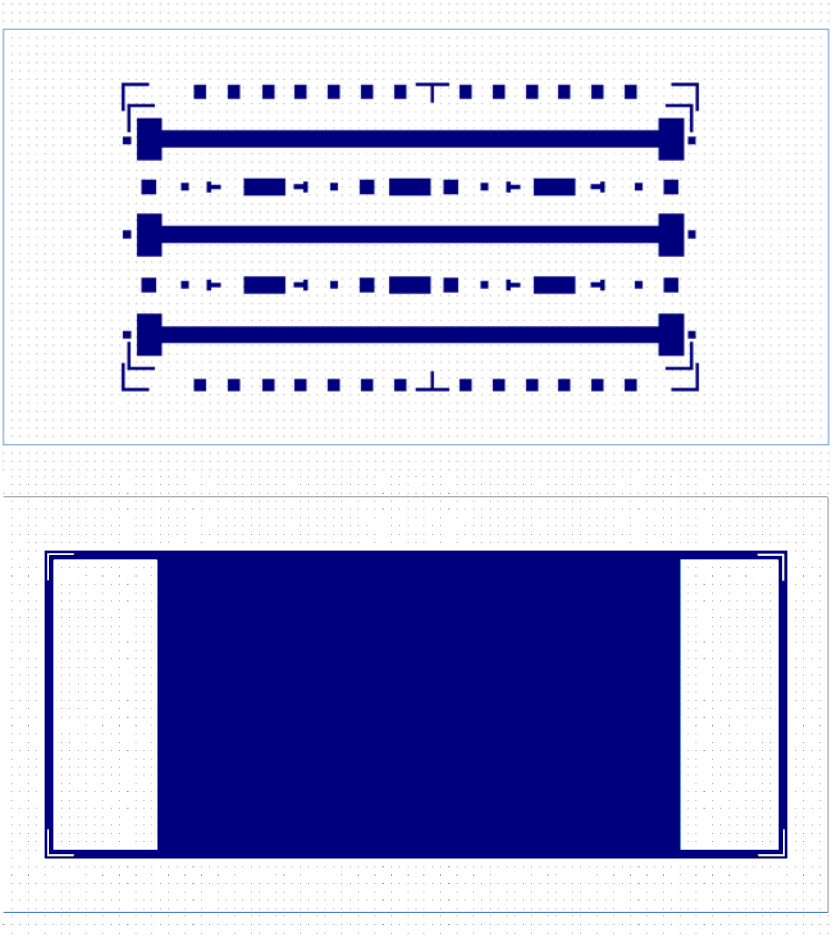

Figure 3-5. Layer 2 for insulating (upper panel) and conducting (lower panel) substrate

The electrode size shown in Figure 3-5 upper panel is 6700 x 200 μm^2, while the metal pad size shown in Figure 3-5 lower panel is 1300 x 3500 μm^2. After having this shapes defined in the photoresist, the insulating substrate layout shall be

submitted to removal techniques in order to remove the bottom layer leaving the bottom electrode shaped; the conducting substrate layout shall be used for metal deposition. After having completed the junction and electrode shape definitions the system needs passivation by a thick insulating layer deposition.

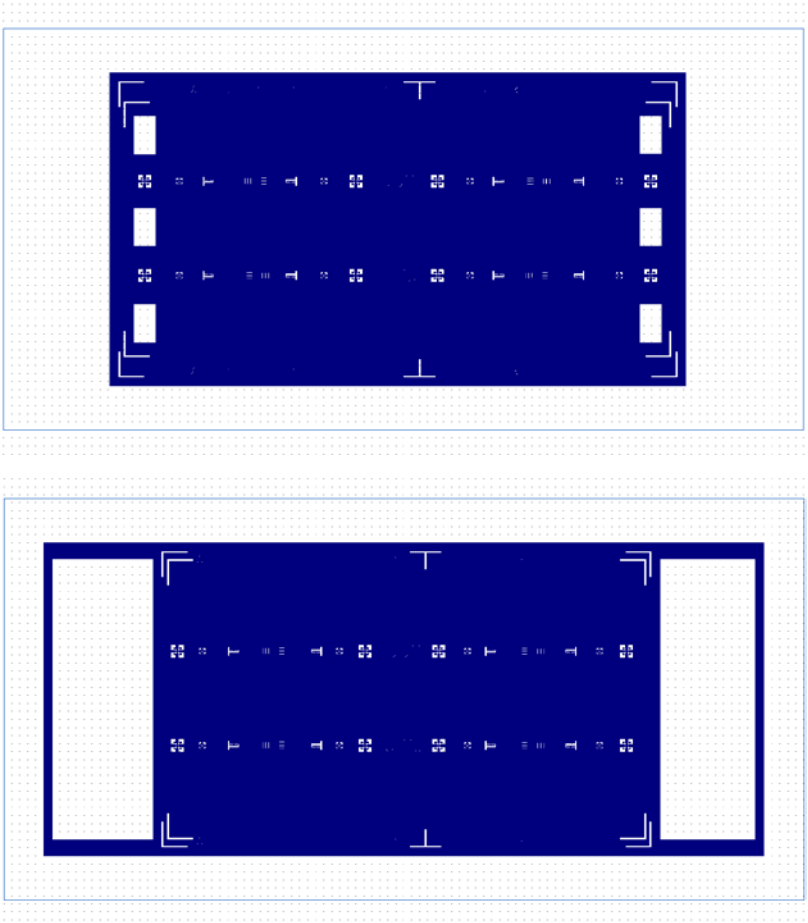

Figure 3-6. Layer 3 mask design for insulating (upper panel) and conductive (lower panel) substrate

It is necessary to dig a path to electrically contact the junctions and the electrodes, thus the layer 3 (Figure 3-6) of the device design is the holes definition into the insulator; a hole is defined on top of each junction, the hole size is smaller than the junction size in all cases because the dry removal technique (plasma etching)

causes a non-negligible under-etching, then it is expected that the hole at the depth of the top metal is slightly wider than the hole at the insulator surface; besides the multiple reflections between the metallic surface and the mask chromium, plus light scattering at the feature edges produce non-perfect vertical walls increasing the undesired shape widening effect.

As the smallest feature size in this layer is 2 x 2 μm^2 (which is also the smallest DF achievable area in the optical lithography system available), the alignment marks shall allow lateral corrections in the order of 500 nm, and then two types of alignment marks are used, the “cross” and the “comb” alignment marks. In the “cross” alignment mark (Figure 3-7 left panel) the thinner line is 5 microns wide, allowing empirical lateral corrections in the order of 1 micron; the gray cross and the four surrounding squares (10 x 10 μm^2) represent the Cr drawing at the optical mask, which shall fit into the blue complementary shape representing the metallic alignment mark in the sample surface.

In the “comb” alignment mark (Figure 3-7 right panel) the different layer teeth (5 x 10 μm^2) are positioned in shifted positions, with a maximum displacement of 1 micron; this 1 micron displacement in the alignment mark allows empirical lateral corrections in the order of 200 nm. When this layer is defined into the resist, selective removal techniques shall be used in order to remove the passivation insulator and not remove the capping metal layer; besides the removal technique shall offer highly directional etching, thus Reactive Plasma Etching is the optimum removal technique to be used at this stage.

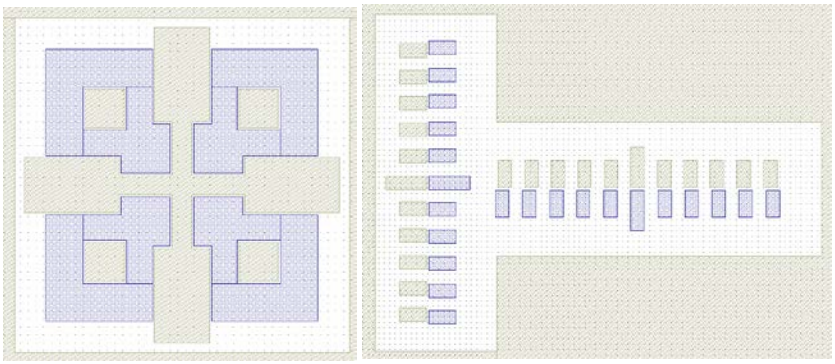

Figure 3-7 Cross (left) and Comb (right) alignment marks, the gray polygons represent Cr drawing in the photomask layer 3, the blue polygons represent metallic alignment marks defined in the sample at layer 1

The last fabrication stage is drawn at layer 4 (Figure 3-9) which contains the metallic contact shapes to be defined by lift-off; each junction has two connection pads, in order to connect correctly the four probes of the measurement configuration (Figure 3-8) as was explained in the *Current Perpendicular to Plane* section, the size of each connection pad is 200 x 250 μm^2.

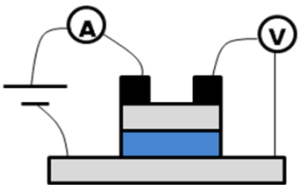

Figure 3-8 Schematic of four probe measurement connection

Highly adhesive metal shall be used in order to guarantee a structurally stable contact that reaches the junction top electrodes through the holes in a continuous layer; after the metal deposition procedure, a lift-off procedure shall be used to remove the metallic layer leftovers. The sequence [*metal deposition / negative resist lithography / metal removal*] can be used instead.

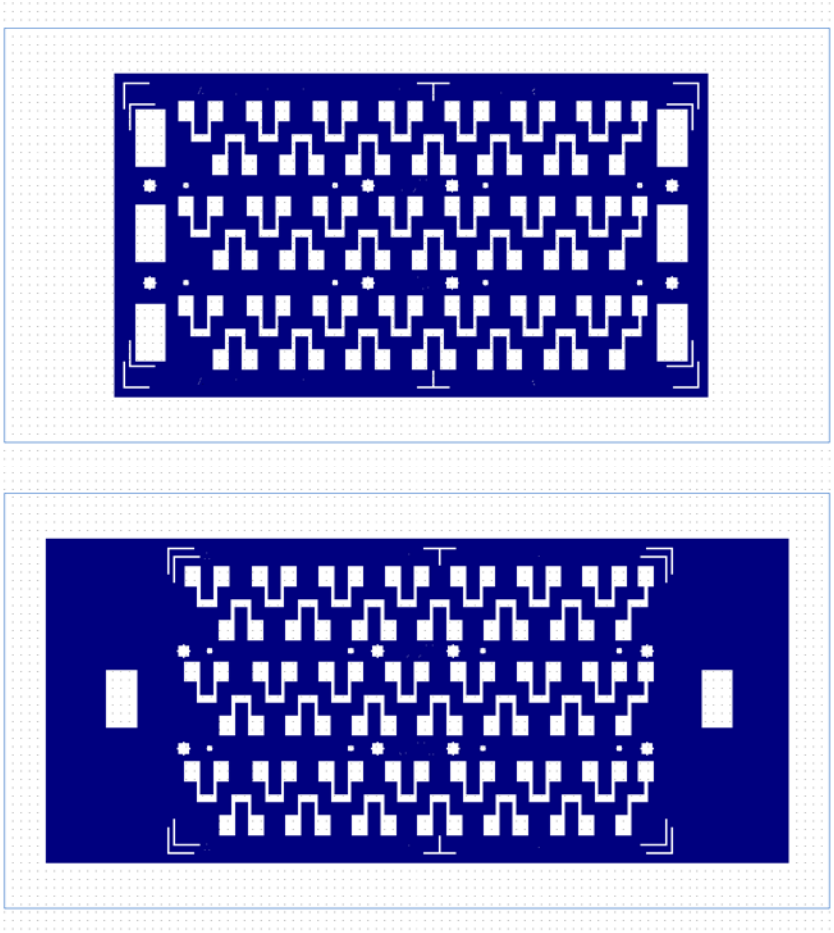

Figure 3-9 Layer 4 mask design for insulating (upper panel) and conductive (lower panel) substrates

3.6 Fabricated Samples

The samples fabricated with the device design described above for the constituent experiments of this thesis, have redundant characteristics according to each layer design needs. Those characteristics are presented in this section. All the metal deposition (sputtering), insulator deposition (sputtering) and material removal stages (Reactive and Ar plasma etching) have been done at the "Universidad Politécnica de Madrid" in collaboration with the "Electronic Materials and Microsystems" group [27-31]. Besides, all of the following issues were discussed and decided with the advice and support offered by collaborators at the Electronic Materials and Microsystems group.

The first metal layer, required before the first lithography step, has been always made of a thin sputtered Ti layer (10 nm) as adhesion layer with a thick sputtered Mo layer (100 to 300 nm) for capping. The first metal removal stage is achieved by reactive plasma etching with 25 sccm flow of SF6 at 20 mTorr partial pressure forming 60 Watt power plasma. Immediately after this metal removal step, the "top electrode" and "barrier" materials are etched by Ar plasma etching with a 25 sccm Ar flow at 5 mTorr partial pressure forming plasma with 170 Watt net power. Figure 3-10 shows the 3D confocal microscopy image of the "cross" alignment mark etched in an Yttria-stabilized Zirconia (YSZ) sample, and Figure 3-11 shows the 3D confocal microscopy image of 1A junction (9 x 18 μm^2) in the LPL27A sample.

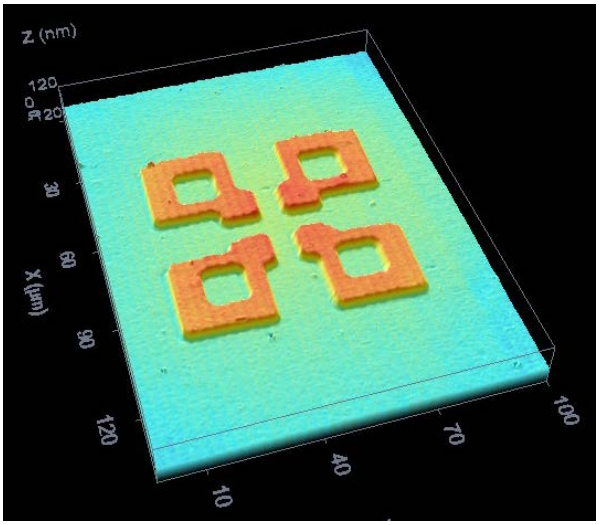

Figure 3-10. Confocal microscopy image of the "cross" alignment mark etched after fabrication stage 1 in an YSZ sample

The particular characteristics of those samples with devices successfully characterized by electrical transport are listed in Table 3-2. In the first fabricated devices (samples labeled AF21 and QLSLSL2A2) the passivation oxide used was Si_3N_4 and although its use allowed the complete device fabrication and characterization processes its adhesion was poor, devices fabricated "a posteriori" with SiO_2 as passivation layer exhibited better adhesion; besides the etching gas used for the former is pure SF_6 while the latter uses a mixture of CHF_3 and SF_6, then the etching stage for holes definition into the Si_3N_4 brings undesired capping metal etching [32], while the same etching stage for SiO_2 brings negligible capping metal etching. These conditions led us to the choice of SiO_2 as passivation material for all of the following devices; the etch conditions for the SiO_2 are (2.5 sccm SF_6) + (50 sccm CHF_3) at 100 mTorr partial pressure forming a 150 Watt plasma.

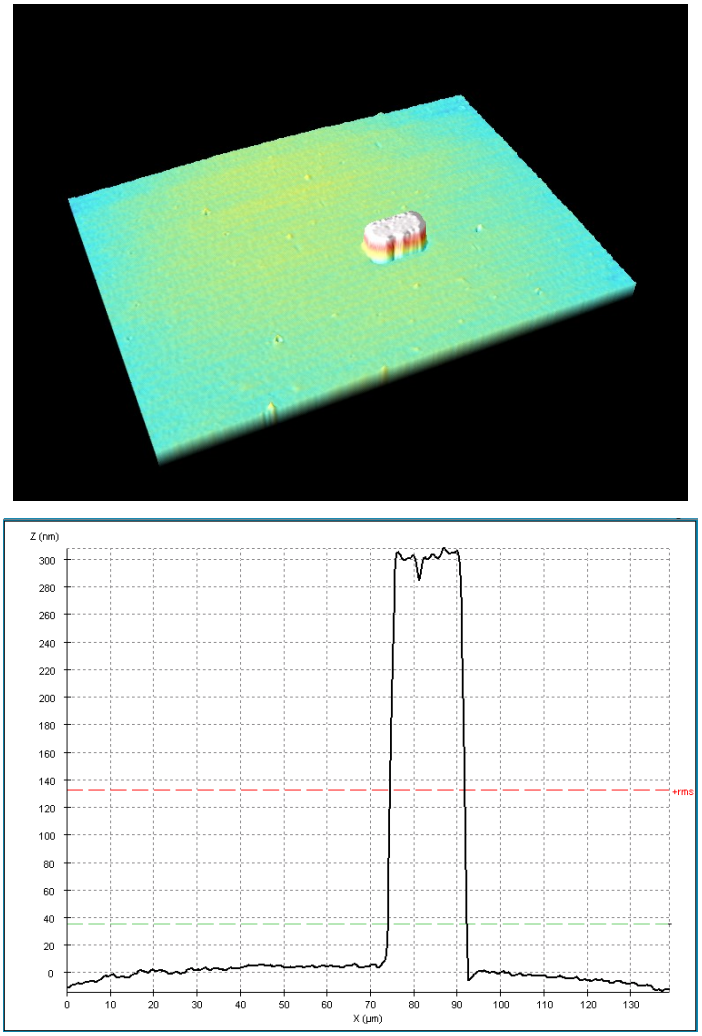

Figure 3-11. 3D confocal microscopy image (upper panel) and depth profile (lower panel) of 1A junction (9 x 18 µm^2) in sample LPL27A

The metal top layer sputtered to make an electric contact with the capping metal layer is again a thin (10 nm) Ti layer covered by a thick (200 to 400 nm) Mo layer that is further used for wire-bonding. A strong ultrasound cleaning is highly recommendable before sputtering the top metal, removal of the loose metal layers and the possible surface contaminants allows a clean and stable electrical contact provided by the top metal layer.

Sample	Capping Metal Thicknesses (Ti/Mo) [nm]	Insulator Composition	Insulator Thickness [nm]	Top Metal Thicknesses (Ti/Mo) [nm]
AF20B	10/100	Si_3N_4	250	10/200
QLSLSL2A2	10/100	Si_3N_4	250	10/200
LCMO217B	90 nm Au	SiO_2	300	10/200
LPL22A	10/200	SiO_2	300	10/400
LPL23A	10/200	SiO_2	300	10/400
LPL25A	10/200	SiO_2	300	10/400
LPL26A	10/200	SiO_2	300	10/400
LPL27A	10/200	SiO_2	300	10/400
LPL28A	10/200	SiO_2	300	10/400
LPL31A	10/200	SiO_2	300	10/400
LP01	10/200	SiO_2	500	10/400

Table 3-2. List of samples fabricated using the designed procedure, with successful electrical characterization

Photographs of the first fabricated devices were taken with an optical microscope, Figure 3-12 left panel shows the devices labeled as 3A, 3B, 3C and 3D in QLSLSL2A2, poor adhesion Si_3N_4 areas can be seen on the left bottom electrode pad, such undesired characteristics do not put in risk the electrical or structural integrity of the contact. Figure 3-12 right panel shows a picture of 1A device, the small rectangle corresponds to the hole etched in the dielectric layer.

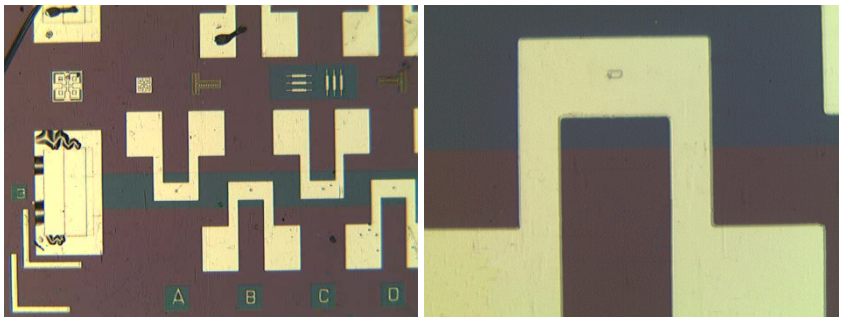

Figure 3-12 Photographs of devices 3A, 3B, 3C and 3D in QLSLSL2A2 (left panel) and 1A (right panel)

3.7 References

[1] R. J. Pedersen and J. F. L. Vernon, Applied Physics Letters 10 (1967) 29.

[2] P. M. Tedrow and R. Meservey, Physical Review B 7 (1973) 318.

[3] R. Meservey, P. M. Tedrow, and P. Fulde, Physical Review Letters 25 (1970) 1270.

[4] P. M. Tedrow and R. Meservey, Physical Review Letters 26 (1971) 192.

[5] J. W. P. Pratt, S. F. Lee, J. M. Slaughter, R. Loloee, P. A. Schroeder, and J. Bass, Physical Review Letters 66 (1991) 3060.

[6] M. A. M. Gijs, J. B. Giesbers, S. K. J. Lenczowski, and H. H. J. M. Janssen, Applied Physics Letters 63 (1993) 111.

[7] S. K. J. Lenczowski, R. J. M. v. d. Veerdonk, M. A. M. Gijs, J. B. Giesbers, and H. H. J. M. Janssen, Journal of Applied Physics 75 (1994) 5154.

[8] D. C. Worledge and D. W. Abraham, Applied Physics Letters 82 (2003) 4522.

[9] W. J. Gallagher, S. S. P. Parkin, Y. Lu, X. P. Bian, A. Marley, K. P. Roche, R. A. Altman, S. A. Rishton, C. Jahnes, T. M. Shaw, and G. Xiao, Journal of Applied Physics 81 (1997) 3741.

[10] F.Houzé, R. Meyer, O. Schneegans, and L. Boyer, Applied Physics Letters 69 (1996) 1975.

[11] K. Bouzehouane, S. Fusil, M. Bibes, J. Carrey, T. Blon, M. L. Dû, P. Seneor, V. Cros, and L. Villa, Nano Letters 3 (2003) 1599.

[12] R. J. S. Jr., J. M. Byers, M. S. Osofsky, B. Nadgorny, T. Ambrose, S. F. Cheng, P. R. Broussard, C. T. Tanaka, J. Nowak, J. S. Moodera, A. Barry, and J. M. D. Coey, Science 282 (1998) 85.

[13] D. C. Worledge and P. L. Trouilloud, Applied Physics Letters 83 (2003) 84.

[14] U. Poppe, N. Klein, U. Dähne, H. Soltner, C. L. Jia, B. Kabius, K. Urban, A. Lubig, K. Schmidt, S. Hensen, S. Orbach, G. Müller, and H. Piel, Journal of Applied Physics 71 (1992) 5572.

[15] I. Brodie and J. J. Muray, The Physics of Micro/Nano-Fabrication, Plenum Press, 1992.

[16] M. Ohring, The Materials Science of Thin Films, 1991.

[17] D. B. Lee, Journal of Applied Physics 40 (1969) 4569.

[18] H. R. S. L. Kaufman, Fort Collins, CO, 80525), R. S. B. C. Robinson, Fort Collins, CO, 80521), and W. E. H. D. Hughes, Annandale, VA, 22003), United States, 1984.

[19] S. B. Ogale, ed., Thin Films and Heterostructures for Oxide Electronics, Multifunctional Thin Film Series, Springer, Maryland, 2005.

[20] Z. Sefrioui, V. Cros, A. Barthelemy, V. Peña, C. León, J. Santamaría, M. Varela, and S. J. Pennycook, Applied Physics Letters 88 (2006) 022512.

[21] Z. Sefrioui, C. Visani, M. J. Calderón, K. March, C. Carrétéro, M. Walls, A. Rivera-Calzada, C. León, R. L. Anton, T. R. Charlton, F. A. Cuéllar, E. Iborra, F. Ott, D. Imhoff, L. Brey, M. Bibes, J. Santamaria, and A. Barthelemy, Advanced Materials 22 (2010) 5029.

[22] N. M. Nemes, C. Visani, C. Leon, M. Garcia-Hernandez, F. Simon, T. Fehér, S. G. E. t. Velthuis, A. Hoffmann, and J. Santamaría, Applied Physics Letters 97 (2010) 032501.

[23] J. Garcia-Barriocanal, F. Y. Bruno, A. Rivera-Calzada, Z. Sefrioui, N. M. Nemes, M. Garcia-Hernández, J. Rubio-Zuazo, G. R. Castro, M. Varela, S. J. Pennycook, C. León, and J. Santamaría, Advanced Materials 22 (2010) 627.

[24] F. Y. Bruno, J. Tornos, M. G. d. Olmo, G. S. Santolino, N. M. Nemes, M. García-Hernandez, B. Mendez, J. Piqueras, G. Antorrena, L. Morellón, J. M. d. Teresa, M. Clement, E. Iborra, C. Leon, and J. Santamaría, Physical Review B 83 (2011) 245120.

[25] J. Garcia-Barriocanal, J. C. Cezar, F. Y. Bruno, P. Thakur, N. B. Brookes, C. Utfeld, A. Rivera-Calzada, S. R. Giblin, J. W. Taylor, J. A. Duffy, S. B. Dugdale, T. Nakamura, K. Kodama, C. Leon, S. Okamoto, and J. Santamaria, Nature Communications (2010)

[26] E. Hartmann, An Introduction to Crystal Physics, University College Cardiff Press, Cardiff, Wales, 1984.

[27] S. Gonzales-Castilla, J. Olivares, M. Clement, E. Iborra, J. Sangrador, J. Malo, and J. I. Izpura, Applied Physics Letters 92 (2008) 183506.

[28] A. Sanz-Hervás, M. Clement, E. Iborra, L. Vergara, J. Olivares, and J. Sangrador, Applied Physics Letters 88 (2006) 161915.

[29] E. Iborra, L. Vergara, J. Sangrador, M. Clement, A. Sanz-Hervás, and J. Olivares, IEEE Transactions on Ultrasonics, Ferroelectrics, and Frequency Control 54 (2007) 2367.

[30] E. Iborra, J. Olivares, M. Clement, L. Vergara, A. Sanz-Hervás, and J. Sangrador, Sensors and Actuators A 115 (2004) 501.

[31] J. Olivares, E. Iborra, M. Clement, L. Vergara, J. Sangrador, and A. Sanz-Hervás, Sensors and Actuators A 123-124 (2005) 590.

[32] P. Walker and W. H. Tarn, eds., Handbook of Metal Etchants, CRC Press LLC, 1991.

4 MANGANITE-TITANATE SCHOTTKY JUNCTIONS

4.1 Motivation

The first milestone at sight is the study of the role that can be played by the $SrTiO_3$ (STO) substrate in our manganites-based devices. Bulk $La_{0.7}Ca_{0.3}MnO_3$ (LCMO) is a ferromagnetic metal above 250 K, and when in thin film its Curie temperature lowers depending on the strain induced by the substrate. When LCMO is grown on top of a (metallic) Nb-doped STO (NSTO) substrate, a Schottky junction is formed. Since a metal-semiconductor interface is formed by joining these two materials, significant charge redistribution is expected to take place due to wave functions overlapping from both sides. The bulk bonds are broken and different bonds are formed. The electronic states that yield charge transfer at the interface are characteristic of the particular metal-semiconductor interface. Manganite-Titanate Junctions have been extensively studied in the literature, since STO is one of the most commonly used substrates for oxide electronics. In a closer relation to the work presented in this chapter, Cobaltite-Titanate *pn* Junctions were studied previously by this research group [1]. Several phenomena have been reported in the literature, such as the rectifying current-voltage (*J(V)*) characteristics with exponential functional behavior, the capacitance behavior under reverse bias, both transport characteristics of semiconductor-metal Schottky Junctions, the doping level dependence of the Schottky model parameters as the barrier height, built-in potential, depletion layer width; and even in some cases Colossal Electroresistance [2]. Scenarios as direct tunneling, assisted tunneling, and thermionic emission have been envisioned as responsible for the transport characteristics in such heterostructures.

This chapter presents the structural and transport characteristics of Nb-doped $SrTiO_3$\\ $La_{0.7}Ca_{0.3}MnO_3$ (NSTO\ LCMO) heterojunctions. First, x-ray diffraction and reflectivity were used to calibrate the (LCMO) growth rate with samples grown on STO substrates. Then, metal to construct the contacts was carefully chosen and non-linearity of the electrical contact was avoided. Having those tasks completed, device samples were grown on NSTO substrates and the fabrication procedure explained in Section 3.5 was applied in order to obtain micron size features LCMO-NSTO heterojunctions. The transport characteristics were measured in a two terminal configuration, using a closed-cycle helium cryostat that allows magneto-transport measurements in the temperature range from 20 to 300 K. Among the fabricated devices, two presented Schottky Junction characteristics and can be successfully explained in terms of Thermally Assisted Tunneling.

4.2 Crystalline Structure – Growth Tuning

The structural quality of $La_{0.7}Ca_{0.3}MnO_3$ (LCMO) manganite thin films grown on STO was checked by x-ray diffraction and x-ray reflectivity. The samples labeled LCMO214 were sputtered during 98 minutes on (5 mm x 5 mm) (100)-cut STO substrates. Figure 4-1 shows the corresponding XRD patterns and x-ray reflectivities. The presence of only the two main substrate peaks and the overlapping two first LCMO peaks proves the absence of manganite phases other than that expected.

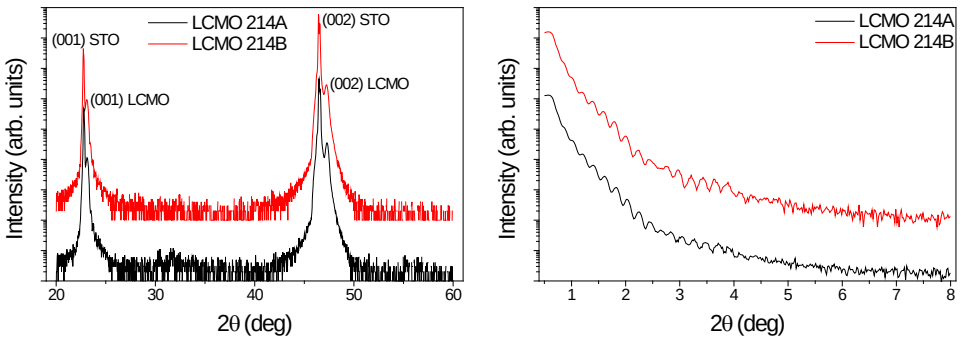

Figure 4-1. XRD (left) patterns and (right) x-ray reflectivities for samples LCMO 214A (black lines) and LCMO 214B (red lines), the red curves are vertically shifted for clarity

The corresponding XRD analysis shows an out of plane lattice parameter of 3.84 Angstrom, which is in agreement with the bulk lattice parameter. The XRR analysis gives the film thicknesses: LCMO214A: 39.0 nm and LCMO214B: 39.3 nm. These values indicate a mean growth rate of 58 seconds per unit cell. The presence of up to 17 finite thickness oscillations indicates high crystalline quality growth and an optimum flatness along the sample surface. Using that calculation, LCMO 215 and LCMO 216 samples were grown in order to corroborate the tuned growth rate using the same procedure. After having fulfilled the thickness growth rate tuning, samples LCMO217A and LCMO217B were grown on NSTO.

4.3 NSTO Electric Contact

The most important part of the characterization performed for these samples is the set of transport measurements. Thus, the desired electric contact with the Nb-doped STO (NSTO) must be assured first, and the following short experiment goes towards such a need; as STO is an insulator with 3.3 eV bandgap [3], according to the Schottky-Mott theory the barrier height for low work function metals as Al (4.2 eV), Pb (4.25 eV) or Ti (4.33 eV) should allow an ohmic contact In fact, T. Shimizu et al. [4] reported the use of Al and Ti to obtain an ohmic contact with NSTO. In this research work two Nb 2% at.-doped $SrTiO_3$ substrates were used to evaluate the contacts conductive characteristics. In both cases S1813 photoresist was spin-cast during 30 seconds at 6000 rpm, with a subsequent 95˚C, 30 minutes annealing; stage 2C from the MTJ photolithography mask (Section 3.5) was used to define the contact surface. Al was evaporated on a sample, and Ti was sputtered on the other one, and their electrical behavior was evaluated.

According to what was found in this research group [1], evaporated Al was annealed at 150˚C during 3 hours, expecting an ohmic contact. However, the transport characteristics obtained here for the Aluminum contact were not completely satisfactory, meanwhile the transport characteristics obtained for the Titanium contact were optimum.

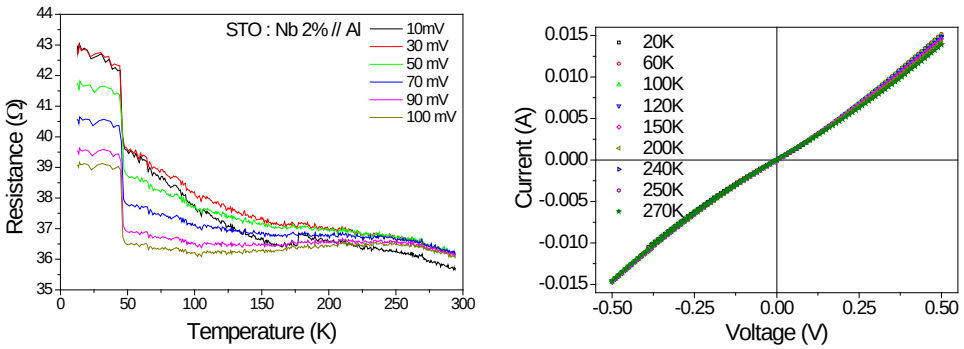

Figure 4-2. NSTO\\ Al transport characteristics

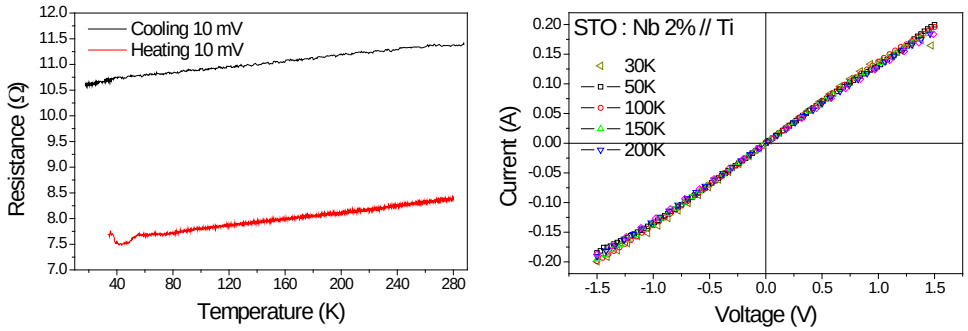

Figure 4-3. NSTO\\ Ti transport characteristics, *R(T)* curves (left) were both measured at 10 mV

The Al contact current vs. voltage (*J(V)*) characteristics (Figure 4-2 right) are sufficiently close to the desired linear behavior, at all the measured temperatures; but the resistance vs. temperature (*R(T)*) (Figure 4-2 left) shown non-linear characteristics, a slowly increasing resistance when decreasing and a very unpleasant characteristic around 46 K. On the other hand, the *R(T)* characteristics of the Ti electrical contact is as desired (Figure 4-3 left), with a slowly increasing resistance with increasing temperature and linear *J(V)* characteristics (Figure 4-3 right). The difference in Cooling Resistance and Heating Resistance of the Ti contact is not considered important, since it is due to the cryostat cables *R(T)* characteristics. The measurement procedure was: Cooling *R(T)*, set of *J(V)* at different temperatures, and finally the Heating *R(T)*. Under the scope of this measurement procedure, a difference in 3 ohms between Cooling and Warming measurements, is not desired, however tolerable. The better structural stability of the Ti is somehow expected, because the Al was evaporated, while the Ti was sputtered, and a higher structural stability is expected from the latter.

In addition, following the report made by L. Granja et al. [5], Au was chosen to make the electric contact with LCMO. Figure 4-4 shows the *R(T)* characteristic measured on LCMO216 at 10 mV.

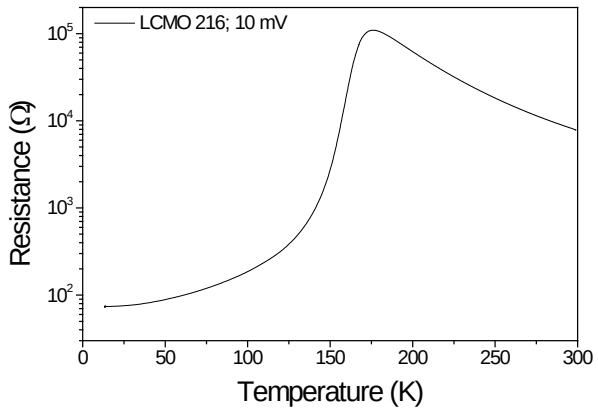

Figure 4-4. 10 mV *R(T)* of LCMO 216, transition temperature is 175 K

Although the bulk manganite in its composition $La_{0.7}Ca_{0.3}MnO_3$ shows the Metal-Insulator Transition (MIT) around 250 K, previous studies of our manganite thin films included in the PhD thesis by V. Peña [6] have shown that, depending on the substrate lattice parameter, the MIT temperature changes from 250 K (when grown on $SrLaAlO_4$) down to 140 K (grown on $NdGaO_3$). Then the observed MIT temperature of LCMO216 at 175 K is as expected, since the substrate used is STO, and the epitaxial strain on our LCMO thin films causes the observed MIT temperature depression.

Having substrate electrical contact and thin film transport checked, the following step is to fabricate the NSTO\ LCMO junctions following the process explained in Section 3.5 and measure according to the procedures described in Section 2.4.2 by using a two-wire configuration measurement. Among the 42 fabricated devices only two of them could be successfully measured and show rectifying behavior. The transport characteristics found are discussed in terms of Schottky Junctions. The remaining junctions were short circuited due to the presence of pinholes or display an open circuit characteristic (actually SiO_2 transport characteristics).

4.4 Schottky Junctions

Since the transport characteristics in complex oxides are governed by the electronic states, the first step in order to understand the measured behavior is to consider the electron – hole populations of the materials involved. As explained in Section 1.9 the parent compounds of both materials are insulators, NSTO is electron doped and LCMO is hole doped. In the NSTO case, the substitutional Nb atom donates one electron to the crystal, then the substrate (with 0.02 %-at doping) has a donor concentration equal to $1.68\times10^{19}cm^{-3}$. And in the LCMO case, the Ca concentration (30%) results in a ferromagnetic metal at low temperature.

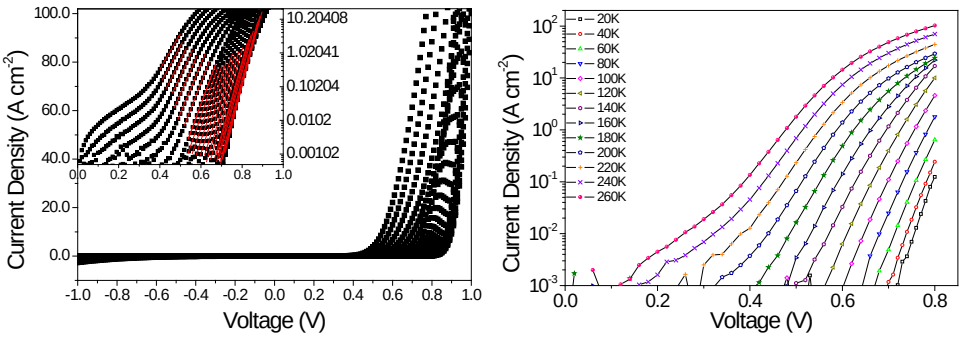

Figure 4-5. 1D junction *J(V)* characteristics measured at temperatures between 20 K and 280 K, inset shows the fits in semi-log scale (left). 3H junction *J(V)* curves for different temperatures

The devices showing a Schottky junction behavior were the Junctions labeled as 1D and 3H as explained in Section 3.5, with a nominal area of $7\times14\mu m^2$ and $8\times8\mu m^2$ respectively. Figure 4-5 shows current vs. voltage (*J(V)*) characteristics at the range temperature 20 K – 280 K for 1D and 3H junctions (left and right panels respectively), evidencing the good rectifying behavior of LCMO-NSTO junctions in the whole temperature range as demonstrated by the strong asymmetry of *J(V)* curves in the linear scale at forward (Figure 4-5) and reverse bias (not shown). The exponential dependence of the current density on applied forward bias for

junction 1D, is shown in the inset to the left panel in Figure 4-5 and in the right panel for junction 3H. A distinct region can be observed at low bias for temperatures above 160 K, where a weaker exponential dependence is observed. The model used to analyze these transport characteristics is the Schottky Junction, this scope has been used before in the literature for complex oxide systems consisting of NSTO-manganite layers [7-10], and usually yields useful results . According to the Schottky Junction model, the thermionic emission current under forward bias conditions can be approximated to

$$J_F \approx J_S(T)\exp\left(\frac{qV}{nkT}\right) \qquad (4.1)$$

in the case where $V >> kT/q$. In the expression above *q* is the electron charge, *k* is the Boltzmann constant, *T* is the junction temperature, and *n* is the ideality factor which equals 1 for an ideal diffusion mechanism. The saturation current density, *Js* is given by

$$J_S(T) = A^* T^2 \exp\left(\frac{-q\Phi_B}{kT}\right) \qquad (4.2)$$

with Φ_B the Schottky barrier height and *A** the effective Richardson constant, defined as

$$A^* = \frac{4\pi m^* k^2}{h^3} \qquad (4.3)$$

in this case, the Richardson constant takes the value $A^* = 156 cm^{-2}K^{-2}$ corresponding to an effective electron mass $m^*/m_0 = 1.3$ for NSTO [11, 12]. Thus we are able to obtain values of Φ_B and *n* at each temperature by fitting experimental data of *J(V)* curves to Eqs. (4.1) and (4.2). These fits are shown in Figure 4-5. It is important to remark that the fits correspond to the intermediate

bias region avoiding the slight deviation from the exponential dependence (probably due to a small series resistance effect) that can be observed at the higher bias region, and avoiding the low bias region for the highest temperatures which may be influenced by carrier recombination or a different transport process. Figure 4-6 (left panel) shows the ideality factor "*n*" which deviates from unity at high temperature ($n \sim 1.7$) and increases strongly at low temperature reaching unphysical values. Similarly, Figure 4-6 (right panel) shows the Schottky barrier height obtained from the fits, it decreases from Φ_B= 0.66 eV at room temperature to unphysical small values approaching zero at the lowest temperatures (Φ_B = 0.1 eV around 20 K). It is indeed remarkable the very similar values obtained for both magnitudes *n* and Φ_B, in the whole temperature range from room temperature down to 20 K, for both measured junctions.

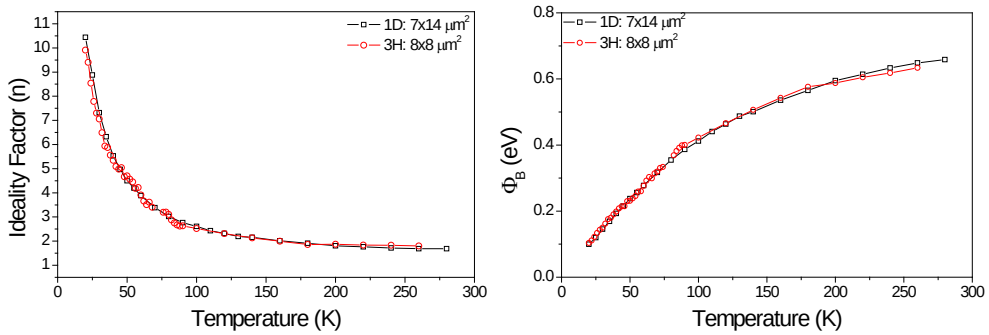

Figure 4-6. Ideality factor obtained from fits to Eq. (4.1) (left) and Schottky barrier height obtained from fits to Eq. (4.2)

Similar deviations of the *J(V)* characteristics from an ideal thermionic emission have been previously reported in heterojunctions of NSTO with other transition metal oxides [7-9], Postma et al. [8] attributed such a deviation to the increase of the dielectric constant of STO at low temperature, but no temperature-varying permittivity model was proposed; Ruotolo et al. [9] attributed it to the increase of the tunneling contribution when reducing the temperature, as it should be directly related to a change in the Schottky barrier height with temperature, the problem still unrevealed and the snake bites its own tail since Schottky barrier height is the

parameter that cannot be extracted in a reliable manner. Thermionic-field emission (or thermally assisted tunneling) has been proposed as a possible mechanism to explain the observed results [10]. In particular, as described next in more detail, a thermionic-field emission process would explain the almost temperature independent slope observed in semi-log *J(V)* curves at low temperatures. A thermally assisted tunneling process in these LCMO-NSTO heterojunctions is sketched in Figure 4-7, illustrating that the electrons between the Fermi level and the bottom of the conduction band (*ξ*) can tunnel from the NSTO to the LCMO if they are first thermally excited to a higher energy below the top of the barrier.

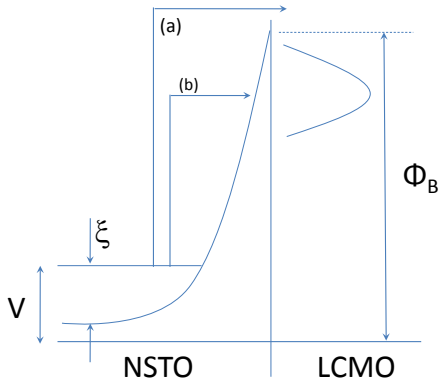

Figure 4-7. Schematic profile of Schottky junction under forward bias (a) Thermionic emission (b) Thermionic-field emission

In the thermally assisted tunneling regime, the forward bias *J(V)* characteristics are expressed as [13]

$$J_F = J_S^*(T)\exp\left(\frac{qV}{E_0}\right) \qquad (4.4)$$

where E_0 is a temperature dependent energy according to

$$E_0 = E_{00}\coth\left(\frac{E_{00}}{kT}\right) \Rightarrow E_{00} = \frac{qh}{4\pi}\sqrt{\frac{N_d}{m^*\varepsilon_r\varepsilon_0}} \qquad (4.5)$$

with h the Planck constant, N_d the donor concentration, ε_r the relative dielectric permittivity and ε_0 is the vacuum permittivity. The temperature dependence of the saturation current in Eq. (4.4) is given by

$$J_S^*(T) = \frac{A^* T^2 \sqrt{\pi E_{00}\left[q(\Phi_B - V) + \xi\right]}}{kT\cosh\left(E_{00}/kT\right)} \exp\left(\frac{\xi}{kT} - \frac{q\Phi_B + \xi}{E_0}\right) \quad (4.6)$$

where ξ is the energy difference between the Fermi level and the bottom of the conduction band.

By comparing Eqs. (4.1) and (4.4), it is clear that the values of E_0 as a function of temperature can be directly obtained from those previously calculated for n since at any fixed temperature the slope of the semi-log $J(V)$ curve is determined by $E_0 = nkT$. In Figure 4-8 it can be seen how E_0 depends weakly on temperature below 60 K on junction 1D, with a value $E_0 = 19 \pm 1$ meV, while it is roughly proportional to temperature close to room temperature, as it would be expected from Eq. (4.5)

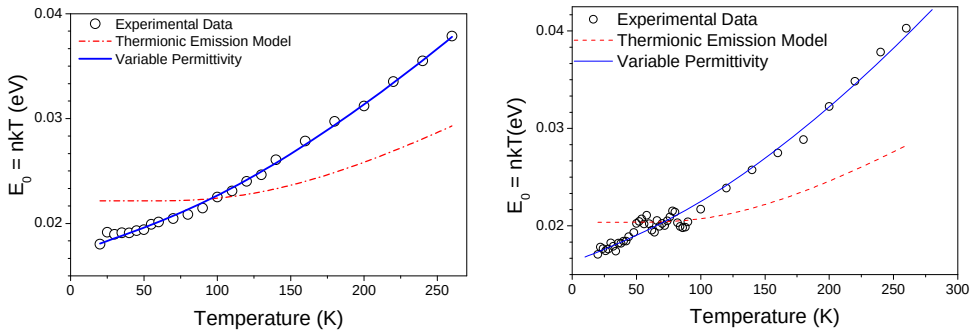

Figure 4-8. E_0 as calculated by using the fitted n values (circles), as obtained with Eq. (4.5) (dashed line) and as calculated letting permittivity change with temperature (solid line), for junctions 1D (left) and 3H (right)

However, the best fit corresponding to Eq.(4.5) is far away from acceptable, as shown in the dashed line in Figure 4-8; E_0 values obtained from $J(V)$ curves at each temperature are not well described by Eq. (4.5) if the value of E_{00} is assumed to be temperature independent. This could be explained as a consequence of NSTO

permittivity temperature dependence. It is well known [14] that STO permittivity ε_r is about 300 at room temperature and increases strongly towards a value of 24000 at low temperature since STO is an incipient ferroelectric material. It has been also shown previously [15] that under a high electric field of the order of 10^7 – 10^8 V/m –like that expected in the space charge region close to the interface with LCMO– the permittivity can be much lower, and although the temperature dependence of ε_r under such high electric field is not well established, it has been reported that it still shows a slight increase when lowering temperature. Thus the E_0 temperature dependence in Figure 4-8 was fitted by using Eqs (4.5) but allowing a temperature dependent value for the dielectric permittivity $\varepsilon_r(T)$ as a fit parameter, following the $\varepsilon(T)$ shape reported by Christen et al. [15] (see Figure 4-9 left) for low applied electric field, which is found to be well described by using a weakly exponential decay with temperature.

$$\varepsilon_r = \varepsilon_r^0 \exp\left(-\frac{T}{B}\right) \qquad (4.7)$$

where ε_r^0 represents the permittivity at zero temperature. Müller and Burkard [14] also reported measurements of the STO "dielectric constant" with a similar shape, also presented a low temperature "dielectric constant" saturation, but such a saturation behavior starts below 10 K; thus, the measurements here presented (T ≥ 20 K) can be expressed by a function that does not include such a saturation, as the proposed exponential decay; such a temperature-independent permittivity was explained by Müller and Burkard in terms of the low-temperature quantum-paraelectricity they reported for STO, and is a behavior that can be only observed well below temperatures as reached in this study. The values here obtained by fitting the experimental data with the expression (4.7) are shown in Figure 4-9 right, which represents the dielectric permittivity temperature dependence chosen for the phenomenological description in the space charge region. The values obtained for ε_r as their temperature dependence are reasonable, when compared

with the expected behavior under a high electric field as previously mentioned [14, 15].

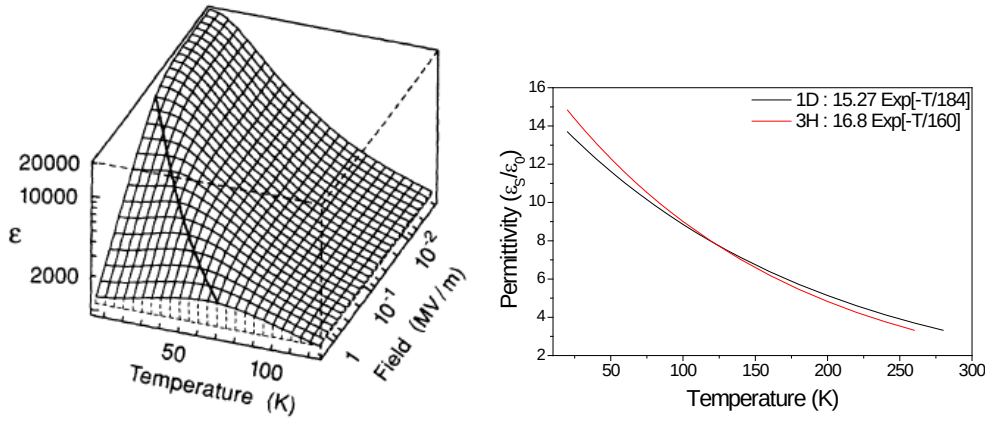

Figure 4-9. (left) Taken from [14], "dielectric constant" of bulk STO vs. temperature and electric field, and (right) relative permittivity obtained by fitting the experimental data with expressions (4.4), (4.5) and (4.7)

These zero temperature values for the dielectric permittivity are quite small for STO ($\varepsilon_r/\varepsilon_0$ = 15.27 for junction 1D and $\varepsilon_r/\varepsilon_0$ = 16.8 for junction 3H), but are reasonable under the scope of an electron-doped STO which is under a high electric field in the space charge region. The use of this expression for temperature dependent permittivity shows its effects on the blue continuous lines shown in Figure 4-8, the remarkable agreement with E_0 values determined from experimental data supports the hypothesis of a temperature dependent ε_r with the functional form of a decaying exponential, and consequently a temperature dependent value of E_{00}.

Further evidence of the thermally assisted tunneling regime dominating the electrical properties of these LCMO-NSTO heterojunctions is obtained from the analysis of the saturation current and its temperature dependence. By inspection of Eq. (4.6) it is concluded that if the energy ξ is small compared with $q\Phi_B$ and kT – since NSTO is an electron-doped semiconductor, it is right to think about the Fermi level going close or into the conduction band – its contribution can be neglected

and thus, taking into account all the temperature-dependent terms of Eq. (4.6), the Schottky barrier height can be extracted from:

$$\ln\left(\frac{J_S^*(T)}{\sqrt{E_{00}}T}\cosh\left(\frac{E_{00}}{kT}\right)\right) vs. \frac{1}{E_0} \qquad (4.8)$$

Open symbols in Figure 4-10 show that such a plot is indeed well described by a linear dependence for the whole temperature range, showing an almost linear behavior, with the Schottky barrier height of Φ_B = 1.09 eV. In the case of junction 1D (left panel) the behavior is linear above 50 K ($1/E_0 < 51.5eV^{-1}$), and the value obtained for the Schottky barrier height is Φ_B = 1.08 eV. These heights are obtained from the slope of the corresponding linear fits (black line). A step further can be envisioned, trying to account for the observed departure at temperatures lower than 50 K by considering the effect of a non-zero value for the energy ξ and to estimate its value from the experimental data. Note that in a closer inspection of Eq. (4.6) we can easily find out that the plot:

$$\ln\left(\frac{J_S^*(T)}{\sqrt{E_{00}}T}\cosh\left(\frac{E_{00}}{kT}\right)\right) - \frac{\xi}{kT} vs. \frac{1}{E_0} \qquad (4.9)$$

must show a linear dependence in the whole temperature range and the slope is then given by $-\left(q\Phi_B + \xi\right)$. Such a plot where the existence of the ξ energy term in Eq. (4.6) is taken into account has been represented in open circles in Figure 4-10. By using ξ = 17 meV for junction 1D, linear behavior is found down to the lowest temperature, corresponding to the value Φ_B = 1.08 + 0.017 eV for the Schottky barrier height, for junction 3H the corresponding calculation gave Φ_B = 1.09 + 0.018 eV, diminishing the point dispersion and including a slight curvature towards low temperatures. The fact that the Schottky barrier is found to be essentially temperature independent when assuming a thermally assisted

tunneling mechanism at the interface gives an additional and strong support to the interpretation that the Thermally Assisted Tunneling dominates the behavior of the *J(V)* characteristics in the LCMO-NSTO heterojunctions [16].

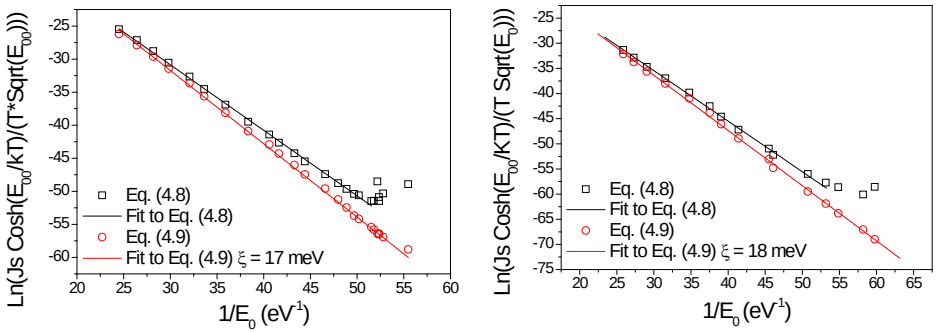

Figure 4-10. Calculated values for Eq. (black squares) and its corresponding fit (black line), as calculated values for Eq. (red circles) with its corresponding fit (red line) for junctions 1D (left) and 3H (right)

Thus, the devices transport characteristics are successfully analyzed and explained in the framework of thermally assisted tunneling (or thermionic-field emission). The energy difference is around 17 meV. Although Eq. (4.7) is proposed without a physical-principles derivation, the inclusion of permittivity as a temperature-dependent parameter, and its effect on the energies E_0 and E_{00} led the analysis towards a more accurate quantitative description of the physical transport properties of the system, and should not be forgotten in future description of the manganite-titanate junction electrical transport behavior.

4.5 References

[1] F. Y. Bruno, J. Garcia-Barriocanal, M. Torija, A. Rivera, Z. Sefrioui, C. Leighton, C. Leon, and J. Santamaria, Applied Physics Letters 92 (2008) 082106.

[2] T. Fuji, M. Kawasaki, A. Sawa, Y. Kawazoe, H. Akoh, and Y. Tokura, Physical Review B 75 (2007) 165101.

[3] C. Park, Y. Seo, J. Jung, and D. W. Kim, Journal of Applied Physics 103 (2008) 054106.

[4] T. Shimizu, N. Gotoh, N. Shinozaki, and H. Okushi, Applied Surface Science 117/118 (1997) 400.

[5] L. Granja, L. E. Hueso, M. Quintero, P. LEvy, and N. D. Mathur, Physica B 398 (2007) 235.

[6] V. Peña, in Applied Physics, Vol. PhD Physics, Universidad Complutense de Madrid, Madrid, 2005, p. 165.

[7] Z. Luo, J. Gao, A. B. Djurisic, C. T. Yip, and G. B. Zhang, Applied Physics Letters 92 (2008) 182501.

[8] F. M. Postma, R. Ramaneti, T. Banerjee, H. Gokcan, E. Haq, D. H. A. Blank, R. Jansen, and J. C. Lodder, Journal of Applied Physics 95 (2004) 7324.

[9] A. Ruotolo, C. Y. Lam, W. F. Cheng, K. H. Wong, and C. W. Leung, Physical Review B 76 (2007) 075122.

[10] T. Susaki, N. Nakagawa, and H. Y. Hwang, Physical Review B 75 (2007) 104409.

[11] T. Shimizu and H. Okushi, Journal of Applied Physics 85 (1999) 7244.

[12] Z. Sroubek, Physical Review B 2 (1970) 3170.

[13] F. A. Padovani and R. Stratton, Solid-State Electronics 9 (1966) 695.

[14] K. A. Müller and H. Burkard, Physical Review B 19 (1979) 3593.

[15] H. M. Christen, J. Mannhart, E. J. Williams, and C. Gerber, Physical Review B 49 (1994) 12095.

5 MANGANITE - TITANATE MAGNETIC TUNNEL JUNCTIONS

Recently large efforts have been devoted to using interfaces between insulating complex oxides as new barriers to expand the possibility range in the design of new spintronics devices. Larger than 100% tunnel magnetoresistance from all-oxide magnetic tunnel junctions with a [$SrTiO_3$\ $LaMnO_3$\ $SrTiO_3$] tunneling barrier sandwiched between two $La_{0.7}Sr_{0.3}MnO_3$ (LSMO) electrodes is shown in this chapter; weak TMR temperature dependence recorded at high applied voltage (200 to 400 mV) is found, while it decreases strongly with increasing temperature at low applied voltages; the results are discussed in terms of an artificially modified magnetic ground state at the interface between $LaMnO_3$ (LMO) and $SrTiO_3$ (STO) layers.

5.1 Motivation

Since the discovery of new and unexpected phases at interfaces between insulating complex oxides [1-4] the search for engineered interfaces with improved physical properties still is a major direction in the design of new spintronics devices. In particular, modifying the interface magnetism may have important implications for the manganese-based perovskite oxides magnetic tunnel junctions (MTJs) development; for instance the ferromagnetic and metallic $La_{0.7}Sr_{0..3}MnO_3$ (LSMO) is a promising material to integrate in oxide MTJs, due to its high Curie temperature (T_c) and high spin polarization [5-7]. However previous studies on oxide MTJs have always shown a strong TMR decrease with increasing applied voltage and/or temperature, vanishing at moderated voltages and/or temperatures far below the bulk electrodes T_C [8-11]. Consequently the optimum TMR value is restricted to low voltage and very low temperatures, and this indicates that device performance is not only determined by the bulk ferromagnetic electrodes intrinsic properties, but also depends on the electrode/insulator interface magnetic state [12-14] where spin scattering has a major impact.

Substantial theoretical work [15-18] has highlighted the role played by a number of interface phenomena (modified screening, band bending, polarity mismatch) in the determination of important electronic parameters (bandwidth, on-site Coulomb interaction) potentially responsible for profound changes in the local charge, spin and orbital structure. In this regard the possibility of artificially manipulating spin states at interfaces is particularly attractive for the design and operation of novel spintronic devices; mixed-valence manganites are ideal systems to investigate this issue due to their strong intrinsic tendency to change their electronic properties under the action of small perturbations such as strain and / or charge transfer [19, 20]. Several works in the present literature deal with the properties of this kind of systems, especially concerning electron coupling or epitaxially strain induced

charge reconstruction in $LaMnO_3$/ $SrMnO_3$ [21-24] and $LaMnO_3$/ $SrTiO_3$ [25] based superlattices; a recently observed new kind of Ti^{3+} ferromagnetism at $LaMnO_3$/ $SrTiO_3$ interfaces is also a consequence of charge transfer [26].

Such an artificially modified interface magnetism between LMO and STO layers is used in this chapter as a new tunnel barrier to examine its effect on [LSMO (50 nm)\ STO (1.2 nm)\ LMO (2.8 nm)\ STO (1.2 nm)\ LSMO (8 nm)] MTJs performance. Spin dependent transport measurements show TMR values in excess of 100% measured at low temperatures and low applied voltage and yield a weak TMR temperature dependence recorded at high applied voltage ranging from 200 to 400 mV and vanishing at the LMO/ STO interface Curie temperature.

5.2 $La_{0.7}Sr_{0.3}MnO_3$

In the renaissance of the study of manganites during the 1990s a considerable emphasis has been given to the $La_{1-x}Sr_xMnO_3$analysis, since its Curie temperature as a function of hole doping is above room temperature and this increases its chances for future practical applications; resistivity vs. temperature and phase diagram for this compound at several doping levels are shown in Figure 5-1(a) and Figure 5-1(b) [27]. The highly spin-polarized ferromagnetic metal (FM) $La_{0.7}Sr_{0..3}MnO_3$ (LSMO) with a Curie temperature (T_C) of 369 K has been used as electrode in the MTJs described in this chapter.

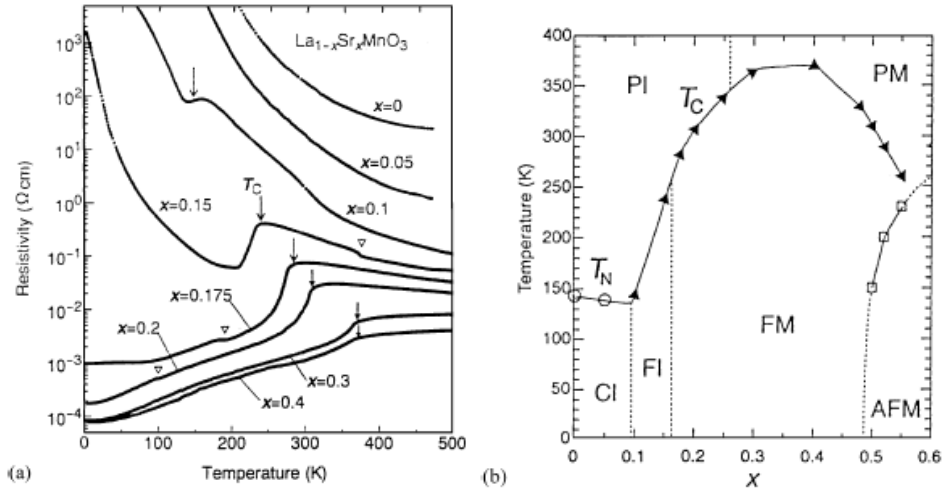

Figure 5-1. (a) Resistivity vs. temperature for various $La_{1-x}Sr_xMnO_3$ single crystals, arrows indicate the Curie temperature, open triangles indicate anomalies due to structural transitions, for more details see [27]. (b) $La_{1-x}Sr_xMnO_3$ phase diagram prepared with data from [27] and [28]; the AFM phase at large x is an A-type AF metal with uniform orbital order. PM, PI, FM, FI, and CI denote paramagnetic metal, paramagnetic insulator, FM metal, FM insulator, and spin-canted insulator states, respectively. T_C stands for Curie temperature and T_N for Néel temperature. Adapted from [29]

5.3 Sample Growth and Structural Characterization

LSMO\ STO\ LMO\ STO\ LSMO heterostructures were grown on (100) $SrTiO_3$ (STO) substrates in a high pressure (3.4 mbar) oxygen and high temperature (810 ºC) sputtering system. STO layers were grown between the two LSMO/ LMO layers in order to provide similar electrode-barrier interfaces at both sides. The junctions were patterned using optical lithography, Ar plasma etching and reactive ion etching (as described in Section 3.5). Magnetic measurements were performed by SQUID magnetometry, and electrical measurements were performed in the current perpendicular to plane (CPP) geometry using a two-terminal dc method with the magnetic field applied parallel to the in-plane [110] sample direction inside a closed cycle He cryostat.

5.3.1 X-ray diffraction

X-ray diffraction was used to determine the LSMO\ STO\ LMO\ STO\ LSMO heterostructures crystalline quality and to confirm the c-axis oriented growth. Figure 5-2 shows x-ray reflectivity and diffraction patterns for the samples listed in Table 5-1, Clear LSMO Bragg peaks labeled (001) and (002) can be observed (Figure 5-2 down); clear finite size oscillations together with an additional modulation (marked by arrows) are observed in the reflectivity (Figure 5-2 up), providing confirmation of high quality interfaces. The total layer thickness t is calculated from the finite size oscillations in the reflectivity (Figure 5-2 up). The inset in Figure 5-3 shows the thickness fit corresponding to the broad oscillation t', of the [STO\ LMO\ STO\ top LSMO] thickness; the straight line fit (both for t and t') demonstrates the accurate deposition rate control.

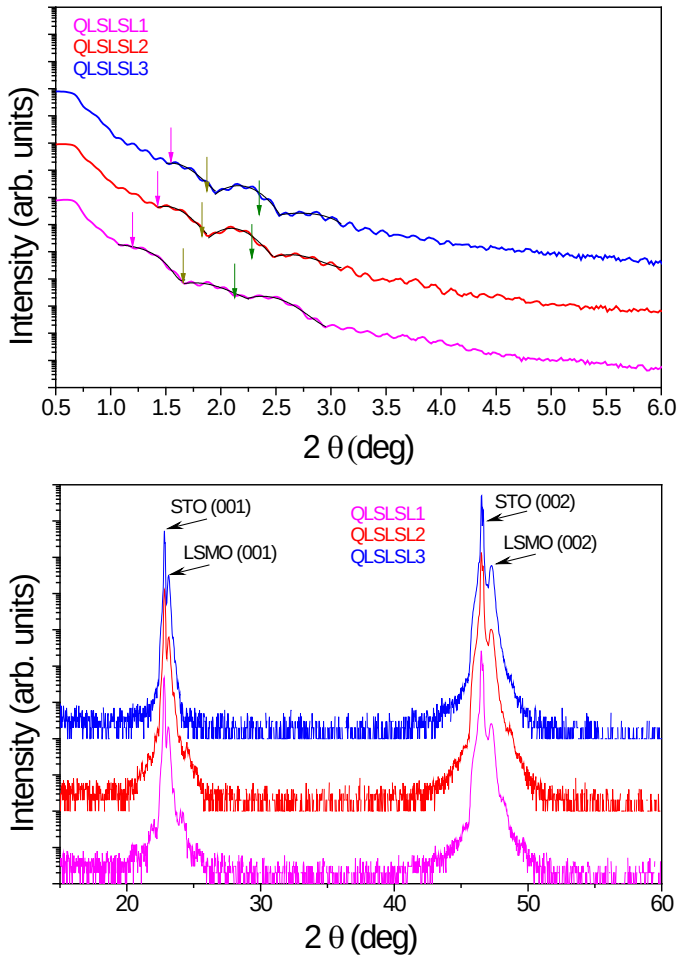

Figure 5-2. X-ray reflectivities (up) and XRD patterns (down), sample description in Table 5-1

SAMPLE	STRUCTURE
QLSLSL1	STO// 50 nm LSMO/ 3 u.c. STO / 12 u.c. LMO / 3 u.c. STO / 8 nm LSMO
QLSLSL2	STO// 50 nm LSMO/ 3 u.c. STO / 7 u.c. LMO / 3 u.c. STO / 8 nm LSMO
QLSLSL3	STO// 50 nm LSMO/ 3 u.c. STO / 5 u.c. LMO / 3 u.c. STO / 8 nm LSMO

Table 5-1. LSMO / STO / LMO / STO / LSMO heterostructures

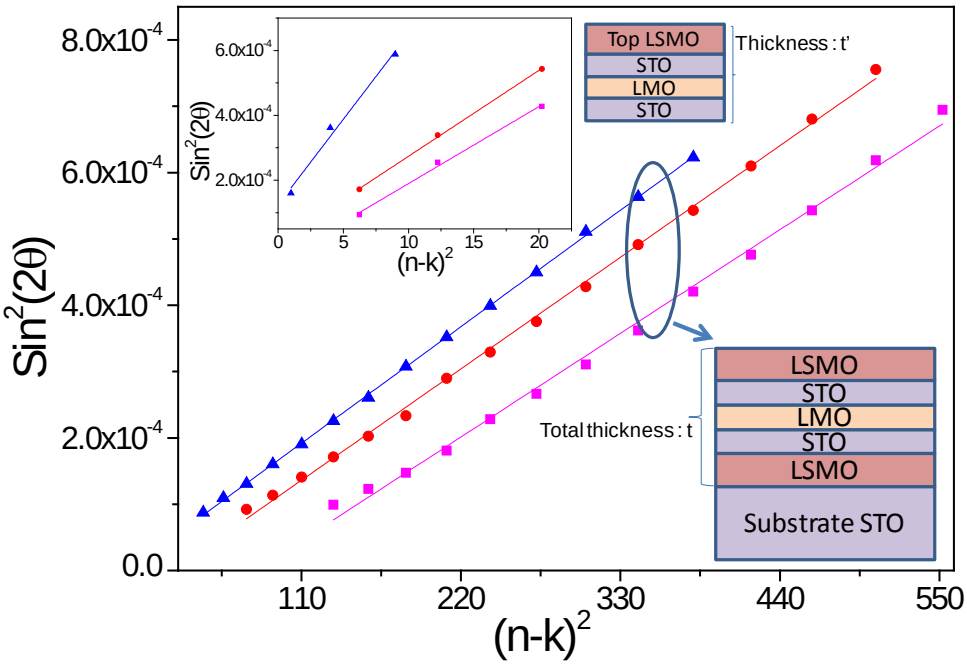

Figure 5-3. Finite thickness oscillation fits, magenta squares for QLSLSL1, red circles for QLSLSL2 and blue triangles for QLSLSL3, inset shows fit for the additional oscillation marked by arrows at Figure 5-2

Sample	Fitted Total Thickness (Å)	Fitted Top Thickness (Å)
QLSLSL1	647	158
QLSLSL2	623	127
QLSLSL3	609	118

Table 5-2. Calculated thicknesses from the fits shown at Figure 5-3

5.3.2 Microscopic Structural Characterization

STEM and EELS measurements were carried out by Maria Varela at Oak Ridge National Laboratory (ORNL), using the UltraSTEM100 equipped with a Gatan Enfina EELS detector. Measurements on sample QLSLSL2A1 were performed with a 100 kV electron beam. Figure 5-4 shows a set of low magnification images, including simultaneous bright field (left) and Z-contrast (right). The upper images have the same magnification and the scale bar is 200 nm long; for the lower images the scale bar represents 100 nm. The images show how the layers are flat and

continuous over long lateral distances, as was expected after the observation of low angle XRR oscillations up to 2Θ = 6. No secondary phases are detected. While some roughness can be seen in the layers, no obvious pinholes are observed.

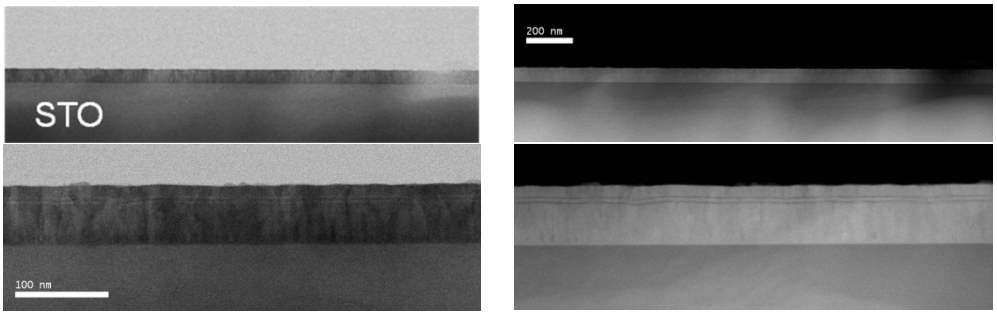

Figure 5-4. Bright Field (BF) (left images) and Annular Dark Field (ADF) (right images) obtained with the 100 kV Ultra-STEM at ORNL

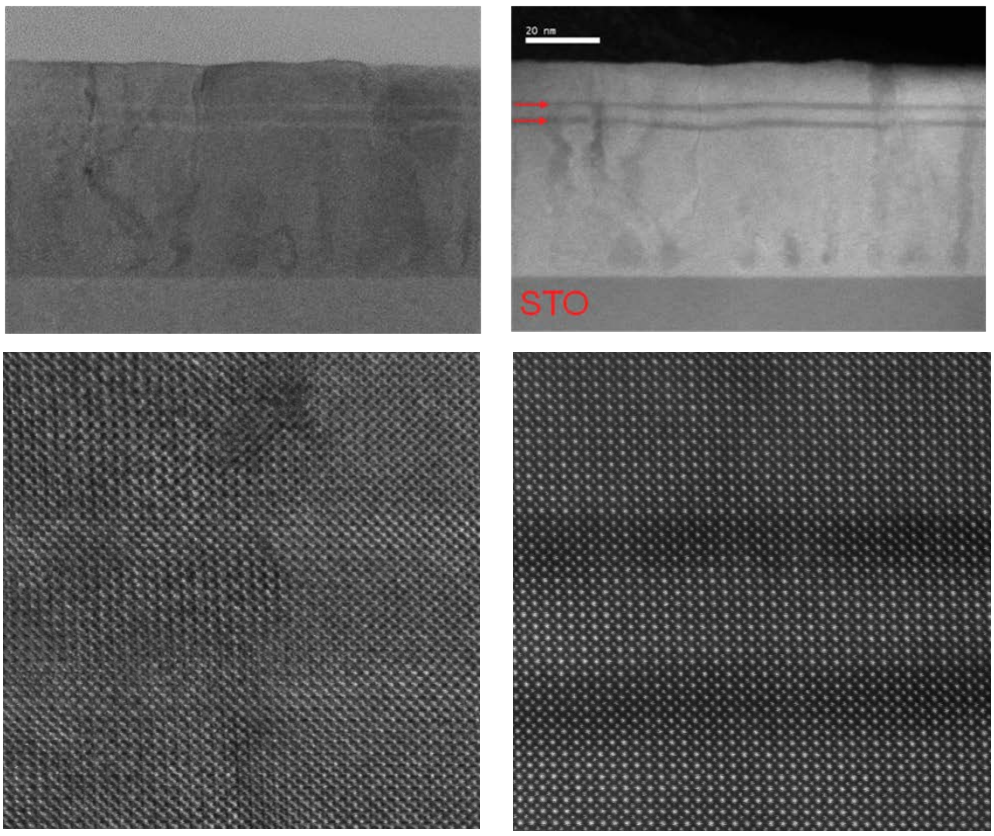

Figure 5-5. BF images (left panel) and ADF images (right panel) with low (upper panels) and high magnifications (bottom panels are 15 nm x 15 nm)

Atomic resolution images were also acquired. The images in Figure 5-5 show how some defects can be observed stemming from the substrate. These defects can be (low angle) grain boundaries, or some array dislocations, that could be involved in the relaxation of epitaxial strain. They are more visible in the BF image (Figure 5-5 left upper panel) that in the ADF (Figure 5-5 right upper panel) image, due to the fact that BF images are coherent. However, ADF images are sensitive to the sample chemistry, and they show that the continuity of the STO layers (red lines) is not interrupted in the heterostructure. The high magnification (lower panel) images in Figure 5-5 show a grain boundary, more visible in the BF (left) than the ADF (right) image. In any case it is clear from the ADF image that the layers are perfectly coherent.

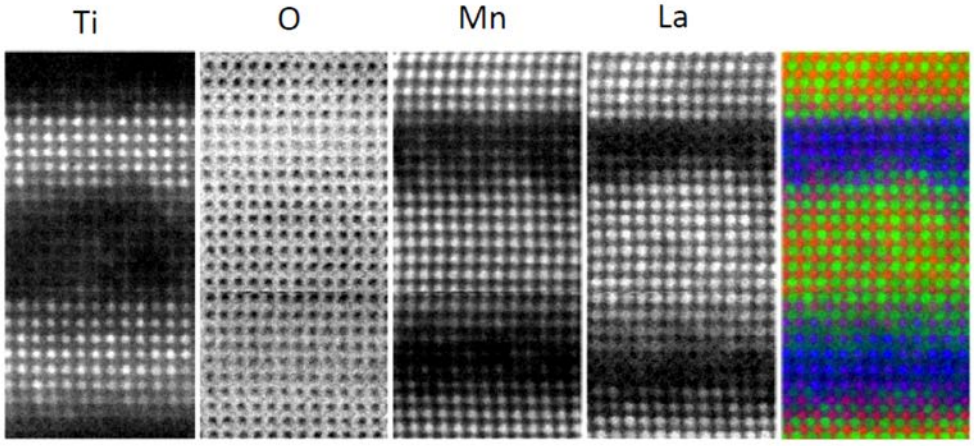

Figure 5-6. EELS spectrum images of a LSMO\ STO\ LMO\ STO\ LSMO heterostructure (from left to right) for Ti, O, Mn, and La in the same area. The rightmost image is the composition of them by assigning colors to each element (Blue = Ti, Red= Mn, Green = La)

Figure 5-6 shows a number of atomic resolution elemental maps obtained from EELS spectrum images (in a 5 nm x 10 nm area). These maps have been obtained by removing the background below the absorption edges via a power law fit, and integrating the remaining intensity for the Ti $L_{2,3}$, the O *K*, the Mn $L_{2,3}$ and the La $M_{4,5}$ edges, respectively. All atomic resolution maps show the lattice associated to every element. The color map is the superposition of the Ti, Mn and La maps (Ti =

Blue, Mn = Red and La = Green). It is observed that LSMO\ STO interfaces (top and bottom) are chemically sharp; however the STO\ LMO\ STO interfaces present some Mn-Ti interdiffusion. Regardless, the middle LMO layer is isolated from the top and bottom LSMO electrodes.

5.4 Magnetic Characterization

In order to examine the electrode-barrier interface magnetism, Barriocanal et al. [25] performed transport and magnetic measurements in LMO\ STO superlattices with different thickness ratio ($t_r = t_{LMO}/t_{STO}$). It is clear that hysteresis loops at 10 K and resistivity vs. temperature curves (Figure 5-7) evidence the presence of ferromagnetism in the samples. It is worth mentioning that 22 unit cell thick LMO thin films exhibited ferromagnetic *M(H)* loops with a saturation magnetic moment of 2.2 μ_B per Mn atom at 10 K, where ferromagnetism is probably due to strain [30] or to the presence of cationic defects, which are known to hole-dope the LMO layers [31-34]. Interestingly, Barriocanal et al. [25] have shown that the ferromagnetic fraction strongly depends on the layer-thickness ratio $t_r = t_{LMO}/t_{STO}$. As shown in Figure 5-7(a) top inset, the 1000 Oe field-cooling (FC) temperature dependent magnetization shows decreasing Curie temperature with t_r, and Figure 5-7 shows decreasing saturation magnetization with t_r.

Corresponding shifts are observed in the metal-insulator transition (MIT) temperature in the resistivity curves displayed in Figure 5-7(b): by reducing t_r the curves progressively change from a metallic behavior (as observed in the $(LMO_{17}\backslash STO_2)_8$ superlattice) to an insulating behavior ($(LMO_3\backslash STO_2)_{30}$ superlattice). The thickness ratio (and most likely the ensuing degree of epitaxial strain) is playing then a determining role in the electronic properties of the system. It is also worth noting that these resistivity measurements rule out any major La-Sr interdiffusion in the system; the $(LMO_3\backslash STO_2)_8$ sample is the most insulating among all of them, and is weakly magnetic. Note that any significant La-Sr interdiffusion would cause the film to resemble the $La_{0.6}Sr_{0.4}MnO_3$ random alloy, however this alloy is metallic and fully ferromagnetic unlike what is observed.

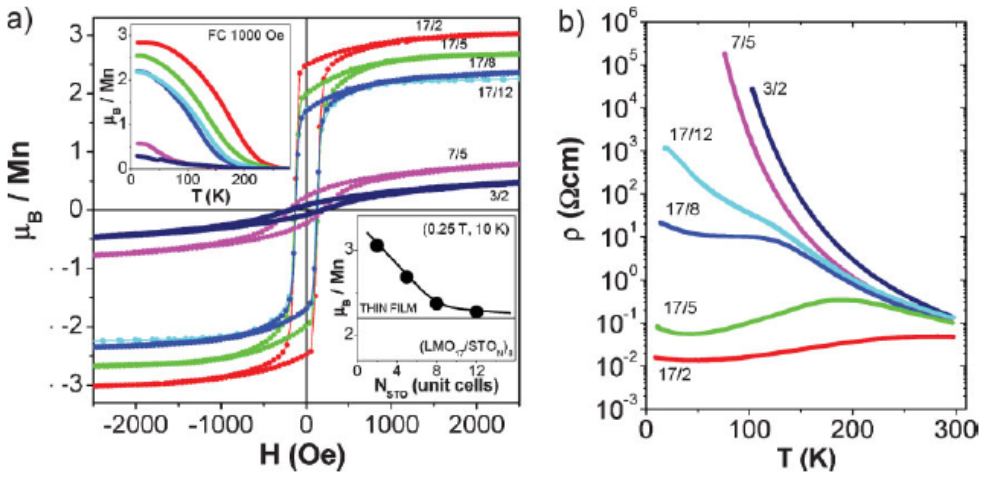

Figure 5-7. a) (SQUID) Hysteresis loops measured at 10 K. The N/M labels correspond to the LMO\ STO layer thicknesses in unit cells. Top inset: FC magnetization versus temperature with an applied magnetic field of 1000 Oe. Bottom inset: Magnetization versus STO thickness of the $(LMO_{17}\backslash STOn)_8$ series measured at 10 K and 2500 Oe. The line represents the magnetization of the 22-unit-cell LMO thin film measured under the same conditions. b) Logarithmic resistivity curves of the same samples. The same label nomenclature and color code has been used in both panels. From Barriocanal et al. [25]

More information on this LMO/STO interface ferromagnetic state can be extracted from –both real (χ_{ac}') and imaginary (χ_{ac}'') components– ac susceptibility temperature dependence; Figure 5-10 shows the temperature dependence of ac susceptibility (χ) measured by a SQUID magnetometer at a frequency of 10 Hz and an amplitude of 1 Oe for LSMO (50 nm)\ STO (1.2 nm)\ LMO (2.8 nm)\ STO (1.2 nm)\ LSMO (8 nm) heterostructure. As mentioned above, two well defined peaks in both susceptibility components are observed at high temperatures and correspond to the bottom and top electrodes response, and a weak upturn of χ_{ac}'' is also observed at much lower temperature. Note that in ferromagnets a susceptibility peak occurring at temperatures lower than the Curie temperature is due to the incoherent initial magnetization rotation contribution, as the temperature approaches *Tc*. Based on the previous work on STO/ LMO heterostructures [20] it is concluded here that the broad peak observed at low temperatures suggests the Curie temperature of the magnetic STO/ LMO interface

is higher than 60 K, in fact XMCD hysteresis loops have shown an induced ferromagnetism at 100 K [20].

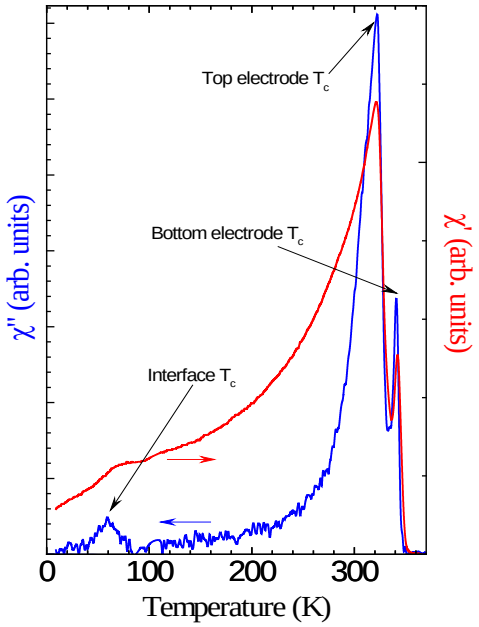

Figure 5-8. Real (χ_{ac}') (red line) and imaginary (χ_{ac}'') (blue line) ac susceptibility temperature dependence measured at 10 Hz, 1 Oe for a LSMO (50 nm)\ STO (1.2 nm)\ LMO (2.8 nm)\ STO (1.2 nm)\ LSMO (8 nm) heterostructure

5.5 Spin Dependent Transport

Among all the fabricated devices in sample QLSLSL2, those labeled as 2N, 3M and 3N (4 x 4 μm^2 nominal lateral size) exhibited tunnel magnetoresistance (TMR). The remaining devices exhibited short circuit behavior (resistance similar to that of the bottom electrode) or open circuit behavior (electrical characteristics of SiO_2).

Resistance vs. temperature (*R(T)*) curves were first measured in search for the typical insulating-like behavior that is expected in a tunnel junction. Figure 5-11 shows such curves for junctions 2N (red line), 3M (black line) and 3N (green line), and the first element to remark is that the three junctions exhibit peaks related to the metal-insulator transition (MIT) of both the top electrode (250 K) and the STO\ LMO interface (116 K). As the expected low temperature insulating-like behavior is only observed for 3N, low TMR performance is expected from the other two devices. In the same way the *R(T)* curves fulfill the requirements, better TMR performance is expected from 3N, then from 2N, and the worst performance is expected from 3M.

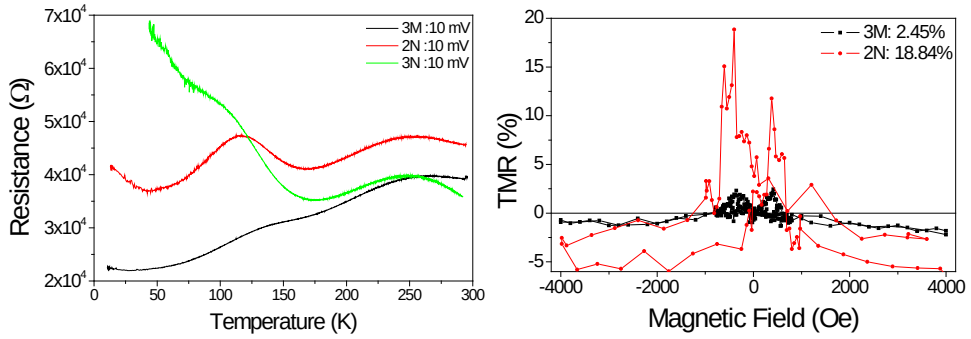

Figure 5-9. *R(T)* (left) and *R(H)* at 20 K and 10 mV (right) curves for junctions 3M (black line), 2N (red line) and 3N (green line)

Resistance vs Magnetic Field (*R(H)*) curves were measured from 15 K up to 210 K, and Figure 5-11 right panel shows the TMR that was defined as $TMR = (R_{ap}-R_p) / R_p$ where R_{ap} and R_p were respectively the tunnel resistances in the antiparallel (AP) and parallel (P) magnetization configurations; as expected from the *R(T)*

characteristics, junction 2N (red line and symbols) exhibits a better performance at 20 K and 10 mV with a 18.84 % maximum TMR than junction 3M (black line and symbols) which exhibits 2.45 % maximum TMR at the same conditions. Also, as expected from the characteristic observed at the *R(T)* curves, the most striking TMR measurement was exhibited by junction 3N with a maximum TMR of 101.8 % (Figure 5-12 left) measured at 15 K with 10 mV, reaching *TMR* = 0 % at 135 K.

The junction 3N resistance switches sharply from P to AP state with TMR value larger than 100%, reflecting the potential of [STO\ LMO\ STO] as a new alternative tunneling barrier in oxide MTJs; furthermore, the resistance versus temperature curve for 3N (Figure 5-11 left) shows a typical resistance increase with decreasing temperature generally observed in MTJs. All these observations indicate that MTJ 3N is pinhole free and that tunneling is the dominant transport mechanism [35].

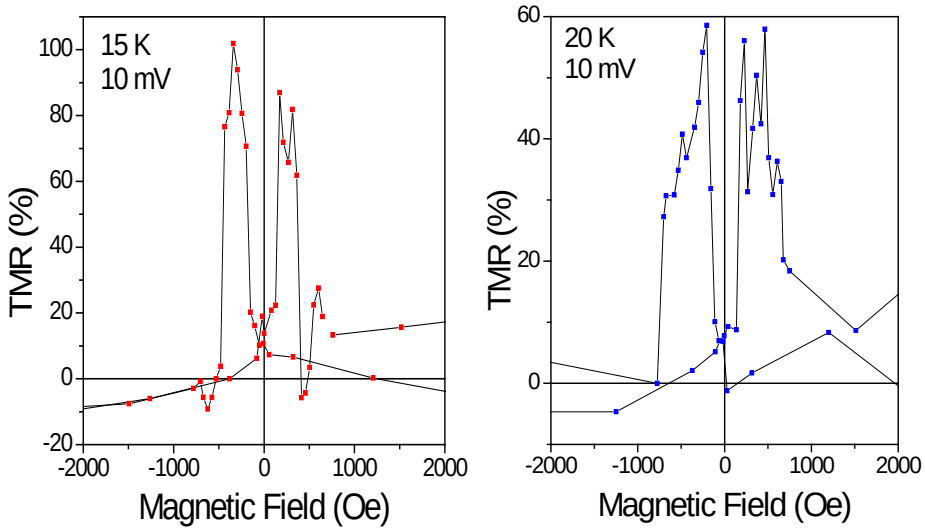

Figure 5-10. Junction 3N *TMR* measured at 15K (left), 20 K (right) and 10 mV

It is important to note that the bottom electrode *R(T)* shows metallic behavior concerning temperature and voltage dependences (Figure 5-13 left), indicating that the bottom electrode was not damaged during the pattering process, the electrode resistance is an order of magnitude lower than the junction resistance in the temperature range of measurement (below 140 K).

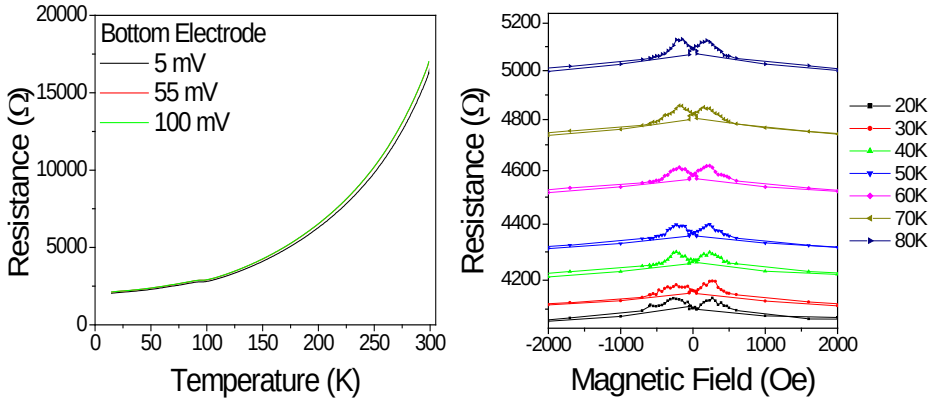

Figure 5-11. Different voltages *R(T)* of bottom electrode #3 (left) and *R(H)* at 10 mV and several temperatures of bottom electrode #2 (right)

5.5.1 Voltage and Temperature Dependence

Current vs. voltage (*I(V)*) characteristics were measured at different temperatures and applied magnetic fields, in such a way that the relative magnetic alignment between electrodes is probed in parallel (P) and antiparallel (AP) configurations. The barrier characteristics obtained following Brinkman's tunneling for asymmetrical barriers model [36] for the lowest temperature (20 K) 3N junction *I(V)* curve in the AP configuration gives an effective barrier thickness (49 Å) in excellent agreement to the nominal barrier thickness (50 Å), with an effective barrier height of 91 meV corresponding to the voltage region where TMR is maximum (V < 100 mV). Figure 5-15 left panel shows the calculated conductance and the corresponding fit used to calculate the barrier parameters [36] in the P configuration (blue line) and AP configuration (black line). Other junctions with lower performance as 3M and 2N give barrier thicknesses of 35 Å and 40 Å respectively. The depressed TMR performance led us to exclude those junctions from the analysis, since they might be affected by pinhole formation, or junction degradation, along the fabrication process.

The use of Jullière formula [37] in terms of currents yields an expression for TMR (see Section 1.3 Eq. (1.13)) as shown in Figure 5-15 right panel, measured at 25 K (black squares) and 60 K (green triangles). TMR from *R(H)* curves at 25 K (red symbols) shows excellent agreement between both approaches, note that *I(V)* curves are nonlinear indicating that the transport is indeed by tunneling (inset in right panel). While a rapid TMR decrease is observed at applied voltage up to 200 mV, TMR measured at 25 K and 60 K remains practically the same at high voltages (200 to 400 mV). A similar TMR drop at low voltage has been reported in MTJs based on manganite electrodes [24, 30], and is believed to be due to magnon excitations at electrode/barrier interfaces [31-34]. However the weak TMR temperature dependence of 3N is against what one would expect from conventional junctions based on complex oxides with insulating barriers which would drop steadily when temperature is increased; this indicates that the induced ferromagnetic state at STO/LMO interface may be connected to the weak temperature dependence of TMR at high applied voltage.

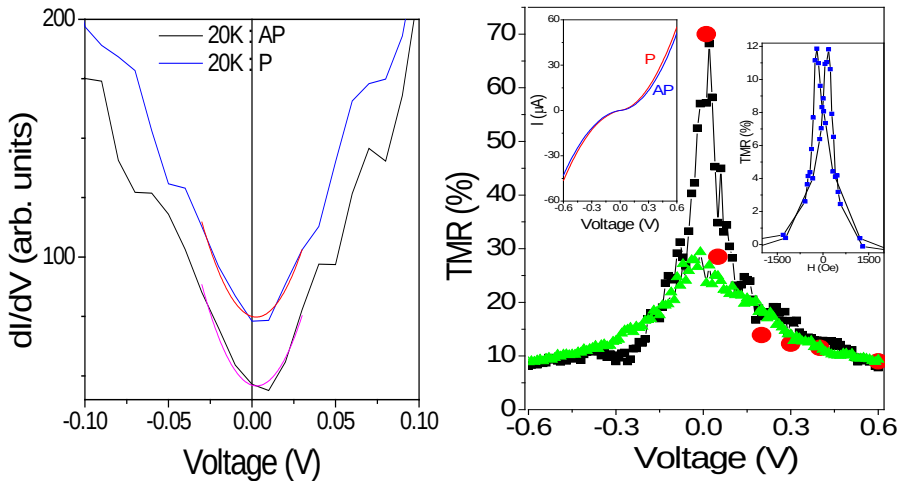

Figure 5-12. Conductance vs. voltage (left) and corresponding fits, (right) TMR vs. applied voltage at 25 K (black symbols) and 60 K (green symbols), the red symbols correspond to *R(H)* measurements, right inset: TMR at 25 K and 300 mV. Left inset: *I(V)* characteristics measured in the P and AP configurations at 25K

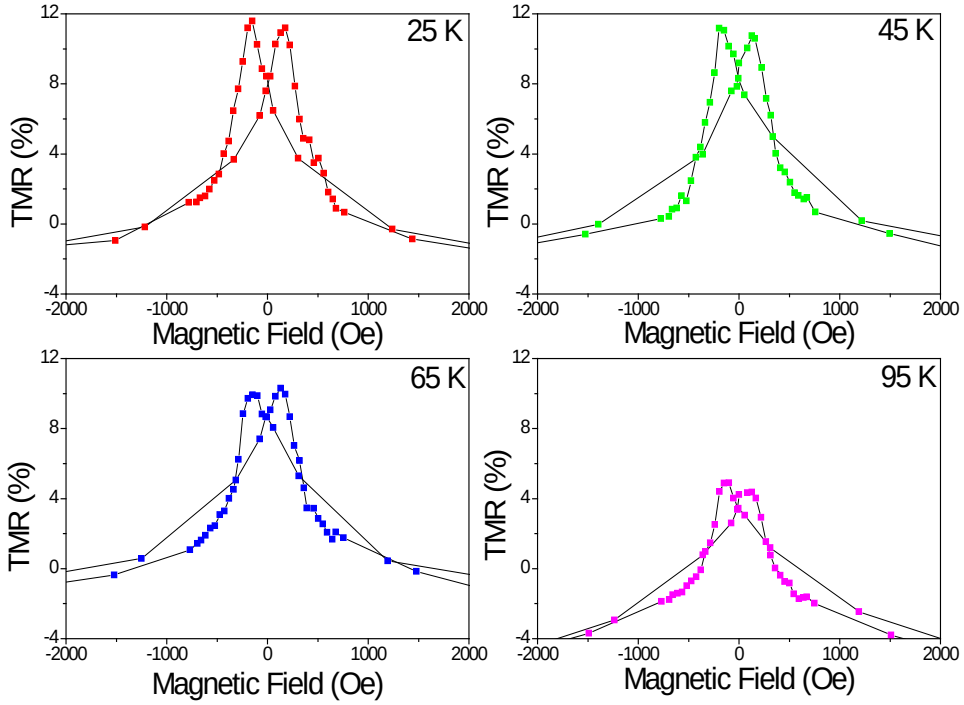

Figure 5-13. TMR vs. magnetic field for QLSLSL2 junction 3N measured at 400 mV and 25 K (red), 45 K (green), 65 K (blue) and 95 K (magenta). Note the relatively large TMR values compared to the AMR contribution measured for bottom electrodes

More details about this smooth TMR decay can be extracted from its temperature dependence measured at different applied voltages; Figure 5-15 shows TMR measured at 400 mV and various temperatures, it is clearly observed how TMR barely changes from 25 K to 65 K. At this point it is important to remark that the resistance change due to magnetization switching to the AP state is not as sharp as observed at low voltage (Figure 5-12), and anisotropic magnetoresistance (AMR) could be assumed as the origin of the resistance change observed at high voltage; however it is a large change (of a few percent) to be explained as due to AMR since *R(H)* curves for the bottom electrodes show very small AMR (less than 0.5 %) as shown in Figure 5-13 right, and the behavior observed in Figure 5-15 is interpreted as mostly due to TMR. Figure 5-16 shows TMR versus temperature recorded at 10 mV (red circles) and at voltages from 200 to 400 mV; whereas 10 mV TMR

decreases rapidly with temperature, high voltage TMR shows a weak temperature dependence. TMR starts to develop at temperatures below the STO/ LMO interface T_C; when temperature is increased above 130 K STO/ LMO interface turns into a paramagnetic state and TMR absence well below the electrodes Curie temperatures may be related to the barrier large thickness.

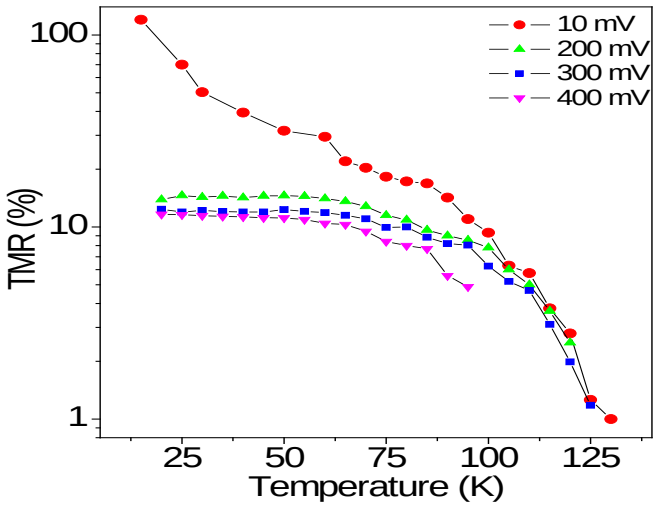

Figure 5-14. ***TMR(T)*** **at 10 mV (red circles), 200 mV (green triangles), 300 mV (blue squares) and 400 mV (magenta triangles)**

Finally it is possible that the ferromagnetic induced state at the barrier may be filtering spins, a detailed study of this artificially induced magnetic interface will be carried out in the future in order to test if it works as a spin filter. The fabrication of a ferromagnetic metal\ engineered interface\ paramagnetic metal heterostructure and further characterization of its structural, magnetic and electrical properties will be carried on. At the present point these results already illustrate how electronic reconstruction phenomena at interfaces between complex oxides may be useful for spintronics devices like MTJs.

5.6 Summary

Engineered STO\ LMO\ STO interfacial state reported by Barriocanal et al. [25] has been used to fabricate MTJs by surrounding it with LSMO electrodes. Structural characterization shows *c*-axis oriented growth with perfect stoichiometry and very accurate rate deposition control; microscopic structural characterization reveals some layer roughness and some defects, accompanied by characteristics as continuous and perfectly coherent layers along large lateral distances, without obvious pinholes observable at the electron microscopy characterization. Heterostructure magnetic characterization reveals a magnetic susceptibility feature above 60 K, with the previous studies done at this research group as background [25, 26], the feature is interpreted as the [STO\ LMO\ STO] trilayer Curie temperature. The novel-tunneling-barrier MTJs performance is excellent, yielding TMR values larger than 100 % at low temperature (15 K), a weak TMR temperature dependence was recorded at high applied voltage. These results suggest that this *improved* high voltage spin dependent transport in QLSLSL MTJs is most likely related to the interfacial modified magnetic ground state between LMO and STO.

5.7 References

[1] A. Ohtomo and H. Y. Hwang, Nature 427 (2004) 423.

[2] A. Brinkman, M. Huijben, M. V. Zalk, J. Huijben, U. Zeitler, J. C. Maan, W. G. V. d. Wiel, G. Rijnders, D. H. A. Blank, and H. Hilgenkamp, Nature Materials 6 (2007) 493.

[3] N. Reyren, S. Thiel, A. D. Caviglia, L. F. Kourkoutis, G. Hammerl, C. Richter, C. W. Schenider, T. Koop, A. S. Ruetschi, D. Jaccard, M. Gabay, D. A. Muller, J. M. Triscone, and J. Mannhart, Science 317 (2007) 1196.

[4] A. D. Caviglia, S. Gariglio, N. Reyren, D. Jaccard, T. Schneider, M. Gabay, S. Thiel, G. Hammerl, J. Mannhart, and J. M. Triscone, Nature 456 (2008) 624.

[5] J. H. Park, E. Vescovo, H. J. Kim, C. Kwon, R. Ramesh, and T. Venkatesan, Nature 392 (1998) 794.

[6] M. Bowen, M. Bibes, A. Berthélémy, J.-P. Contour, A. Anane, Y. Lemaître, and A. Fert, Applied Physics Letters 82 (2003) 233.

[7] M. Viret, M. Drouet, J. Nassar, J. P. Contour, C. Fermon, and A. Fert, Europhysics Letters 39 (1997) 545.

[8] V. Garcia, M. Bibes, A. Barthelemy, M. Bowen, E. Jacquet, J. P. Contour, and A. Fert, Physical Review B 69 (2004) 052403.

[9] M.-H. Jo, N. D. Mathur, N. K. Todd, and M. G. Blamire, Physical Review B 61 (2000) R14905

[10] Y. Lu, X. W. Li, G. Q. Gong, G. Xiao, A. Gupta, P. Lecoeur, J. Z. Sun, Y. Y. Wang, and V. P. Dravid, Physical Review B 54 (1996) R8357.

[11] Z. Sefrioui, V. Cros, A. Barthelemy, V. Peña, C. León, J. Santamaría, M. Varela, and S. J. Pennycook, Applied Physics Letters 88 (2006) 022512.

[12] E. Y. Tsymbal, O. N. Mryasov, and P. R. LeClair, Journal of Physics : Condensed Matter 15 (2003) R109.

[13] M. Bibes and A. Barthelemy, IEEE Transactions on Electron Devices 54 (2007) 1003.

[14] B. B. Nelson-Cheeseman, R. V. Chopdekar, L. M. B. Alldredge, J. S. Bettinger, E. Arenholz, and Y. Suzuki, Physical Review B 76 (2007) 220410.

[15] S. Okamoto and A. J. Millis, Nature 428 (2004) 630.

[16] S. Yunoki, A. Moreo, E. Dagotto, S. Okamoto, S. S. Kancharla, and A. Fujimori, Physical Review B 76 (2007) 064532.

[17] B. R. K. Nanda, S. Satpathy, and M. S. Springborg, Physical Review Letters 98 (2007) 216804.

[18] M. J. Calderón, J. Salafranca, and L. Brey, Physical Review B 78 (2008) 024415.

[19] M. Imada, A. Fujimori, and Y. Tokura, Reviews of Modern Physics 70 (1998) 1039

[20] K. H. Ahn, T. Lookman, and A. R. Bishop, Nature 428 (2004) 401

[21] A. Bhattacharya, X. Zhai, M. Warusawithana, J. N. Eckstein, and S. D. Bader, Applied Physics Letters 90 (2007) 222503.

[22] A. Bhattacharya, S. J. May, S. G. E. t. Velthuis, M. Warusawithana, X. Zhai, B. Jiang, J. M. Zuo, M. R. Fitzsimmons, S. D. Bader, and J. N. Eckstein, Physical Review Letters 100 (2008) 257203.

[23] C. Adamo, C. A. Perroni, V. Cataudella, G. d. Filippis, P. Orgiani, and L. Maritato, Physical Review B 79 (2009) 045125.

[24] C. Aruta, C. Adamo, A. Galdi, P. Orgiani, V. Bisogni, N. B. Brookes, J. C. Cezar, P. Thakur, C. A. Perroni, G. d. Filippis, V. Cataudella, D. G. Schlom, L. Maritato, and G. Ghiringhelli, Physical Review B 80 (2009) 140405(R).
[25] J. Garcia-Barriocanal, F. Y. Bruno, A. Rivera-Calzada, Z. Sefrioui, N. M. Nemes, M. Garcia-Hernández, J. Rubio-Zuazo, G. R. Castro, M. Varela, S. J. Pennycook, C. León, and J. Santamaría, Advanced Materials 22 (2010) 627.
[26] J. Garcia-Barriocanal, J. C. Cezar, F. Y. Bruno, P. Thakur, N. B. Brookes, C. Utfeld, A. Rivera-Calzada, S. R. Giblin, J. W. Taylor, J. A. Duffy, S. B. Dugdale, T. Nakamura, K. Kodama, C. Leon, S. Okamoto, and J. Santamaria, Nature Communications (2010)
[27] A. Urushibara, Y. Moritomo, T. Arima, A. Asamitsu, G. Kido, and Y. Tokura, Physical Review B 51 (1995) 14103.
[28] H. Fujishito, M. Ikebe, and Y. Konno, Journal of the Physical Society of Japan 67 (1998) 1799.
[29] E. Dagotto, T. Hotta, and A. Moreo, Physics Reports 344 (2001) 1
[30] C. Aruta, M. Angeloni, G. Balestrino, N. G. Boggio, P. G. Medaglia, A. Tebano, B. Davidson, M. Baldini, D. D. Castro, P. Postorino, P. Dore, A. Sidorenko, G. Allodi, and R. D. Renzi, Journal of Applied Physics 100 (2006) 023910.
[31] J. Töpfer and J. B. Goodenough, Journal of Solid State Chemistry 130 (1997) 117.
[32] J. M. D. Coey and M. Viret, Advances in Physics 48 (1999) 167.
[33] C. Ritter, M. R. Ibarra, J. M. d. Teresa, P. A. Algarabel, C. Marquina, J. Blasco, J. García, S. Oseroff, and S.-W. Cheong, Physical Review B 56 (1997) 8902.
[34] R. Mahendiran, S. K. Tiwary, A. K. Raychaudhuri, T. V. Ramakrishnan, R. Mahesh, N. Rangavittal, and C. N. R. Rao, Physical Review B 53 (1996) 3348.
[35] J. J. Akerman, J. M. Slaughter, R. W. Dave, and I. K. Schuller, Applied Physics Letters 79 (2001) 3104.
[36] W. F. Brinkman, R. C. Dynes, and J. M. Rowell, Journal of Applied Physics 41 (1970) 1915.
[37] M. Jullière, Physics Letters A 54 (1975) 225

6 ALL-MANGANITE MAGNETIC TUNNEL JUNCTIONS

In previous work by this research group, Sefrioui et al. [1] reported the existence of a bias-dependent tunneling magnetoresistance (TMR) in symmetrical STO\\ $La_{0.7}Ca_{0.3}MnO_3$ (50 nm)\ $La_{0.3}Ca_{0.7}MnO_3$ (1.2 nm)\ $La_{0.7}Ca_{0.3}MnO_3$ (8 nm) magnetic tunnel junctions (MTJs) with a magnetically active interface, measured below and above the induced magnetic transition of the interface. As a further characterization of that system, this thesis includes also the study of asymmetrical Nb-STO\\ $La_{0.3}Ca_{0.7}MnO_3$ (1.2 nm)\ $La_{0.7}Ca_{0.3}MnO_3$ (20 nm) tunnel junctions (SFJs) with only one ferromagnetic electrode, where the spin dependent transport (SDT) characteristics support a spin filtering (SF) behavior with abrupt resistance switching from parallel (P) to antiparallel (AP) magnetic configurations, a monotonic TMR decrease with applied bias is observed. Symmetrical tunnel junctions show the expected crossover from direct tunneling to spin-selective onsets of FN [2] tunneling with increasing voltage. This is due to different barrier heights originated by ferromagnetic exchange splitting in the magnetically induced state at the insulating layer, and the LCMO counter-electrode half-metallic nature. At high temperatures SDT behaves similar to conventional MTJs with paramagnetic tunnel barriers. An exchange splitting estimated value and its temperature dependence are extracted.

6.1 Motivation

Searching for active barriers with novel functionalities in complex oxide magnetic tunnel junctions is a major direction in the design of novel spintronic devices, particularly ferroelectric [3-8], ferromagnetic insulating (FMI) [9-11] or multiferroic [12-16] materials are interesting possibilities as functional barriers; for instance, FMI barriers are promising materials to integrate in MTJs due to their capability to select one spin-polarized carrier type from a nonmagnetic material. Tunneling from a nonmagnetic electrode through a FMI makes a *spin filtering* device, where the SDT may be controlled through tunneling current modulation by the different barrier heights for each spin orientation, originated at the FMI barrier exchange splitting. Most noticeable is the relatively large TMR observed at low temperatures in EuS based MTJs [10, 17]. However, the rapid TMR decrease with temperature due to the very low Eu chalcogenides Curie temperature, together with their low chemical compatibility with other electrodes, limit their practical potential for spin filtering. In this regard, large efforts have been made in using FMI complex oxides with high Curie temperature as new barriers to integrate in MTJs, but the scarce examples of FMI complex oxides based tunnel junctions show a rapid TMR decrease with increasing temperature, vanishing at temperatures well below the bulk FMI barrier Curie temperature [14, 18-20]; thus, the use of *native* FMI complex oxides spacers has remained as a very limited choice and their operation restricted to very low temperatures. An alternative to the use of native FMI barriers is exploiting new artificial magnetic states *induced* at interfaces between non-magnetic and magnetic materials.

Interfaces in complex oxides, whose ground state can be modified by electronic reconstruction, charge transfer and/or charge leakage may act as active barriers and may inspire novel device concepts [21-29]. Tailoring these

interfacial modified electronic structures opens new directions for new active barriers for oxide MTJs design. More specifically, manganites are promising materials for this issue due to their strong intrinsic tendency to change their electronic properties under small perturbations such as strain and / or charge transfer [30-32]. The combined effects between electronic reconstruction and / or charge transfer may also give rise to new and unexpected phases at interfaces between manganites [33]. Recent reports have highlighted the role played by the strong tendency of manganites towards phase separation stabilizing an induced magnetic moment at antiferromagnetic (AFM) manganite / half-metallic ferromagnetic interfaces [34-36]. This artificially modified magnetic ground state is attractive to be used as active interface for new barriers in spintronics systems such as MTJs.

This chapter contains the complementary research work about the role played by the interface in Nb-STO\ $La_{0.3}Ca_{0.7}MnO_3$ (LC7MO)\ $La_{0.7}Ca_{0.3}MnO_3$ (LCMO) SFJs, and the previous results on the STO\\ LCMO\ LC7MO\ LCMO all-manganite MTJs. SFJs exhibit spin filtering effect with a monotonic TMR decrease with applied bias, while MTJs display a complex bias dependence, clearly indicating how spin transport takes place through spin-selective onsets of Fowler-Nordheim [2] tunneling below the interface induced Curie temperature. Although the spin filtering effect is not found in these MTJs above that temperature, the conventional tunnel magnetoresistance is still observed up to the Curie temperature of the ferromagnetic electrodes.

This chapter contains structural, in-plane transport and magnetic properties characterization of unpatterned bilayers with thick LC7MO layer, and an ultrathin FM layer insertion in order to reveal the presence of exchange bias (EB), and next the results of tunneling experiments in two sets of junctions, namely asymmetrical SFJs (metallic substrate\ AFM manganite\ FM-metallic manganite) and symmetrical MTJs (FM-metallic manganite\ AFM manganite\ FM-metallic manganite).

6.2 Sample Growth and Structural Characterization

Films were grown on (100) $SrTiO_3$ (STO) and Nb-doped: SrTiO3 (NSTO) substrates in high-pressure (3.4 mbar) pure oxygen sputtering system at high temperature (900 ºC). This technique provides a very thermalized and ordered growth which allows an accurate layer thickness control. In the trilayer system the bottom electrode was grown thicker (50 nm) than the top electrode (8 nm) in order to ensure different coercivities of both electrodes and to optimize the electrode-junction resistance ratio.

6.2.1 X-ray reflectivity and x-ray diffraction

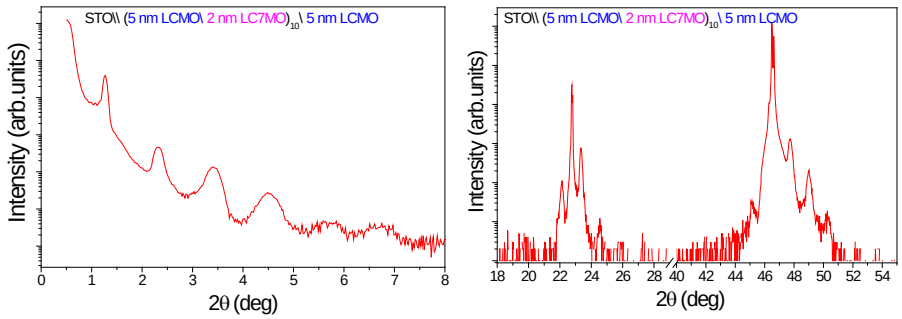

Figure 6-1. X-ray reflectivity (left) and x-ray diffraction (right) of a superlattice

Controlling the barrier thickness is a major issue to face up in growth process, in order to ensure the accurate thickness control in the ultrathin LC7MO layer growth to be used as barrier, superlattices were first grown and characterized by x-ray reflectivity (XRR) and x-ray diffraction (XRD). Figure 6-1 shows the XRR (left) and XRD pattern (right) measured on sample SLFA15 (STO\\ [5 nm LCMO\ 2 nm LC7MO]$_{10}$\ 5 nm LCMO). The modulation length obtained from the X-ray reflectivity is 7.1 nm, in perfect agreement to the nominal modulation length (Figure 6-2). Superlattice satellite peaks in the XRD pattern show high definition, this characteristic indicates a very short

diffraction broadening originated at very flat interfaces in the heterostructure. The corresponding fits (inset in Figure 6-2) result in a modulation length equal to 7.5 nm, evidencing high control over LC7MO and LCMO sputtering deposition rates.

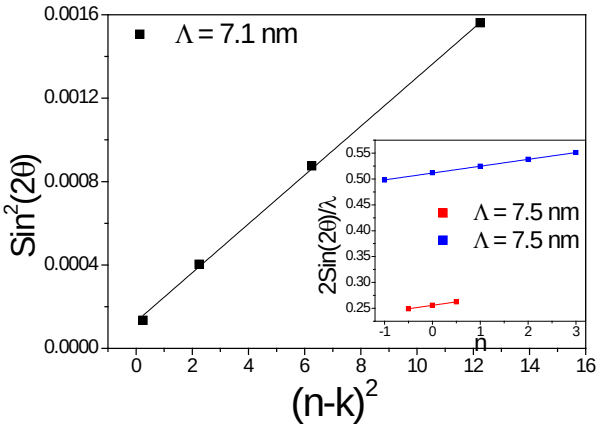

Figure 6-2. XRR peaks fit and (inset) XRD superlattice peaks fits

6.2.2 STEM and EELS characterization

Atomic-scale structural, chemical and electronic properties of the $La_{0.7}Ca_{0.3}MnO_3$ (LCMO) / $La_{0.3}Ca_{0.7}MnO_3$ (LC7MO) interface were characterized by using a NION Ultra-STEM located in Orsay (France), equipped with a tungsten cold field-emission gun and a spherical aberration corrector [37]. The accelerating voltage used for these experiments was 100 keV. The High Angle Annular Dark Field (HAADF) detector had an effective inner collection angle of 70 mrad. A post-column ENFINA Gatan spectrometer was used at an energy dispersion of 0.5 eV per channel in order to collect all the considered core-loss edges simultaneously. Figure 6-3 shows STEM-EELS characterization of a representative STO (001)\\ LCMO (13 nm)\ LC7MO (1.2 nm)\ LCMO (10 nm) trilayer sample. The electron distribution scattered at high angle by the specimen (see the high-angle annular dark-field HAADF image in Figure 6-3 a) is very sensitive to the

average atomic number and the local thickness of the specimen, and reveals the presence of a richer in the light element Ca nanometric layer (darker contrast) with atomic resolution. The energy distribution of electrons transmitted through the cross-section sample (EELS) combined with the spectrum-image technique allows chemical map extraction of La (green) and Mn (red), revealing atomic columns in <100> direction (Figure 6-3 b). The reference theoretical (La, Ca)MnO_3 perovskite structure projected in this direction is represented below the map. Figure 6-3 c shows a La/Ca ratio mapping close to the LC7MO layer collected with a probe step of 0.9 Å. Ca, O, Mn and La elemental profiles extracted using the spectrum-image technique and coupled to the HAADF profile are represented in Figure 6-3 d. As expected from the layers' nominal composition, La/Ca atomic concentration ratio decreases from ≈2 in the electrodes to ≈0.53 in the insulating barrier. Notice also that elemental maps suggest stabilization of a (one unit cell thick) interfacial layer with La/Ca ratio equal to 1. The Mn level remains perfectly stable throughout the structure, whereas a very slight decrease in oxygen (2 %) is visible in the barrier. From different regions analyses, inferred chemical roughness at either interface is rarely more than one atomic step.

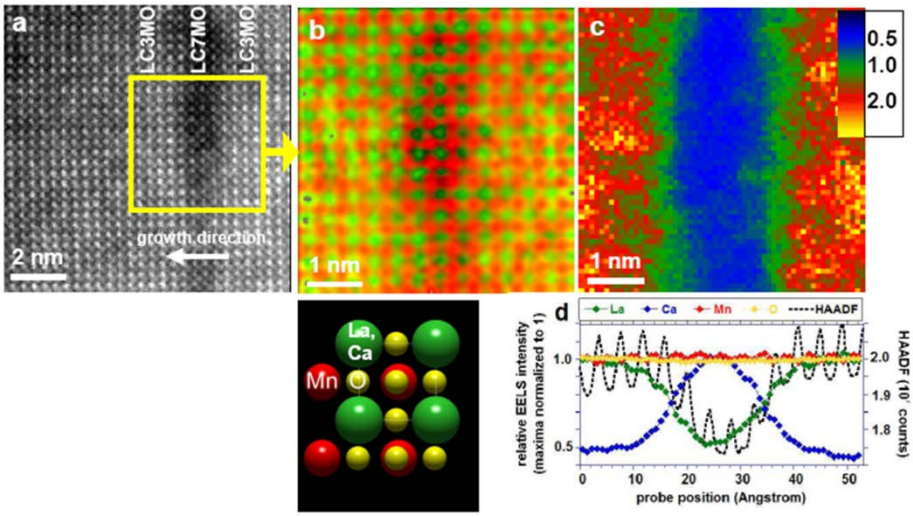

Figure 6-3. TEM and EELS atomic-scale structural and chemical characterization, (a) HAADF USTEM image of a LCMO\ LC7MO\ LCMO interfaces (b) Atomic columns chemical map showing La (green) and Mn (red); the corresponding LCMO projected structure is in the diagram below. (c) La/Ca concentration ratio mapping spectrum image (d) Average EELS intensity profiles corresponding to La, Ca, Mn and O core-loss signals superimposed to the HAADF profile

6.3 Magnetic Characterization

6.3.1 Vibrating sample magnetometry

Figure 6-4 shows typical hysteresis loops measured by a vibrating sample magnetometer (VSM) (red squares) and magnetoresistance (blue circles) measured at 15 K in the current in-plane (CIP) geometry after FC from room temperature with the external magnetic field applied parallel to the in-plane direction in a LC7MO (20 nm)\ LCMO (4 nm) bilayer. It is clear that both curves display a significant shift along the magnetic field axis, evidencing ferromagnetic domains coupling to uncompensated moments at the interface between both materials [38, 39].

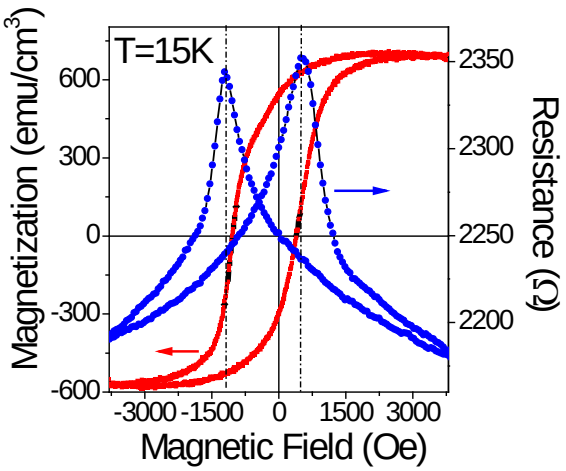

Figure 6-4. Hysteresis loop (red squares) and resistance (red circles) vs. magnetic field for a LC7MO (20 nm)\ LCMO (4 nm) bilayer measured at 15 K after field cooling

Exchange bias (EB) is defined as $H_E = \frac{H_C^L + H_C^R}{2}$, where H_C^L and H_C^R are left and right coercive field respectively, more details on the EB present in $La_{0.7}Ca_{0.3}MnO_3$ / $La_{0.3}Ca_{0.7}MnO_3$ bilayers can be extracted from its temperature dependence. EB as function of temperature is plotted in Figure 6-5 for several bilayers with different thicknesses. As a result EB decreases

with increasing temperature and disappears above 140 K. This behavior is consistent with other conventional EB systems [38] suggesting a Néel temperature about 140 K, which strongly agrees with the bulk $La_{0.3}Ca_{0.7}MnO_3$ (LC7MO) Néel temperature previously reported by Fernández et al. [40]. The observed exchange bias in LCMO/ LC7MO bilayer together with the measured insulating character of a single LC7MO film (not shown) provides strong evidence to support that thick LC7MO layers are indeed AFM insulators.

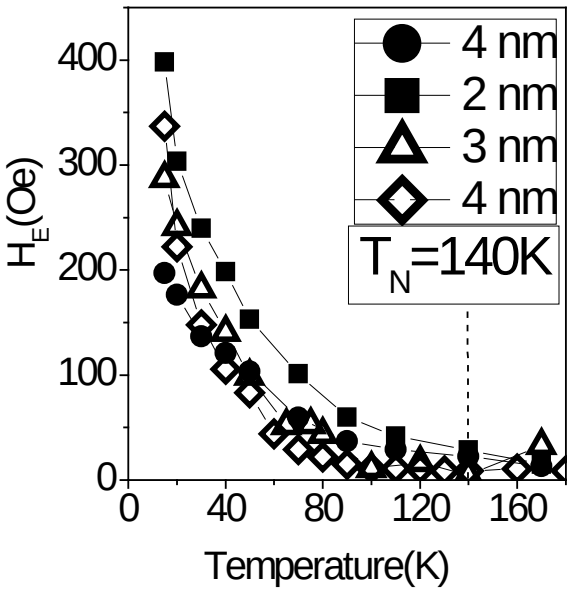

Figure 6-5. Exchange bias as function of temperature for several bilayers. Antiferromagnetic (AF) layer thickness is always 20 nm, and ferromagnetic (F) layer thickness is shown in the legend, open symbols are for STO\\F\AF bilayers, solid symbols are for STO\\B\AF\F bilayers where a buffer LCMO layer (B) is used

6.3.2 Polarized neutron reflectivity

First insights on the LC7MO\ LCMO interfacial magnetic structure were obtained from CRISP time-of-flight neutron reflectometer polarized neutron reflectivity (PNR) experiments at the Rutherford Appleton Laboratory; the studied sample was a [LCMO (7.5 nm)\ LC7MO (1.2 nm)]$_5$\ LCMO (7.5 nm)

superlattice grown on a 1 cm^2 (001)-STO substrate, measurements were carried out at 150 K and 5 K after Zero Field Cooling (ZFC), a saturating field of 3 kOe was applied parallel to the sample surface along the [110] direction as in the TMR experiments. The PNR results are shown in Figure 6-6 at 5 K (left) and 150 K (right).

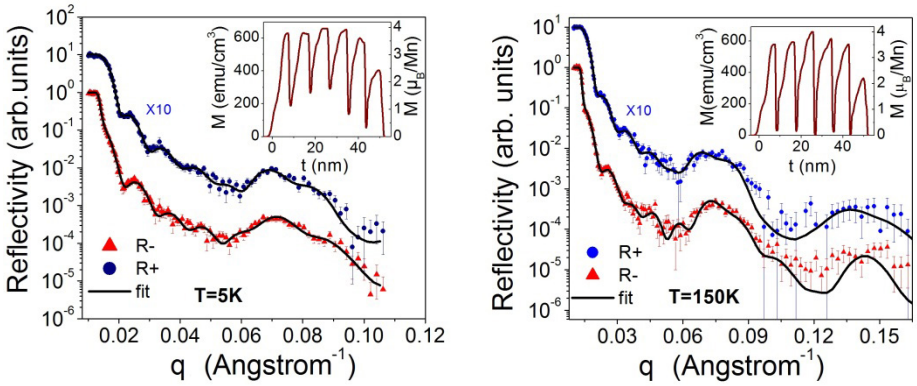

Figure 6-6. PNR data for a [LCMO (7.5 nm)\ LC7MO (1.2 nm)]$_5$\ LCMO (7.5 nm) superlattice at 5 K (left) and 150 K (right). Insets show magnetic profiles deduced from the best fits to experimental data

Measurement at 5 K (Figure 6-6 left) focused on a "*q*" range from 0.01 to 0.1 $Å^{-1}$ to get better statistics around the first Bragg peak, both curves were generated from the two polarized intensities R+ and R-, and the fit results (see inset) show an asymmetric profile in the LCMO layers and a reduced magnetization at the interface with the substrate. Magnetic moment at the LC7MO layers was about 200 emu/cm^3 (~1.3 μ_B/Mn). It is important to note that setting the magnetization to zero inside the LC7MO layers resulted in worse chi-square values and non-realistic magnetic profiles.

At 150 K (Figure 6-6 right) the normal wave vector transfer *q* covered a range from 0.01 to 0.17 $Å^{-1}$, showing two Bragg peaks resulting from the superlattice modulation, the first one is situated around 0.07 $Å^{-1}$, and the second around 0.14 $Å^{-1}$ is barely visible above the instrumental background; data fit results (see inset) show an asymmetric profile in the LCMO where magnetization is enhanced close to the antiferromagnetic layer upper face

and reduced at the bottom side; a ~0.9 nm magnetically dead layer appears at the interface with the substrate, magnetization at this temperature is close to zero in the LC7MO layers.

PNR results support the existence of a ferromagnetic moment in the originally antiferromagnetic insulating barrier, a ferromagnetic insulating phase within the $La_{1-x}Ca_xMnO_3$ phase diagram is only observed at low Ca content ($x \approx 0.10$) [41] which is far from the actual layer compositions; however at manganite interfaces and surfaces different electronic phases (from those of the bulk compounds) may be stabilized [13, 16, 21-23] as a consequence of a subtle competition between kinetic energy (favors ferromagnetism) and localizing interactions (favors antiferromagnetism and insulating behavior). In this case a possible scenario is the ferromagnetic-metallic (FM) electrodes altering the ultrathin LC7MO layer magnetic state, acquiring a finite ferromagnetic moment while keeping its insulating character.

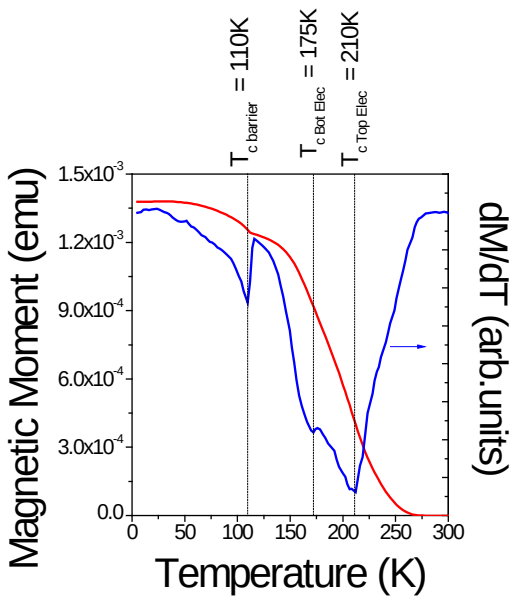

Figure 6-7. M (T) (red curve) and its derivative (blue curve) for a LCMO (50 nm)\ LC7MO (1.2 nm)\ LCMO (8 nm) trilayer

In order to illustrate more clearly the interfacial LC7MO\ LCMO magnetic transition, SQUID magnetization measurements were obtained from a LCMO (65 nm)\ LC7MO (1.2 nm)\ LCMO (10 nm) trilayer. From the magnetization with temperature derivative, three minima are visible (Figure 6-7), the two higher temperatures correspond to the LCMO layers Curie temperatures, which are about 200 K and 175 K for the 65 nm-thick bottom and the 10 nm-thick top layer respectively; a third transition is also present about 110 K, likely corresponding to the barrier induced Curie temperature.

6.4 Spin Dependent Transport Characterization

6.4.1 NSTO\ LC7MO\ LCMO heterostructures

In order to examine the role of interface-induced magnetism on the spin dependent transport (SDT) characteristics, paramagnetic metallic\ FM insulator\ FM metallic structures were studied; a 1%-Nb-doped STO single-crystalline substrate (NSTO) was selected as paramagnetic-metallic, and NSTO\\ LC7MO (1.2 nm)\ LCMO (20nm) bilayers were grown in order to fabricate tunnel junctions. Sample labeled AF20B was used for junction patterning using the four-step process combining optical lithography, Ar plasma etching and reactive ion etching as described in Section 3.5. Electrical measurements were performed in the current-perpendicular-to-plane (CPP) geometry using a two-terminal dc method with the magnetic field applied parallel to the sample (110) in-plane direction.

After field cooling at 4 kOe TMR was measured at fixed temperatures and different applied voltages. Figure 6-8 (left) shows TMR measured at 10 mV as a function of magnetic field for a 9 x 18 μm^2 MTJ at 50 K, and a 6 x 12 μm^2 MTJ (right) measured at 60 K.

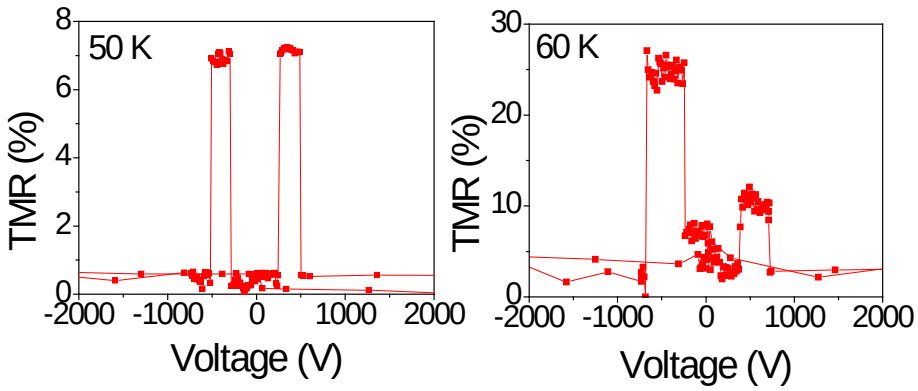

Figure 6-8. TMR versus magnetic field for sample AF20B MTJs 9 x 18 μm^2 (left) and 6 x 12 μm^2 (right) measured at 10 mV

The abrupt resistance switching from P (low resistance) to AP (high resistance) can only be explained under the spin filtering (SF) scenario resulting from the ferromagnetism induced in the nominally antiferromagnetic LC7MO layer; positive TMR values indicate that interface-spin polarization remained positive, acting as electron spin selector.

Bias-dependent TMR measured in the same junction (AF20B/ 9 x 18 μm^2) is shown in Figure 6-9, and monotonic TMR decrease is observed in the whole voltage range instead of the usual Spin Filtering *TMR(V)* bias dependence [42, 43]. Similar TMR TMR decrease with increasing bias is a common characteristic in FM\ I\ FM tunnel junctions and is ascribed to magnon excitations at the electrode-barrier interfaces [44, 45] and has been previously observed in native spin filters based on oxide MTJs [18, 46] and attributed to magnon excitations, and highlighting the importance of the energy dependence of the decay rates for spin-up and spin-down evanescent states when crossing the barrier [20].

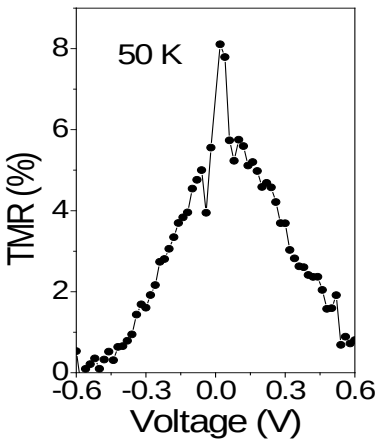

Figure 6-9. *TMR(V)* for AF20B/ 9 x 18 μm^2 MTJ

Interface-induced spin filtering persists up to 130 K (Figure 6-10) vanishing above 140 K, and the same TMR decrease with applied bias is also observed at lower temperatures; it is worth mentioning that additional experiments were carried out on NSTO\\ LCMO (20 nm) junctions (ultrathin nominally-

AFM barrier removed) and the results are the content of Chapter 4: rectifying current-voltage characteristics were observed over a wide temperature range without showing magnetoresistance, indicating typical p-n junctions transport mechanisms [47, 48]; this result also supports the induced-spin filter device intrinsic behavior appearing as a consequence of an induced magnetic moment at LC7MO / LCMO interface.

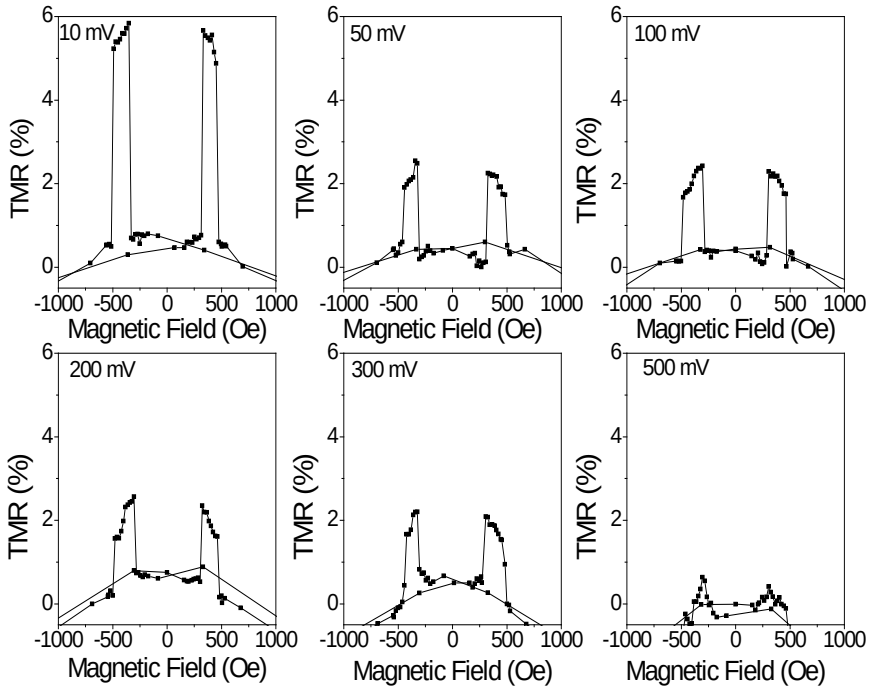

Figure 6-10. TMR measured at 130 K for different applied voltages

6.4.2 LCMO\ LC7MO\ LCMO heterostructures

Junctions were fabricated in trilayer heterostructures in order to enhance the induced spin-filtering device SDT response, where the metallic bottom layer (substrate) was replaced by a FM-metallic LCMO electrode; electrical measurements were carried out with the four-terminal CPP method.

Figure 6-11 left shows TMR curves measured at 35 K under -10 mV (higher TMR), -120 mV and -200 mV (lower TMR) for a STO\\ LCMO (50 nm)\ LC7MO (1.2 nm)\ LCMO (8 nm) tunnel junction (TJ).

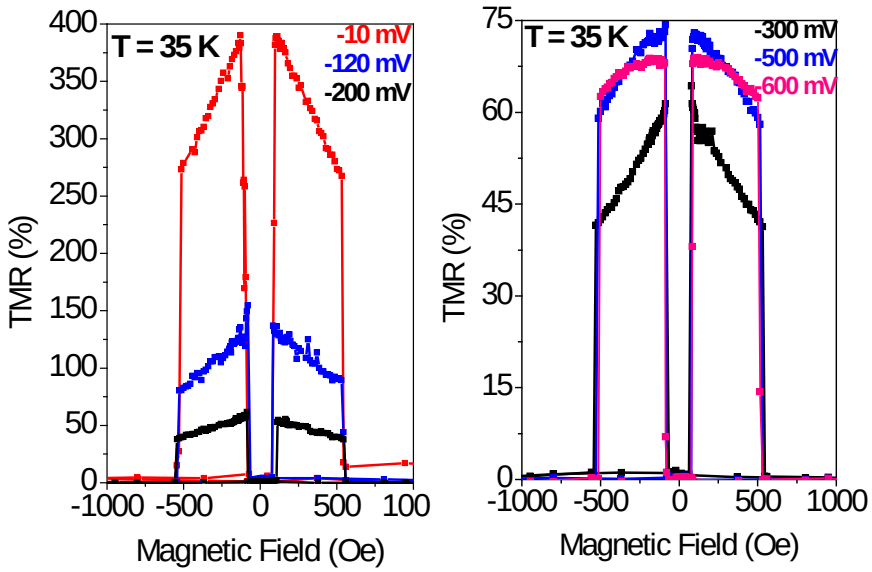

Figure 6-11. TMR for a TJ measured at (right) -10, -120 and -200 mV, and (left) -300, -500 and -600 mV for 35 K

Besides the abrupt resistance switching from parallel (low resistance) to antiparallel (high resistance) state, the high TMR value obtained evidences that the electrodes are indeed highly spin-polarized as expected from their predicted half-metallic nature [48]. TMR displays a monotonic decreasing behavior with applied voltage magnitude increasing up to -200 mV (Figure 6-11 left). Such a low bias TMR decrease has been reported in MTJs based on manganite electrodes [49] and as already noted it is ascribed to magnon excitations at electrode-barrier interfaces [45, 50]. Figure 6-11 right shows a different TMR scenario when voltage is further increased in magnitude beyond -200 mV, TMR exhibits a significant increase as the applied voltage goes to -500 mV and gradually decreases up to -600 mV.

Such enhanced TMR at applied voltages ranging from -200 to -500 mV in MTJs has been confirmed by TMR data extracted from *I(V)* curves in P and AP

magnetic configurations [41]. This TMR increase with applied voltage is in agreement with the spin filtering scenario: the interface between both materials is acting as a spin selective barrier creating an additional tunneling barrier height ($\Phi_{\downarrow}$) for minority spins; according to Nagahama et al. [43] MTJs' TMR based on *pure* spin filtering barriers should increase as the applied bias is increased reaching a maximum when majority spins travel by FN tunneling ($\Phi^{\uparrow} \leq V < \Phi^{\downarrow}$). However, when the FN tunneling is also established in the spin-down channel ($V \geq \Phi^{\downarrow}$) TMR is expected to decrease gradually since the electrode Fermi level exceeds the barrier height for minority spins ($\Phi^{\downarrow}$). TMR measured at temperatures above the interfacial-induced magnetic moment Curie temperature results in a monotonic TMR decrease in the whole voltage range (Figure 6-12). This TMR (V) change with temperature supports the active interface magnetic transition from a ferromagnetic-like (spin filtering) to a non-ferromagnetic tunneling barrier.

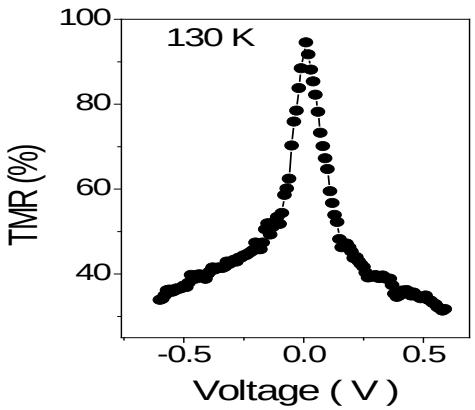

Figure 6-12. TMR Bias dependence at 130 K

Further support for the active interface transition from spin-selective FN to normal tunneling is based on the tunneling conductance G (V), measured below and above the barrier magnetic transition.

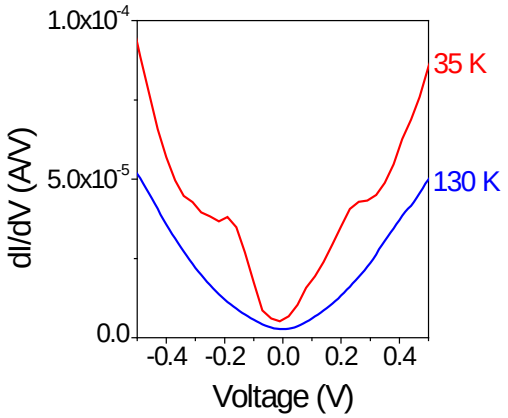

Figure 6-13. Conductance (dI/dV) vs. V at 35 K (red line) and 130 K (blue line) in the antiparallel magnetization state

Figure 6-13 shows *dI/dV(V)* measured at 35 K (red) and 130 K (blue) in the antiparallel magnetization state. As observable from these conductance curves the *dI/dV(V)* shapes at 35 K and 130 K are completely different, indicating that a fundamental change in the spin-transport process has occurred at some temperature between 35 K and 130 K; while the *dI/dV(V)* behavior at 130 K is the expected one for manganite junctions with non-magnetic barriers [51], the *dI/dV(V)* behavior at 35 K is the expected one for spin-filters (with a ferromagnetic barrier) [52], showing two distinct inflection points at intermediate (V ~ 200 mV) and high applied bias (V ~ 400 mV). This *dI/dV(V)* behavior change (when the barrier is ferromagnetic) has been attributed to the spin-selective onsets of FN tunneling due to the different barrier heights originated at the ferromagnetic insulating barrier exchange splitting [52].

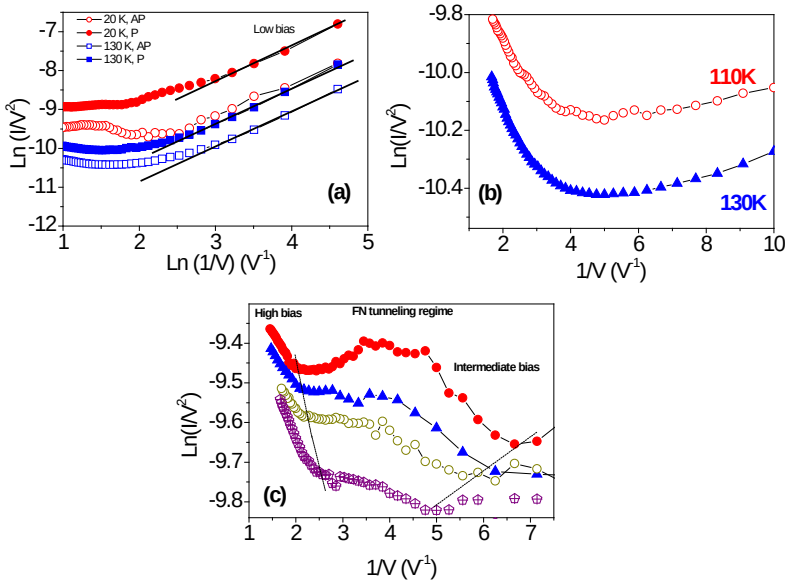

Figure 6-14. (a) *Ln(I/V²)* vs. *Ln(1/V)* at 20 K and 130 K for a STO\\ LCMO (50 nm)\ LC7MO (1.2 nm)\ LCMO (8 nm) tunnel junction, in both P and AP configurations, (b) *Ln(I/V²)* vs. *1/V* at 110 K and 130 K, (c) *Ln(I/V²)* vs. *1/V* at 20, 50, 60 and 70 K in the same tunnel junction

As proposed by Müller and co-workers [52], current-voltage characteristics can be used to extract information about tunneling in the low and high bias regime. Figure 6-14 a shows *Ln(I/V²)* vs. *Ln(1/V)* plot calculated from the *I(V)* at 20 K and 130 K for the same LCMO\ LC7MO\ LCMO junction. This plot reveals two different behaviors, as the bias is increased a clear change in the decaying slopes is observed, indicating two distinct voltage regimes; first the curves for both temperatures (above and below the interface magnetic transition) clearly display a linear behavior at low applied bias, this result supports SDT in terms of direct tunneling (both in P and AP configurations) [52]; second, at high applied voltage the curve shape at 20 K and 130 K is completely different. While a monotonic increase is observed at 110 K and 130 K (Figure 6-14b) a crossover from intermediate to high applied bias is observed when the interface acts as a spin-filter (Figure 6-14c). In this regard it is worth emphasizing that the crossover observed at low temperatures

evidences the spin-selective onsets of FN tunneling with two distinct increased tunneling current corresponding to spin-up and spin-down channels as occurs in native spin filters [52]. At intermediate bias regime the FN tunneling is established in the spin-up channel giving rise to an increase of tunneling current, while upon further raising the bias voltage and when the tunneling electrons' energy exceeds the minority spins barrier height, a further tunnel current increase is also reached (Figure 6-14c). These results evidence spin filtering at high applied bias, and show that spin-selective onsets of FN tunneling are the key ingredient for the enhanced (decreased) TMR at intermediate (high) applied bias occurrence in the trilayer junctions (Figure 6-11 right). However, direct tunneling which occurs at low applied bias seems to give rise to a monotonic decrease of TMR observed in Figure 6-11 left.

Assuming $\Phi^{\uparrow}$ and $\Phi^{\downarrow}$ approximate barrier height values from the two FN tunneling onsets marked by dashed lines in Figure 6-14c, an exchange splitting estimate ($2\Delta E_{ex} = \Phi^{\downarrow} - \Phi^{\uparrow}$) can be extracted. Figure 6-15 shows ΔE_{ex} plotted as a function of temperature, and it is found that ΔE_{ex} rapidly decreases with increasing temperature, and vanishes close to the magnetic interface-induced Curie temperature.

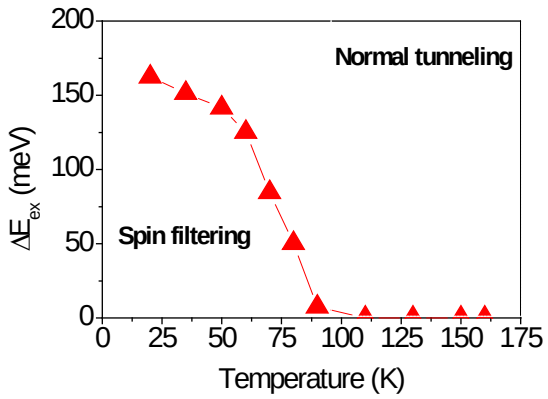

Figure 6-15. Estimated exchange splitting (ΔE_{ex}) as a function of temperature

The ΔE_{ex} decrease with temperature arises as a consequence of the barrier height $\Phi^{\uparrow}$ ($\Phi^{\downarrow}$) increase (decrease) when temperature approaches the interface Curie temperature (T_{CI}) (Figure 6-16). Moreover, an approximate barrier height value at $T > T_{CI}$, Φ_0, can be extracted from direct to FN tunneling crossover, which is about $\Phi_0 \sim 200$ mV (Figure 6-14b and Figure 6-16). Most noticeable, Φ_0 is temperature independent which is typical for tunneling through non-magnetic and insulating barriers.

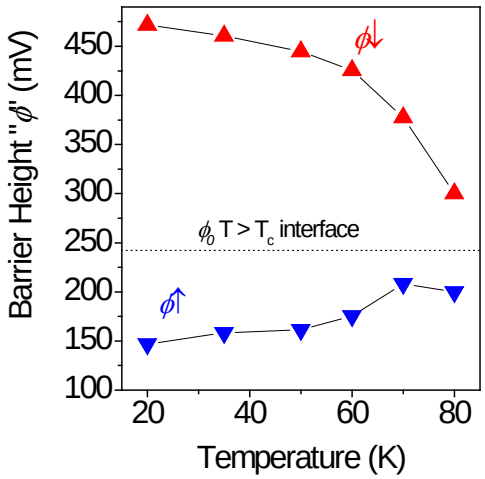

Figure 6-16. Estimated barrier heights $\Phi^{\uparrow}$ (blue) and $\Phi^{\downarrow}$ (red) as a function of temperature

6.5 Summary

In this chapter, interface-induced barrier magnetism in MTJs was investigated. It has been shown how this artificially modified magnetic ground state acts as a spin filter in MTJs and operates at relatively high temperatures. TMR enhancement with applied bias was not observed in asymmetrical SFJs probably due to the dominant magnon excitations [44, 45]. From the analysis proposed by Müller and co-workers [52], it was shown that magnetically active interface SDT at high applied bias in symmetrical MTJs takes place through spin-selective onsets of FN tunneling. While the low bias response is due to direct tunneling, spin-selective onsets of FN tunneling give rise to enhanced TMR with applied bias. Direct tunneling leads to a typical TMR monotonic decrease at low applied voltages. Besides its fundamental interest, artificially manipulating interfacial magnetic ground state may offer the opportunity to extend the range of possibilities in the design of novel spintronic devices with additional functionalities.

6.6 References

[1] Z. Sefrioui, C. Visani, M. J. Calderón, K. March, C. Carrétéro, M. Walls, A. Rivera-Calzada, C. León, R. L. Anton, T. R. Charlton, F. Ott, D. Imhoff, L. Brey, M. Bibes, J. Santamaría, and A. Barthélémy, in 16th International Workshop on Oxide Electronics, ICMAB, Tarragona, Spain, 2009.

[2] R. H. Fowler, F. R. S., and L. Nordheim, Proceedings of the Royal Society A 119 (1928) 173.

[3] S. Mathews, R. Ramesh, T. Venkatesan, and J. Benedetto, Science 276 (1997) 238.

[4] O. Auciello, J. F. Scott, and R. Ramesh, Physics Today 51 (1998) 22.

[5] V. Garcia, M. Bibes, L. Bocher, S. Valencia, F. Kronast, A. Crassous, X. Moya, S. Enouz-Vedrenne, A. Gloter, D. Imhoff, C. Deranlot, N. D. Mathur, S. Fusil, K. Bouzehouane, and A. Barthélémy, Science 327 (2010) 1106.

[6] V. Garcia, S. Fusil, K.Bouzehouane, S. Enouz-Vedrenne, N. D. Mathur, A. Barthélémy, and M. Bibes, Nature 460 (2009) 81.

[7] S. Sahoo, S. Polisetty, C.-G. Duan, S. S. Jaswal, E. Y. Tsymbal, and C. Binek, Physical Review B 76 (2007) 092108.

[8] E. Y. Tsymbal and H. Kohlstedt, Science 313 (2006) 181.

[9] J. S. Moodera, X. Hao, G. A. Gibson, and R. Meservey, Physical Review Letters 61 (1988) 637

[10] J. S. Moodera, T. S. Santos, and T. Nagahama, Journal of Physics : Condensed Matter 19 (2007) 165202.

[11] A. V. Ramos, M.-J. Guittet, J.-B. Moussy, R. Mattana, C. Deranlot, F. Petroff, and C. Gatel, Applied Physics Letters 91 (2007) 122107.

[12] J. Wang, J. B. Neaton, H. Zheng, V. Nagarajan, S. B. Ogale, B. Liu, D. Viehland, V. Vaithyanathan, D. G. Schlom, U. V. Waghmare, N. A. Spaldin, K. M. Rabe, M. Wuttig, and R. Ramesh, Science 299 (2003) 1719.

[13] W. Eerenstein, N. D. Mathur, and J. F. Scott, Nature 442 (2006) 759.

[14] M. Gajek, M. Bibes, S. Fusil, K. Bouzehouane, J. Fontcuberta, A. Barthélémy, and A. Fert, Nature Materials 6 (2007) 296.

[15] T. Kimura, T. Goto, H. Shintani, K. Ishizaka, T. Arima, and Y. Tokura, Nature 426 (2003) 55.

[16] N. Hur, S. Park, P. A. Sharma, J. S. Ahn, S. Guha, and S.-W. Cheong, Nature 429 (2004) 392.

[17] P. LeClair, J. K. Ha, H. J. M. Swagten, J. T. Kohlhepp, C. H. v. d. Vin, and W. J. M. d. Jonge, Applied Physics Letters 80 (2002) 625.

[18] M. Gajek, M. Bibes, A. Barthélémy, K.Bouzehouane, S. Fusil, M. Varela, J. Foncuberta, and A. Fert, Physical Review B 72 (2005) 020406(R).

[19] U. Lüders, A. Barthélèmy, M. Bibes, K. Bouzehouane, S. Fusil, E. Jacquet, J. P. Contour, J. F. Bobo, J. Foncuberta, and A. Fert, Advanced Materials 18 (2006) 1733.

[20] U. Lüders, M. Bibes, K. Bouzehouane, E. Jacquet, J. P. Contour, S. Fusil, J. F. Bobo, J. Foncuberta, A. Barthélèmy, and A. Fert, Applied Physics Letters 88 (2006) 082505.

[21] A. Ohtomo and H. Y. Hwang, Nature 427 (2004) 423.

[22] A. Brinkman, M. Huijben, M. V. Zalk, J. Huijben, U. Zeitler, J. C. Maan, W. G. V. d. Wiel, G. Rijnders, D. H. A. Blank, and H. Hilgenkamp, Nature Materials 6 (2007) 493.
[23] N. Reyren, S. Thiel, A. D. Caviglia, L. F. Kourkoutis, G. Hammerl, C. Richter, C. W. Schenider, T. Koop, A. S. Ruetschi, D. Jaccard, M. Gabay, D. A. Muller, J. M. Triscone, and J. Mannhart, Science 317 (2007) 1196.
[24] A. D. Caviglia, S. Gariglio, N. Reyren, D. Jaccard, T. Schneider, M. Gabay, S. Thiel, G. Hammerl, J. Mannhart, and J. M. Triscone, Nature 456 (2008) 624.
[25] S. Okamoto and A. J. Millis, Nature 428 (2004) 630.
[26] S. Smadici, P. Abbamonte, A. Bhattacharya, X. Zhai, B. Jiang, A. Rusydi, J. N. Eckstein, S. D. Bader, and J.-M. Zuo, Physical Review Letters 99 (2007) 196404.
[27] A. Ohtomo, D. A. Muller, J. L. Grazul, and H. Y. Hwang, Nature 419 (2002) 378.
[28] J. Garcia-Barriocanal, F. Y. Bruno, A. Rivera-Calzada, Z. Sefrioui, N. M. Nemes, M. Garcia-Hernández, J. Rubio-Zuazo, G. R. Castro, M. Varela, S. J. Pennycook, C. León, and J. Santamaría, Advanced Materials 22 (2010) 627.
[29] J. Garcia-Barriocanal, J. C. Cezar, F. Y. Bruno, P. Thakur, N. B. Brookes, C. Utfeld, A. Rivera-Calzada, S. R. Giblin, J. W. Taylor, J. A. Duffy, S. B. Dugdale, T. Nakamura, K. Kodama, C. Leon, S. Okamoto, and J. Santamaria, Nature Communications (2010)
[30] E. Dagotto, T. Hotta, and A. Moreo, Physics Reports 344 (2001) 1
[31] M. Imada, A. Fujimori, and Y. Tokura, Reviews of Modern Physics 70 (1998) 1039
[32] K. H. Ahn, T. Lookman, and A. R. Bishop, Nature 428 (2004) 401
[33] M. J. Calderón, J. Salafranca, and L. Brey, Physical Review B 78 (2008) 024415.
[34] S. Yunoki, A. Moreo, E. Dagotto, S. Okamoto, S. S. Kancharla, and A. Fujimori, Physical Review B 76 (2007) 064532.
[35] D. Niebieskikwiat, L. E. Hueso, J. A. Borchers, N. D. Mathur, and M. B. Salamon, Physical Review Letters 99 (2007) 247207.
[36] J. Salafranca, M. J. Calderón, and L. Brey, Physical Review B 77 (2007) 014441.
[37] P. W. Hawkes, Biology of the Cell 93 (2001) 432.
[38] J. Nogués and I. K. Schuller, Journal of Magnetism and Magnetic Materials 192 (1999) 203.
[39] A. L. Kobrinski, A. M. Goldman, M. Varela, and S. J. Pennycook, Physical Review B 79 (2009) 094405.
[40] M. T. Fernández-Díaz, J. L. Martínez, J. M. Alonso, and E. Herrero, Physical Review B 59 (1999) 1277.
[41] Z. Sefrioui, C. Visani, M. J. Calderón, K. March, C. Carrétéro, M. Walls, A. Rivera-Calzada, C. León, R. L. Anton, T. R. Charlton, F. A. Cuéllar, E. Iborra, F. Ott, D. Imhoff, L. Brey, M. Bibes, J. Santamaria, and A. Barthelemy, Advanced Materials 22 (2010) 5029.
[42] A. Saffarzadeh, Journal of Magnetism and Magnetic Materials 269 (2004) 327.
[43] T. Nagahama, T. S. Santos, and J. S. Moodera, Physical Review Letters 99 (2007) 016602.

[44] X.-F. Han, A. C. C. Yu, M. Oogane, J. Murai, T. Daibou, and T. Miyazaki, Physical Review B 63 (2001) 224404.
[45] S. Zhang, P. M. Levy, A. C. Marley, and S. S. P. Parkin, Physical Review Letters 79 (1997) 3744.
[46] U. Lüders, M. Bibes, S. Fusil, K.Bouzehouane, E. Jacquet, C. B. Sommers, J.-P. Contour, J.-F. Bobo, A. Barthélémy, and P. M. Levy, Physical Review B 76 (2007) 134412.
[47] F. Y. Bruno, J. Garcia-Barriocanal, M. Torija, A. Rivera, Z. Sefrioui, C. Leighton, C. Leon, and J. Santamaria, Applied Physics Letters 92 (2008) 082106.
[48] A. Yamamoto, A. Sawa, H. Akoh, M. Kawasaki, and Y. Tokura, Applied Physics Letters 90 (2007) 112104.
[49] M. Bowen, A. Barthelemy, M. Bibes, E. Jacquet, J. P. Contour, A. Fert, F. Ciccacci, L. Dùo, and R. Bertacco, Physical Review Letters 95 (2005) 137203.
[50] E. Y. Tsymbal, O. N. Mryasov, and P. R. LeClair, Journal of Physics : Condensed Matter 15 (2003) R109.
[51] M.-H. Jo, N. D. Mathur, N. K. Todd, and M. G. Blamire, Physical Review B 61 (2000) R14905
[52] M. Müller, G.-X. Miao, and J. S. Moodera, Europhysics Letters 88 (2009) 47006.

7 MANGANITE - CUPRATE MAGNETIC TUNNEL JUNCTIONS

This chapter contains the study of $PrBa_2Cu_3O_7$ (PBCO) as a barrier sandwiched between $La_{0.7}Ca_{0.3}MnO_3$ (LCMO) electrodes. Fert et al. [1] explored in 1997 the possibility of using PBCO as a barrier material in a magnetic tunnel junction (MTJ), but the mentioned report is mostly centered in the STO-based devices and no further details about PBCO (only that it is a suitable material) as a barrier are reported, probably due to its semiconducting nature making the PBCO-based MTJs TMR performance less attractive if compared to the STO-based MTJs electrical performance.

The study started by sample growth, barrier thickness tuning, and structural characterization by X-ray methods; followed by STEM and EELS structural and chemical characterization. Magnetic characterization by VSM and PNR reveal magnetocrystalline anisotropies in an unexpected configuration. Spin dependent transport characteristics exhibited anomalous low temperature TMR suppression; a non-conventional high field TMR contribution which is explained in basis of the different biaxial anisotropy corresponding to each electrode layer; and a negative-like TMR contribution explained in the basis of the anisotropy and the interfacial magnetism present at manganite-cuprate interfaces.

7.1 Motivation

Since the discovery of high-T_C superconductivity in $YBa_2Cu_3O_7$ (YBCO), this so-called 1:2:3 compound has been extensively investigated; when discussing the role of magnetism in this system two different effects shall be distinguished: first, superconductivity is suppressed by a few mole percent Cu substitution by magnetic *3d* elements like Fe or Ni, and the suppression scales can be explained by the Abrikosov - Gor'kov theory [2] in which superconductivity is suppressed by spin-exchange scattering at a few mole percent of magnetic impurities; second, the complete substitution of Y by magnetic rare-earth elements do not affect the superconductivity significantly [3] and T_C may even be increased. At low temperatures rare-earth ions magnetic order and superconductivity coexist, this coexistence of magnetism and superconductivity can be understood as two almost decoupled electronic subsystems, which are spatially separated in these layered structures of the 1:2:3 systems. It would be expected that $PrBa_2Cu_3O_7$ (PBCO) had T_C = 97 K and $T_N \leq$ 0.5 K, however the Pr 1:2:3 system does not become superconducting at all, it behaves as a semiconductor. Lots of efforts were put in order to explain the superconductivity suppression in PBCO [4-9].

Very recent studies [10-12] focus on the manganite-cuprate interface, mainly in the case of LCMO and high-*Tc* superconducting cuprate $YBa_2Cu_3O_7$ (YBCO). Among these works, the contribution by Chakhalian et al. has a particular relevance since it demonstrates the role played by orbital hybridization at the (LCMO-YBCO) manganite – cuprate interface. By using x-ray linear dichroism in fluorescence yield mode (FY), the absorption spectra near the Cu L_3-edge the $2p^6 3d^9 \rightarrow 2p^5 3d^{10}$ transition was found for Cu and the oxygen ligand, but with a slight energy shift indicating a change in the Cu valence state for the interface. This constitutes evidence of the expected charge transfer in the cuprate-manganite interface [13] where the YBCO hole density is reduced at the interface. Moreover, the Cu $d_{3z^2-r^2}$

hole occupation is at least equal to that of the $d_{x^2-y^2}$ orbital corresponding to an orbital reconstruction at the interface. The hybridized orbital at the interface is not subject to the formation of a Zhang-Rice singlet state (localized state which keeps the Cu plane site nominal valence state as 2+ while the hole density in the CuO_2 sheets is tuned by hole doping) [14]. XMCD clearly shows that a hybridized hole is subject to a strong AF exchange coupling which gives rise to an interfacial negative spin polarization at the cuprate side.

The motivation for the experiment described in this chapter is the presence of magnetic moment at the interfacial Cu atoms, which could be used in the LCMO\ PBCO\ LCMO system to yield a new form of magnetic coupling between the electrodes, being mediated by the localized (spin-polarized) Cu electrons in the CuO_2 planes. It is shown in this chapter that such a magnetic coupling indeed exists in the LCMO\ PBCO\ LCMO MTJs, and that this coupling can be modulated with an electric field, which permits changing the electrodes magnetization in absence of an applied magnetic field.

7.2 Sample Growth and X-Ray Characterization

In ultrathin layer growth it is necessary to take into account nucleation-spread effects. In the very early stages of the first and second monolayers the growth rate is not the same as the subsequent layers. Therefore, it is necessary to determine the growth time for the smallest barrier thicknesses. In order to obtain [LCMO\ PBCO\ LCMO] (LPL) trilayers with calibrated barrier thickness, a set of superlattice samples was grown as indicated in Table 7-1. The manganite layers always had the same thickness (9 unit cells) while the cuprate thickness was changed as indicated by the letter "x" in the configuration expressed by:

STO\\ [(9 u.c.) LCMO\ (x u.c.) PBCO]$_6$ \ (9 u.c.) LCMO

Sample Label	Growth Time (s)	PBCO Nominal Thickness (u.c.)
SLLP03	168	2
SLLP05	252	3
SLLP04	336	4
SLLP06	504	6

Table 7-1. Superlattice sample set

All the grown samples were characterized by X-ray diffraction (XRD) and X-ray reflectivity (XRR) techniques, and the obtained spectra were analyzed by using the finite thickness oscillations method (Section 2.1.3) in order to determine the total sample thickness. The Scherrer Coherence Length method (Section 2.1.2) (red lines in left panel of Figure 7-1, calculated "*z*" parameter agrees with a 3 u.c. barrier layer) in order to obtain an approximate PBCO layer thickness measurement. And the superlattice peak method (Section 2.1.4) (satellite peaks indicated around manganite (001) peak in Figure 7-1 left panel) in order to obtain an accurate estimate of PBCO layer thickness. Such an analysis allowed a PBCO growth rate calibration (Figure 7-1 right panel) obtained for the small PBCO thickness range. Note that as expected, the growth rate is linear (not shown) for thicknesses larger than 6 u.c.

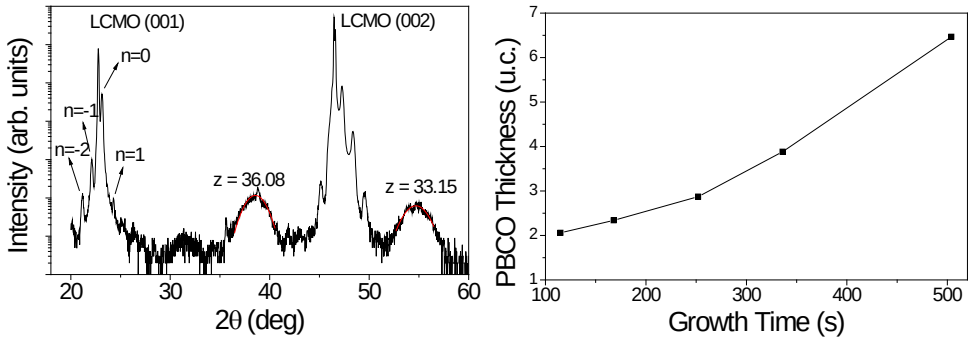

Figure 7-1. (left) X-ray diffraction pattern for a (3 u.c. PBCO) SLLP sample (b) calibrated growth time used for LPL samples

By using the obtained PBCO layer growth rate, a set of trilayer samples (Table 7-2) was grown for the fabrication of MTJs. There are three different bottom electrode thicknesses (15, 20 and 50 nm) with the barrier thicknesses ranging from 1 to 6 unit cells, while the top electrode layer was always kept to 8 nm.

Sample Label	LCMO Thickness (nm)	PBCO Thickness (u.c.)
LPL17	50	5
LPL20	50	5
LPL21	50	5
LPL22	50	6
LPL24	15	1
LPL23	15	2
LPL25	15	3
LPL26	15	4
LPL27	15	5
LPL28	20	1
LPL29	20	2
LPL30	20	3
LPL31	20	4
LPL32	20	5

Table 7-2. LPL sample set

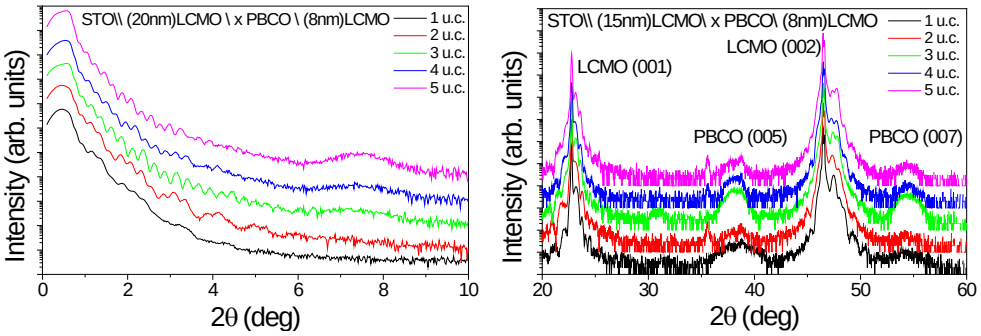

Figure 7-2. (left) X-ray reflectivities for the 20 nm bottom electrode sample set (right) XRD patterns for the 15 nm bottom electrode sample set, peaks labeled (005) and (007) correspond to PBCO

X-ray reflectivities and XRD patterns show the excellent crystalline quality of these samples. X-ray reflectivities (Figure 7-2 left panel) show between 11 (for LPL27 in black line) to 18 (LPL29 in green line) finite thickness oscillations, which is a signature of excellent flatness for long lateral distances. XRD patterns (Figure 7-2 right panel) shows (001) and (002) manganite Bragg peaks besides (005) and (007) Bragg peaks for the cuprate layer. XRR and XRD data are vertically shifted for clarity. As previously observed for superlattices, epitaxial growth is confirmed by these diffraction spectra.

7.3 Microscopy Characterization

7.3.1 STEM and EELS characterization

STEM and EELS measurements were carried out at Oak Ridge National Lab (ORNL) by Maria Varela and Gabriel Sanchez in the Nion Ultra-STEM operated at 100 kV on several LPL samples. As previously found in the YBCO, the CuO_2 chains in PBCO get amorphous when ion etched [15-17], and therefore the STEM sample preparation is a cumbersome process, with an especial difficulty in obtaining representative and measurable samples. Images shown here correspond to sample LPL36B which has the nominal structure:

STO \\ LCMO 15 nm \ PBCO 2 u.c. \ LCMO 8 nm

Figure 7-3. Medium magnification STEM HADF image of LPL36B

Figure 7-3 shows a medium magnification STEM HADF image of LPL36B where the white bar corresponds to a 10 nm length. It can be seen how the layers are continuous, flat and homogeneous, and top and bottom LCMO layers are defect-free. Bottom LCMO layer is very close to the nominal thickness (16.5 nm), and also

top LCMO layer thickness (9 nm). Concerning the PBCO barrier, there are no pinholes observed, and as already mentioned the CuO_2 chains (darker lines at the image) get amorphous at sample preparation and are not observable at TEM. A small waviness is observed probably due to in-plane compressive strain over the ultrathin layer; it has regions with nominal thickness (2 u.c.) and regions where the last Ba plane is not complete, then the observed thickness is lower than the nominal thickness.

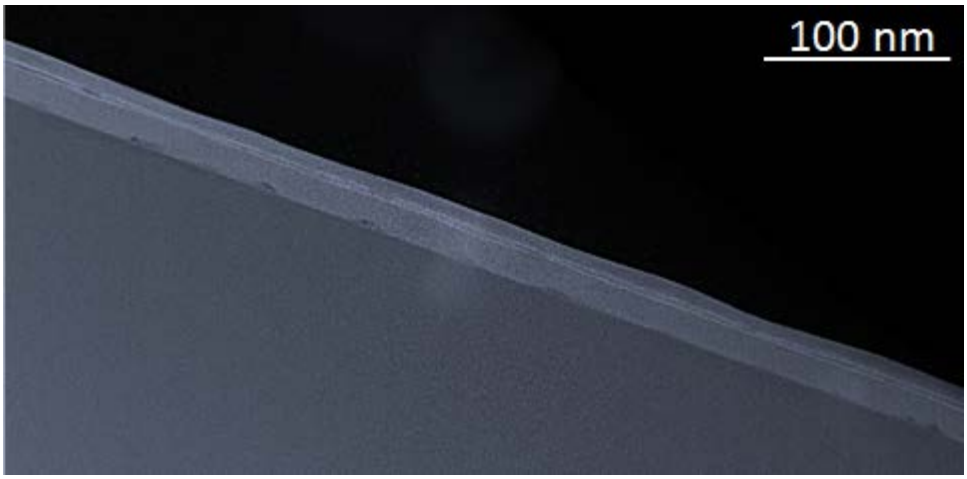

Figure 7-4. Low magnification STEM HADF image of LPL36B

In the low magnification image (Figure 7-4) the white bar corresponds to 100 nm. It can be observed that the bottom LCMO layer is flat, continuous and homogeneous over large lateral distances. Some defects are observed very close to the substrate interface and probably correspond to grain boundaries. The barrier layer has no visible pinholes, although it presents some waviness probably related to in-plane compressive strain, in such a way that the nominal thickness is not perfectly conserved across large lateral distances. The top LCMO layer is continuous, defect free and the observable waviness in the layer surface is inherited from the barrier layer.

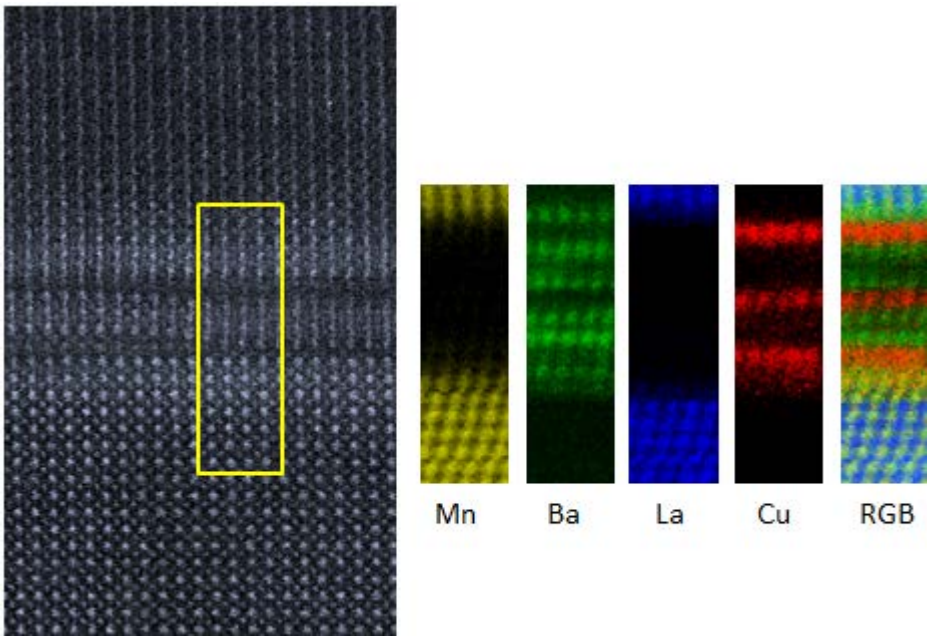

Figure 7-5. EELS analysis, the yellow box at the left image shows the area used for elemental identification, for visualization the elemental maps have been colored and superimposed in the rightmost image

Figure 7-5 shows the two manganite-cuprate interfaces with the top and bottom LCMO layers. The left image shows a high magnification image where the white bar corresponds to 2 nm and the yellow box marks the region of interest used to obtain the chemical maps shown on the right side. The chemical map images are distorted in the lower layer due to sample drift during the spectrum image acquisition. The scan time was 0.05 seconds per pixel resulting in a total time scan time of 3 minutes; in that time window the sample drifted the last minute to a final displacement of 3 angstrom towards left, and the drift presence is corroborated in the leftmost image where no position distortion is observed. Elemental identification images have been colored for interpretation ease (Mn: Yellow, Ba: Green, La: Blue, Cu: Red). It can be seen how the bottom LCMO layer ends in Mn plane and the PBCO layer starts in a Ba plane, which is in agreement to previous observations in cuprate-manganite interfaces [11, 12]. The PBCO barrier ends in a Ba atomic plane followed by a Mn plane. Three CuO planes are observed

corresponding to two PBCO unit cells, and as previously mentioned the CuO_2 chains are not observable due to amorphization. No interdiffusion is observed at the images.

7.3.2 3D reconstructions by confocal microscopy

After having started the MTJ fabrication process (Section 3.5) confocal microscopy was used in order to image the junction's morphology. As shown in Figure 7-6, the junction has a very good shape considering the optical lithography limitations. Figure 7-6 left panel shows a 3D reconstruction of the larger junction (1A : 9 x 18 μm^2) in sample LPL27A. Considering that with the wavelength used in the optical lithography process it is not possible to obtain well defined square corners for such a junction size, the observed "rectangular" shape has the expected characteristics. Figure 7-6 right panel shows the depth profile, where it can be observed that the junction height is in agreement with the nominal one (20 nm bottom electrode \ 5 nm barrier \ 8 nm top electrode = 33 nm height) and its surface roughness is considered good as being around 5 Å. After having demonstrated good junction shape quality, the fabrication process was continued and finished with 11 samples to characterize electrically as explained in Section 2.4.

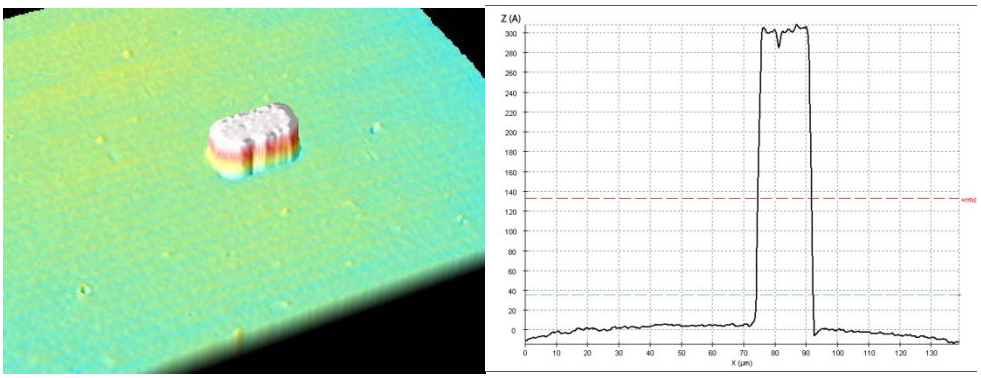

Figure 7-6. 3D confocal microscopy image (left) and depth profile (right) for 1A junction (9x18 μm^2) in sample LPL27A

7.4 VSM and SQUID Magnetic Characterization

VSM and SQUID measurements were done on the sample set with a 15 nm thick bottom electrode and on a sample (LPL22B) with 50 nm thick bottom electrode. These measurements were done with the collaboration of N.M. Nemes and M. García-Hernadez at the ICMM scientific facilities. The sample was mounted with the field applied along the [100] direction.

The samples with thinner bottom electrode exhibit spontaneous magnetization (as shown by the Zero Field Cooling measurement in Figure 7-7 for LPL25B) starting at 150 K in the lowest case (LPL23B) and 168 K in the highest case (LPL27B). While the sample with a thicker bottom electrode (LPL22B) exhibits spontaneous magnetization starting at 205 K. As can be seen the thickest sample exhibits the higher magnetic transition temperature and it is still far from the bulk material Curie temperature (T_C = 250 K), besides their low temperature saturation magnetizations (M_S) are also depressed when compared to the bulk one (LPL25B has almost 300 emu/cm^3 and LPL22B has almost 400 emu/cm^3 while bulk is M_S ~560 emu/cm^3). Although such a magnetic depression is usually explained in the literature by the presence of a "magnetically dead layer" [18], it is known that in this case the origin lies on the strain induced by the substrate lattice parameter on the bottom manganite layer [19, 20], and its effect is more pronounced in the thinnest layer than in the thicker ones. This explains the stronger suppression for the small thickness samples, not so pronounced in the large thickness sample.

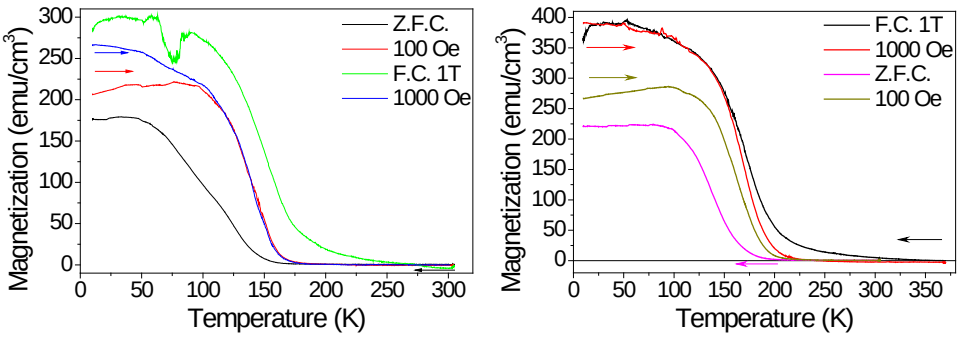

Figure 7-7. *M(T)* measurements on (left) LPL25B and (right) LPL22B

In the low field measurements (ZFC and 100 Oe) there is a positive slope below 100 K where a saturation plateau is expected, such a behavior is explained when considering the layers' anisotropy and is to be discussed at the next section.

The hysteresis loops (Figure 7-8 left) behave as expected showing the already observed M_S at low temperatures (almost 300 emu/cm^3 for LPL25B and almost 400 emu/cm^3 for LPL22B) with coercive fields and M_S decreasing as temperature increases. The hysteresis loops show how the layers are not fully saturated even under the applied field of 1T and, in accordance to the measured *M(T)* above 200 K, there is no magnetic response.

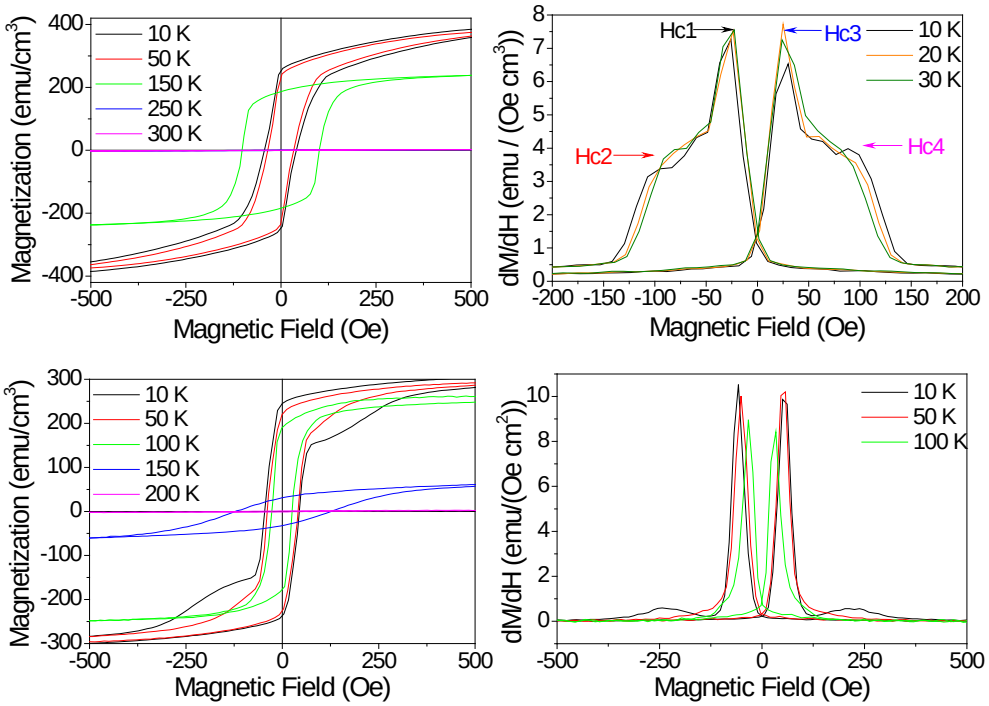

Figure 7-8. (left) Hysteresis loops and (right) their derivatives for (up) LPL22B and (down) LPL25B, LPL27B

The coercive fields here observed will not be the same that in the magneto-transport measurements because of the further modified shapes and sizes. It could be expected to find plateaus in the field values between each layer's switching fields. Although low temperature hysteresis loops present a "bump" that could be interpreted as such, a feature that can be rigorously considered as a signature of

independent switching is not obviously observed. As it is necessary to know if both manganite layers can switch magnetization independently, right panel in Figure 7-8 show the derivatives of the hysteresis loops, where the first layer switching (most probably the bottom electrode) is evidenced at the low field peaks and the independent switching of the second layer (most probably the top electrode) is evidenced at the “bumps” observed at slightly higher field values. Independent switching is not obviously observed in the hysteresis loops because both coercive field values are too close to generate a clear plateau.

7.5 Polarized Neutron Reflectivity

In order to further characterize the ferromagnetic top and bottom layers magnetic structure, PNR and complementary SQUID measurements were carried out by Yaohua Liu and Suzanne G.E. te Velthuis in ASTERIX at Los Alamos Neutron Science Center (LANSCE) in a sample with 15 nm bottom LCMO electrode and 2 u.c. PBCO barrier layer, and a size of 1 x 1 cm^2. Three different temperatures were used for measurements: 5, 50 and 90 K, and the film was field cooled to 5 K in a magnetic field of 5 kOe before data collecting.

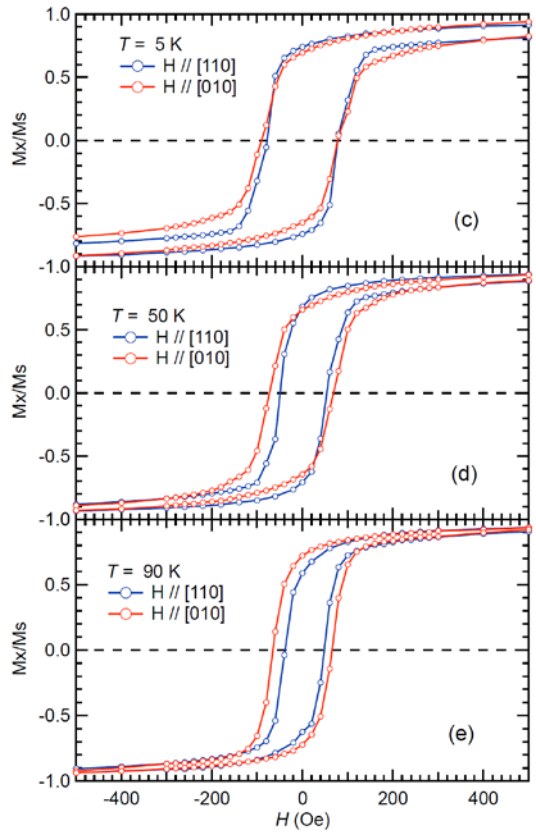

Figure 7-9. Magnetization hysteresis loops along the [110] (blue lines) and [010] (red lines) directions at (c) 5 K, (d) 50 K and (e) 90 K. The maximum applied field was ± 5 kOe

As it can be observed in Figure 7-9 the remanent magnetization $M^R_{[010]} > M^R_{[110]}$ for T > 90 K, however $M^R_{[010]} < M^R_{[110]}$ at 5 K and 50 K; this cannot be explained if both

top and bottom LCMO layers have the same biaxial easy axes along [010] and [100] directions, as initially expected [12, 20]. Liu and Velthuis also measured *M(T)* in a SQUID characterization system applying three different fields (20 Oe, 100 Oe and 5 kOe). It can be seen in Figure 7-10 how $M_{[010]}$ gradually increases for $T > 90$ K at all the three fields, but are almost constant when $T < 90$ K. At low temperatures ($T < 50$ K) $M_{[010]} < M_{[110]}$ for all the three fields.

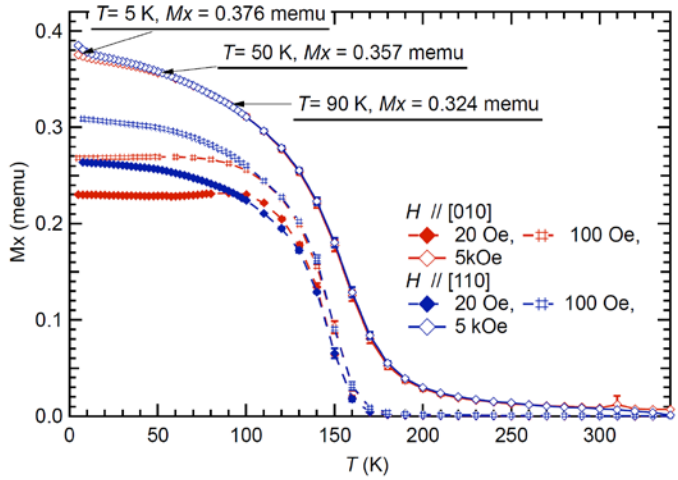

Figure 7-10. Magnetization temperature dependence along [010] and [110] directions under 20 Oe, 100 Oe and 5 kOe annealing fields. The data were collected during cooling

The magnetic characterization data collected suggests that the bottom layer has $T_C \sim 165$ K and the top layer has $T_C \sim 105$ K. In the region $T > 105$ K the magnetization increase when lowering temperature is due to spontaneous magnetization in the bottom LCMO layer. Since $M_{[110]}^{20Oe} < M_{[010]}^{20Oe}$ but $M_{[110]}^{100Oe} > M_{[010]}^{100Oe}$, the bottom LCMO layer with higher T_C has its easy axis along the [010] direction and the anisotropy field is smaller than 100 Oe for $T > 105$ K with respect to the [110] direction. For 50 K < T < 105 K the top LCMO layer contributes dominantly to the magnetization increase, however $M_{[110]}^{20Oe} < M_{[010]}^{20Oe}$ and $M_{[110]}^{100Oe} < M_{[010]}^{100Oe}$ for $T < 90$ K. Then LCMO top layer has its easy axis along the [110] direction and the anisotropy field is much larger than 100 Oe for $T < 90$ K, so that M^{top} at low fields

does not increase as temperature decreases when the field is along the hard axis (the [010] direction); for T < 50 K the top LCMO layer is so hard that 5 kOe field along [010] direction is not able to saturate it completely.

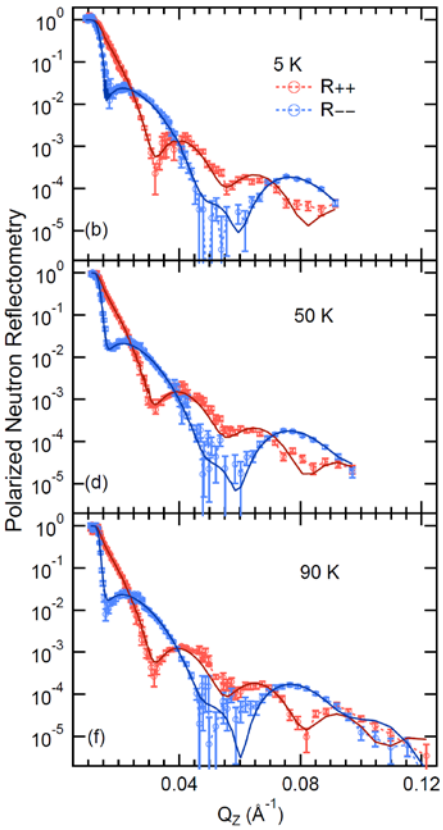

Figure 7-11. Polarized neutron reflectivity at 5 K (upper), 50 K (middle), and 90 K (bottom)

For the neutron reflectivity experiments (Figure 7-11) the field was applied in the [010] direction, and at each temperature $\pm$ 5 kOe fields were used to saturate the film. A 5 kOe field was also applied when changing temperature between measurements. XRR and 5 kOe PNR data at the three temperatures were fitted simultaneously; the model used to fit the data has the same chemical structure, but the magnetic structure is allowed to change between temperatures. The X-ray scattering length density (SLD) and neutron nuclear SLD are linked together via the nominal compositions. The integrated magnetic SLDs are proportional to the magnetizations and constrained to have the same ratio as the magnetization

determined from SQUID magnetometry, as the film is “saturated” at 5 kOe magnetization rotation is not considered. Both the top and bottom LCMO layers are split into two layers to allow the LCMO films at both the top surface and the film/substrate interface have slightly different density to the other parts of the LCMO films [21]. However the magnetizations are constrained to be the same ($M_1^{top} = M_2^{top}$ and $M_{bot}^1 = M_{bot}^2$), leaving then four independent fitting parameters in the current model to describe the magnetic structure at all three temperatures. Three of them are the average magnetic SLDs in the top LCMO layer at 5 K, 50 K and 90 K, and the fourth is the average magnetic SLDs in the bottom LCMO layer at 5 K. The best fit shows that the sample magnetic structure is:

STO\\ (10+2.8) nm LCMO\ 4.2 nm PBCO\ (1.2+5.6) nm LCMO

As shown in Figure 7-12 (b) M_{bot}^{5kOe} keeps increasing as temperature decreases, but M_{top}^{5kOe} shows a maximum at 50 K, this result is consistent if the field direction is along the easy axis of the bottom LCMO layer, but the hard axis of the top LCMO layer. At 5 K, the top LCMO layer magnetocrystalline anisotropy is so high that even a 5 kOe field along the hard axis is not enough to saturate it, which is fully consistent with the SQUID data.

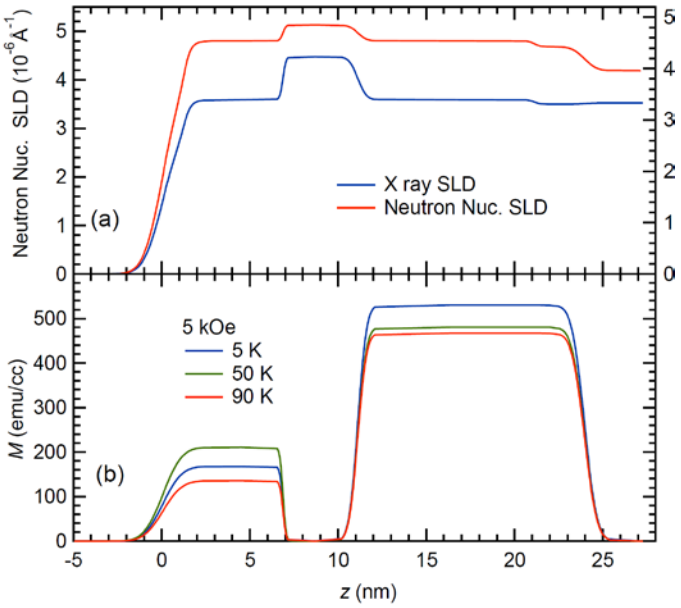

Figure 7-12. (a) Depth profiles of X ray and neutron nuclear SLD (b) Depth profiles of magnetization in a 5 kOe field at 5 K, 50 K and 90 K

The PNR data at low fields show that spin-flip (SF) reflectivity peaks at fields where the spin asymmetry (not shown) changes the sign. Even at these fields the SF reflectivity is only 3% of non-spin-flip (NSF) reflectivity at the critical edge; considering the polarization efficiency of ASTERIX (the average SF ratio is ~ 30) this suggests that there is no significant magnetization rotation during the magnetization switching. The bottom LCMO layer is relatively thicker and has a higher M_S than the top LCMO layer so that its rotation would dominate the SF reflectivity, in contrast with previous PNR studies with 50 nm LCMO bottom layer [12, 22], where the field was along [110] direction and the maximum SF reflectivity at critical edge was 30% of the NSF reflectivity during magnetization switching; the significant difference of the SF reflectivity amplitudes in the PNR experiments is consistent with the bottom LCMO layer easy axis along [100].

Therefore the magnetization switching process is now better understood: the top LCMO layer is very hard at low temperatures (the top layer hard axis is along the [010] direction) and breaks in domains (since they are observable they are small)

domains, the bottom LCMO layer does not break in domains (or they are very large and are thus not observable), and the appearance of “plateaus” in the magnetic hysteresis loops at low temperatures (Figure 7-9 (c)) does not correspond to perfect antiparallel magnetic alignment (AP) states. In fact this is because the bottom LCMO layer hysteresis loop is slanted and its coercivity increases at low temperatures. Well defined AP states were not achieved at 100 Oe in the continuous film for external field along [010].

Strain effect on magnetic anisotropy has been studied by several groups [19, 23-29], and it has been found that epitaxial strain is the major source of the observed anisotropy. The biaxial LCMO strain behaves such that relaxed LCMO layers have [110] easy axis and [100] hard axis, while an in-plane strained layer has [100] easy axis and [110] hard axis; thus the bottom manganite layer (bulk lattice parameter is 3.86 Å) when grown on STO (bulk lattice parameter is 3.905 Å) is [100] strained, and exhibits its magnetic easy axis in that direction, while the top layer has less in-plane compressive strain due to the PBCO (bulk lattice parameter is 3.86 Å) resulting in [110] easy axis biaxial anisotropy.

7.6 Magneto-Transport Characterization

7.6.1 Bottom electrode thickness

An important issue in manganite trilayer junctions is the TMR decay upon temperature increase, as it disappears at the electrode's T_C [22, 30] obtaining electrodes with the highest T_C as possible is a first requirement. In order to increase the success probability of a pinhole-free / defect-free barrier layer growth, it needs to be grown on the flattest possible surface, and as the perfect desirable "integer unit cell number growth" is not the natural objective of growth dynamics [31], the use of the thinnest as possible thicknesses is one of the requirements to increase the success probability in the whole fabrication process. Having all of these ideas into consideration it is necessary to find the lower thickness limit for the manganite being metallic, ferromagnetic and with the highest T_C as possible, to be used as bottom electrode.

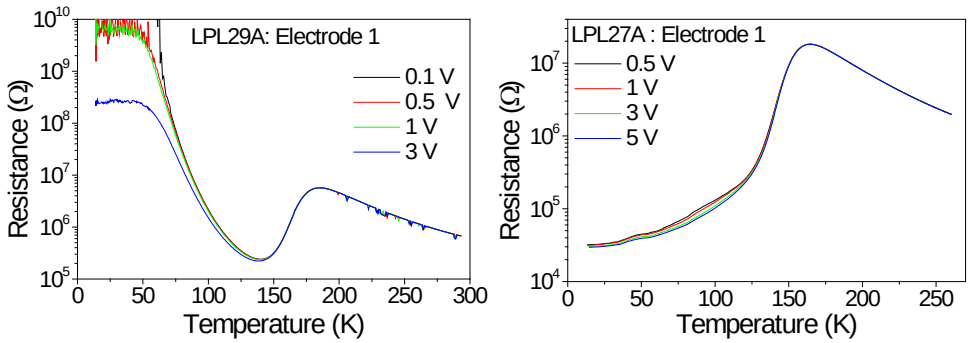

Figure 7-13. (left) non-metallic *R(T)* measured on LPL29A electrode 1, (right) metallic *R(T)* measured on LPL27A electrode 1

Its tendency to phase-separation is one of the reasons why LCMO has been so widely studied [32-35]. After the first and second Ar+ plasma etching steps (MTJ fabrication is described in Section 3.5) there is a probability of having damaged the bottom LCMO layer. As the plasma etching process removes in first instance the lightest atoms, oxygen is the first element to be removed from LCMO, and it is expected that all of the etched LCMO areas may have a deoxygenated surface,

leaving a LCMO layer whose total thickness is not equal to the fully-oxygenated layer, and thus fully metallic-ferromagnetic manganite thickness. Then three different bottom electrode thicknesses were studied by measuring their transport characteristics in the two-wire configuration. With the metallic behavior as a linear *I(V)* and a decreasing resistance when lowering temperature (see Figure 7-13 right panel), and considering the presence of nonlinear *I(V)* and/or increasing resistance when lowering temperature as a non-metallic behavior (see Figure 7-13 left panel), 53 % of the 15 nm electrodes were metallic, 67 % of the 20 nm electrodes were metallic and 100% of the 50 nm electrodes were metallic. Only metallic electrodes were used to measure MTJs, those junctions placed above non-metallic electrodes were not measured because any MTJ transport phenomena found would be influenced by the bottom electrode non-linear characteristics.

The several orders in magnitude resistance change is one of the LCMO's most attractive characteristics [36], the peak electrode resistance (near the MIT temperature) was never lower than 1 MΩ (Figure 7-13 right panel) for the 15 nm and the 20 nm sample sets, the peak resistance for the 50 nm electrode was 0.1 MΩ at the MIT. Junctions with lower resistance were found, as a clear indication of short circuit at the barrier, and they all showed nonmagnetic dependent transport except for the CMR [33] effect.

According to Section 2.4.2, the electrode resistance can lead to an erroneous determination of the junction resistance if the wrong configuration measurement is used, and this fact was always considered in the measurements. Among the three studied electrode thicknesses the best one to be used for bottom electrode is 50 nm due to the lower resistance and the higher success rate in obtaining patterned metallic bottom electrodes; however the 15 nm bottom electrode sample set had more working junctions than the 20 nm, and those two more than the 50 nm (see Table 7-2 and Table 7-3), in agreement to the initial guess about the bottom layer thickness effect on the MTJ fabrication success rate.

A great impact on the device performance is related to the magnetocrystalline anisotropy. As shown in the PNR study (previous Section) the thin electrode samples have different biaxial anisotropies for the top and bottom layers, which is in agreement to previous studies where the film thickness has an important role to play via the layer strain [12].

7.6.2 Magnetocrystalline anisotropy and TMR

The presence of the different top and bottom layer magnetocrystalline anisotropies means that perfect antiparallel magnetic alignment cannot be achieved, which may lead to no TMR observation. Despite of the difference in the layer anisotropies TMR was measured for several junctions and Table 7-3 lists all MTJs showing TMR with applied field along [100] , separated in sample sets.

Sample	Barrier Thickness (unit cells)	Junction	Area (μm^2)
15 nm Bottom Electrode			
LPL23A	2	1E	6 x 12
LPL25A	3	1B	9 x 18
LPL25A	3	1I	5 x 10
LPL26A	4	1B	9 x 18
LPL26A	4	1C	7 x 14
LPL26A	4	1G	6 x 12
LPL27A	5	1M	4 x 8
20 nm Bottom Electrode			
LPL28A	1	1B	9 x 18
LPL28A	1	1K	4 x 8
LPL31A	4	1A	9 x 18
LPL31A	4	1C	7 x 14
50 nm Bottom Electrode			
LPL22A	6	1M	4 x 4

Table 7-3. Measured junctions showing TMR

The 15 nm sample set exhibited TMR at high temperature (T ~100 K), the 20 nm sample set exhibited TMR in the temperature range from 20 K to 80 K mostly, and the MTJ from the 50 nm bottom layer sample set exhibited TMR in the temperature range between 60 K and 90 K.

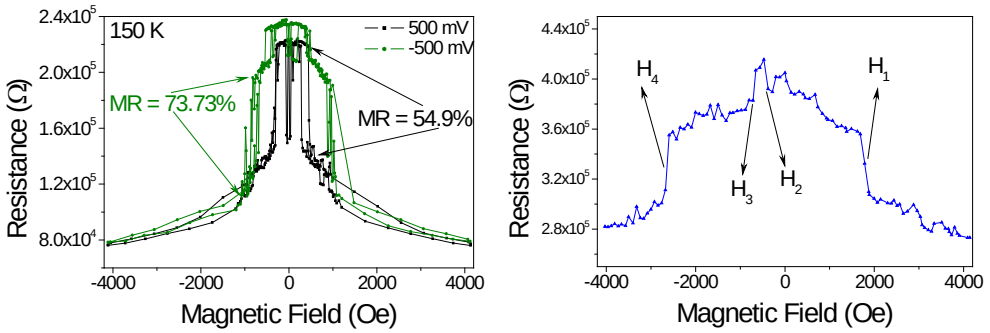

Figure 7-14. Two different TMR contributions measured on (left) LPL25A: 1I at 150 K (right) LPL22A: 2M at 82 K

Figure 7-14 left shows an additional non-conventional TMR on LPL25A junction 1I. Figure 7-14 right shows four resistance changes on the first half *R(H)* loop measured on LPL22A junction 2M, where the changes corresponding to the coercive fields of both magnetic layers (labeled H_2 and H_3) are the conventional TMR, and those changes observed at unusually high field values (labeled H_1 and H_4) are the nonconventional contribution to TMR. This nonconventional TMR was observed in several (but not all) junctions, in some junctions overlaying with conventional TMR and in some junctions without an observable conventional TMR contribution.

The scenario explaining this phenomenon involves the magnetocrystalline anisotropy, layer domain breaking according to the PNR results (top layer breaks in domains while bottom layer does not), and the concept of *tunneling density of states* introduced by Stearns [37] relative to the effective number of electrons which can tunnel from one ferromagnetic metal and the number of effective empty states available in the other ferromagnetic metal.

The tunneling DOS is identified as the Fermi wavevectors of the itinerant electrons with *corresponding spin*; assuming that the conductance is proportional to the DOS of these itinerant electrons the spin polarization for the ferromagnet can be written as

$$P_{FM} = \frac{k^{\uparrow} - k^{\downarrow}}{k^{\uparrow} + k^{\downarrow}} \tag{0.0}$$

Now consider a LCMO layer with its magnetization lying along [110], its number of majority itinerant electrons can be expressed as a superposition of electrons with spins along [100] and spins along [010], then the tunneling DOS corresponding to only spins along [100] has decreased in such a [110] magnetized layer[38].

Figure 7-15 shows a cartoon for a half *R(H)* loop, and the rectangles drawn below it represent the top and bottom layers magnetic configuration where the applied magnetic field lies horizontal and points right when positive. The first magnetic configuration (A) corresponds to the saturation field range: (4200 Oe > *H* > 1100 Oe) and the tunneling resistance is low corresponding to the parallel magnetic alignment, when lowering the applied magnetic field (B: 1100 Oe > *H* > -80 Oe) the top layer breaks into domains with magnetizations lying along the biaxial easy axis $[110]$ and $[1\bar{1}0]$, in such a way that any perpendicular magnetization component is zero. The magnetic configuration is stable because there are no uncompensated stray fields since the total layer magnetization lies along [100]. The tunneling DOS for spins pointing along [100] has lowered, and thus the tunneling resistance is higher than that from the saturation configuration. After the applied field changes its direction and the bottom layer coercive field is reached (region C : -80 Oe > *H* > -440 Oe) its magnetization switches towards the opposite direction, then the top layer total magnetization is still positive while the bottom layer magnetization is negative and that higher tunneling resistance corresponds to the antiparallel magnetic alignment.

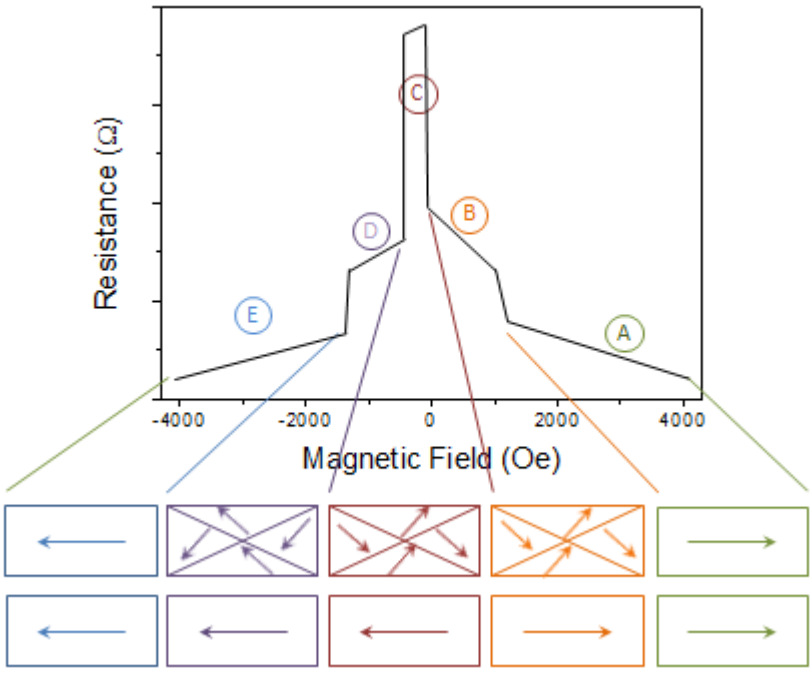

Figure 7-15. Cartoon showing the domain configuration proposed to explain the nonconventional TMR observed at high temperatures

Immediately afterwards, the magnetic field keeps going more negative and the top layer domains switch their magnetizations (D: -440 Oe > *H* > -1300 Oe) still along the easy axis $[\bar{1}10]$ and $[\bar{1}\bar{1}0]$, such that the total layer magnetization is negative and any perpendicular component equals zero, then the tunneling resistance lowers because both total magnetizations are parallel. Finally the magnetic field is strong enough to make the top magnetization lie along its hard axis $[\bar{1}00]$, the top layer total magnetization is higher and its tunneling DOS corresponding to $[\bar{1}00]$ has increased, and then the low tunneling resistance corresponds to the parallel saturation alignment again.

This nonconventional TMR has been observed in rectangular junctions measured with the external field pointing along [100], besides LPL22A junction 2M (square) exhibited nonconventional TMR when measured along [100], and nonconventional

TMR was not observed when measured along [110] (top layer easy axis), in perfect accordance to the anisotropy scenario used to explain the phenomenon.

The number of sizable domains in a 9 x 18 μm^2 or a 4 x 4 μm^2 top electrode is a very relevant question. PNR allows the observation of domain breaking but the only information about domain size is that they are larger than the neutron coherence length. If the LCMO top electrode size is too small to contain several domains then the presented scenario would be not enough to explain the non-conventional TMR observed. Boschker et al. [39] have estimated a manganite thin film domain size of 500 nm. Although Boschker analysis was done for a different facet grown LSMO, the domain size order of magnitude should be similar since the leading phenomena are the same: one is that the magnetism comes from the same Mn ordering and doping under strain effects, and the other is the anisotropy corresponding to the thin film scenario.

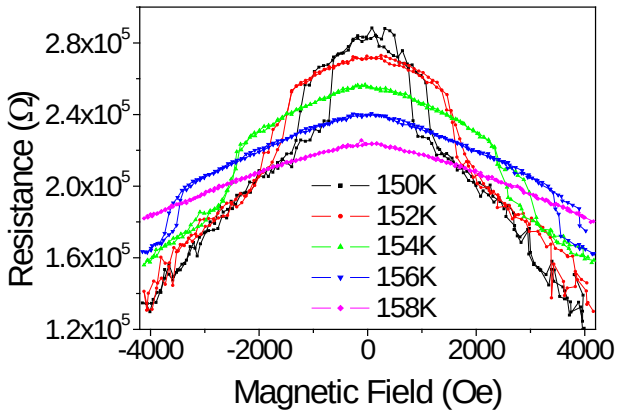

Figure 7-16. R(H) temperature scan on LPL25A junction 1I, the nonconventional switching field increases with temperature

Such a nonconventional contribution to TMR is only observed at high temperatures and as shown in Figure 7-16 the switching field increases with temperature starting 10 K below the MIT temperature, and increases up to the point where it cannot be measured with the available magnetic field.

According to the scenario used to explain the nonconventional TMR, the switching fields H_1 and H_4 correspond to the anisotropy fields with respect to the [100]

direction; in order to understand its behavior with temperature the anisotropy's temperature behavior is taken into account, it is expected that magnetic anisotropy decreases when temperature increases, O'Donnell et al. [26] have reported (among other energies and quantities) $E_{[110]} - E_{[100]}$ anisotropy energy vs. temperature for LCMO thin films; in that work it can be seen how anisotropy decays most strongly when temperature approaches T_C (see Figure 7-17), that behavior explains why nonconventional TMR is observed at such high temperatures, when the magnetocrystalline anisotropy has gone weak the external field is able to orient the top layer magnetization along its hard axis [100], and for lower temperatures it is not possible. Then Figure 7-15 cartoon scenarios "A" and "E" do not happen at low temperatures, and nonconventional TMR is not observed for $T < (T_C - 10\ \text{K})$. The reader might be thinking in the phenomena reported by Singh-Bhalla et al. [40, 41] where manganite phase separation is responsible for observed TMR very similar to the nonconventional TMR here studied, but there are important differences between this study and the reports by Singh-Bhalla et al. which are: (a) its dependence on the relative orientation between external magnetic field and magnetocrystalline anisotropy axes; if the phenomenon here studied would be due to manganite phase separation it would be insensitive to magnetocrystalline anisotropy, then it would be observed whether measuring along the easy or the hard axis or even perpendicular to the film plane (as reported by Singh-Bhalla), which is not this case; and (b) PNR characterization would have shown the presence of both phases, mostly because the PNR experiment was carried out under the same conditions that make nonconventional TMR become observable (external field along [100]).

Figure 7-16 shows how the switching fields H_1 and H_4 increase with temperature, probably because the external field needed to keep the top layer magnetization pointing along the hard axis increases due to the thermal energy "opposition" to the magnetization, thus H_1 and H_4 increase with temperature in such a pronounced way because temperature is very close to T_C and the material magnetization is

almost “insensitive” to the external applied field; or simply the ordered state consistent in all spins pointing along the same direction is unreachable due to the disorder introduced by the thermal energy. The external field necessary to achieve a certain magnetization is higher when temperature increases and this effect is more noticeable when *T* approaches T_C, where the ferromagnetic *M(T)* characteristic has the maximum slope [42].

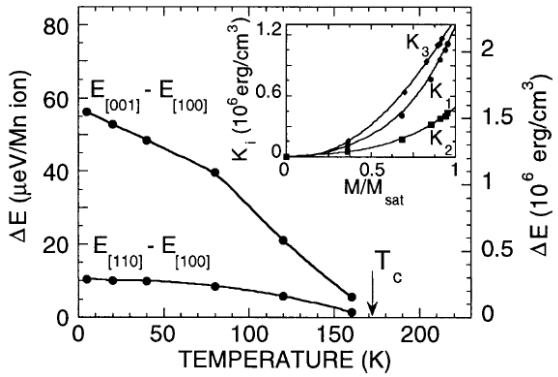

FIG. 2. Demagnetization-corrected anisotropy energies vs temperature. Curves are to guide eye. Inset: anisotropy constants vs magnetization. K_1 data is fit to single-ion theory. K_2 and K_3 curves are to guide eye.

Figure 7-17. LCMO thin film anisotropy energies vs. temperature, figure and caption taken from [26]

Shape anisotropy might play a role as well, but the data collected for this work is not enough to make any conclusion about its possible role.

7.6.3 Barrier characterization

The current density vs. voltage (*J(V)*) measurements can be used to obtain barrier characteristics, the Simons and Brinkman models are explained in Section 1.2; as those models work for low temperature range, the lowest stable temperature obtainable (20 K) is used to measure *I(V)* curves and then *J(V)* is calculated by using the nominal MTJ area. Among the working devices Table 7-4 lists the

obtained barrier characteristics for those samples which were measured at the lowest temperature.

Sample / Junction	Nominal Barrier Thickness (Å)	Brinkman Barrier Thickness (Å)	Brinkman Barrier Height (meV)
20 nm Sample Set			
LPL28A / 1B	11.7	26	760
LPL28A / 1K	11.7	26	580
LPL31A / 1A	46.8	43	93
LPL31A / 1C	46.8	38	140
50 nm Sample Set			
LPL22A / 2M	70.2	59	97

Table 7-4. Barrier characteristics obtained for the measured *J(V)*s at lowest temperature

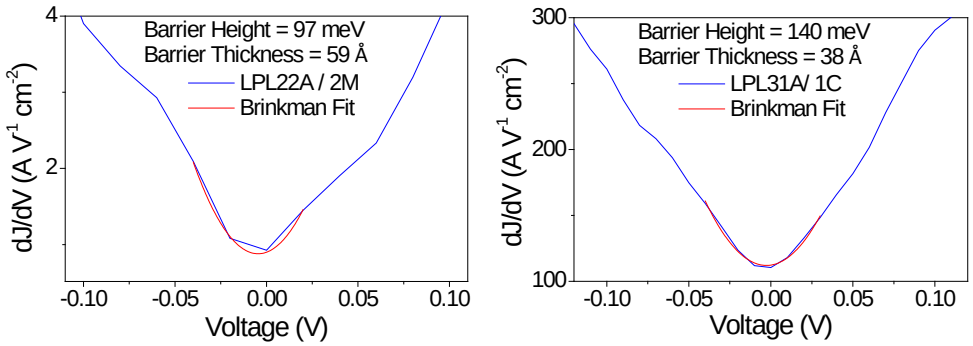

Figure 7-18. *dJ/dV* curves calculated from *I(V)* curves at 20 K and their corresponding Brinkman fits for (left) LPL22A MTJ 2M and (right) LPL31A MTJ 1C

The worst fits are obtained for junctions from sample LPL28A, where the nominal thickness corresponds to 1 u.c. and the two fitted measurements gave a value closer to 2 u.c., on the other hand the other three fitted measurements gave good results in the u.c. orders of magnitude.

7.6.4 TMR temperature and bias dependence

Figure 7-19 shows TMR measured at 100 mV for LPL22A /2M at different temperatures, junction resistance switches sharply from the P to the AP state (and

vice versa), Figure 7-20 shows how at low temperature *TMR(100 mV)* is larger than *TMR(10 mV)*, in striking contrast with previous results on junctions with similar electrodes.

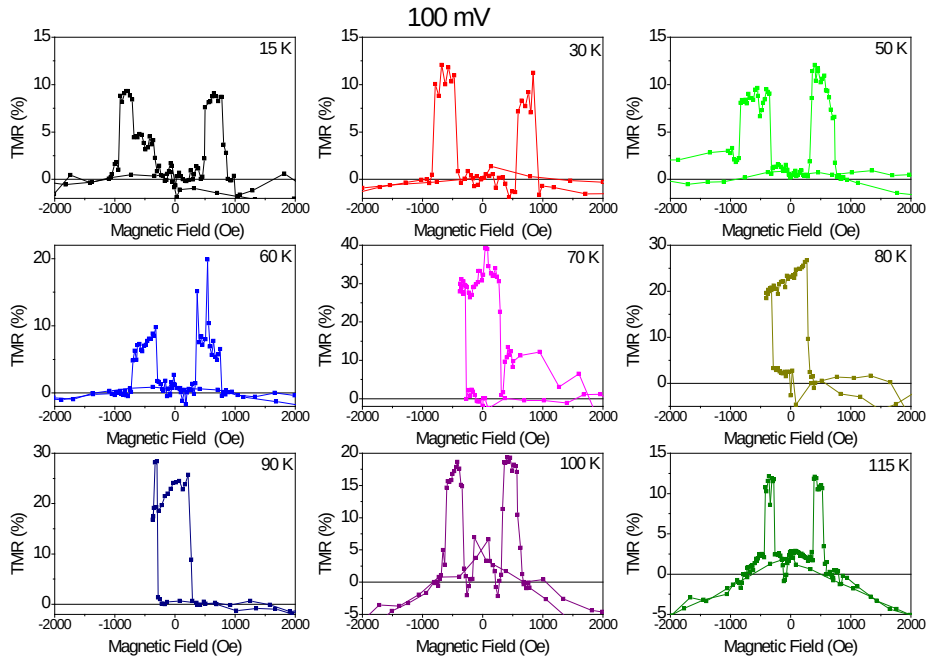

Figure 7-19. TMR for LPL22A/2M junction at 100 mV and temperatures ranging from 15 K to 115 K

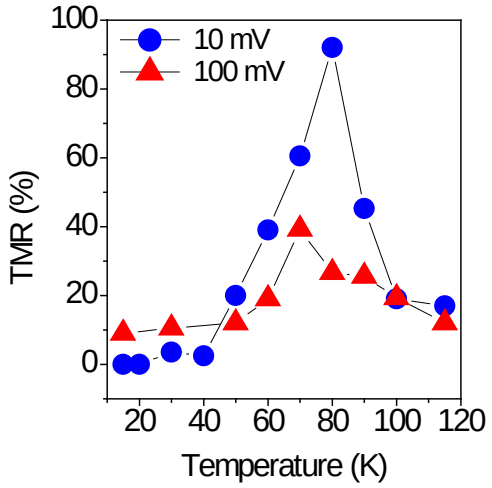

Figure 7-20. TMR vs. temperature for LPL22A/2M junction at 10 mV (blue circles) and 100 mV (red triangles)

To better characterize the spin-dependent transport mechanisms, P and AP states *I(V)* curves where measured (Figure 7-21 left), the *I(V)* curves are non-linear as expected for a tunneling transport mechanism; the current in the P state is always larger than in the AP state resulting in a positive TMR. *TMR(V)* calculated from both *I(V)* curves (Figure 7-21 right) and the *R(H)* data (Figure 7-22) agree well with each other and a practically symmetric dependence is obtained, as expected for MTJs with similar electrodes. At low bias, no TMR was observed, while upon further increasing the bias voltage, the TMR exhibits a significant increase up to ± 100 mV, and finally gradually decreases again for larger voltages. This non-monotonic dependence differs fundamentally from that found in conventional MTJs (TMR progressively decreases over the whole bias range, the observed TMR increase with voltage at low temperatures recalls the behavior of spin filtering junctions) [43].

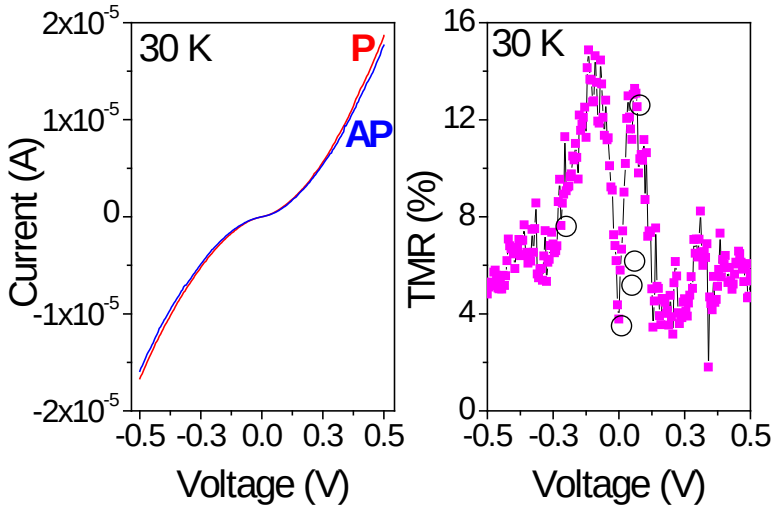

Figure 7-21. (left) *I(V)* measured in the P and AP state at 30 K and (right) *TMR(V)* as calculated from *I(V)* curves (squares) and as obtained from *R(H)* curves (open circles)

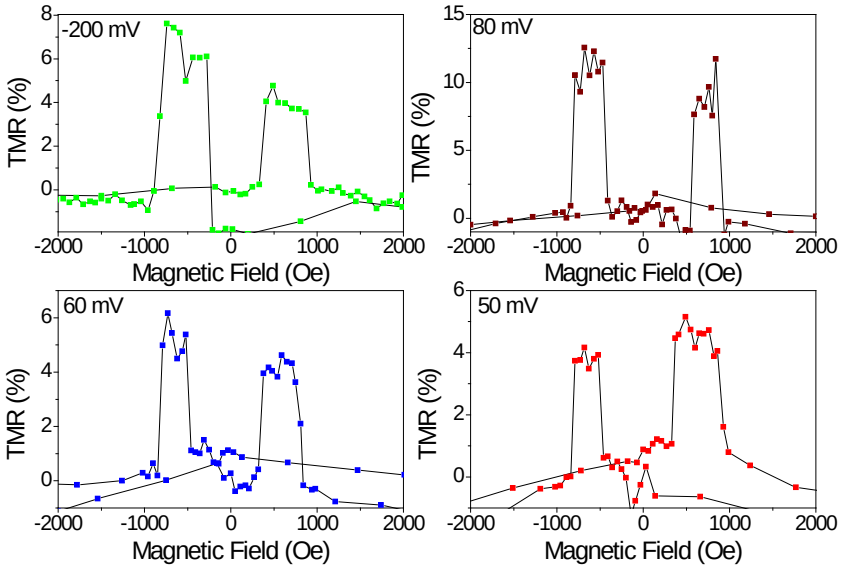

Figure 7-22. TMR for LPL22A/2M junction at different voltages and 30 K

However at temperatures from 50 to 90 K TMR decreases monotonically with increasing voltage (Figure 7-23), as occurs in conventional manganite-based MTJs [44], that behavior is ascribed to magnon excitations induced by the tunneling electrons[45].

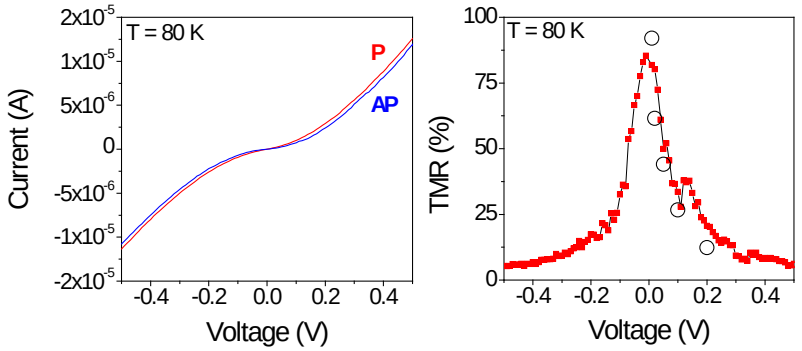

Figure 7-23. (left) *I(V)* curves measured in P and AP state at 80 K and (right) calculated from both *I(V) TMR(V)* (red squares) in accordance with *TMR(V)* from *R(H)* curves (open circles)

7.6.5 Electric field-controlled TMR

A negative-like TMR contribution is observed for temperatures higher than 90 K, in a voltage range that changes with temperature. Figure 7-24 shows the negative-like TMR contribution at 94 K that starts developing at 20 mV and increases in magnitude up to 150 mV; for lower and higher voltages that negative-like TMR contribution is not observed. When increasing temperature (i.e. 100 K) the negative-like TMR contribution appears above 100 mV and TMR is positive for $V <$ 100 mV. Figure 7-25 left shows a *TMR(H)* minor loop measured at 92 K and -20 mV, inset shows the same data in a wider field range; and Figure 7-25 right shows a *TMR(H)* major loop at -150 mV in junction LPL22A/2M; it is clear that the junction resistance steeply increases in high field values up to the high resistance state (HR), then sharply switches to the low resistance state (LR) at a lower field value (-150 Oe) than the coercive field of the electrodes (see figures 7-25 (left)). At enough high bias voltages a "conventional" positive TMR is observed, and by sweeping the field the resistance changes from HR state to a state of still higher resistance (Figure 7-24 right) between the top and bottom electrodes coercive fields. This negative-like TMR contribution is in striking contrast with previous results on junctions with manganite electrodes for which TMR is always positive [46].

The same response is observed at different temperatures inside the range (90 K < T < 100 K); the crossover bias for which the negative-like TMR contribution appears increases as the temperature is increased. As previously mentioned, at intermediate temperatures (i.e. 94 K), the conventional (positive-only) TMR is observed at low and high voltages (Figure 7-24 measurements at 5 mV, 250 mV and 450 mV) while the negative-like TMR contribution is observed at intermediate voltages (Figure 7-24 measurements from 20 mV to 150 mV). It is important to note that the resistance value in the LR *R(-150 Oe)* is almost equal to the high field resistance *R(4 kOe)* in the parallel magnetic configuration state.

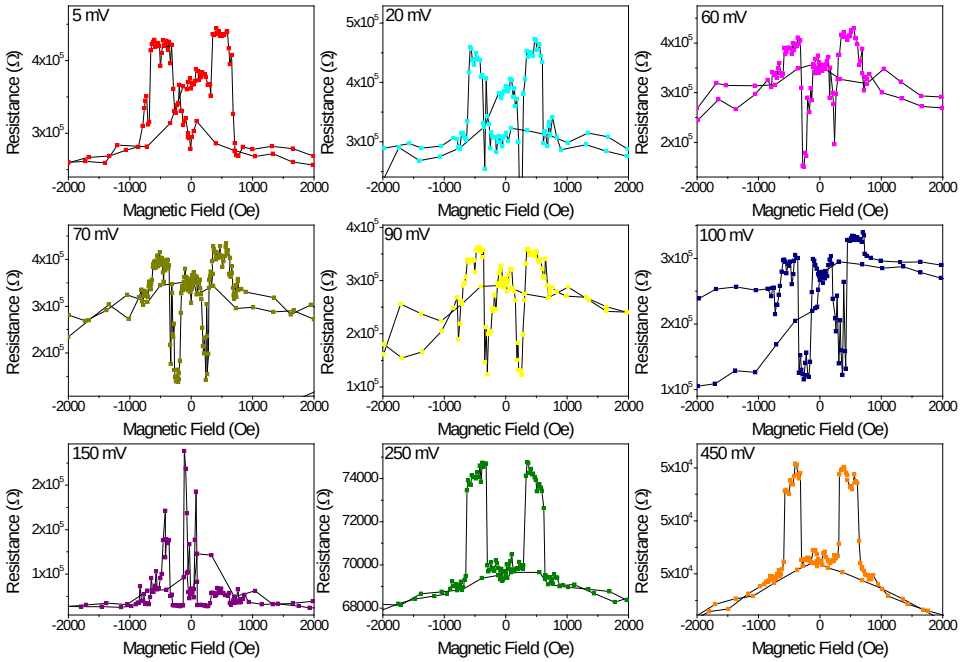

Figure 7-24. *R(H)* for LPL22A/2M measured at voltages ranging from 5 to 450 mV at 94 K

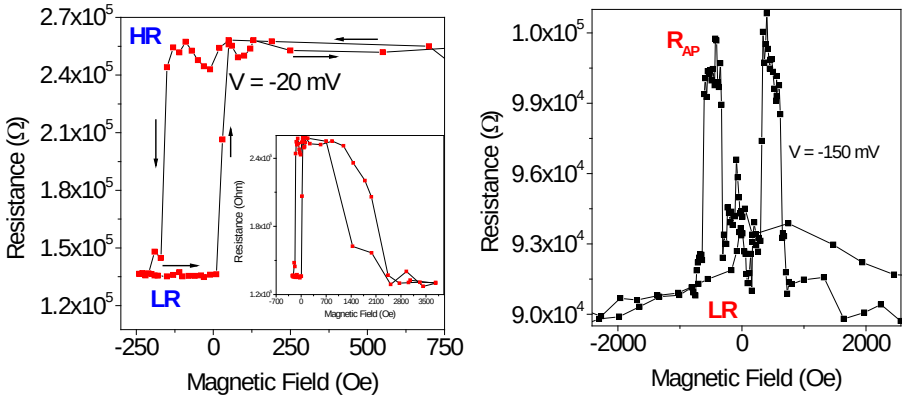

Figure 7-25. 92 K TMR for LPL22A/2M at (left) -20 mV, inset shows the same data in a wider field range, and (right) -150 mV

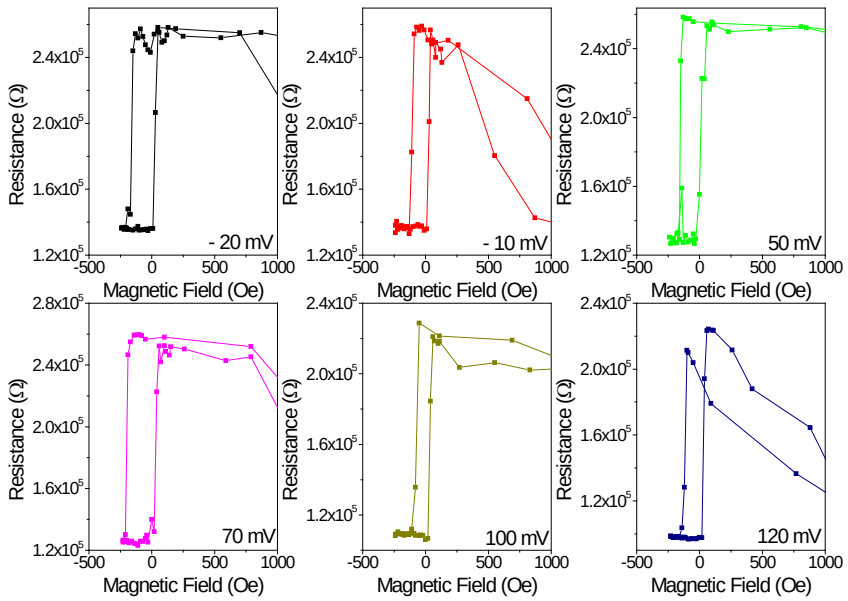

Figure 7-26. 92 K *R(H)* measurements from LPL22a/2M at voltages lower than 150 mV

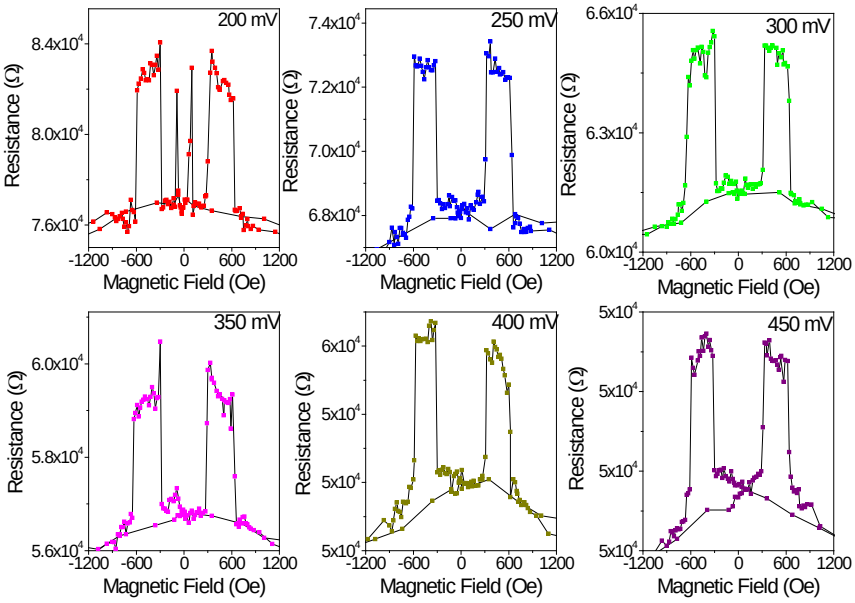

Figure 7-27. 92 K *R(H)* measurements for LPL22A/2M at voltages higher than 150 mV

Figure 7-26 and Figure 7-27 show the same scenario at 92 K, where the negative-like TMR contribution is observed for $V \leq 120$ mV and it is not observed when measurement voltage is $V \geq 150$ mV. Figure 7-28 illustrates the negative-like TMR

contribution observation at 100 K, where its voltage range has changed, now conventional TMR is observed whenever $|V| \leq 80$ mV, and negative-like TMR contribution is observed for $|V| \geq 250$ mV.

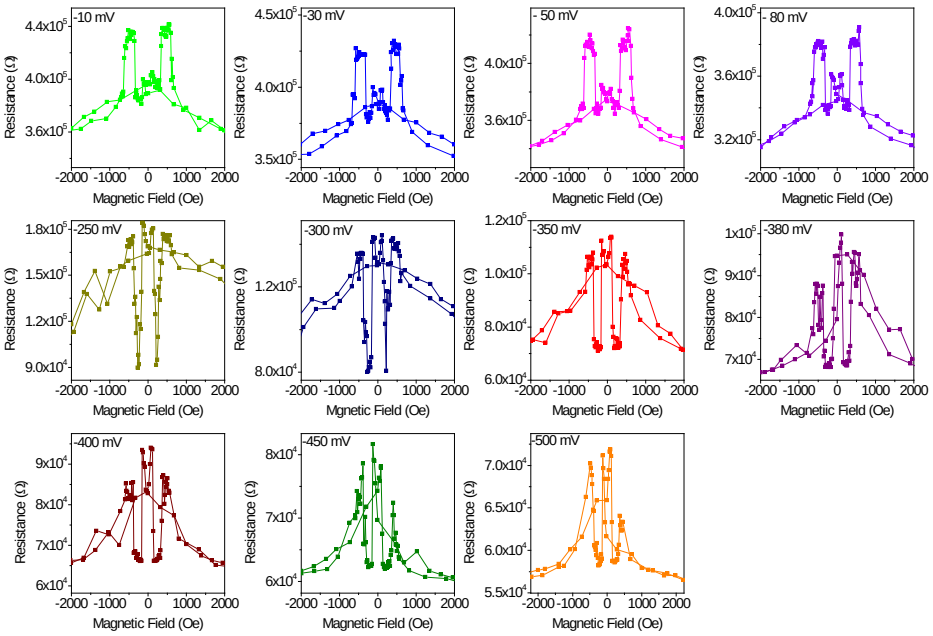

Figure 7-28. 100 K *R(H)* measurements LPL22A/2M at voltages from -10 mV to -500 mV

Both HR and LR states are obtainable at zero magnetic field as shown in Figure 7-26. i.e., after reaching any of those in a *R(H)* sweep, magnetic field can be ramped down and they remain stable at zero field.

Figure 7-29 shows the *I(V)* curves in both states at 92 K, 94 K, and 100 K; blue curves were measured when HR was the initial state and red curves were obtained when started at LR.

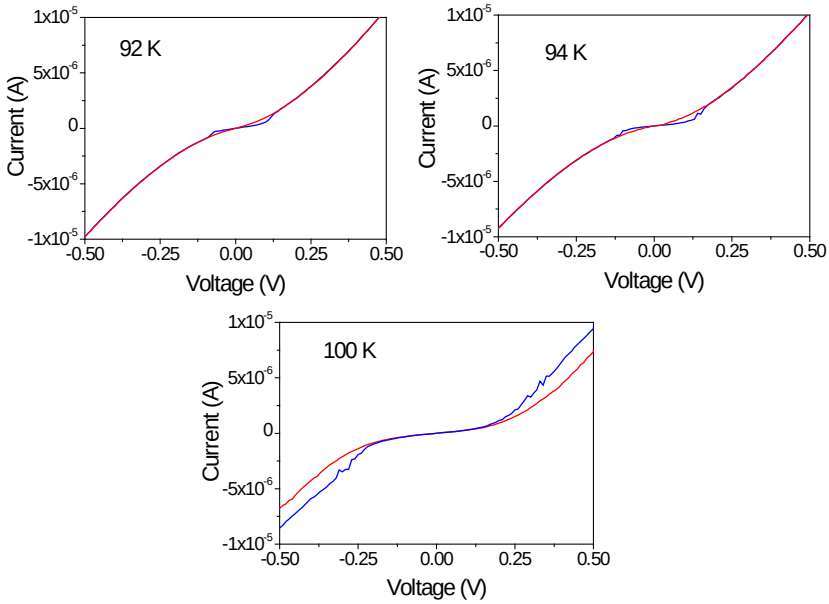

Figure 7-29. *I(V)* curves measured in high resistance state (blue) and low resistance state (red) at 92 K, 94 K and 100 K

In order to quantify the negative-like TMR contribution, Figure 7-30 shows *TMR(V)* calculated as $TMR = 100\left(\frac{I_{HR}}{I_{LR}} - 1\right)$.

TMR(V) calculated from Figure 7-29 *I(V)* curves with the above relation (lines in Figure 7-30), and the calculated from *R(H)* curves (symbols in Figure 7-30) show good agreement with each other with a virtually symmetric dependence obtained; thus the negative-like TMR contribution calculated is meaningful as its quantification proves reproducible.

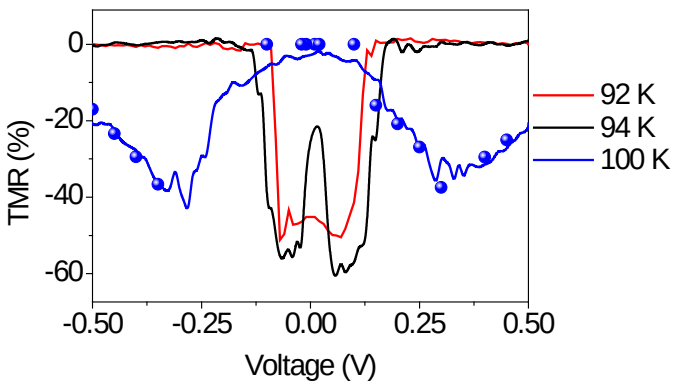

Figure 7-30. High temperature negative-like *TMR(V)* obtained from *I(V)* curves at (red line) 92 K, (black line) 94 K and (blue line) 100K; and as calculated from 100 K *R(H)* (blue symbols)

I(V) curves were measured sweeping the applied bias from negative to positive (and vice versa) and hysteretic behavior was found for the *I(V)* curve measured at HR state, while LR *I(V)* curves were perfectly reversible (see Figure 7-31 left). This hysteretic *I(V)* curve in HR state differs fundamentally from what has been found and is expected in conventional MTJs. This hysteretic *I(V)* curve thus contains two different accessible states that can be reached by simply changing the applied electric field at zero magnetic field. In fact, the observed *I(V)* hysteresis is reminiscent of the MTJs fabricated with materials that exhibit *magneto-electric* coupling [47], although this set of experiments do not provide conclusive evidence about the presence of such a phenomenon. Similar results were obtained at different temperatures, as shown in Figure 7-32, it can be observed how 93 K and 100 K *I(V)* curves display similar hysteresis behavior, with the hysteretic characteristic shifting towards higher applied voltages as temperature increases.

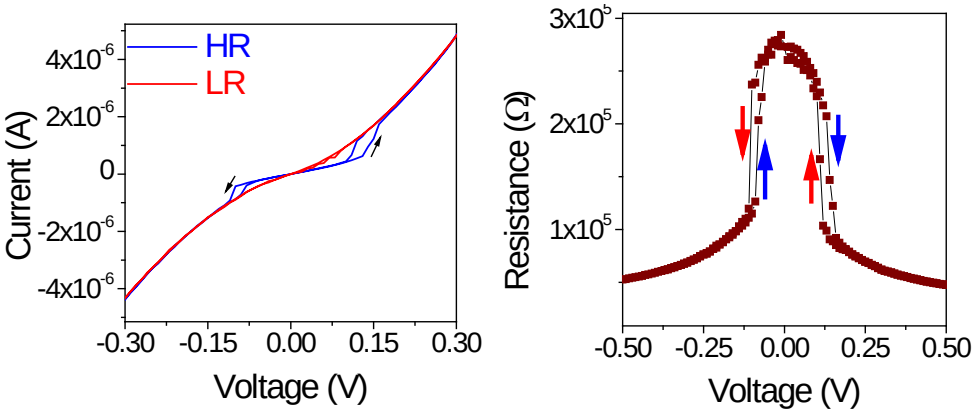

Figure 7-31. 93 K (left) *I(V)* curves recorded in HR state (blue) and LR state (red) at 93 K, and (right) calculated *R(V)* for the HR state

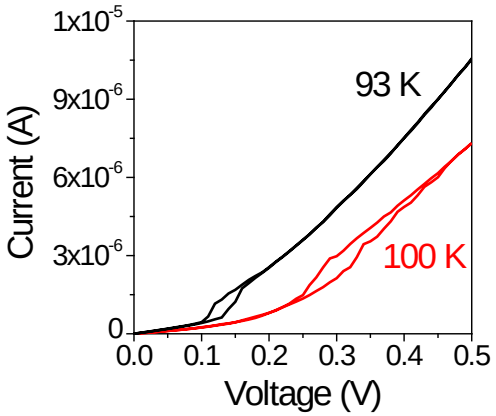

Figure 7-32. HR state *I(V)* curves measured at (black) 93 K and (red) 100 K

Further knowledge about the electric field-induced state switching in LPL22A/2M MTJ is desirable; up to this point LR and HR states were shown to be stable at zero magnetic field with *R(H)* minor loops, and different *I(V)* transport characteristics depending on the initial state were measured; now it is worthy to explore the possibility of having resistance state switching by only changing the applied voltage at zero magnetic field in the *I(V)* curves hysteretic region.

At 95 K and zero magnetic field the *I(V)* hysteretic region contains the value 130 mV, then a voltage sweep is carried on from -500 mV up to 130 mV, at that voltage value a *R(H)* curve is measured and the obtained measurement is shown in Figure 7-33 in red squares, then the resistance state obtained for zero magnetic field is

HR. The second voltage sweep starts at -500 mV up to 500 mV and then goes down to 130 mV, at that voltage value a *R(H)* curve is measured and the result is shown in Figure 7-33 in blue triangles, then the zero magnetic field resistance state obtained is LR. Open symbols in Figure 7-33 show the *R(H)* curve after the first voltage sequence, but with magnetic field changing in the opposite direction. Both voltage sequences were executed under *zero* applied magnetic fields. Note that both resistance states are stable; HR state switches to LR at $H = \pm 110$ Oe, and LR destabilizes at -340 Oe.

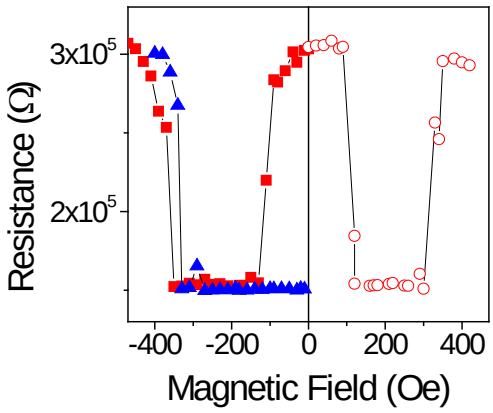

Figure 7-33. 95 K *R(H)* curves obtained with 130 mV after voltage sweeps, from -500 mV up to 130 mV (red squares), and from -500 mV up to 500 and then down to 130 mV (blue triangles). Both curves started at H = 0

In order to understand the origin of the observed phenomena, interface magnetic configuration is explained in the next section.

7.7 X-Ray Magnetic Circular Dichroism

XMCD experiments were carried out by Yaohua Liu and Suzanne G.E. te Velthuis at the Advanced Photon Source (APS) Argonne National Laboratory (ANL) on the samples LPL18 (50 nm bottom LCMO) and LPL23 (15 nm bottom LCMO) with applied field along both magnetocrystalline anisotropy directions [100] and [110]. While Total Electron Yield (TEY) and Fluorescence Yield (FY) data were found to be noisy, XMCD Reflectivity results clearly shows an induced magnetic moment in Cu at the interfaces. Note that neither XMCD reflectivity signal nor its sign are proportional to the material magnetization, and thus the Y axis representation is always shown in arbitrary units.

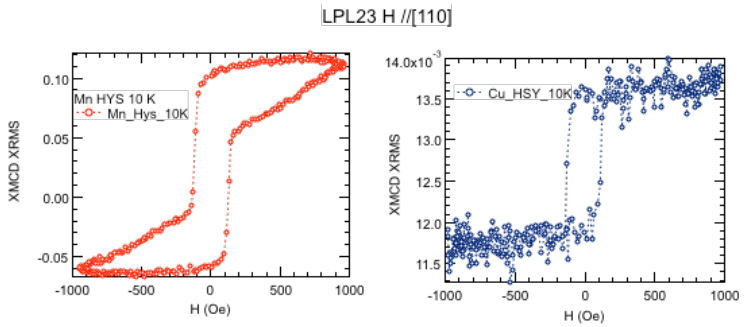

Figure 7-34. XMCD hysteresis loops for Mn *L2*-edge (left) and Cu *K*-edge (right)

Figure 7-34 shows Mn *L2*-edge (left) and Cu *K*-edge (right) XMCD hysteresis loops at 10 K and applied field along [110] for sample LPL23. Figure 7-35 also shows Mn *L2*-edge (left) and Cu *K*-edge (right) XMCD hysteresis loops, but with applied field along [100] for 10 K (upper loops) and 20 K (down loops). Magnetic moment is observable in both atoms Mn and Cu at low temperature, and their relative alignment is antiferromagnetic. When applied field is [110] oriented the Mn hysteresis loop has high remanence. According to the anisotropy determination from PNR experiments, the top layer switches quickly ($|H| < 200$ Oe) and the bottom Mn contribution can be observed in the almost linear magnetization increase (200 Oe < $|H|$ < 1000 Oe). As the barrier thickness is small (2 u.c.) the

bottom Mn signal can be also probed, and the linear contribution corresponds to bottom Mn atoms switching along their hard axis.

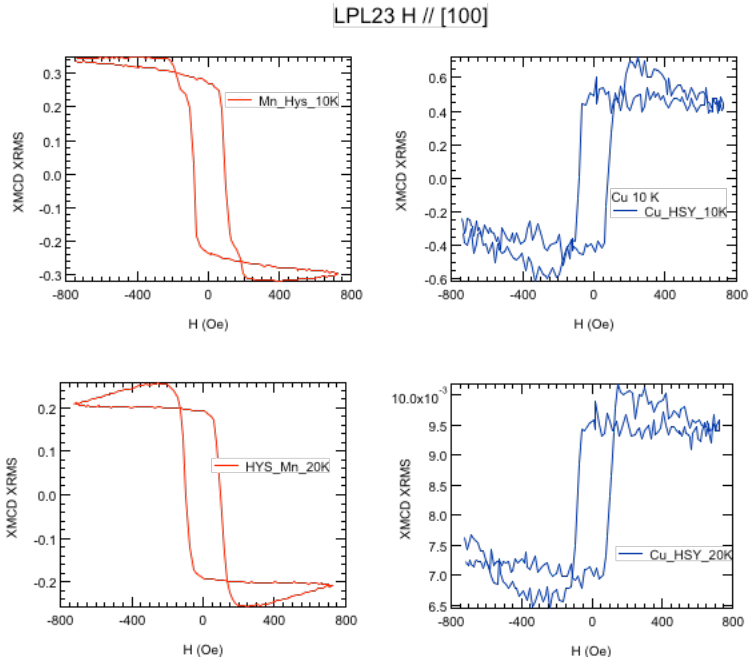

Figure 7-35 XMCD hysteresis loops for Mn L2-edge (left) and Cu K-edge (right)

Figure 7-36 shows energy scans at the Cu *K*-edge, the dichroic signal is different from zero (red is 60 Oe and blue is -60 Oe above 10 K, at 10 K red is 740 Oe and blue is -740 Oe) in the temperature range 10 K < *T* < 60 K. These measurements show how Cu presents induced magnetic moment due to the interaction with the interfacial Mn atoms in antiferromagnetic alignment. Above 60 K there is no induced Cu moment detected in this sample, although it is not clear the reason why, since it has been detected in similar samples up to the Curie temperature of the manganite.

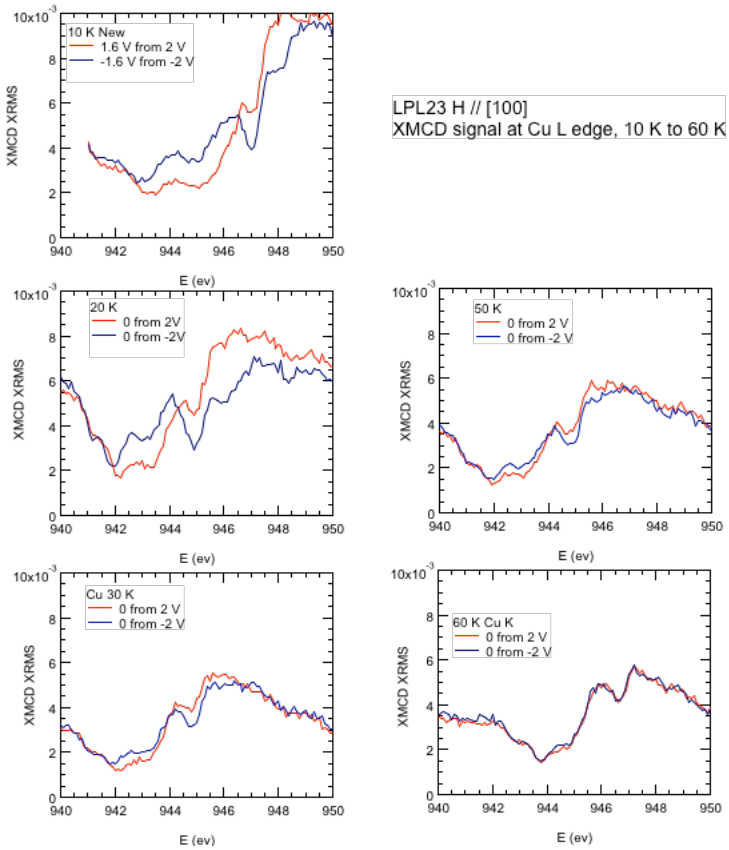

Figure 7-36. Energy scans at the Cu K-edge at temperatures 10 K ≤ T ≤ 60 K

As XMCD probing depth decays exponentially with thickness, the trilayer sample is used to predominantly measure the top PBCO \LCMO interface, but in order to measure the bottom LCMO \PBCO interface a bilayer (LP01B) was also measured. Figure 7-37 shows LP01B XMCD hysteresis loops measured at Mn *L*-edge, Cu *L*-edge and O *K*-edge; the presence of O *K*-edge hysteresis signal, and the antiferromagnetic alignment between Cu and Mn moments, indicate that super-exchange is the phenomenon leading the interfacial magnetic interaction. Hysteresis loops were measured at 10 K, and the magnetic signal at the Cu *L*-edge was observed up to the Mn Curie temperature, indicating that the Cu magnetic moment is induced by the neighboring Mn atom.

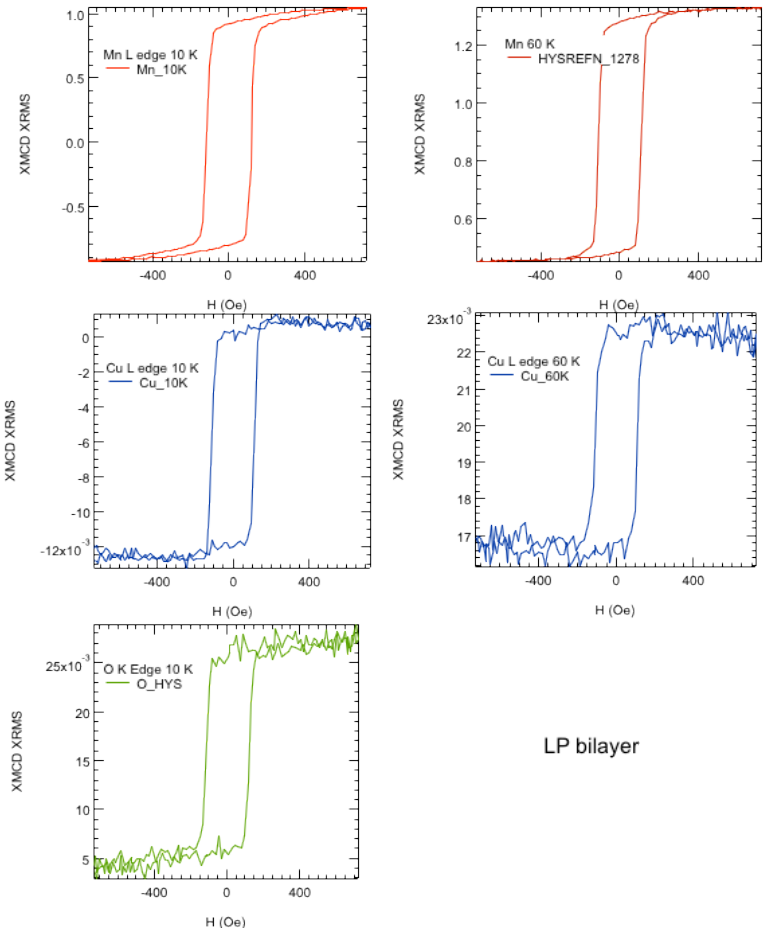

Figure 7-37. LP01B bilayer XMCD hysteresis loops measured at Mn *L2*-edge (upper panel), Cu *L*-edge (medium panel) and O *K*-edge (bottom) at 10 K (left) and 60 K (right)

7.8 Discussion

In order to understand the observed behavior in TMR bias and temperature dependence, magnetic interactions shall be analyzed. It has been shown that one of the leading interactions present is magnetocrystalline anisotropy, where the different biaxial easy axis for top and bottom electrodes avoids perfect magnetic parallel alignment states at low magnetic fields. As the last experiment evidenced, there is also a competing interaction that seems controlled by the electric field; and XMCD experiments evidenced an induced magnetic moment in the Cu at the interface.

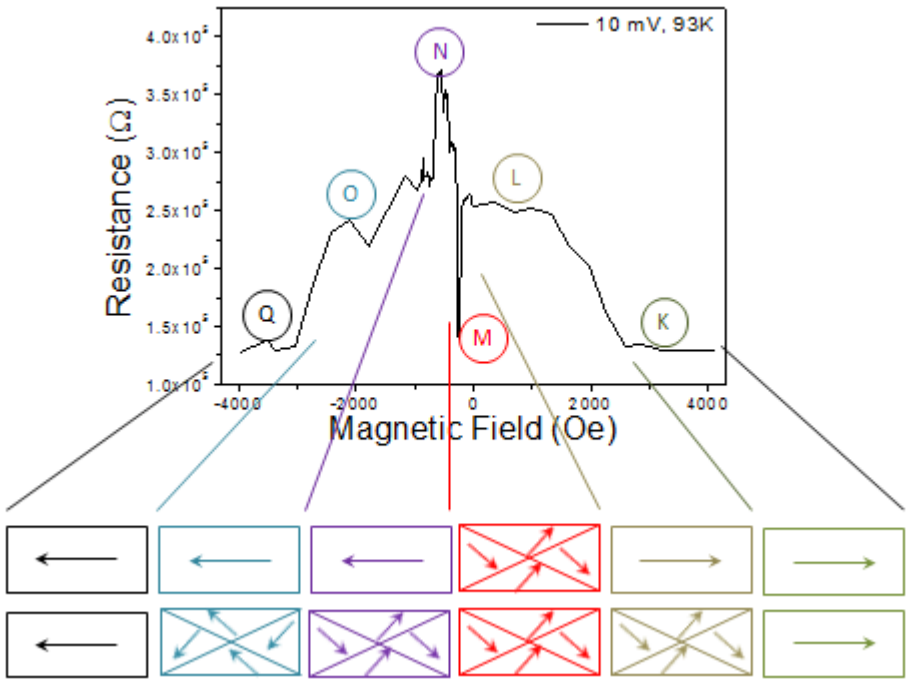

Figure 7-38. Half *R(H)* loop, the below boxes represent the layers magnetization configuration providing the observed resistance changes

Figure 7-31 right evidenced that the electric field induces a transition from a HR state (labeled "L" at Figure 7-38) into a lower resistance state (labeled "M" at Figure 7-38, note that this state is not equal to LR state labeled "K" at Figure 7-38), and that this transition is hysteretic in electric field. On the other hand *I(V)* curves

in the LR state remain always in that state. It is thus evident that although the high bias voltage resistance levels (Figure 7-29) coincide in the *I(V)* curves, they cannot be from the same LR state because in one of them (red curve) the transition to the high resistance HR state at low bias is not observed. Using the same representation used in Figure 7-15, Figure 7-38 represents the scenario explaining the resistance changes in terms of magnetic configurations of the layers, with the difference that the Figure 7-38 half *R(H)* loop was measured with the magnetic field applied along [110] direction, now the top layer is magnetized along its easy axis and the bottom layer is magnetized along its hard axis; thus, bottom layer tends to be broken in domains in order to follow its magnetic easy axis while the total layer magnetization follows the external magnetic field. Note that "K" and "M" states present the same resistance level, although their magnetic configuration corresponds to two mono-domain layers at "K" state, and two multi-domain layers at "M" state. Thus the *I(V)* curves measured at zero magnetic field show how the applied voltage changes the magnetic configuration from the state labeled "M" to the state labeled "L" and vice versa.

As already stated at the Motivation Section, it is known from the previous work by Chakhalian et al. [11] that orbital reconstruction becomes active at the cuprate-manganite interfacial $3z^2$ level, these orbitals hybridize at both sides of the interface, as a result the antibonding $3z^2$ orbital has higher energy than the x^2-y^2 cuprate levels and the Cu hole occupies the up spin antibonding orbital. This is the phenomenon responsible of the antiferromagnetic character (superexchange interaction), consequently, of the coupling strength dependence on electric field. Increasing bias would align the Cu hole (in the up spin orbital) with the Mn $3z^2$ level. This energy shift is possible due to a large interface resistance expected at these interfaces. It is then proposed that electric field modulates coupling strength between electrodes, mediated by the Cu electrons interface-induced spin polarization.

Salafranca and Okamoto [10] have theoretically found the Cu induced moment length scale in manganite-cuprate interfaces, over a 1 to 3 unit cells magnetic coherence length was found with an exponentially decaying tail determined by the *c*-direction hopping rate. Interfacial effective coupling field is very strong (several hundred Tesla) and clamps the Cu moment in antiparallel direction to the neighboring Mn atom, effective coupling field decays exponentially as distance from the interface increases. For thin barrier thicknesses, each interfacial Cu interacts with its first-neighboring Mn exchange field, besides the exchange field from the opposite interface Mn atom. As a result, there is the possibility of magnetic coupling through Cu moments at the barrier; therefore, the equilibrium Mn moments relative orientation at both electrodes will be determined by two competing energy scales: ferromagnetic coupling and magnetic anisotropy, and the electric field may modify the balance between both interactions and induce magnetization state switching at the electrodes.

When the Cu hole (at the up spin antibonding orbital) and the Mn $3z^2$ orbitals are aligned, resonant transport through barrier localized states may occur, yielding a form of double exchange interaction with dissimilar atoms as described in [10]. This double exchange interaction will tend to ferromagnetically align the up spin Cu band and the polarizing electrode Mn band and thus will favor antiferromagnetic alignment between Mn spins and Cu. This interaction exerts a torque on the electrode moment favoring electrodes ferromagnetic coupling. Most likely bottom layer flips because it is magnetically softer, as found in PNR measurements.

I(V) curves hysteretic behavior (Figure 7-31 and Figure 7-32) could be originated by interface charge trapping, although it is also possible an induced electric polarization resulting from the breakdown of inversion symmetry at the interface (in the sense described by Rondinelli et al. in [48]). Spin transfer can be ruled out as the ferromagnetic coupling source since: 1) the current densities values are too

small (10^{-6} A/100x10^{-8} cm^2 = 1A/ cm^2) and 2) the effect is symmetric under inversion of the current direction.

Concerning the narrow temperature range over which this effect is observed, it occurs only at temperatures close to the top layer Curie temperature (between 90 K and 100 K), because only at these high temperatures the magnetic anisotropy is small enough to compete with the ferromagnetic interaction. At lower temperatures anisotropy dominates and a perfectly parallel magnetization state is never stabilized, providing also an explanation for the low temperature TMR suppression.

7.9 Summary

The non-superconducting cuprate PBCO was used as a tunnel barrier for manganite (LCMO\ PBCO\ LCMO) MTJs; PBCO is known to be a semiconductor with localized electrons at the CuO_2 planes. In sufficiently thin barriers the induced moment at interfacial Cu atoms may yield a novel form of magnetic coupling between both manganite electrodes, mediated by the localized (spin polarized) Cu electrons in the CuO_2 planes.

It was shown how an electric field can be used to access different resistance states that can be switched under zero applied magnetic fields. These results constitute an example of electric-field-controlled magnetization switching with zero applied magnetic field which has never been observed before in MTJs.

7.10 References

[1] M. Viret, M. Drouet, J. Nassar, J. P. Contour, C. Fermon, and A. Fert, Europhysics Letters 39 (1997) 545.

[2] J. H. Park, E. Vescovo, H. J. Kim, C. Kwon, R. Ramesh, and T. Venkatesan, Physical Review Letters 81 (1998) 1953.

[3] P. H. Hor, R. L. Meng, Y. Q. Wang, L. Gao, Z. J. Huang, Z. Bechtold, K. Forster, and C. W. Chu, Physical Review Letters 58 (1987) 1891.

[4] V. Nekvasil, Journal of Magnetism and Magnetic Materials 140-144 (1995) 1265.

[5] S. Uma, W. Schnelle, E. Gmelin, G. Rangarajan, S. Skanthakumar, J. W. Lynn, R. Walter, T. Lorenz, B. Büchner, E. Walker, and A. Erb, Journal of Physics : Condensed Matter 10 (1998) L33.

[6] H.-D. Jorstarndt, Physical Review B 46 (1992) 14872.

[7] M. E. López-Morales, D. Ríos-Jara, J. Tagüeña, R. Escudero, S. L. Placa, A. Bezinge, V. Y. Lee, E. M. Engler, and P. M. Grant, Physical Review B 41 (1900) 6655.

[8] H. D. Yang, M. W. Lin, C. K. Chiou, and W. H. Lee, Physical Review B 46 (1992) 1167.

[9] R. Fehrenbacher and T. M. Rice, Physical Review Letters 70 (1993) 3471.

[10] J. Salafranca and S. Okamoto, Physical Review Letters 105 (2010) 256804.

[11] J. Chakalian, J. W. Freeland, H. U. Habermeier, G. Cristiani, G. Khaliullin, M. v. Veenendaal, and B. Keimer, Science 318 (2007) 1114.

[12] C. Visani, in Applied Physics, Vol. PhD in Physics, Universidad Complutense de Madrid, Madrid, 2010.

[13] S. Yunoki, A. Moreo, E. Dagotto, S. Okamoto, S. S. Kancharla, and A. Fujimori, Physical Review B 76 (2007) 064532.

[14] F. C. Zhang and T. M. Rice, Physical Review B 37 (1988) 3759.

[15] S. J. Pennycook, M. F. Chisholm, D. E. Jesson, D. P. Norton, D. H. Lowndes, R. Feenstra, H. R. Kerchner, and J. O. Thomson, Physical Review Letters 67 (1991) 765.

[16] M. S. Louis-Weber, V. P. Dravid, and U. Balachandran, Physica C 243 (1995) 273.

[17] H. W. Zandbergen, C. Hetherington, and R. Gronsky, Journal of Superconductivity 1 (1988) 21.

[18] J. Z. Sun, D. W. Abraham, R. A. Rao, and C. B. Eom, Applied Physics Letters 74 (1999) 3017.

[19] N. M. Nemes, M. García-Hernandez, Z. Szatmári, T. Fehér, F. Simon, C. Visani, V. Peña, C. Miller, J. García-Barriocanal, F. Bruno, Z. Sefrioui, C. León, and J. Santamaría, IEEE Transactions on Magnetics 44 (2008) 2926.

[20] V. Peña, in Applied Physics, Vol. PhD Physics, Universidad Complutense de Madrid, Madrid, 2005, p. 165.

[21] A. Hoffmann, S. G. E. t. Velthuis, Z. Sefrioui, J. Santamaría, M. R. Fitzsimmons, S. Park, and M. Varela, Physical Review B 72 (2005) 140407.

[22] Z. Sefrioui, V. Cros, A. Barthelemy, V. Peña, C. León, J. Santamaría, M. Varela, and S. J. Pennycook, Applied Physics Letters 88 (2006) 022512.

[23] V. Peña, Z. Sefrioui, D. Arias, C. León, J. Santamaria, M. Varela, S. J. Pennycook, M. Garcia-Hernandez, and J. L. Martinez, Journal of Physics and Chemistry of Solids 67 (2006) 472.

[24] A. Alberca, N. M. Nemes, F. J. Mompean, N. Biskup, A. d. Andres, C. Munuera, J. Tornos, C. Leon, A. Hernando, P. Ferrer, G. R. Castro, J. Santamaria, and M. Garcia-Hernandez, Physical Review B 84 (2011) 134402.
[25] J.-P. Renard and M. Velázquez, European Physical Journal B 34 (2003) 41.
[26] J. O'Donnell, M. S. Rzchowski, J. N. Eckstein, and I. Bozovic, Applied Physics Letters 72 (1998) 1775.
[27] T. K. Nath, R. A. Rao, D. Lavric, C. B. Eom, L. Wu, and F. Tsui, Applied Physics Letters 74 (1999) 1615.
[28] I. C. Infante, J. O. Ossó, F. Sánchez, and J. Foncuberta, Applied Physics Letters 92 (2008) 012508.
[29] A. M. Haghiri-Gosnet, J. Wolfman, B. Mercey, C. Simon, P. Lecoeur, M. Korzenski, and M. Hervieu, Journal of Applied Physics 88 (2000) 4257.
[30] M. Bowen, J.-L. Maurice, A. Barthélémy, M. Bibes, D. Imhoff, V. Bellini, R. Bertacco, D. Wortmann, P. Seneor, E. Jacquet, A. Vaurès, J. Humbert, J.-P. Contour, C. Colliex, S. Blügel, and P. H. Dederichs, Journal of Physics : Condensed Matter 19 (2007) 315208.
[31] H. Ibach, Physics of Surfaces and Interfaces, Springer-Verlag, Berlin, 2006.
[32] E. Dagotto, Nanoscale phase separation and colossal magnetoresistance: the physics of manganites and related compounds, Springer, 2003.
[33] Y. Tokura, Colossal magnetoresistive oxides, Gordon and Breach Science Publishers, 2000.
[34] I. O. Troyanchuk, Journal of Experimental and Theoretical Physics 75 (1992) 132.
[35] S. Yunoki, J. Hu, A. L. Malvezzi, A. Moreo, N. Furukawa, and E. Dagotto, Physical Review Letters 80 (1998) 845.
[36] S. Jin, T. H. Fiefel, M. McCormack, R. A. Fastnacht, R. Ramesh, and L. H. Chen, Science 264 (1994) 413.
[37] M. B. Stearns, Journal of Magnetism and Magnetic Materials 5 (1977) 167.
[38] D. J. Craik and R. S. Tebble, Reports on Progress in Physics 24 (1961) 116.
[39] H. Boschker, J. Kautz, E. P. Howman, G. Koster, D. H. A. Blank, and G. Rijnders, Journal of Applied Physics 108 (2010) 103906.
[40] G. Singh-Bhalla, A. Biswas, and A. F. Hebard, Physical Review B 80 (2009) 144410.
[41] G. Singh-Bhalla, S. Selkur, T. Dhakal, A. Biswas, and A. F. Hebard, Physical Review Letters 102 (2009) 077205.
[42] K. H. J. Buschow and F. R. d. Boer, Physics of Magnetism and Magnetic Materials, Kluwer Academic, New York, 2003.
[43] J. S. Moodera, X. Hao, G. A. Gibson, and R. Meservey, Physical Review Letters 61 (1988) 637
[44] E. Y. Tsymbal, O. N. Mryasov, and P. R. LeClair, Journal of Physics : Condensed Matter 15 (2003) R109.
[45] S. Zhang, P. M. Levy, A. C. Marley, and S. S. P. Parkin, Physical Review Letters 79 (1997) 3744.
[46] M. Bibes and A. Barthelemy, IEEE Transactions on Electron Devices 54 (2007) 1003.
[47] V. Garcia, M. Bibes, L. Bocher, S. Valencia, F. Kronast, A. Crassous, X. Moya, S. Enouz-Vedrenne, A. Gloter, D. Imhoff, C. Deranlot, N. D. Mathur, S. Fusil, K. Bouzehouane, and A. Barthélémy, Science 327 (2010) 1106.

[48] J. M. Rondinelli, M. Stengel, and N. A. Spaldin, Nature Nanotechnology 3 (2008) 46.

8 CONCLUSIONS

The experiments conducted along this thesis were aimed to the development and study of magnetic tunnel junctions based on new interface states and artificially induced interface states emerging at complex oxides heterostructures. Novel functionalities were obtained in oxide-based spintronics devices, and these results contribute to the understanding of the subtle details behind the unexpected found phenomena, as the induced ferromagnetism in LC7MO\ LCMO interface, or the important role played by the localized Cu hole in the manganite-cuprate interface orbital hybridization in the ferromagnetic coupling between electrodes in LCMO\ PBCO\ LCMO magnetic tunnel junctions. The particular and detailed conclusions of each experiment described in this thesis work are listed below.

LCMO epitaxial layers were grown on NSTO substrates by using a high oxygen pressure sputtering system, and their high structural quality was confirmed by x-ray diffraction and reflectivity techniques. Micron-size features were defined by the junction fabrication process designed in order to measure transport perpendicular to the NSTO\ LCMO interface. The current-voltage characteristics of these junctions were analyzed and well described in terms of the Schottky model. Assuming a thermionic emission transport mechanism, the Schottky barrier height values and the ideality factor are found to be physically meaningless, since they are outside the range expected for the model. However, good agreement was found between experimental data and the theoretical model by using a thermally assisted tunneling mechanism for electronic transport, in particular when considering an approach presented in this thesis for the first time taking into account that the dielectric permittivity of STO is temperature dependent [1].

In a previous work by Barriocanal et al. [2, 3] an interfacially-induced magnetic moment was reported between two nonmagnetic and insulating materials (LMO\ STO). In order to explore this new electronic state as a possible insulating barrier in magnetic tunnel junctions, STO\\ LSMO\ STO\ LMO\ STO\ LSMO heterostructures were grown using a high oxygen pressure sputtering system. A high structural quality of these heterostructures was determined by x-ray diffraction and reflectivity techniques. Electron microscopy characterization evidenced coherent layers over large lateral distances, with neither interdiffusion nor obvious pinholes. The AC magnetic susceptibility characterization revealed the top and bottom LSMO layers magnetic transitions, besides the STO\ LMO\ STO magnetic transition that was observed at 60 K. The heterostructures were processed in order to define micron sized MTJs, and the magneto-transport characteristics exhibited TMR almost temperature independent for the voltage range 200 mV < V < 400 mV below 60 K. At lower voltages the maximum TMR obtained was 100 %, observed at 15 K and 10 mV; this maximum is followed by a rapid *TMR(T)* decrease up to 135 K where TMR reaches its zero value. This characteristic set leads to conclude that the magnetic state induced at the STO\ LMO\ STO trilayer is responsible for the high temperature TMR stability up to 60 K. It is then demonstrated how the use of engineered interfaces can increase the devices magneto-transport performance. Particularly this result leaves an open new branch for future research using artificial states as an active element in complex oxide devices, with a large set of unexplored possibilities.

NSTO\\ LC7MO\ LCMO bilayers (SFJs) and STO\\ LCMO\ LC7MO\ LCMO heterostructures were grown using a high oxygen pressure sputtering system, and their structural quality was checked by x-ray diffraction and reflectivity techniques. Electron microscopy characterization confirmed the

different Ca concentration in the middle LC7MO layer and chemical roughness lower than one atomic step, without obvious pinholes observable. Micron-size featured junctions were patterned using the fabrication process to define pillars as spin filter junctions (SFJs) and magnetic tunnel junction (MTJs) devices. The SFJs magneto-transport characteristics exhibited TMR with a maximum magnitude of 20 % at 60 K and 10 mV. When increasing temperature up to 140 K the TMR diminishes, and above this temperature there is no TMR observable. The *R(T)* characteristics shows two metal-insulator-transitions corresponding to both manganite layers at 250 K for LCMO and 140 K for LC7MO. The observed transport characteristics are only consistent under the spin filtering scenario since only one ferromagnetic-metallic layer is present at the devices. The most probable physical scenario corresponds to induced ferromagnetism at the ultrathin LC7MO layer or at the manganites (LC7MO\ LCMO) interface, in such a way that the transport is analogous to that coming from a device with an ultrathin-ferromagnetic-insulator. This is the first time for induced ferromagnetism evidenced at the LC7MO\ LCMO system by means of spin filtering [4], and this is also the first spin filter device based on complex oxides operating up to temperatures as high as 140 K (spin filtering is usually observed below 10 K).

In a previous report by Sefrioui et al. [5] LCMO\ PBCO\ LCMO MTJs were studied, and TMR was reported in the range 80 K < *T* < 110 K. In this thesis a comprehensive study of these MTJs was conducted. Besides different bottom electrode thicknesses were studied searching for the optimum ferromagnetic- metallic LCMO electrode thickness. LCMO\ PBCO\ LCMO trilayers were grown using a high oxygen pressure sputtering system, their structural quality was confirmed by x-ray diffraction and reflectivity techniques; electron microscopy confirmed coherent layers over large lateral distances without obvious pinholes observable. Polarized Neutron

Reflectivity evidenced the magnetocrystalline anisotropy for each layer, the bottom layer had [100] directed biaxial anisotropy, and the top layer had [110] directed biaxial anisotropy, resulting in misaligned magnetocrystalline anisotropies of the bottom and top manganite layers. This was identified as the reason for the TMR suppression observed at low temperatures, the high magnetocrystalline anisotropy dominates and the AP magnetic alignment state is not achievable. Only for higher temperatures the anisotropy energy can be counterbalanced by competing interactions. A non-conventional (in high magnetic fields ~ 2 KOe - 3 KOe) TMR contribution was observed and explained in terms of the magnetic anisotropy and the domain dynamics revealed by the PNR characterization.

A negative-like TMR contribution was observed for the temperature range 90 K < *T* < 100 K, with the particular characteristic of an unexpected state revealed by the magneto-transport characterization. This new state occurs at zero magnetic field and allows switching the resistance values from a high resistance state (different to the AP magnetic alignment resistance) to a low resistance state (magnetically different to the P magnetic state at high field, but electrically equivalent) by changing the applied electric field only. This is a highly relevant finding since lots of research efforts have been put in search of a zero magnetic field mechanism allowing resistance switching in order to diminish the devices power consumption and the advantages of getting rid of the magnetic field in the magnetic storage devices. X-ray magnetic circular dichroism was measured for interfacial magnetization characterization, and an induced magnetic-moment at the first Cu atoms was evidenced at the LCMO/ PBCO interface. Similarly to other manganite-cuprate studies reported [6] the Cu moment is observable as long as its first-neighboring-Mn atom exhibits magnetic moment. The negative-like TMR state is explained in terms of the ($3z^2$ antibonding orbital which is spin polarized) Cu hole

population being accessible by hole-band alignment electrically driven. The antiferromagnetic coupling between Mn and Cu moments at each interface would result in a ferromagnetic coupling interaction between both LCMO electrodes if PBCO barrier is thin enough. Finally, the hysteretic behavior of *I(V)* curves can be originated by interface charge trapping; this state is only observable at high temperatures because the interface ferromagnetic interaction is not able to compete at lower temperatures where the magnetic anisotropy dominates all the magneto-transport dynamics.

8.1 References

[1] K. A. Müller and H. Burkard, Physical Review B 19 (1979) 3593.

[2] J. Garcia-Barriocanal, F. Y. Bruno, A. Rivera-Calzada, Z. Sefrioui, N. M. Nemes, M. Garcia-Hernández, J. Rubio-Zuazo, G. R. Castro, M. Varela, S. J. Pennycook, C. León, and J. Santamaría, Advanced Materials 22 (2010) 627.

[3] J. Garcia-Barriocanal, J. C. Cezar, F. Y. Bruno, P. Thakur, N. B. Brookes, C. Utfeld, A. Rivera-Calzada, S. R. Giblin, J. W. Taylor, J. A. Duffy, S. B. Dugdale, T. Nakamura, K. Kodama, C. Leon, S. Okamoto, and J. Santamaria, Nature Communications (2010)

[4] Z. Sefrioui, C. Visani, M. J. Calderón, K. March, C. Carrétéro, M. Walls, A. Rivera-Calzada, C. León, R. L. Anton, T. R. Charlton, F. A. Cuéllar, E. Iborra, F. Ott, D. Imhoff, L. Brey, M. Bibes, J. Santamaria, and A. Barthelemy, Advanced Materials 22 (2010) 5029.

[5] Z. Sefrioui, V. Cros, A. Barthelemy, V. Peña, C. León, J. Santamaría, M. Varela, and S. J. Pennycook, Applied Physics Letters 88 (2006) 022512.

[6] J. Chakalian, J. W. Freeland, H. U. Habermeier, G. Cristiani, G. Khaliullin, M. v. Veenendaal, and B. Keimer, Science 318 (2007) 1114.